

# Structure and Stability of Biological Materials – Characterisation at the Nanoscale

Dissertation  
der Fakultät für Geowissenschaften  
der Ludwig-Maximilians-Universität  
München



vorgelegt von  
Marek Janko

München, 17.10.2011

Erstgutachter: Prof. Dr. Robert Stark  
Zweitgutachter: PD Dr. Albert Zink  
Disputation: 07.02.2012

# TABLE OF CONTENTS

|   |            |
|---|------------|
| <b>Table of Contents .....</b>  | <b>I</b>   |
| <b>Abstract .....</b>   | <b>III</b> |
| <b>1. Introduction .....</b>  | <b>1</b>   |
| 1.1 Decay and Preservation.....   | 1          |
| 1.2 The Iceman.....   | 3          |
| <b>2. Experimental Methods.....</b>   | <b>5</b>   |
| 2.1 Atomic Force Microscopy .....   | 5          |
| 2.1.1 Microscope Principle and Imaging Modes .....  | 5          |
| 2.1.2 Local Force Measurements.....   | 10         |
| 2.1.3 Contact Mechanics.....  | 12         |
| 2.2 Raman Spectroscopy.....   | 17         |
| 2.2.1 Scattering of Light in Matter .....   | 17         |
| 2.2.2 Raman Spectroscopy and Raman Effect.....  | 19         |
| 2.2.3 The Confocal Microscope Setup.....  | 21         |
| <b>3. Ancient Tissue Preservation .....</b>   | <b>23</b>  |
| 3.1 Collagen .....  | 23         |
| 3.1.1 Collagen-based Tissues and Properties.....  | 23         |
| 3.1.2 Formation and Stabilisation of Collagen .....   | 24         |
| 3.1.3 Characterisation of Recent Collagen .....   | 26         |
| 3.1.4 Preservation of Ancient Collagen .....  | 29         |
| 3.2 Red Blood cells .....   | 33         |
| 3.2.1 The Coagulation of Blood.....   | 33         |
| 3.2.2 RBC Preservation in Icemen Tissue .....   | 34         |
| 3.2.3 Secondary Conclusions from Iceman RBCs.....   | 37         |
| <b>4. Summary .....</b>   | <b>39</b>  |
| <b>5. Bibliography .....</b>  | <b>41</b>  |
| <b>6. List of Abbreviations.....</b>  | <b>50</b>  |
| <b>7. List of Figures .....</b>   | <b>51</b>  |
| <b>8. Publications.....</b>   | <b>54</b>  |
| 8.1 Anisotropic Raman scattering in collagen bundles.....   | 55         |
| 8.2 Nanostructure and mechanics of mummified type I collagen from the 5300-year-old Tyrolean Iceman ..... | 58         |
| 8.3 Preservation of 5300 year old Red Blood Cells in the Iceman .....                                     | 70         |
| 8.4 Blood platelet adhesion to printed von Willebrand factor .....  | 81         |
| 8.5 Raman spectroscopy of laser-induced oxidation of titanomagnetites.....                                | 88         |

|  |            |
|--|------------|
| <b>9. Appendix .....</b>   | <b>94</b>  |
| 9.1 Evidence of Dyschondrosteosis and Dicrocoeliasis in a Bog Body from<br>the Netherlands ..... | 95         |
| <b>Acknowledgements.....</b>   | <b>119</b> |
| <b>Curriculum Vitae .....</b>  | <b>120</b> |

## ABSTRACT

Mummies are witnesses of the past harbouring information about the lives and fates of our ancestors. By examining them, the conditions of living, dietary, lifestyle and cultural habits as well as maladies in ancient times can be revealed. Knowledge of these maladies can be used to ascertain the evolution of diseases and may be helpful in characterising and treating them today.

Uncovering information from mummies, however, depends on the preservation of the mummy tissue. Once degradation sets in, the molecular structure of the tissue is changed, and much information is lost. Favourable environmental conditions can slow down the process of decay and, hence, preserve organic material for long periods of time. As discussed in this work, biological tissue, which has substructural arrangements that are advantageous for withstanding mechanical load, might also be particularly favourable for preservation after the organism's death.

To address the question concerning the degree of preservation and to retrieve additional information from ancient tissue, two quasi-non-invasive analysis techniques, atomic force microscopy and Raman spectroscopy, were used. With these methods, the submicron structure, chemical composition, and nanomechanical properties of small mummified tissue samples were determined. In preliminary tests on recent collagen, the main connective tissue protein of vertebrates, results showed that in addition to imaging by atomic force microscopy, Raman spectroscopy is able to verify the alignment of this protein. Based on this knowledge, the arrangement and degree of collagen preservation in mummified human skin was investigated. Samples extracted from a 5300-year-old glacier mummy, the Iceman, were analysed. Extremely well-preserved collagen fibrils, in which the micro, ultra, and molecular structure were largely unaltered, were found. These results were in contrast, to the collagen fibrils found in the dermis of the Zweeloo mummy, a bog body of a female dating to the Roman period (78–233 AD). The Zweeloo mummy collagen fibrils showed moderate decomposition likely due to the acidic environment in the bog. Therefore, mummification due to freeze-drying, as in the Iceman, seems to be particularly beneficial for tissue preservation. The Iceman collagen, moreover, was found to be slightly stiffer than recent collagen, indicating that dehydration due to freeze-drying changed the mechanical properties of the tissue. This change likely improves the resilience of the freeze-dried collagen, stiffens the skin, and in turn maintains the skin's protective function that prevents the underlying tissue from decomposing.

Finally, also the preservation of red blood cells in wound tissue samples from the Iceman was observed. Single and clustered red blood cells were found whose morphological and molecular characteristics were similar to those of recent red blood cells. The ancient corpuscles moreover featured the typical red blood cell structure that indicates the preservation of healthy cells in Iceman tissue. Because fibrin, a protein formed during blood coagulation, was also detected, it appears that the clustered cells resembled remnants of a

blood clot. The structure of the blood clot, stabilised by fibrin, may have been a protective envelope, which prevented the red blood cells from decomposing. Nonetheless, Raman spectra of the cells provided first indications of slight red blood cell degradation.

These investigations emphasise the fundamental importance of the substructure and molecular arrangement of tissues, indicating that a tissue's overall function and stability correlate with its molecular properties, in particular, the degree of cross-linking and the arrangement of the tissue molecular constituents. Last but not least the results show that ancient tissue can be preserved and its molecular properties probed and addressed even after millennia.

# 1. INTRODUCTION

## 1.1 DECAY AND PRESERVATION

The process of fragmentation into molecular building blocks, defined as decay or decomposition, is common for biologic soft tissue. While anorganic materials of vertebrates such as hydroxyapatite in bone or tooth enamel are more resistant, organic compounds such as the proteins of the cytoskeleton or the phospholipid membrane of vertebrate cells are usually prone to decay because organic intra- and inter-molecular bonds are weaker than those in anorganic structures. The weaker bonding facilitates the decomposition of biological soft tissue, which is important because the disassembly of complex biological structures liberates their molecules and makes them available to be recycled in new living tissue [1].

Decay first and foremost arises from enzymatic activity. Usually, the enzymes involved in the decay of organic tissue emanate from the body's own cells. They originally catalyse various processes such as the digestion of nucleic acids, proteins, carbohydrates, and lipids. Once an organism dies, the cells are no longer supplied with nutrients and oxygen. Hence, also the cells perish, lose their capacity to regulate their enzymes, and are subsequently themselves digested or autolysed. In the later stages of decomposition, enzymes may also be secreted from bacteria that infest the dead. Additionally, non-enzymatic mechanisms such as environmental influences; the action of insects or other scavengers; or chemical changes, e.g., oxidation, hydrolysis, or esterification, can cause biomolecular degradation [1].

Nonetheless, fortunate circumstances may prolong the process of decay. If the enzymatic and non-enzymatic activities are slowed down or hindered by rapid desiccation, changes in the pH, low temperatures, or a protective environment, decomposition is decelerated [1]. Protective environments seem to be particularly beneficial for preserving biomolecules in fossil samples. Fragile organic substances can be protected in sandy lagerstätten from degradation by ultraviolet (UV) irradiation, oxidation, or changes in temperature and pH [2]. When additionally encapsulated within anorganic matrixes such as the mineral phase of bone or mineralised soft tissue [2; 3], organic biomolecules have been preserved in prehistoric samples as old as 80 million years. For example, protein fragments were found in fossilised bones of *Brachylophosaurus canadensis* [4], *Tyrannosaurus rex*, *Triceratops horridus* [5; 6], and *Mastodon*, and their peptide sequences have been identified [4; 7].

Contrary to fossilised tissue, in which anorganic minerals replace the majority of organic molecules, soft organic tissue can be found in considerable quantities in younger samples. Mummified tissue, dead organic tissue that was transferred into a state of arrested decay resembling the morphology of the living [1], is particularly rich in biomolecules. The process of mummification may thereby be the reason why biomolecules are so well preserved in some samples. The most common mechanism that causes mummification is desiccation, i.e., drying by the removal of water. Desiccation can occur spontaneously under suitable climatic conditions such as in dry, hot, or cold regions, which are typical of highlands [8] or deserts

[9]. Additionally, mummification can be induced by ventilation [10], i.e., a continuous or frequent airflow, as found in caves, crypts, or at high altitudes. Dehydration of the tissue may also occur spontaneously or artificially if the tissue encounters alcohol or salt (natron), which withdraws the water from it.

Revealing preserved prehistoric or ancient biomolecules is of utmost interest because uncovering their genetic code provides insight into evolutionary adaptation processes, evolutionary relationships between species [6; 11; 12], and the evolution of diseases [13; 14; 15]. For example, the characterisation of prehistoric collagen samples supported the bird-dinosaur clade [4], the analysis of ancient Neanderthal deoxyribonucleic acid (DNA) revealed that modern humans and Neanderthals diverged approximately 500,000 years ago [12], and preserved mammoth DNA revealed that mammoths were more closely related to Asian than to African elephants [16]. In addition, analysing preserved organic molecules can reveal the health status of an individual and aid in reconstructing living conditions millennia ago. Finally, uncovering ancient soft tissue can offer insights in the resistance to degradation of certain biomolecules, and investigating their composition or mechanical properties may provide insight on tissue preservation.

Although finding, identifying, and analysing ancient biomolecules is still challenging, this work addresses these issues and provides lessons learned from biomolecules found in the 5300-year-old tissue of the glacier mummy, the Iceman.



## 1.2 THE ICEMAN

In late summer of 1991, the melting snow and ice and retreating glaciers in the Alps uncovered a human corpse at an altitude of 3210 meters above sea level at the Tisenjoch in South Tyrol, Italy. The naturally mummified body of a man, the so-called *Iceman*, and several artefacts were found, lying distributed in an approximately 40-m long, 5- to 8-m wide and 2- to 3-m flat hollow in which they were presumably protected from being dragged and crushed by the glacier ice that slowly flowed across them. After recovery, radiocarbon dating (C-14) revealed that the man and the objects were witnesses of an era roughly 5300 years ago [17]. Thus, this mummy is one of the oldest human mummies worldwide. In addition to its historic age, the quantity and type of associated finds are unique.

The artefacts found with the mummy from the Tisenjoch appear to be ordinary equipment for daily use in late Neolithic times. The finds included the clothes that the mummy was dressed in (fur coat, leather leggings, leather belt, leather loincloth, fur moccasins, fur hat) [18] and several pieces of equipment such as a back-carrier frame, a bow, a quiver with arrows, and a hatchet with a copper blade, to name a few.

Moreover, the mummy itself attracts great interest because the corpse was extremely well preserved over the millennia. All body parts [19] as well as the skeletal and some nervous tissue components were found intact [20]. Analysis of tissue fatty acid profiles revealed that the Iceman was better preserved than much younger corpses buried in neighbouring glaciers [21]. Also, the gross structure of the mummy skin was intact, exhibiting the distinct layers of stratum corneum and the dermal skin layer, although the epidermis was missing [22]. While these results shed light onto the degree of preservation, several questions such as the process of mummification and the events leading to Iceman's death, still remain. In the cases of other freeze-dried mummies, for example, the crew members of the Franklin expedition found in the ice of the Canadian Arctic [23], the mummies of Scythian chiefs that were naturally preserved in ice lenses that arose within their kurgans (tombs) [24], and the mummified bodies of mammoths found in permafrost soil [25; 26], low temperatures coupled with tissue desiccation promoted mummification, preserving mummified tissue for up to some 10,000 years [27]. In the case of the Iceman, the situation seems to be slightly more complex. The Iceman is a wet mummy, with the body tissue being still moist. Thus, the mummy did not completely desiccate. Some theories account for this suggesting that the corpse was rapidly desiccated by wind, covered by a protecting layer of snow shortly afterward and subsequently enclosed in ice. Before or during the mummification, however, the body may have been exposed to water [21; 28]. Another theory suggests that the mummy was freeze dried and that most of the water in the frozen tissue was sublimated into air bubbles, which are commonly present in ice [1]. Both scenarios are conceivable, and even a combination of them is possible. Nonetheless, these theories are still under debate and remain to be clarified.

Finally, the obscure circumstances leading to the death of the man have to be addressed. Shortly after the Iceman's recovery, it was proposed that the man might have been in a state of exhaustion, had laid down, fallen asleep and froze to death with subsequent mummification as a consequence of adverse weather conditions [19]. Later, radiological analyses revealed a

series of fractures and fissures of the skull and ribs, which were interpreted as resulting from a violent conflict or an accident that the man suffered prior to his death [29]. This hypothesis was extended to a disaster theory proposing that the Iceman sustained physical injuries and the loss of or damage to parts of his equipment in unusual violent events [30]. Nowadays, it seems clear that the man died a violent death. Although some of the bone fractures may have been caused while the mummy was encased in or removed from the glacier ice, further X-ray examinations disclosed a hole in the left shoulder blade and an arrowhead in the mummy's thorax [31]. The arrowhead was surrounded by dense tissue interpreted as a haematoma. Pathologic investigations also revealed a fresh skin wound, presumably the arrowhead point of entry, on the Iceman's left back leading to a tunnel through the shoulder blade hole [31]. Further re-examinations of the mummy revealed another wound on the right hand [32]. Histological and histochemical analyses showed that the Iceman may have sustained this stab wound a few days before his death [32; 33]. The arrow wound and a small suffusion lesion on the back, however, seem to be fresh injuries that were not survived for long [33]. Although there was no direct determination of blood or its residuals in the wound tissue, which could clarify the chronological suffering of the injuries, the Iceman's cause of death was presumably the injury of the brachial artery by the arrowhead, which caused acute inner bleeding [33; 34].

These circumstances and discoveries make the Iceman an extremely valuable and interesting mummy for scientific investigations. In this work, the analysis of the Iceman's tissue is described. Molecular properties of preserved biomolecules were analysed and used to draw insights into their resistance to degradation. Moreover, some of the results confirm the Iceman's final trauma theory and provide an explanation for the overall tissue preservation. In the following chapter, the experimental methods used, atomic force microscopy (AFM) for high-resolution imaging and mechanical property investigations on the nanoscale as well as Raman spectroscopy for molecular composition testing, are explained. In chapters 3 and 4, the unique structural arrangements of the main structural proteins and the major blood corpuscle of vertebrates, collagen and red blood cells, are given. Subsequently, clear evidence for their preservation is shown. Finally, the experimental results are followed by a summary, references, and the referring articles.

## 2. EXPERIMENTAL METHODS

To study ancient tissue, scientific techniques customary in medicine, molecular biology or genetics are being used. Optical microscopy or radiographic methods such as two-dimensional X-ray imaging [35] and three-dimensional visualisation by computerised X-ray Tomography (CT) [36; 37; 38] are common. Also, newer imaging and analysis techniques such as nuclear magnetic resonance imaging (NMR) [39; 40; 41; 42] scanning electron microscopy (SEM) and transmission electron microscopy (TEM) are being used more frequently. Moreover, genetic sequencing of minute quantities of ancient DNA can be achieved after the DNA fragments are amplified by the polymerase chain reaction (PCR) [43].

In the following sections, AFM and Raman spectroscopy, two quasi-non-invasive measurement techniques used for imaging, testing the mechanical properties, and molecular characterising of rare and valuable ancient samples, are introduced.

### 2.1 ATOMIC FORCE MICROSCOPY

Since its invention in 1986 [44], atomic force microscopy (AFM) has become an invaluable technique in surface science. Its popularity is due to its versatility [45]. Among other applications, the microscope combines imaging at atomic resolution [46; 47; 48; 49], probing mechanical properties [50; 51; 52; 53; 54], and nanoscale structuring of surfaces [55; 56; 57]. It can be operated at ambient conditions, in liquids or in vacuum, and there are no restrictions on the sample material analysed. Inorganic, organic, conductive and isolating samples can be probed. Images are obtained with nanometre or even angstrom resolution that can facilitate single-molecule spectroscopy and the determination of molecular structures [58; 59; 60; 61]. In addition, the nanomechanical properties, such as elasticity, hardness, adhesion, or surface charge, of a material or a thin surface layer can be examined by nanoindentation, or force spectroscopy measurements.

#### 2.1.1 Microscope Principle and Imaging Modes

As the name implies, atomic force microscopy probes the forces acting between the atoms of two separated surfaces, those of a sample and those of the AFM tip. The tip (typical radius of curvature 10-20 nm) is thereby an integral part of a flexible cantilever (figure 2). The tip and the cantilever are usually microfabricated from silicon or silicon nitride [62]. The forces acting between the atoms of the tip and the atoms of the sample surface are either attractive, repulsive, or both and scale by the tip-sample distance. Long-range surface forces such as magnetic, electrostatic and van der Waals interactions can impair the cantilever up to distances of microns. In contrast, short-range forces, such as Pauli repulsion, dominate near

the surface. The Pauli repulsion and van der Waals attraction are often combined in the Lennard-Jones potential  $V_{LJ}(d)$  (figure 1) as approximated by

$$V_{LJ}(d) = 4\varepsilon \left\{ \left( \frac{\sigma}{d} \right)^{12} - \left( \frac{\sigma}{d} \right)^6 \right\}, \quad \text{Eq. (1)}$$

where the factor  $\varepsilon$  correlates with the depth of the potential energy minimum;  $\sigma$  is the distance at which the tip-sample potential equals zero, and  $d$  represents the instantaneous tip-sample distance. The negative term in equation 1 accounts for the attractive van der Waals forces. These intermolecular dipole interactions arise from temporary charge fluctuations in the atoms of the tip or the sample, e.g., changes in the electron density of the atomic orbitals [63; 64]. The positive term indicates the short range Pauli repulsion, which occurs when the electron orbitals of the tip atoms and sample atoms overlap, as is the case in the AFM contact mode.

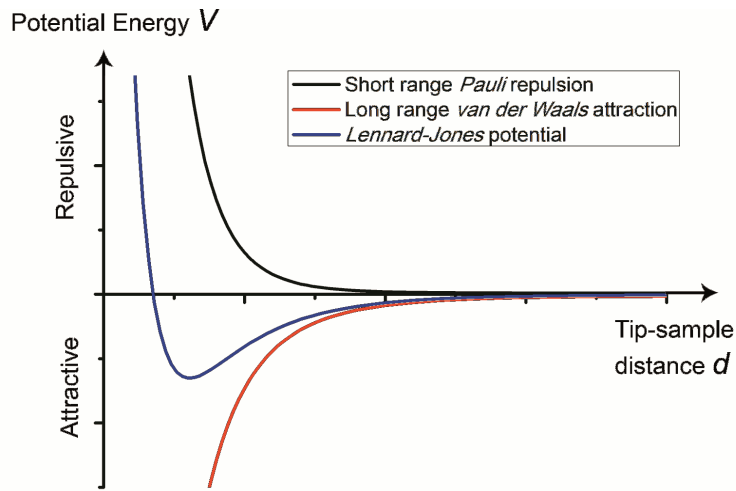


Figure (1): Lennard-Jones potential describing the distance dependence of the interaction forces between the tip and sample. The red curve accounts for the attractive van der Waals forces; the black curve indicates the Pauli repulsion. The addition of these two terms, corresponding to the Lennard-Jones potential, is shown in blue.

In this basic operation mode, the tip is brought into mechanical contact with a sample surface and scanned over it. Such surface scans are actuated by piezo-electric elements that are capable of accurate movements with angstrom precision. By measuring the tip-sample interaction forces on consecutive positions, a topographic map of the surface is created. The tip-sample interaction forces are thereby converted to a cantilever deflection. Using the optical lever method [65], in which a laser beam is focused on the back side of the cantilever and reflected to a position-sensitive quadrant photodetector, the sample topography can be reconstructed from the cantilever deflection (figure 2).

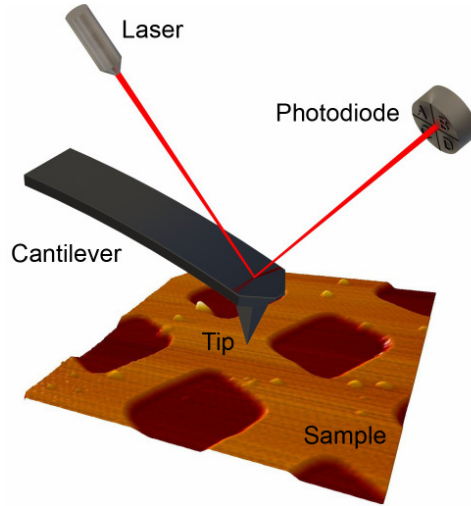


Figure (2): Centrepieces of an AFM setup. A microfabricated tip, the integral part of the cantilever, is in close proximity to the sample surface. While scanning across the surface, the cantilever deflects depending on the sample topography. The deflection is detected by a laser-photodiode system (Drawing courtesy of S. Kloft).

At the resting position, i.e., when the cantilever is far away from the sample and there are no tip-sample interaction forces, the reflected laser beam is centred on the photodiode. As a result, the current induced in each segment is equal, and the difference between the signal from the top and bottom or the left and right detector segments compensates each other. As the cantilever approaches the sample, the tip-sample interactions increase, causing the cantilever to deflect and the photocurrent signal to change.

In contact mode, the differential signal between the top and bottom photodiode segments is a function of the vertical bending of the cantilever and thus the sample topography. The differential signal between the left and right segments corresponds to the horizontal deflection of the cantilever and is attributed to frictional forces acting between the tip and the sample [66]. In constant force mode, a feedback system adjusts the cantilever-sample distance and hence the force,  $F_c$ , applied by the tip on the sample. Using Hook's law, the loading force can be calculated as follows:

$$F_c = -k_c d_c. \quad \text{Eq. (2)}$$

Here,  $d_c$  corresponds to the cantilever deflection, and  $k_c$  is the cantilever spring constant. For a rectangular cantilever, the spring constant is given by

$$k_c = \frac{Ewt_c^3}{4L^3}, \quad \text{Eq. (3)}$$

where  $E$  is the cantilever's Young's modulus, and  $w$ ,  $t_c$ , and  $L$  are its width, thickness, and length, respectively [67]. However, the thickness is rarely accessible and determining the Young's modulus is difficult because cantilevers are often made of several materials. Therefore, calculating the cantilever spring constant based on its geometry is problematic. Currently, the thermal noise method [68; 69] is used to define the cantilever spring constant. The calibration is based on the Brownian motion of molecules in a fluid (e.g., air) that hits the

cantilever and excites it to freely oscillate. The Hamiltonian of a harmonic oscillator driven by this thermal noise is

$$H = \frac{p^2}{2m} + \frac{1}{2}m\omega_0^2 d_c^2, \quad \text{Eq. (4)}$$

with  $p$  being the momentum of the oscillator,  $m$  its mass, and  $\omega_0$  its angular resonant frequency. Concerning the equipartition theorem, in which the average energy of each quadratic Hamiltonian term and thus each degree of freedom equals  $k_B T/2$ , one obtains [68]

$$\left\langle \frac{1}{2}m\omega_0^2 d_c^2 \right\rangle = \frac{1}{2}k_B T, \quad \text{Eq. (5)}$$

where  $k_B$  is the Boltzmann constant and  $T$  the temperature of the system. Considering small cantilever deflections and neglecting other elastic modes due to their much higher spring constants, the AFM cantilever can be modelled as a simple harmonic oscillator with one degree of freedom [68]. With an angular resonant frequency of  $\omega_0^2 = k_c/m$ , equation 5 yields

$$k_c = \frac{k_B T}{\langle d_c^2 \rangle}. \quad \text{Eq. (6)}$$

Hence, the spring constant can be derived from the mean-square cantilever deflection  $\langle d_c^2 \rangle$  due to thermal fluctuations. These assumptions are adequate, although some corrections are necessary to compensate for higher modes of vibration [70].

In addition to the static contact mode, AFM can also be conducted in dynamic modes. These modes facilitate less sample and tip wear, result in higher resolution, and can allow for chemical identification of surface atoms and measure of short-range forces.

In the so-called tapping or amplitude modulated (AM) mode, the cantilever is externally driven, oscillating close to or at its first flexural resonant frequency [71]. Rather than the static deflection of the cantilever in the contact mode, the value of the cantilever oscillation amplitude is used as the feedback signal. The AM mode was originally established to measure surface forces without tip-sample contact [72]. The cantilever was operated far away from the surface in the attractive van der Waals force interaction regime [72]. Performing the AM mode in the repulsive force regime [71] established the use of tapping mode AFM for high resolution sample imaging [73]. In the tapping mode, the AM feedback system controls the cantilever-sample distance so that, at the lower turning point of an oscillation, the AFM tip shortly “touches” or “taps” the sample [74]. This temporary contact eliminates lateral shear forces and enables the imaging of soft and delicate materials. The force acting between the tip and the sample is proportional to the difference between the amplitude of the freely oscillating cantilever and the surface-damped cantilever oscillation [71; 75]. Thus, the feedback system also indirectly regulates the applied force while imaging. Due to the relatively large oscillation amplitude, usually 20 nm to 100 nm [71], repulsive and attractive tip-sample interaction forces affect the cantilever. During one oscillation cycle, the tip passes the upper oscillation turning point, i.e., the point at which the tip-sample distance is at its maximum and

van der Waals attraction prevails, and the lower oscillation turning point, i.e., the point at which the tip touches the sample and the force interaction is dominated by the Pauli repulsion. Near the surface, short-range Pauli repulsion forces induce changes in the oscillation amplitude due to damping and energy dissipation [76; 77]. The feedback system detects this perturbation and readjusts the amplitude setpoint value by changing the cantilever-sample distance. However, changes in the oscillation amplitude are a consequence of a shift in the cantilever resonance frequency. As elucidated in figure 3 [78], a shift in the cantilever resonance frequency, e.g., due to energy dissipation, causes a phase shift  $\Delta\phi$  between the cantilever resonant frequency and the excitation frequency and, as a result, changes the oscillation amplitude [76; 79].

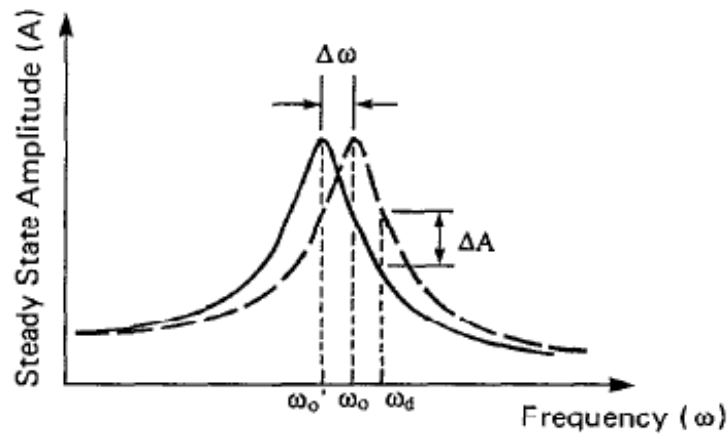


Figure (3): Effect of frequency and amplitude shift in amplitude-modulated AFM imaging. “Reprint with permission from T. R. Albrecht, Journal of Applied Physics, 69, 2, (1991). Copyright 1991, American Institute of Physics” [78].

The angular resonant frequency of the cantilever is given by  $\omega_0^2 = k_{eff}/m$ , where  $k_{eff}$  is the effective spring constant and  $m$  the effective mass of the cantilever. The effective spring constant is the sum of the cantilever spring constant  $k_c$  and the force gradient  $\partial F / \partial z$  acting on it [78].

$$k_{eff} = k_c + \partial F / \partial z \quad \text{Eq. (7)}$$

The effect of a phase shift, which can provide information about adhesion forces between the tip and sample surface [80; 81] and illustrate the energy dissipation of the sample [74; 76], is utilised in phase imaging.

Compared to amplitude modulation AFM, in frequency modulation AFM (FM-AFM), also called non-contact mode AFM (NC-AFM), the cantilever is excited to oscillate with a constant amplitude,  $A_0$  [78; 82]. Although the AFM tip is oscillating in proximity to the surface, the amplitude is kept small so that the tip never touches the surface. The cantilever-sample distance is in the attractive regime of the surface potential. Raster scanning the tip over the surface creates an image of the force gradient variations above the surface. In the non-contact mode, two feedback loops, an amplitude-controlled and a distance-controlled loop, are used [66; 78]. To maintain constant amplitude, the cantilever deflection signal is measured, filtered through a bandpass and fed into a so-called *rms-dc* converter [82]. Here,

the *rms* value of the cantilever oscillation amplitude is converted to a *dc* signal output. This *dc* signal is added to the inverted value of a *rms* setpoint amplitude [82]. This yields the amplitude error, which is subsequently processed in a controller, multiplied with a  $\pi/2$  phase shifted cantilever oscillation and finally fed back to drive the cantilever actuator [82]. Such a setup adjusts itself, i.e., the positive feedback actuates the cantilever oscillation and drives it solely at the actual resonance frequency. The second feedback loop is used to control the cantilever-sample distance. Once the cantilever deflection signal is filtered, it is fed into an analogue frequency-voltage converter, a digital frequency counter or a phase-lock-loop (PLL) detector to measure the oscillation frequency [78]. The shift in resonance frequency  $\Delta f$  due to detuning of the oscillation by a force gradient  $\partial F/\partial z$  is detected and used as feedback to control the cantilever-sample distance [78; 82]. This signal corresponds to the topography of the surface. In FM-AFM, true atomic resolution of sample surfaces is feasible [47; 83]. Besides, single atom manipulation [84] and single atom chemical identification [85] are now routinely performed.

### 2.1.2 Local Force Measurements

Apart from high-resolution imaging, AFM can be used to determine the local mechanical properties of a material by performing AFM force measurements. A defined tip geometry and size enables direct observation of the force interactions between nanoscale objects such as single molecules [59]. In force measurements, the force  $F$  acting between the tip and the sample is plotted as a function of the vertical tip-sample distance  $d$  [86; 87]. The so-called  $F$ - $d$  curve is obtained by approaching and retracting the AFM tip perpendicularly (*z*-piezo approach) towards the sample and simultaneously recording the *z*-piezo displacement  $z$  and the cantilever deflection  $d_c$  [88; 89]. These values are later converted to the applied force and tip-sample distance.

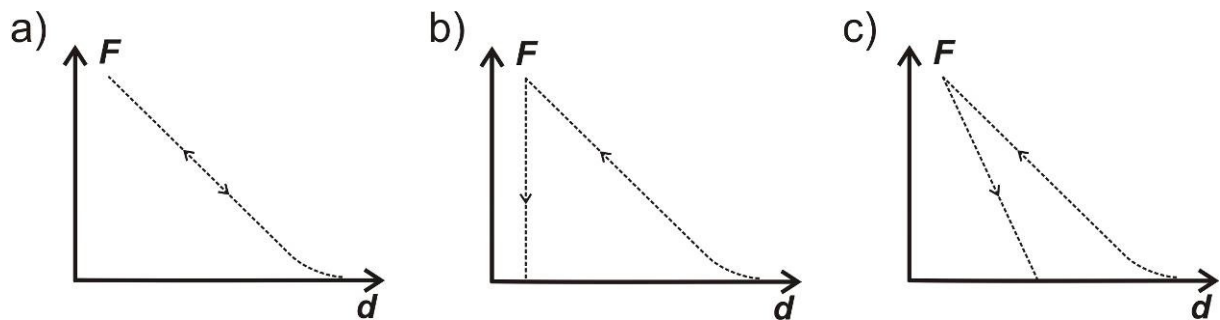


Figure (4): Basic  $F$ - $d$  curves obtained on an ideally elastic (a), ideally plastic (b), and an elasto-plastic (c) material.

By analysing the approach and withdraw segments of  $F$ - $d$  curves, three different material responses can be observed [90; 91]. If the approach and withdraw curve coincide, then the elastic behaviour of a sample is measured (figure 4a). Here, the sample elasticity causes the specimen to regain its original shape. The force that drives shape recovery is as large as the penetration force of the tip and acts against it.

If the force in the unloading curve drops instantaneously to zero (figure 4b), then the sample is an ideal plastic. Here, the specimen undergoes an irreversible deformation during the



loading and does not regain its shape after unloading. The plastic deformation will then equal the maximal penetration depth [88; 91].

The most common case is a combination of the two behaviours, elastic and plastic, described above [88; 91]. In the elasto-plastic behaviour, the sample first responds elastically to a load. As soon as the acting force exceeds a sample-specific value, the material deforms plastically. The reset force of the unloading curve will be less than the force of the loading curve (figure 4c).

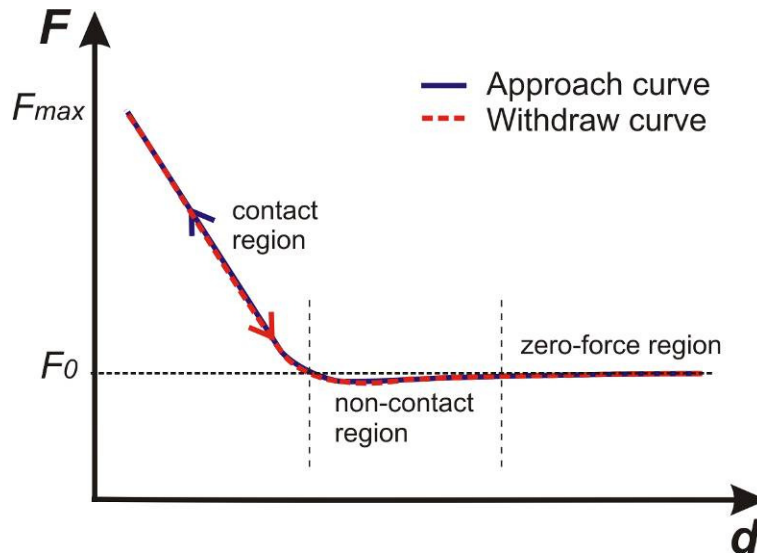


Figure (5): Basic Force vs. distance curve for an ideally elastic sample with marked interaction regions. The approach and withdraw curves are coloured in blue and red, respectively. The line at  $F_0$  defines the zero-force, the non-contact and the contact region.

A basic  $F-d$  curve of an ideally elastic sample is shown in figure 5. In general,  $F-d$  curves can be divided into three interaction regions [86; 92]. The zero force region is where the tip is far away from the sample and only long-range electrostatic or magnetic forces prevail. The non-contact region describes where attractive interaction forces between the tip and sample, mainly van der Waals and capillary forces, begin to pull the AFM tip towards the surface [86; 93] and bend the cantilever downwards. Finally, the contact region is where the tip is in contact with the surface and further approach causes the cantilever to deflect upwards and the  $F-d$  curve to become sloped. The slope of the curve thereby represents a qualitative value of the stiffness of a sample [53; 89].

As soon as the maximum force or setpoint cantilever deflection is reached, the tip is withdrawn from the surface. The unloading force then continuously decreases, and the three  $F-d$  curve regions are run in reverse order. In the beginning of the non-contact region, the tip is separated from the sample. This separation occurs when the pull-off force equals the adhesive tip-sample interaction forces. Finally, the cantilever returns to the zero force region, the quasi-equilibrium position far away from the surface [89].

### 2.1.3 Contact Mechanics

Analysing  $F$ - $d$  curves can reveal a large number of surface features such as the chemical, mechanical and adhesive properties of a material. Contact mechanic theories are applied to extract information on the elastic properties of a material from the  $F$ - $d$  curves. These theories relate the load applied, to the deformation and Young's modulus of the sample [89]. The basic contact mechanic model is the Hertz theory, which describes the deformation of two elastic spheres pressed against one another [94]. This model can be easily applied to the flat punch between a tip and a sample. However, the Hertz model is only suitable if adhesion forces are neglectable or are much smaller than the maximum load applied. If adhesion occurs [87], then the Derjaguin-Muller-Toporov (DMT) model, which considers adhesive forces acting outside the contact area, or the Johnson-Kendall-Roberts (JKR) model, which considers adhesive forces acting inside the contact area, can be used. The most general theory, however, is the Maugis-Dugdale model, which combines the Hertz, DMT and JKR models and describes the elastic deformation of all samples in the presence of adhesion (figure 6). In all models, the samples are assumed to be solid, continuous elastic media, i.e., plastic deformations are ignored [88].

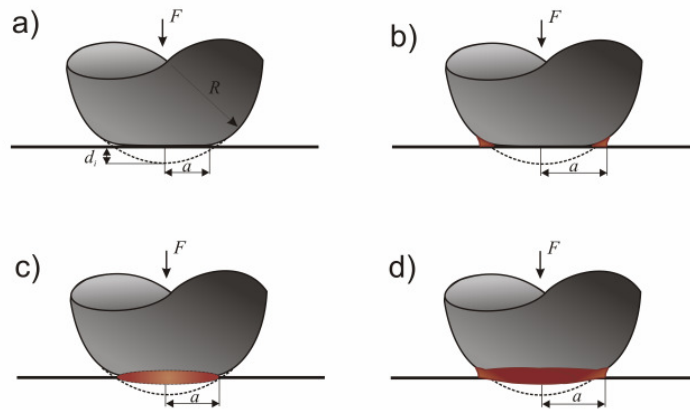


Figure (6): Hertz (a), DMT (b), JKR (c), and Maugis-Dugdale (d) model of an elastic sphere with radius  $R$  indenting a rigid flat sample. The contact radius,  $a$ , between the sphere and the sample surface depends on the loading force,  $F$ . The Hertz theory neglects surface forces and adhesion between the two bodies. In the DMT model, adhesion is only considered outside the contact area. The JKR theory considers adhesion inside the contact region. The Maugis-Dugdale model covers the interaction of surface forces around and within the contact region of the bodies.

The crucial parameter in each model is the contact radius  $a$ . In the Hertz theory,  $a$  can be derived from geometrical considerations and the reduced Young's modulus. Assuming a limiting case of the Hertz model (the radius of one sphere tends to infinity) in which a smooth elastic sphere (indenter) with radius  $R$  is pressed against a flat rigid surface (sample) with an external force  $F$  (figure 6a), the contact radius  $a$  is [88] given by

$$a = \left( \frac{RF}{E^*} \right)^{1/3}, \quad \text{Eq. (8)}$$

in which the reduced Young's modulus  $E^*$ , a combination of the Young's moduli and Poisson ratios of the sample ( $E_s, \nu_s$ ) and the indenter ( $E_i, \nu_i$ ) [90; 95; 96] is given by

$$\frac{1}{E^*} = \frac{3}{4} \left( \frac{1-\nu_s^2}{E_s} + \frac{1-\nu_i^2}{E_i} \right) \quad \text{Eq. (9)}$$

The deformation,  $d_i$ , of the spherical indenter can then be calculated by

$$d_i = \frac{a^2}{R} = \left( \frac{F^2}{R(E^*)^2} \right)^{1/3} \quad \text{Eq. (10)}$$

Transferring the Hertz model to a rigid AFM tip pressed against an elastic surface (figure 7) requires extending the model [95] because indentations may not be shallow and the deformation of the sample and tip must be taken into account [97].

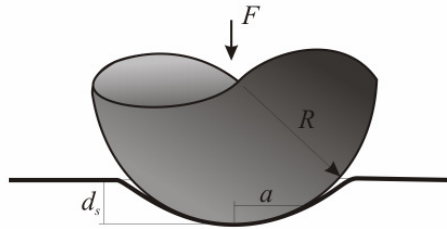


Figure (7): Deformation of a sample surface due to an indenting tip with radius  $R$ . The surface is indented by the distance  $d_s$ .

For a spherical indenter, the surface deformation,  $d_s$ , of the sample [97] is given by

$$d_s = \frac{1}{2} a \ln \left( \frac{R+a}{R-a} \right) \quad \text{Eq. (11)}$$

The force,  $F$ , exerted by the tip on the surface results to

$$F_{\text{sphere}} = \frac{E_s}{2(1-\nu_s^2)} \left[ (a^2 + R^2) \ln \left( \frac{R+a}{R-a} \right) - 2aR \right] \quad \text{Eq. (12)}$$

The force,  $F$ , applied by other rotationally symmetric indenters such as a conical tip or a parabolic shaped indenter [54; 95; 96], is defined as

$$F_{\text{cone}} = \frac{\pi}{2} \left( \frac{E}{1-\nu^2} \right) d_s^2 \tan \theta \quad \text{Eq. (13)}$$

$$F_{\text{paraboloid}} = \frac{4}{3} \left( \frac{E}{1-\nu^2} \right) \sqrt{R} d_s^{3/2} \quad \text{Eq. (14)}$$

and the contact radii  $a$  are given by

$$a_{\text{cone}} = \frac{2 \tan \theta}{\pi} d_s, \quad \text{Eq. (15)}$$

$$a_{\text{paraboloid}} = \sqrt{R d_s}, \quad \text{Eq. (16)}$$

with  $\theta$  being the half cone angle of the conical indenter. The cone approximation is suitable when soft samples are analysed, whereas a spherical or paraboloid approximation is appropriate for harder samples [98] because at the same loading force, the indentation into a soft sample is larger compared to the radius of curvature of the tip. Thus, the contact area becomes more conically shaped. For rigid surfaces, the indentation is small; hence, only the spherical apex of the tip penetrates the sample.

If surface forces between the tip and the sample cannot be ignored, the Hertz theory has to be modified.

In the DMT model [99], not only the applied loading force,  $F$ , but also the forces acting outside the contact region between the sphere and the rigid flat surface are considered (figure 6b). The deformation of the elastic sphere is described in accordance to the Hertz theory, but additional van der Waals forces that increase the contact radius  $a$  between the sphere and the solid plane surface are introduced. The increase in the contact radius  $a$  [88] is given by

$$a = \left( \frac{RF}{E^*} + \frac{2\pi R^2 W}{E^*} \right)^{1/3}. \quad \text{Eq. (17)}$$

The first term accounts for the contact radius following the Hertz theory. The second term represents the adhesive surface forces around the contact area with  $W$  being the adhesion work at contact. The latter can be calculated from the jump-off-contact region in the  $F$ - $d$  curve. The deformation of the spherical tip [89] is given by

$$d_i = \frac{a^2}{R} = \left( \frac{(F + 2\pi R W)^2}{R(E^*)^2} \right)^{1/3}. \quad \text{Eq. (18)}$$

Upon withdrawing the tip from the sample, the contact area decreases until, at zero loading force, the pull-off or adhesion force reaches its maximum. The corresponding contact radius  $a_0$  is

$$a_0 = \left( \frac{2\pi R^2 W}{E^*} \right)^{1/3}. \quad \text{Eq. (19)}$$

In the non-adhesive case, the contact radius is confined to the radius given by the Hertz model. The DMT model is applicable for rigid surfaces with low adhesion and for small indenter radii [88]. In the case of highly adhesive soft samples and AFM tips with large radii,

the Hertz equation is modified, as in the JKR model [100]. In this theory, long-range forces outside the contact area are neglected, and only short range forces inside the contact region are considered (figure 6c) [88]. In contrast to the DMT model, the surface deformation of the sample due to adhesion forces is taken into account. The contact radius  $a$  is given by

$$a = \left( \frac{RF + 3\pi R^2 W + \sqrt{6\pi R^3 W F + 9\pi^2 R^4 W^2}}{E^*} \right)^{1/3}. \quad \text{Eq. (20)}$$

Again, in the non-adhesive case, i.e., when  $W$  equals zero, the JKR model coincides with the Hertz model. The sample deformation [88] is

$$d_s = \frac{a^2}{R} - \frac{2}{3} \sqrt{\frac{6\pi R W}{E^*}}. \quad \text{Eq. (21)}$$

When unloading the sample, a neck between the tip and the surface is formed, which abruptly ruptures once the pull-off force exceeds the adhesion force. The contact radius of the finite contact area between the tip and sample at zero load equals

$$a_0 = \left( \frac{6\pi R^2 W}{E^*} \right)^{1/3}. \quad \text{Eq. (22)}$$

The JKR theory accurately predicts the force-deformation relation for high-surface energy materials and large tip radii. The DMT model more precisely describes stiff bodies with small surface energies and small tip radii. Both theories, however, lack the scope of elastic deformations between these limiting cases. The Maugis-Dugdale model [101] (figure 6d) is the most complete theory describing the elastic deformation of materials with the dimensionless parameter  $\eta$  given by

$$\eta = \frac{2.06}{D_0} \left( \frac{R W^2}{\pi (E^*)^2} \right)^{1/3}, \quad \text{Eq. (23)}$$

where  $D_0$  is a typical atomic dimension [89]. For soft, large and adhesive materials, the parameter  $\eta$  becomes large, whereas hard, small, and low surface energy materials have a small  $\eta$ . The Maugis-Dugdale model treats adhesion as it were a steady stress acting circularly around the contact region [88]. The dimensionless contact radius  $\gamma$  is given by

$$\gamma = \left( \frac{E^*}{\pi W R^2} \right)^{1/3} a, \quad \text{Eq. (24)}$$

and the dimensionless penetration depth  $\delta$  is calculated from

$$\delta = \left( \frac{(E^*)^2}{\pi^2 W^2 R} \right)^{1/3} d. \quad \text{Eq. (25)}$$

The penetration depth can also be written as a function of the dimensionless contact radius  $\gamma$  [88] yielding

$$\delta = \gamma^2 - \frac{4}{3}\eta\gamma\sqrt{m_M^2 - 1}, \quad \text{Eq. (26)}$$

where  $m_M$  is the ratio between an circular adhesion region around the contact area, and the contact radius  $a$ . For  $\eta \rightarrow 0$  or for  $\eta \rightarrow \infty$ , the corresponding DMT or JKR sample deformations, respectively, are revealed [88].

The  $F$ - $d$  curves analysed in this study were evaluated using the Hertz model because sample indentations were small and sample deformations were within the elastic regime. Due to the small sample indentation, the area of contact was smaller than the radius of the tip and the sample. In addition, adhesion forces are negligible in mummified, dried, ancient tissue samples.

## 2.2 RAMAN SPECTROSCOPY

Based on the assumptions of Compton, which explain X-ray (high energy photons) scattering in matter (Compton effect), C. V. Raman and K. S. Krishnan examined the scattering of monochromatic light (lower energy photons) in liquids and gases. Similar to the Compton effect, they discovered that two types of photons scattered on the molecules of the media. The scattered light predominantly had the same wavelength as the incident light; however, a small amount of the scattered photons had a lower frequency and thus larger wavelength (Raman effect) [102; 103; 104]. Because this energetic shift in the photons depends on the scattering partners involved, the frequency shift of the scattered photons provides a molecular fingerprint of the analysed sample. As for AFM, there are nearly no limitations on the material examined by Raman spectroscopy. The Raman effect, however, may not be observed in all samples. For example, the autofluorescence of certain materials may superimpose the Raman spectrum. The process of light scattering that determines Raman spectroscopy is discussed in more detail in the following sections.

### 2.2.1 Scattering of Light in Matter

The propagation of electromagnetic waves is significantly influenced by the medium they travel through. Interactions between electromagnetic radiation, such as light, and the molecules or atoms of a sample, result in reflection, diffraction, absorption, or scattering of the incident photons (figure 8).

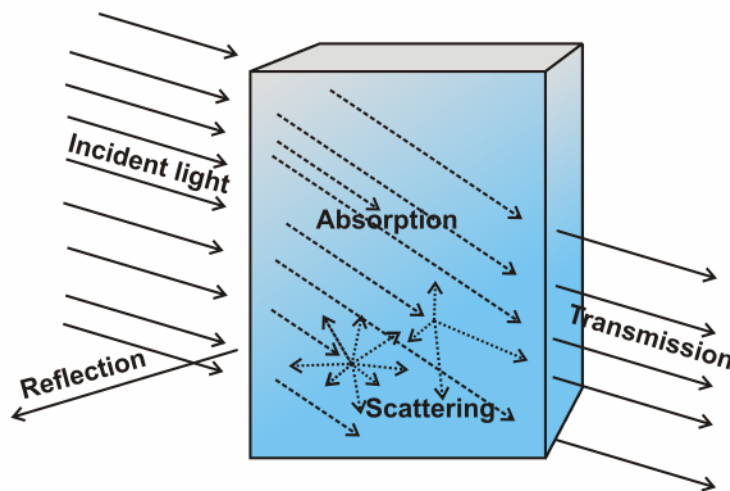


Figure (8): Possible interaction processes between light and matter. Amongst others, the incident photons may experience reflection, diffraction, absorption or scattering.

Absorption and scattering are usually accompanied by a transfer of energy. In general, as stated by Bohr's frequency condition, the energy transfer from an electromagnetic field to an atom or molecule can only appear if

$$\Delta E = hf = h \frac{c}{\lambda} \quad \text{Eq. (27)}$$

is satisfied [105]. Here,  $h$  is Planck's constant;  $f$  is the frequency of the electromagnetic wave;  $\lambda$  is its wavelength, and  $c$  is the velocity of light. Once the energy of the incident photons matches the energy difference,  $\Delta E$ , between two energy states of an atom or a molecule, absorption can occur. As a result, the atom or molecule is excited into a higher electronic or vibrational state. While relaxing, the absorbed energy,  $\Delta E$ , is released via non-radiative (heat) or radiative (fluorescence) transitions [106].

Scattering occurs when the incident photon energy does not match  $\Delta E$  between two real energy states. In this case, the electromagnetic wave stimulates oscillations in the atoms or molecules, inducing dipoles, which themselves emit electromagnetic radiation in diverse spatial directions. The scattering can be either coherent or incoherent. Coherent scattering occurs when the excited sample atoms oscillate in phase and emit electromagnetic radiation in designated spatial directions. Although every atom can emit energy isotropically, the total direction of the radiation is given by the constructive interference of the waves of all the dipoles. Thus, irradiating a crystal with regularly arranged atoms, in which the distance between the atoms is small compared to the wavelength of the incident light, the propagation of the overall electromagnetic wave front will be in the direction of the incident plane-polarised electromagnetic wave. This process does not occur for irregularly arranged or thermally fluctuating atoms. The incident radiation induces or boosts the oscillations of the atoms, which oscillate without any phase coherence, leading to a statistically distributed emission of electromagnetic waves and incoherent scattering [107].

Scattering is also classified in terms of energy. Elastic scattering can be described as a particular case of an elastic collision between an incident photon and matter. It is considered as the absorption of the incident photon by the matter and, thus, an excitation of the matter followed by an immediate relaxation by emission of heat or reemission of a photon [106]. Because no energy transfer occurs in elastic scattering, the wavelength and frequency of the reemitted photon is equal to that of the incident photon.

In contrast, the energy of an inelastic scattered photon is different than the energy of the incident photon. Inelastic collisions between photons and matter cause a partial transfer of energy from the photons to the matter, e.g., the excitation of phonons in a crystal lattice or the induction of molecular vibrations (energy transfer to the matter). Depending on the excitation state of the matter, both a loss and a gain in the energy of the scattered photons are feasible (energy transfer to the photon). As a consequence, the photon energy is different from the energy of the incident photon.

A mathematical description of Raman spectroscopy and the Raman effect is given in the following section. The elucidations are based on the book "Introductory Raman Spectroscopy" by Ferraro et al. [105].



## 2.2.2 Raman Spectroscopy and Raman Effect

In Raman spectroscopy, the elastically scattered (Rayleigh) and inelastically scattered (Raman) photons, induced by the Raman effect, are analysed to address the molecular composition of a sample. The sample is irradiated with intense monochromatic light, usually from a laser beam in the UV, visible, or near-infrared spectral range, and the backscattered light is detected. Intense excitation beams must be used because Raman scattering is a rare process. Only a small amount of the incident photons are scattered inelastically and spectrally shifted. The shift of the incident photon frequency,  $f_0$ , depends on the vibrational frequency,  $f_m$ , of the sample molecules. The Raman spectrum thus represents the shift in frequency relative to the excitation frequency. Describing the electric field strength ( $\Phi$ ) of the incident photon as

$$\Phi = \Phi_0 \cos 2\pi f_0 t, \quad \text{Eq. (28)}$$

where  $\Phi_0$  is the vibrational amplitude of the wave and  $t$  the time of the fluctuation, the process of Raman scattering can be explained classically. Upon irradiating a diatomic molecule with a laser, an electric dipole moment,  $P$ , is induced, which is given by

$$P = \alpha\Phi = \alpha\Phi_0 \cos 2\pi f_0 t. \quad \text{Eq. (29)}$$

The proportionality constant  $\alpha$  therein denotes the affinity of the charge distribution of the molecule, i.e., the electron cloud of the molecule, to be distorted by the electric field of the photons. This affinity is called polarisability and is typically dependent on the orientation of the molecular axis relative to the incident electric field. Given that the diatomic molecule vibrates with the frequency  $f_m$  and the vibrational amplitude  $q_0$ , its nuclear displacement,  $q$ , can be written as

$$q = q_0 \cos 2\pi f_m t. \quad \text{Eq. (30)}$$

If the vibrational amplitude is small, then the polarisability  $\alpha$  is a function of the nuclear displacement,  $q$ , with

$$\alpha = \alpha_0 + \left( \frac{\partial \alpha}{\partial q} \right)_0 q + \dots \quad \text{Eq. (31)}$$

Here, the polarisability at the equilibrium position is  $\alpha_0$  and  $\left( \frac{\partial \alpha}{\partial q} \right)_0$  gives the change in polarisability as a function of the charge,  $q$ . Combining equations 29, 30, and 31, the electric dipole moment,  $P$ , can be rewritten as

$$P = \alpha_0 \Phi_0 \cos 2\pi f_0 t + \left( \frac{\partial \alpha}{\partial q} \right)_0 q_0 \Phi_0 \cos 2\pi f_0 t \cos 2\pi f_m t, \quad \text{Eq. (32)}$$

and with  $\cos x \cos y = 1/2(\cos(x-y) + \cos(x+y))$ , we obtain

$$P = \alpha_0 \Phi_0 \cos 2\pi f_0 t + \frac{1}{2} \left( \frac{\partial \alpha}{\partial q} \right)_0 q_0 \Phi_0 [\cos\{2\pi(f_0 - f_m)t\} + \cos\{2\pi(f_0 + f_m)t\}] \quad \text{Eq. (33)}$$

The first term in equation 33 represents the oscillation of the induced dipole, which emits light with the same frequency,  $f_0$ , as the incident photons (elastic scattering). The second term describes the Raman scattered photons, which are frequency shifted by  $f_0 - f_m$  and  $f_0 + f_m$ . The shift  $f_0 - f_m$  is called the Stokes shift and corresponds to the loss of energy due to the transfer of energy from the photon to the matter. This transfer occurs when the incident photons excite the matter into a virtual intermediate state, and the matter subsequently relaxes to a vibrational state above the ground state via the emission of photons with reduced frequency [106].

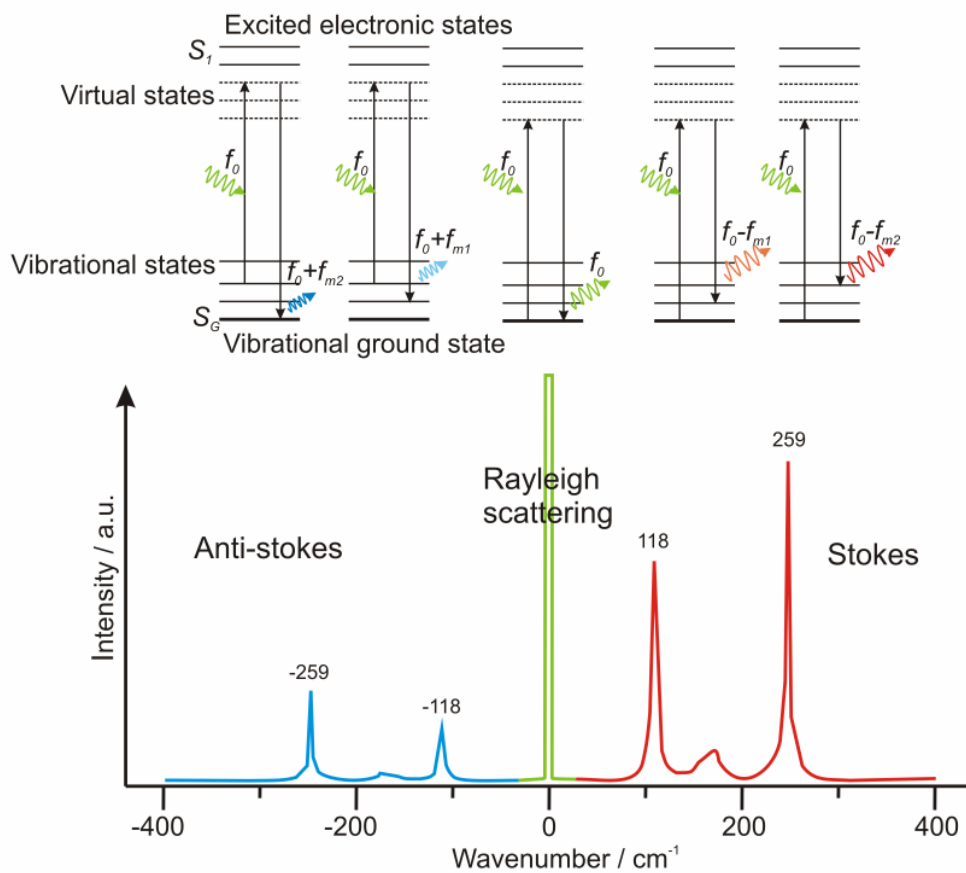


Figure (9): Jablonski diagrams showing possible transitions between electronic states in association with a schematic Raman spectrum. The Jablonski diagrams describe the excitation of a molecule from the vibrational ground state,  $S_G$ , to a virtual state below a real excited electronic state,  $S_1$ . In elastic scattering (Rayleigh scattering), the molecule is excited by an incident photon from the ground state into a virtual state and subsequently relaxes to the ground state. The released energy is emitted as a photon with the same energy, and thus frequency ( $f_0$ ), as the incident photon. Inelastically scattered photons are slightly detuned compared to the incident photons. Their frequency is either shifted to lower (Stokes shift) or to higher (anti-Stokes shift) frequencies.

If the matter is already in an excited vibrational state, then the scattered photons may gain energy from the excited matter [108]. This will increase the frequency of the scattered

photons and thus their energy. In equation 33, a gain in energy is indicated by the frequency shift  $f_0 + f_m$ , denoted the anti-Stokes shift. Inelastic scattering occurs if oscillations or vibrations of chemical bonds, or in case of a crystal, of phonons, are excitable. However,

when the polarisability is constant, and thus the change of polarisability  $\left(\frac{\partial\alpha}{\partial q}\right)_0$  equals zero, only Rayleigh scattering occurs, and the molecule vibration is not Raman active.

A generic Raman spectrum, in combination with a Jablonski diagram, illustrating the transitions between the electronic states of a molecule, is shown in figure 9. As shown, the Stokes and anti-Stokes shifts provide the same spectroscopic information, and it is thus only necessary to record one of them. In accordance with the Maxwell-Boltzmann distribution law, the Stokes lines are stronger, and therefore, usually only the Stokes photons are recorded.

### 2.2.3 The Confocal Microscope Setup

According to the Rayleigh criterion, the diffraction limited spatial resolution of a conventional optical microscope depends on the wavelength of the excitation source and the numerical aperture of the objective. The resolution can be enhanced by reducing the wavelength of the incident light or increasing the numerical aperture of the optical components. Practically, however, aberrations or the sample analysed can also restrict the resolution. To remedy these shortcomings, a confocal microscope setup can be used. Compared to a standard light microscope, in which a wide area of the sample is illuminated and imaged instantaneously, in confocal microscopy only a small focal spot on the sample is irradiated and examined. By raster scanning the sample or the illumination spot and recording the intensity of the light emitted from each sample point, an image of the specimen can be created point-by-point or pixel-by-pixel. The restriction on the analysed sample volume reduces interfering background signals from outside the focal area and improves the microscopic lateral and vertical resolution [106]. Confocal microscopy, therefore, also enables thin sample sections to be imaged, facilitating three-dimensional sample reconstructions. One crucial element in a confocal microscope is the pinhole, which is located in the image plane of the optical beam path before the spectroscopic detection unit. The size of the pinhole restricts the focal depth from which the light is collected (figure 10).

For the measurements presented in this work, a commercial confocal Raman microscope (WiTec alpha 300 R, Ulm, Germany) equipped with an frequency doubled Nd:YAG laser (laser wavelength  $\lambda = 532$  nm) with an maximum laser power  $P_{max}$  of 22.5 mW was used. The light scattered from the sample was detected in backscattering geometry with a vacuum sealed, high-sensitivity, back-illuminated CCD camera cooled to  $-65^\circ\text{C}$  ([www.witec.de](http://www.witec.de)). To obtain either full Raman spectra or high-resolution spectra, the CCD spectrometer was operated with a 600 1/mm or an 1800 1/mm grating, respectively. Spectral resolutions of approximately  $3\text{ cm}^{-1}$  ( $0 - 3600\text{ cm}^{-1}$ ) or  $1\text{ cm}^{-1}$  ( $0 - 1200\text{ cm}^{-1}$ ) per CCD-pixel, were achieved. A multimode optical fibre with a 50- $\mu\text{m}$  core diameter representing the pinhole and a standard air object lens with 100x magnification and a numerical aperture NA of 0.90 complete the microscope setup. Therewith Raman spectra from a sample volume of roughly 1  $\mu\text{m}$  in focal depth and a spot diameter of approximately 400 nm were recorded.

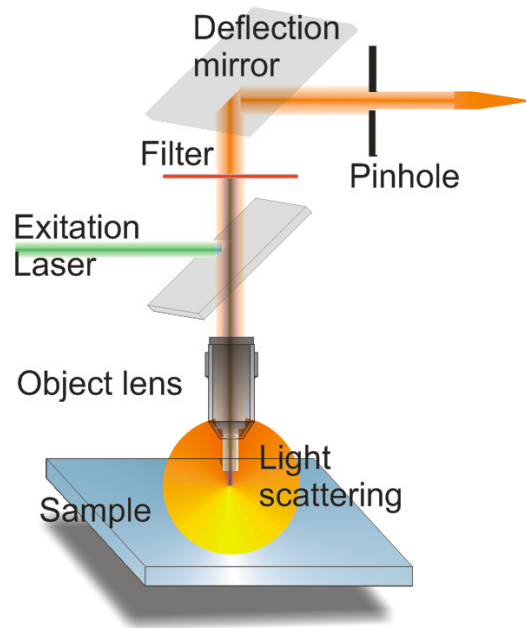


Figure (10): Schematic setup of the confocal Raman microscope. The excitation wavelength is coloured in green, the backscattered light is indicated in orange.

## 3. ANCIENT TISSUE PRESERVATION

### 3.1 COLLAGEN

Collagen is the most abundant and versatile biomechanical scaffold protein in the connective tissue of animals [109]. In mammals, it is present in the skin, vessel walls, tendons, ligaments, and as the organic component of bones and teeth. It promotes the resilience of those tissues, maintaining their structure and geometry, and provides them with the required stiffness, strength, and toughness. In humans, there are approximately 28 different collagens, which are subdivided depending on their function and occurrence [110]. Of those, collagen I may be the most important. Besides the above mentioned appearance, collagen I is also common in scar tissue, the end product when tissues heal by repair, and in the cornea, where it accounts for the optical power of the eye.

#### 3.1.1 Collagen-based Tissues and Properties

As its presence in joints or other load-bearing tissues already implies, collagen is a structural protein, important for maintaining the mechanical properties of connective tissues. While minerals and other organic molecules are also involved, the diverse mechanical requirements of the connective tissue are generally met by the arrangement of the collagen fibrils [110].

Tendons and ligaments are fibrous collagen-rich tissues that are crucial in facilitating the locomotion of animals. In both tissues, collagen implements high stiffness and tensile strength [111]. In tendons, these characteristics allow for the transmission of forces from contracting muscles to the skeleton, whereas in ligaments, they connect bones and support the joints to prevent abnormal movements [112]. In tendons, the collagen fibrils are densely packed and primarily aligned parallel to the longitudinal tendon axis and thus in the direction of the prevalent load. On the micrometer scale, the collagen assembly in tendons moreover shows some interweaving, which improves the tendon flexibility and elasticity [111; 113; 114]. This interweaving enables the tendon to uptake and release energy of motion with little losses, which saves muscular energy [115] and is why tendons are regarded as biological springs [116; 117]. Ligaments, in contrast, are more subject to multidirectional load. Therefore, the collagen fibrils are less ordered, and the mechanical properties of ligaments are slightly more isotropic than those of tendons [112].

Collagen is also an integral component of skin, confined to the second primary skin layer, the dermis. The dermis is streaked by blood vessels, harbours the roots of hairs, multiple glands, and is responsible for the skin's resilience. Close to the epidermis, the topmost layer of skin, the collagen fibrils in the dermis are arranged in sheet-like structures that run parallel to the skin surface. In deeper regions of the dermis, the collagen is less regularly arranged, is frequently interwoven, and forms loosely organised networks [118]. The overall fibril

direction remains parallel to the skin surface. The collagen networks strengthen the dermis, provide support for the epidermis, and thus maintain the skin's structure.

Collagen not only improves the mechanical properties of tissues but also provides unique optical properties, which is why the cornea, which is the front part of the eye, is composed of collagen [119]. In the cornea, the collagen fibrils are aligned with a high degree of lateral order [120] in parallel, lamellar structures and preferentially oriented horizontal and vertical to the eye surface [121]. This regular arrangement promotes destructive interference of scattered light and the transparency of the cornea [120]. Ultimately, however, collagen also conditions the cornea's strength to withstand the pressure within the eye and the pulling of the eye muscles [110].

Apart from collagen's high tensile strength, elasticity and optical properties, its stability is exceptional.

### **3.1.2 Formation and Stabilisation of Collagen**

As discussed, due to the specific tissue needs, collagen is assembled into either ordered or random structures. The mechanical properties of collagens are, however, predominantly determined on the molecular level. The collagen composition, in general, and the degree of collagen cross-linking, in particular, are thereby crucial factors.

Collagen is produced and secreted by several cells of the connective tissue such as fibroblasts, chondroblasts, and osteoblasts. Its biosynthesis takes place on ribosomes where single polypeptide  $\alpha$ -chains (procollagens) become compounded and subsequently transferred into the endoplasmic reticulum [122]. These procollagen chains are composed of a repeating amino acid sequence, Gly-X-Y, in which every third position is a glycine [123; 124; 125]. The residues X and Y can be any other amino acid, but in roughly 20 % of cases, proline is located at the X-position, and hydroxyproline is at position Y [110; 126; 127].

In the endoplasmic reticulum, the procollagen chains undergo enzymatic modifications that convert specific proline and lysine residues to hydroxyprolines and hydroxylysines, respectively. The collagen is formed once three modified procollagen chains associate [110; 122]. The collagen monomer, also called tropocollagen [128; 129], is a roughly 300-nm long and 1.5-nm thick, twisted, right-handed triple helix formed by the folding of three left-handed helical polypeptide  $\alpha$ -chains [130]. It is the basic structure of all types of collagen. In tropocollagen, the glycine residues face towards the core of the fibril, whereas the residues at X and Y are oriented towards the chain surface [110; 131]. This triple helix structure is stabilised by one inter-chain hydrogen bond per sequence between the amide (N-H) group of a glycine with the carbonyl (C=O) group of a proline at the X-position in an adjacent chain [125; 132]. Moreover, an extensive hydration network of water molecules stabilises the structure by forming additional hydrogen bonds within the same chain or between adjacent chains within the bonding distance of the water bridges (figure 11) [133; 134; 135]. The water thereby saturates the available carbonyl and hydroxyl groups of hydroxyproline and maintains the intermolecular spacing between neighbouring polypeptide chains [133; 134].

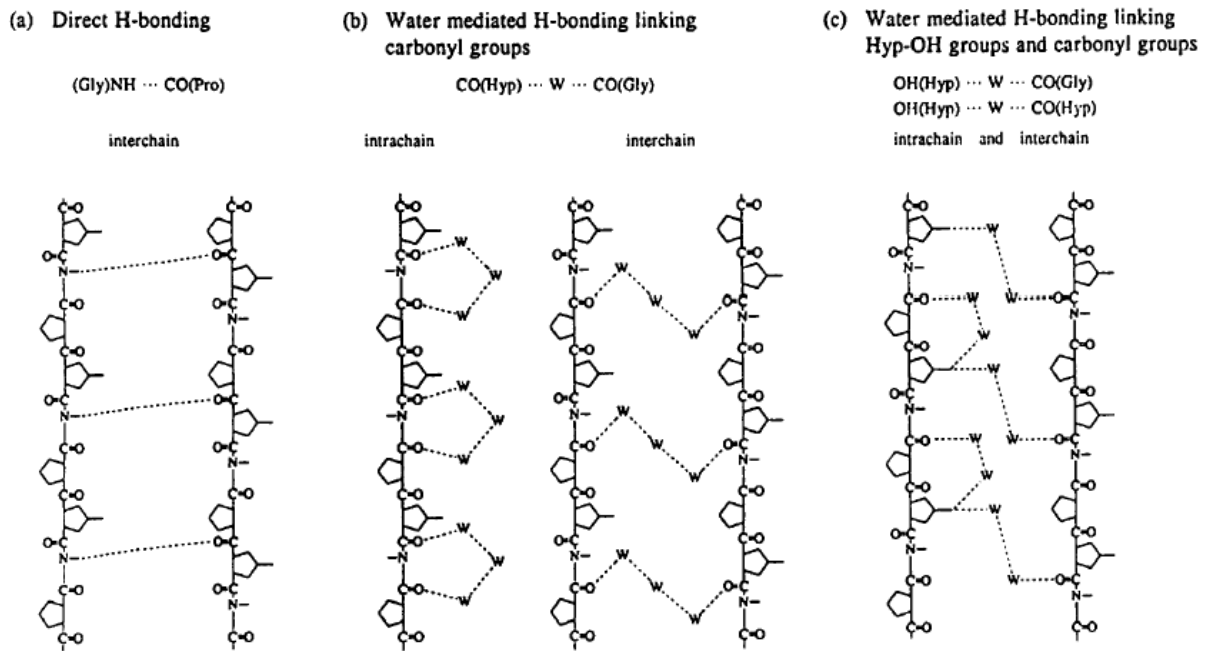


Figure (11): Possible interchain and intrachain hydrogen networks in the triple helix of a collagen molecule. “Reprint from *Matrix Biology*, 15, 8, B. Brodsky and J. A. M. Ramshaw, *The collagen triple-helix structure*, 545-554, Copyright (1997), with permission from Elsevier” [135].

The final step of the collagen fibril assembly is initiated by the release of the collagen monomers into the extracellular space. Here, the monomers form insoluble collagen fibrils by forming covalent cross-links between each other. Five, or a multiple of five, collagen monomers arrange themselves in a parallel stack, slightly shifted to one another by 67 nm [136]. Thus, the offset between the neighbouring, staggered, 300-nm long tropocollagens creates a region where all five fibrils overlap and a gap region where only four of them are side by side [137]. This arrangement gives the collagen fibril a characteristic 67-nm banding pattern, the so-called D-period. Further monomers then attach head to tail and extend these structures. The process of cross-linking the monomers is mainly enzymatically driven, primarily catalysed by lysyl oxidase (LOX), a copper-based amine oxidase [110].

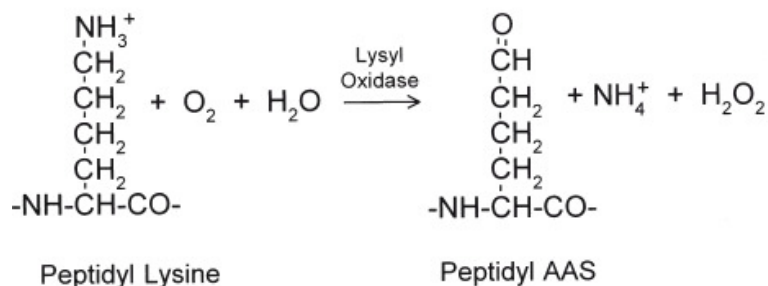


Figure (12): The deamination and oxidation of lysine by the enzymatic activity of lysyl oxidase. “Copyright Birkhäuser Verlag, Basel, *Cellular and Molecular Life Science*, 63, 19-20, (2006), 2304-2316, *Lysyl oxidase: an oxidative enzyme and effector of cell function*, H. A. Lucero and H. M. Kagan, figure 1. With kind permission from Springer Science+Business Media” [138].

LOX oxidises and deaminates amino groups at specific hydroxylysine and lysine sites, creating reactive aldehyde residues (figure 12) [139; 140]. These aldehydes react with neighbouring amino groups of unmodified hydroxylysine or lysine, creating a Schiff base and thus an intermolecular covalent cross-link between adjacent collagen monomers [138]. Without these stabilising cross-links, the fibrils have little or no strength. Collagen fibrils are finally packed and organised into bundles or meshwork.

### 3.1.3 Characterisation of Recent Collagen

Prior to ancient tissue investigations, recent reference collagen samples were characterised. To this end, bovine Achilles tendon and recent human skin were processed to two-micrometer-thick histological sections following standard protocols. The specimens were fixed, embedded in paraffin wax, cut and transferred onto glass slides. Before analysis, the paraffin was dissolved in xylene. Subsequently, the sections were rehydrated with a descending alcohol series, rinsed with ultra pure water, and dried under ambient conditions. After drying, collagen-rich areas were identified by AFM.

High-resolution AFM images revealed the orientation and banding pattern of the fibrils. In bovine Achilles tendon, collagen fibrils were found in parallel, highly ordered structures with a distinct uniaxial orientation (figure 13c). The structures featured the typical D-periodic banding pattern of roughly 67 nm. Fibrils were tightly packed, and single fibrils were hardly distinguishable.

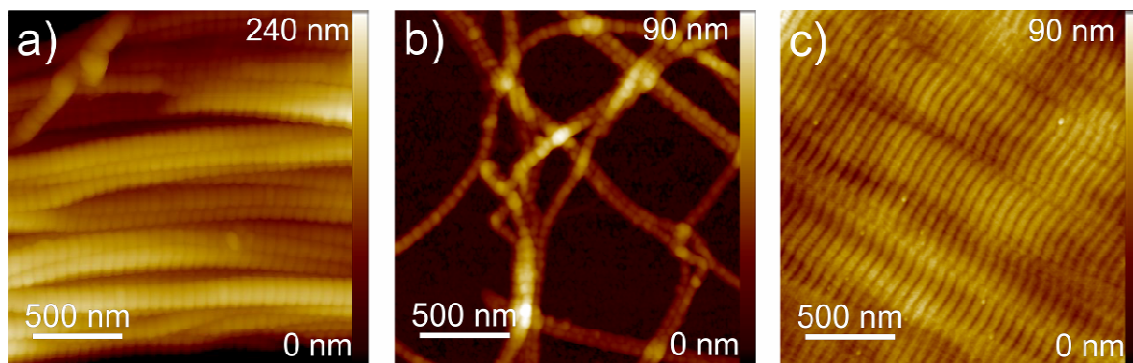


Figure (13): AFM images of (a), (b) human skin collagen ( $2 \times 2 \mu\text{m}$ ) and (c) bovine Achilles tendon collagen ( $2 \times 2 \mu\text{m}$ ). The fibrils in the skin are either arranged in parallel (a) or meshwork (b) structures. Collagen fibrils in tendons are more densely packed and aligned in highly ordered parallel structures. The characteristic D-period banding pattern is prevalent in all fibrils.

As in tendons, also human skin contained well-aligned collagen fibrils stacked in sheet-like structures. These structures, however, were less densely packed, slightly more random in orientation and sometimes overlapping. The D-period was  $65.2 \text{ nm} \pm 2.0 \text{ nm}$ , which is consistent with the banding pattern of tendons and literature values [126; 137; 141]. As is characteristic of the skin, additional networks of unsorted, often overlapping single collagen fibrils were observed (figure 13b). The collagen assemblies identified thus matched the collagen fibril arrangements typical of tendons and skin.



The molecular composition of the reference samples was quantified spectroscopically. Characteristic Raman spectra of collagen were obtained. The spectra featured the amide I (C=O stretching vibration mode) [142] and amide III (C-N stretching and N-H in-plane deformation mode) [142] bands, which represent peptide bonds within proteins such as collagen. These bands indicate the helical conformation of the collagen molecules and thus the intact collagen substructures within the tissues [128; 129; 142]. Also, the protein-typical vibration of methyl (CH<sub>3</sub>) and methylene (CH<sub>2</sub>) groups [143] were observed. Nevertheless, highly ordered collagen arrangements also showed anisotropic scattering properties. On fibrils aligned in parallel to one another, intensity variations in several Raman bands with respect to the polarisation of the incident laser were observed [144]. The amide I and amide III bands are among these, as shown in figure 14.

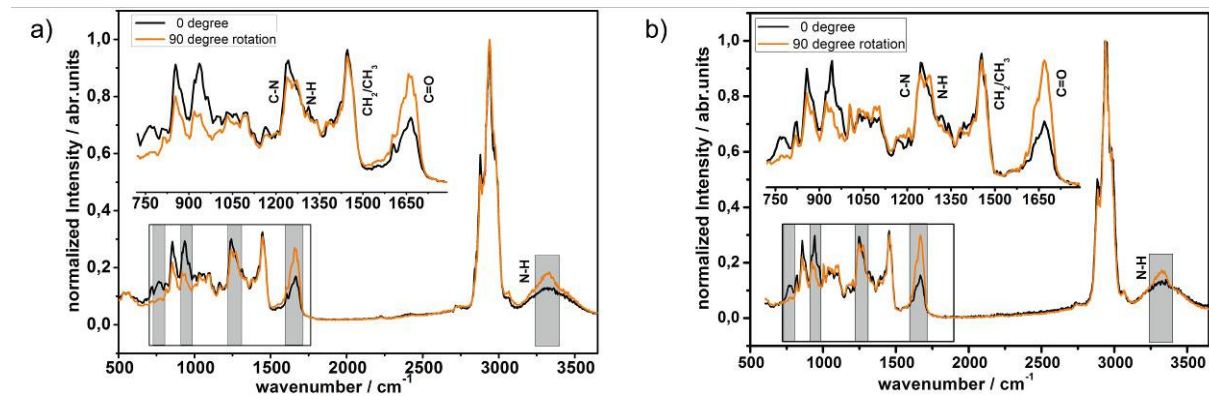


Figure (14): Normalised Raman spectra of collagen bundles in human skin (a) and in bovine Achilles tendon (b). Depending on the orientation of the collagen fibril to the incident laser beam, the intensity of specific bands changes. The grey squares mark the bands with the strongest anisotropic Raman scattering [144].

Other collagen bands exhibiting anisotropic Raman scattering were observed at approximately 766 cm<sup>-1</sup>, 780 cm<sup>-1</sup> (CCO) [145], 939 cm<sup>-1</sup> (C-C stretch), and 3321 cm<sup>-1</sup>, which corresponds to another N-H vibration mode of the amides in the protein backbone [146]. This anisotropic scattering is also shown in polar diagrams (figure 15). The intensity of the bands at 766 cm<sup>-1</sup>, 1246 cm<sup>-1</sup>, 1271 cm<sup>-1</sup>, 1451 cm<sup>-1</sup>, 1668 cm<sup>-1</sup> and 3321 cm<sup>-1</sup> as a function of the collagen orientation is shown. The bands at 1246 cm<sup>-1</sup>, assigned to the deformation vibration of N-H groups in a disordered phase [145], and 1451 cm<sup>-1</sup>, the deformation vibrations of methyl (CH<sub>3</sub>) and methylene (CH<sub>2</sub>) [142; 143], are included for comparison. These bands are not affected by the alignment of the collagen fibrils or the polarisation of the incident laser light.

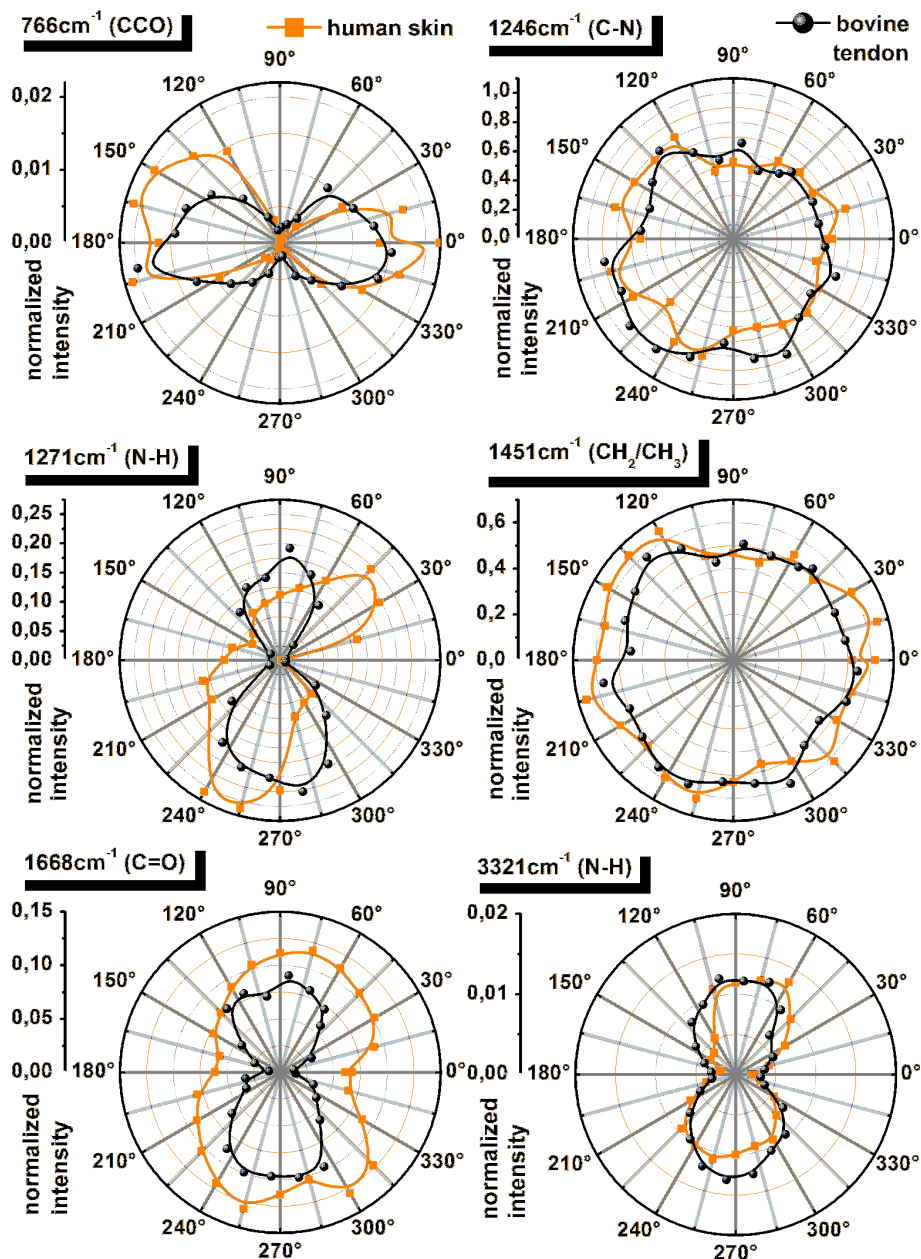


Figure (15): Polar diagrams of the intensity of selected Raman bands as a function of the collagen fibril orientation [144].

Both bands correspond to the Raman scattering of molecules that are equally distributed across the collagen amino acid sequence and thus show homogeneous Raman scattering.

In summary, the arrangement, conformation and orientation of collagen-rich reference samples were characterised by AFM and Raman spectroscopy. AFM imaging revealed collagen assemblies typical of tendons and skin. The molecular conformation of the biopolymer was determined by Raman spectroscopy. Characteristic collagen spectra were obtained. A collagen alignment-dependent anisotropic Raman scattering was observed, indicating that the orientation of Raman-active subunits of an ordered macromolecular protein can be determined by Raman spectroscopy. The orientation-dependent scattering enables the optical characterisation of the alignment of collagen fibrils and must be considered in the analysis of sample spectra.

### 3.1.4 Preservation of Ancient Collagen

To draw conclusions on the macroscopic preservation of tissue, it is necessary to analyse the individual subunits of the tissue because stabilisation of the material is determined on the molecular level. Ancient, collagen-based tissues show high stability and resistance to decay [20; 22; 147; 148; 149; 150; 151]. Thereby the collagen composition may affect the overall material properties and facilitate preservation. Skin is the anatomic outer shielding of the body, and even when mummified, it guards the underlying tissue from external influences and degradation. To quantify this protective function and to determine the degree of preservation, the structural and molecular integrity of mummy skin collagen must be investigated. Samples were drawn from the naturally mummified Tyrolean Iceman and measurements on the skin collagen of a bog body were conducted for comparison.

As for the reference skin samples, morphologically intact single collagen fibrils in meshwork and sheet-like structures were observed in the Iceman skin (figure 16) [152]. Single collagen fibrils in networks were unsorted and partly overlapped. Their D-period was roughly 67 nm. Fibrils were well preserved without any breaks or evidence of fragmentation. Excellent structural preservation was also observed for fibrils in stacked sheet-like structures (figures 16b and c).

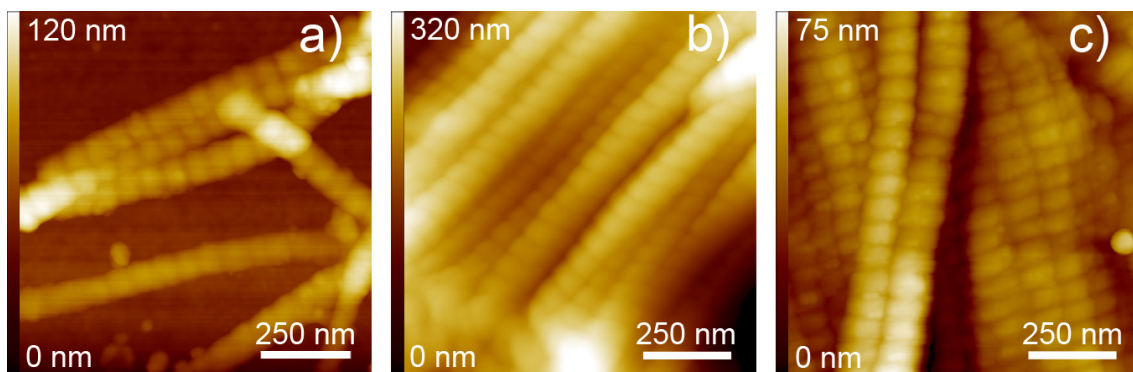


Figure (16): AFM images of collagen structures found in mummified human skin. In (a) single collagen fibrils in a meshwork are shown ( $1 \times 1 \mu\text{m}$ ). Images (b) and (c) show collagen fibrils arranged in parallel well-ordered sheet-like structures. All fibrils show the characteristic D-period banding pattern of 67 nm [152].

As in the AFM results, the Raman measurements also indicated that the ancient Iceman collagen is intact. The Raman spectra feature the characteristic amide I and amide III bands, suggesting the helical collagen conformation. Moreover, the positions of the Iceman Raman bands are similar to those of recent collagen (figure 17). Therefore, molecular degradation of the collagen can be excluded.

Based on these observations, it can be concluded that the ultrastructure of the collagen fibrils was not altered and that no decomposition of the fibril structure occurred.

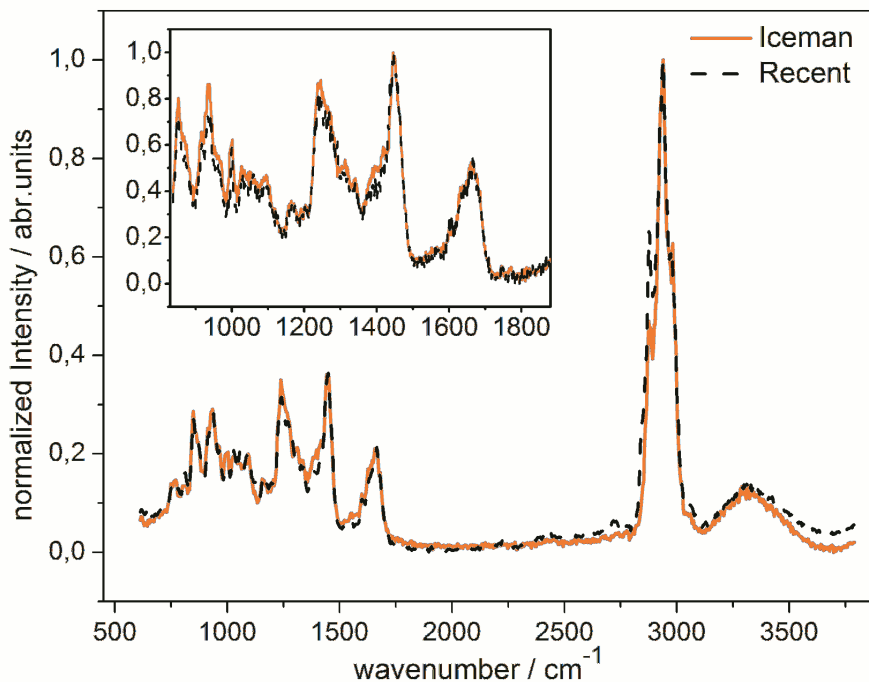


Figure (17): Average Raman spectrum (600–3600  $\text{cm}^{-1}$ ) of recent human skin collagen (dashed black line) and of Iceman skin collagen (solid orange line). The spectrum of the mummy collagen is similar to the recent collagen spectrum. The inset shows a close-up from 840 to 1900  $\text{cm}^{-1}$  wavenumbers. The spectra were normalised to the 1448  $\text{cm}^{-1}$  peak.

Additionally, the elasticity of the single Iceman collagen fibrils was tested by nanoindentation measurements. The obtained F-d curves were analysed using the Hertz model. Although AFM images and Raman spectroscopy showed that the collagen was molecularly and structurally intact, differences in the mechanical behaviour of recent and ancient fibrils were revealed. The Young's modulus of the Iceman collagen was  $4.1 \pm 1.1$  GPa, whereas the modulus of recent skin collagen was  $3.2 \pm 1.0$  GPa [152], indicating that the ancient collagen was slightly stiffer. Dehydration, and thus the removal of the interstitial water, could have brought the collagen subfibrils closer together, enabling the formation of additional interpeptide H-bonds or covalent cross-links [153] between the collagen molecules, which would lead to this increase in fibril stiffness [154]. Such a reinforcement of the collagen structures by supplementary cross-linking could have increased the collagen stability and resistance to decay. This result demonstrates the importance of dehydration for the mummification of connective tissue and presumes that the dehydrated skin maintained its protective function and prevented the underlying tissue from decomposition. Last but not least, this result supports the theory that the Iceman was covered by snow and ice immediately after his death [28; 155] and that periodic freeze-thaw cycles likely caused advanced desiccation by the sublimation of the majority of the water in the frozen tissue [1].

For comparison, the preservation of collagen in the skin of a mummified human bog body was examined. Investigations were carried out on the skin of an adult female, the so-called Zweeloo Woman, which was found in 1951 by peat cutters in a bog in Damsel, Netherlands. The female bog body was radiocarbon dated to the Roman period (78-233 AD). The woman's cause of death is unknown. Like the reference skin and the Iceman skin samples, the collagen

fibrils in the Zweeloo Woman skin were arranged in networks or sheet-like structures and featured a periodic banding pattern (figure 18 and 19). However, compared to the Iceman collagen or to collagen bundles found in the dermis of other bog bodies [147], the Zweeloo mummy collagen indicates moderate decomposition. The fibrils show considerable differences in fibril contour and size compared to the collagen found in recent human skin or in other mummies. The contour of the fibril structure is very faint, and the banding pattern of  $62.8 \pm 4.2$  nm is smaller than that reported in the literature.

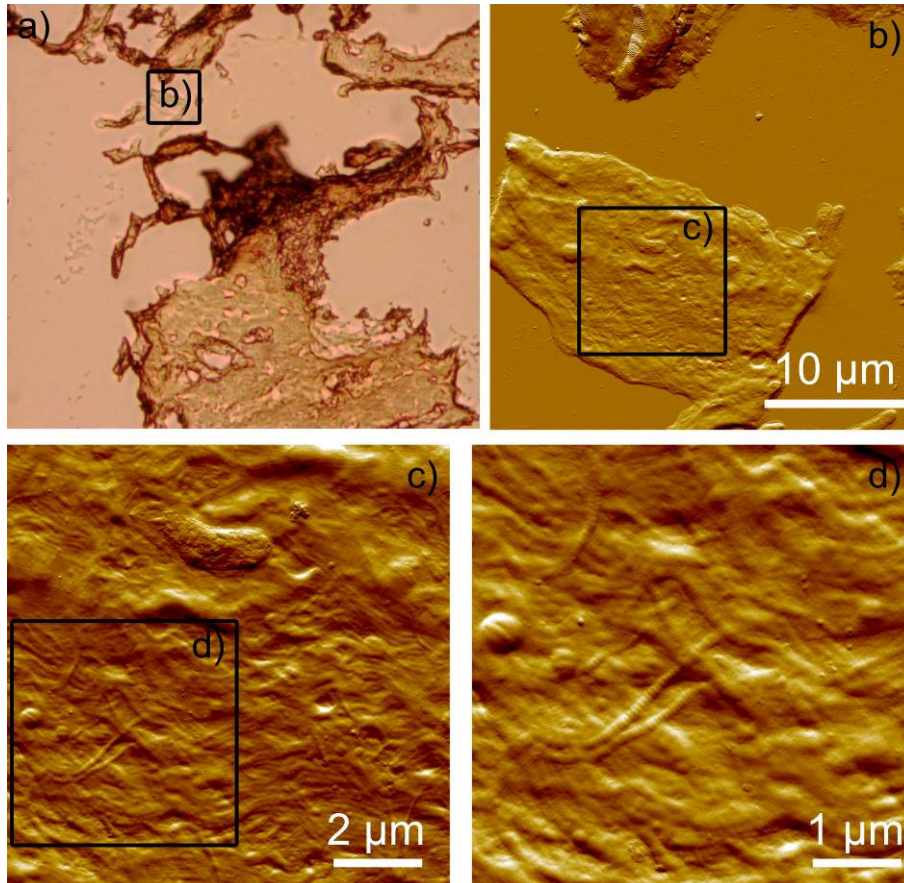


Figure (18): Optical (a) and AFM amplitude images (b), (c), and (d) of collagen structures found in the mummified skin of a bog body. The optical image of the histological section was taken with 100x magnification. Figures (b) to (d) show the AFM amplitude images of the areas outlined. In (d), unsorted and overlapping fibrils in a network-like structure are shown. Each fibril features a periodic substructure.

The reduction in the fibril dimensions may be caused by the decomposition of the collagen fibrils as observed in previous AFM studies [156; 157] that show the degradation of type I collagen by enzymatic activity, e.g., by collagenase or papain-gel. The enzymes seem to decompose the entire fibrillar structure in a non-specific manner causing the fibrils to become shorter and thinner.

An analogous effect may have occurred in the bog, causing the mummy collagen to slightly degrade and thus decrease in size. The degree of degradation is likely a function of the bog composition, e.g., its acidity.

While the acidity likely leads to degradation of collagen tissues, it is on the other hand also essential for the development of bog bodies. The acidic milieu decelerates the decay of organic tissue in a bog and promotes preservation. In particular, tannin, a polyphenolic compound in the plant cells of the peat bog moss *sphagnum*, is responsible for the bog acidity. As the plant dies, its phenolic compounds are released. The hydroxyl and carboxylic groups of tannins bind to proteins and form strong complexes [1], which may have enhanced the cross-links in the skin collagen of the Zweeloo Woman, thus stabilising and preserving it.

The molecular composition of the Zweeloo woman collagen could, however, not be determined by Raman spectroscopy due to strong fluorescence of the sample.

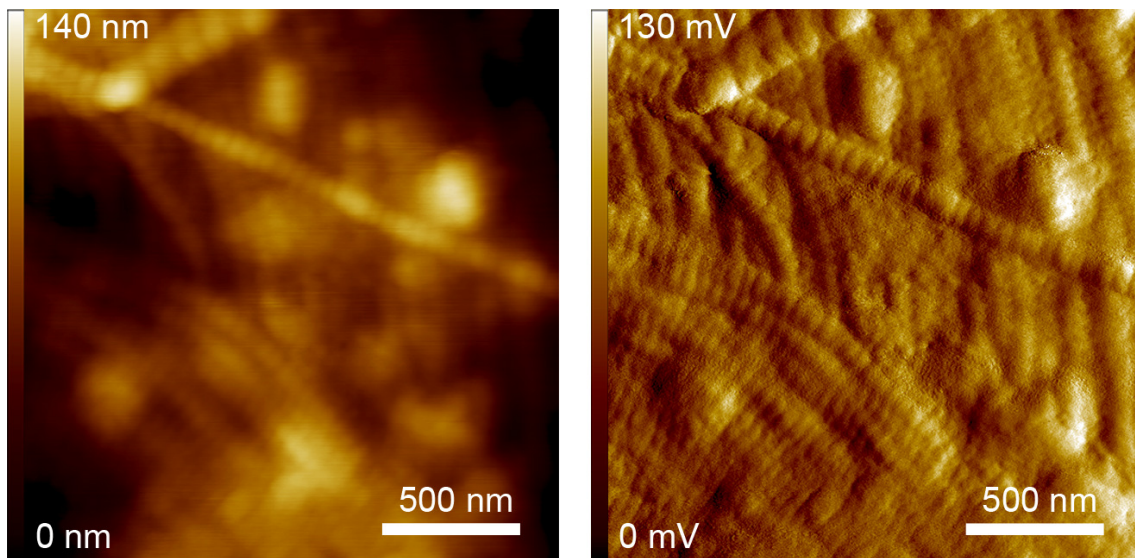


Figure (19): High-resolution AFM topography (a) and amplitude image (b) of collagen structures found in the histological skin sample of the Zweeloo Woman. In figure (a), ( $2 \times 2 \mu\text{m}$ ) collagen fibrils with a characteristic banding pattern are revealed. The fibrils form a network-like structure and sometimes overlap. The contours of the fibrils are faint. The amplitude image (b) shows the fibril contours in more detail.

In conclusion, the data demonstrate the outstanding resilience of collagen to decay and the excellent degree of preservation of the naturally mummified Iceman skin collagen.

## 3.2 RED BLOOD CELLS

**B**lood is a suspension of a liquid, known as plasma, and cellular corpuscles such as platelets, white blood cells and red blood cells. It regulates the body temperature, supplies cells with nutrients, is involved in immune defence, and regulates the process of haemostasis, wherein a damaged blood vessel is sealed by a blood clot and repaired. Red blood cells (RBCs) are the commonest blood corpuscle in the blood. They transport oxygen from the lungs to the cells and in return carry carbon dioxide to the lung. While flowing in the cardiovascular system, they are subject to deformation. The cells feature an elastic biconcave-shaped membrane [158] with a diameter of 6 to 8  $\mu\text{m}$  and a height of approximately 2.0  $\mu\text{m}$ . This structure makes them highly deformable and enables them to pass through capillaries as thin as 4  $\mu\text{m}$  to reach tissues [159; 160; 161].

The main biomolecule in RBCs is haemoglobin, a tetrameric protein made of four pyrroline chains, each of which carries an iron atom. The pyrroline subunits are interconnected via methine bridges (=CH-). A dried RBC consists of approximately 97 % haemoglobin. In vivo haemoglobin composes 34 % of the red blood cell content, water represents 65 %, and approximately 1 % of the RBC volume consists of enzymes and other proteins. RBCs are a fine indicator for diseases because their shape, molecular structure, and elasticity are prone to disease-specific alterations. The discovery of blood elements in ancient mummified human bodies, therefore, could help determine the immune status of an individual and explore the evolution of diseases.

### 3.2.1 The Coagulation of Blood

**B**lood coagulation leads to the formation of a solid blood clot. In vertebrates, this mechanism is the most complex part of haemostasis, in which damaged endothelial cells of blood vessels are identified, sealed, and finally repaired or dissolved and replaced. The complexity of coagulation is due to different pathways related to diverse injuries and several safety mechanisms that prevent unwanted blood clotting [162]. In general, the process of blood coagulation is a cascade of gradually activated clotting factors obliged to stop blood loss by creating a solid thrombus that forms immediately after an injury and covers the region of vascular damage [163].

The formation of a thrombus involves a cellular blood clotting mechanism, known as primary haemostasis, in which platelets, activated by glycoproteins that bind to their membrane, adhere to subendothelial collagen or von Willebrand factor (vWF) and form a platelet clot at the site of the vessel injury. Simultaneously, the plasmatic blood clotting or secondary haemostasis mechanism takes place. In this secondary mechanism, plasma proteins, called coagulation factors, are activated and form fibrin fibres, which provide the framework of the clot. Secondary haemostasis is divided into an intrinsic and extrinsic pathway, although both pathways presumably operate in parallel [164].

The initial point of coagulation is always an endothelial defect. Coagulation may result from several different events such as mechanical trauma, electrical trauma, vessel ligation or inflammation. Inflammation can be schematically modelled by a laser injury, inducing a heat impact that affects only a finite region and does not cause degradation of the vessel wall. In contrast, a model akin to mechanical trauma can be created by inducing oxidative endothelial damage with e.g. ferric chloride. Here, the endothelium becomes ablated, and the subendothelial matrix, consisting of collagen and bound vWF, is laid open [165].

Regardless of the cause of injury, blood passes through the injured blood vascular, and platelets interact with tissue factor (TF), collagen or vWF in the endothelium. The vWF therein initiates the connection of the platelets with the injured vessel wall through specific receptor interactions, resulting in the adhesion and aggregation of the platelets (primary haemostasis). The release and production of further coagulation factors activates and mobilises further platelets and causes them to become involved in the thrombus formation [165]. In addition, actin and myosin filaments rise from the activated platelet surface, creating a dense network between the platelets.

Co-instantaneous to platelet adhesion and aggregation, secondary haemostasis takes place. In this process, several other factors are released, activated, or generated [162; 163; 166], which, together with phospholipids of platelets or tissue and calcium ions  $\text{Ca}^{2+}$ , leads to the production of thrombin. Thrombin is the activated form of the enzymatically cleaved, inactive prothrombin [166; 167] and is crucial for secondary haemostasis because it converts soluble fibrinogen to the insoluble fibrous protein fibrin. Thrombin activates a fibrin-stabilising enzyme that cross-links fibrin monomers, resulting in a network that stabilises the platelet clot [168]. Dependent on the size of an injury, the fibrin thrombus may also contain RBCs. Due to their structure, blood clots are highly resilient. In combination with desiccation, they may provide a protective environment for blood residues embedded therein and preserve these residues for a long time.

### **3.2.2 RBC Preservation in Icemen Tissue**

This postulation is particularly meaningful when examining the oldest human glacier mummy, the Iceman, who sustained a lethal arrow wound immediately before his death [33]. X-ray and CT images of the arrow wound gave the first hints of the presence of blood residues. Inhomogeneous tissue areas were found and interpreted as a dehydrated haematoma [31; 169] associated with the lesion of the left subclavian artery that could have led to severe inner bleeding, a haemorrhagic shock, and the Iceman's death [34]. Additionally, haemoglobin was detected in the skin of the Iceman's right hand by a Guajac-based test [32], also suggesting a wound. However, in contrast to the good overall preservation of the tissue, no blood cells had been found.

To study the presence of human red blood cells in the tissue of the 5300-year-old Iceman, samples were extracted from the right hand stab trauma and from the arrowhead entry wound at the Iceman's back and examined by AFM. Some isolated single corpuscles with the approximate size and shape of normal RBCs [170] were identified (table 1).



The corpuscles featured the typical discoidal and concave shape of RBCs, which arises during the early stages of RBC development in the bone marrow when the cell nucleus is discarded, leaving an impressed membrane behind. Moreover, their morphology was without any evidence of degradation or damage. In addition to the single corpuscle, an agglomeration of several randomly distributed particles was found in the arrowhead wound (figure 20f).

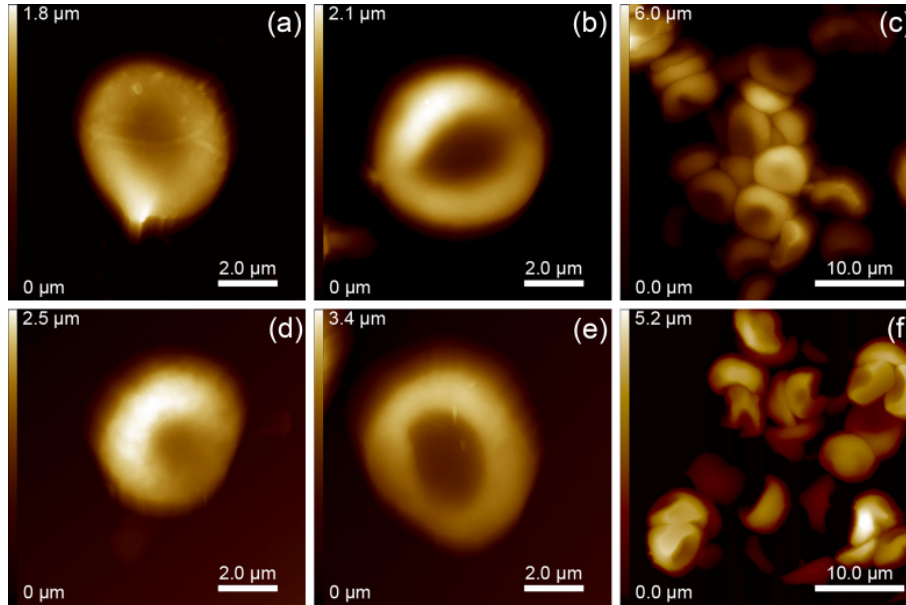


Figure (20): AFM images of RBCs. Images (a) and (b) show single RBCs from recent human tissue. Image (c) displays an assembly of RBCs. In images (d) and (e), single corpuscle, found in the Iceman right hand wound and arrowhead wound, are shown. Also an assembly of several randomly distributed corpuscles, similar to those in the recent sample (c), was found in the Iceman arrowhead wound (f). The imaged corpuscle (d-f) have the characteristic discoidal and concave surface of RBCs.

Table 1: Dimensions of recent RBCs and ancient corpuscle

| Sample            | Quantity | Height ( $\mu\text{m}$ ) | Diameter ( $\mu\text{m}$ ) | Area ( $\mu\text{m}^2$ ) | Volume (fl)     |
|-------------------|----------|--------------------------|----------------------------|--------------------------|-----------------|
| Recent RBCs       | 19       | $2.0 \pm 0.5$            | $6.3 \pm 0.4$              | $31.0 \pm 3.7$           | $40.0 \pm 12.2$ |
| Ancient corpuscle | 3        | $2.5 \pm 0.2$            | $6.0 \pm 0.3$              | $28.8 \pm 3.2$           | $42.1 \pm 4.1$  |

To verify the presence of RBCs, Raman spectra were taken from the Iceman samples and compared to reference whole blood and RBC spectra. The chemical composition and molecular conformation of the ancient corpuscle was revealed, showing the stretching vibration modes  $\nu_{37}$ ,  $\nu_{20}/\nu_{29}$ ,  $\nu_{21}$ , and  $\nu_{15}$  of porphyrin, the characteristic building unit of the RBC protein haemoglobin [171; 172; 173]. These data suggest that the ancient particles are RBCs. Nonetheless, it was also observed that the specific Raman bands were an order of magnitude weaker in the Iceman RBC spectra than in the reference RBC spectra (figure 21). This result indicates that the molecular conformation of the Iceman's RBCs had changed and that the majority of the haemoglobin had disappeared over time. The altered molecular structure may be due to degradation of the haemoglobin.

Furthermore, bands typical of other protein components, such as the twisting deformation mode of methylene, the deformation vibration of methyl molecules, the vibration mode of phenylalanine, and the amide III band, which represents peptide bonds [108; 142; 145], were

identified. These bands indicate that the Raman spectra of the Iceman corpuscle are composed of haemoglobin and other proteinaceous components. The proteinaceous compounds may originate from residues of proteins that were components of a former blood clot. This hypothesis is consistent with measurements on recent dried blood, which showed that the Raman spectrum of dried whole blood is a combination of the two main Raman-active components, namely, haemoglobin and fibrin [174].

This last assumption was validated by the Raman spectra obtained from the mummy corpuscle of the agglomerate. The spectra lacked the above-mentioned porphyrin modes and showed mainly bands characteristic of the blood protein fibrin (figure 21). As described, fibrin is the end product of a complex cascade of coagulation reactions that are initiated at the moment of a vascular injury. Fibrin is produced when thrombin cleaves fibrinogen and catalyses the polymerisation of fibrin, which subsequently generates a meshwork around a platelet plug and reinforces it [175].

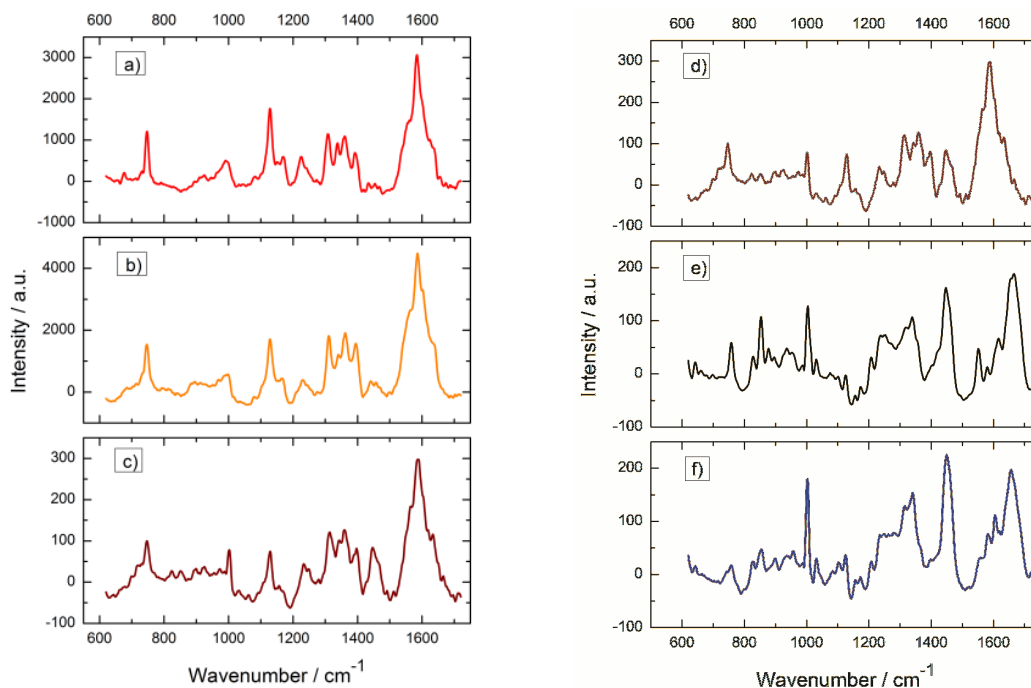


Figure (21): Raman spectra of air-dried whole blood (a), a single red blood cell (b), and a single corpuscle found in the Iceman tissue (c and d). All spectra show peaks at  $1586\text{cm}^{-1}$ ,  $1395\text{cm}^{-1}$ ,  $1308\text{cm}^{-1}$ , and  $747\text{cm}^{-1}$ , which are characteristic of porphyrin. With the exception of a few bands, the spectra show considerable similarities. Also shown are Raman spectra of a fibrin meshwork (e), and the agglomerated corpuscles found in the Iceman arrowhead wound (f). The spectrum obtained from the agglomerated corpuscles differs from that of the single Iceman corpuscle. It has features that are considerably similar to the spectrum of fibrin.

The Raman spectra and AFM images thus indicate that the single particles and the agglomerate of corpuscles (figure 22) in the wound tissue are the remnants of a haemostatic plug that formed after the Iceman was wounded. It can also be inferred that the fibrin surrounding the haemostatic clot decomposed over the millennia leaving only RBCs and possibly some fibrin fragments behind because neither a meshwork nor single fibrin fibrils were detected by AFM. The decrease in the specific haemoglobin Raman peak intensities

suggests that the majority of the ancient RBC haeme groups were altered or disappeared over the years.

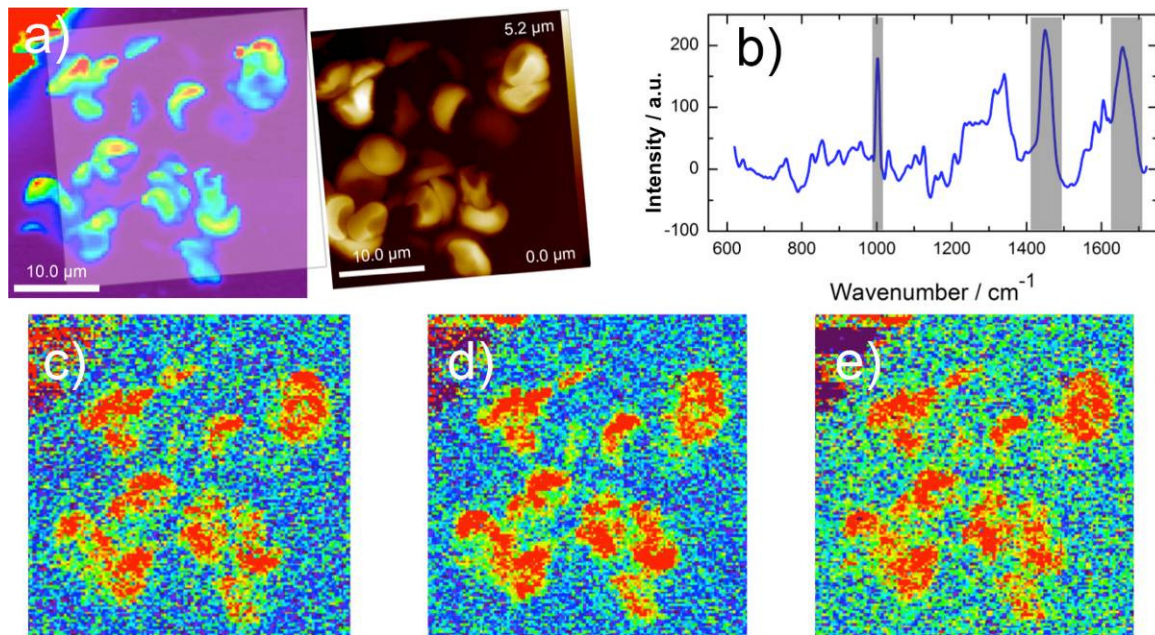


Figure (22): (a) Raman scan ( $35 \times 35 \mu\text{m}$ ) and AFM image ( $30 \times 30 \mu\text{m}$ ) of the RBC agglomerate. Recalculation of the Raman scan for selected Raman bands (b) gives the intensity distribution of the selected bands. (c-e) Raman map for fibrin-characteristic bands at approximately  $1000 \text{ cm}^{-1}$ ,  $1450 \text{ cm}^{-1}$ , and  $1660 \text{ cm}^{-1}$ . Red pixels define an area with high band intensity; blue and violet pixels represent a sample area with the lowest Raman band intensity. The highest band intensities are found at the sites of RBCs, indicating the presence of fibrin residues.

### 3.2.3 Secondary Conclusions from Iceman RBCs

The mechanical properties of RBCs are an indicator for disease and can provide insight into their molecular preservation. Reduced mechanical deformability, together with increased RBC membrane stiffness, has been reported in infections with the malaria parasite [176; 177; 178]. A similar phenotype appears in blood disorders such as sickle-cell disease, hereditary elliptocytosis, and hereditary spherocytosis, in which the deformability of the RBC membrane is reduced due to a strongly altered cell shape [178; 179; 180].

Although pre-processing the tissue samples does not allow one to draw conclusions on disease-specific mechanical changes in the RBC membrane, a relative comparison of the recent RBCs and the equally processed mummy RBCs should indicate the degree of tissue preservation over the past millennia. By performing nanoindentation measurements and analysing the obtained  $F-d$  curves with the Hertz model, the elasticity of the ancient corpuscles was assessed (figure 23).

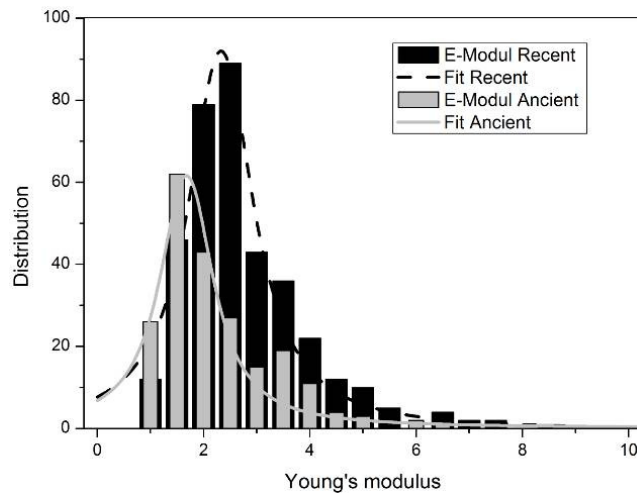


Figure (23): The distribution of the Young's moduli from the corpuscle of Iceman sample *B* and contemporary single RBCs. The Young's modulus of the mummy particles (grey) is significantly lower than that of the recent RBCs (black).

Mummy RBCs were slightly softer than recent RBCs, which may indicate a degradation of the RBC membrane framework. As observed in the Raman spectra, where the mummy RBCs showed a decrease in the RBC-specific porphyrin vibrations, these mechanical changes could originate from external influences, including damage to the RBC scaffold by crystallisation of ice during freezing, irradiation by UV light or wound healing-specific transformation processes that occur during the stages of blood clot degradation [181].

In conclusion, the structural, molecular and mechanical analyses of ancient corpuscles verified the preservation of RBCs in the 5300-year-old mummy tissue. Moreover, the structure and Raman spectra of some corpuscles point to remnants of a haemostatic clot. These data confirm that the Iceman sustained several injuries before his death. The samples contained RBCs with normal morphology. Blood disorders caused by red blood cell membrane defects, such as sickle-cell disease, elliptocytosis, and spherocytosis, can thus be excluded.

## 4. SUMMARY

It has recently been established that soft tissue or its fragments can be preserved in fossilised biological structures such as shells or bones. Likewise, it was experimentally verified that collagen and haeme-containing compounds can resist decay and that small round microstructures similar in size and shape to RBCs can be preserved in vessels from the demineralised bone of dinosaurs. In fossilised samples, the organic material is most likely preserved due to its encapsulation within the anorganic matrix or mineralised soft tissue.

In this work, it was postulated that if biological tissues have substructural arrangements that are advantageous to withstand mechanical loads, i.e., high elasticity and resilience, they might also have a favourable structure to become preserved in mummified tissue. Using the non-invasive analysis techniques AFM and Raman spectroscopy, the structural and molecular arrangement and the degree of tissue preservation were determined. Raman spectroscopy was utilised to reveal the tissue's molecular composition, and AFM was used to show the tissue's ultrastructure and mechanics. Both techniques were initially applied to characterise reference samples. The Raman spectra of the reference collagen contain bands whose intensities are specific for the conformation and alignment of the collagen fibrils. These observations were subsequently used to characterise ancient samples.

By analysing mummified skin collagen in samples drawn from the Iceman, exceptionally well-preserved collagen was found. The observed fibrils featured the typical collagen arrangement, either in parallel ordered sheet-like structures or in a random meshwork. Additionally, a collagen-specific banding pattern was observed. In addition to their morphology, the characteristic molecular structure of collagen, an intact triple helical fibril conformation, was ascertained. However, considerable differences were observed between the Iceman skin and samples drawn from a bog mummy. Although the skin collagen of the bog body was without any evidence of breaks or fragmentation and it exhibited the typical arrangements of skin, the fibrils appeared slightly degraded, indicating poorer preservation. The collagen showed only faint banding patterns and fibrils of inferior size. The acidic environment of the bog probably caused the collagen to degrade and thus altered its morphology and reduced its size. The mummification process of the Iceman, in contrast, seems to have a superior effect on preservation. Nanoindentation measurements revealed a higher elasticity of the Iceman collagen compared to recent collagen. Dehydration, i.e., the loss of interstitial water between the collagen molecules, may have compressed the ancient fibrils, thus enabling the generation of additional cross-links and causing an additional stiffening of the mummy skin. This stiffening may have improved the skin's protective function and its resistance to degradation by UV irradiation, freeze-thaw cycles, and the action of microorganisms.

Outstanding structural and molecular preservation was also obtained for mummified red blood cells. In the living organism, these blood corpuscles circulate throughout the cardiovascular system, passing diverse blood vessels, and are subject to deformation. To withstand this mechanical load, the cells have an elastic biconcave-shaped membrane.

Structural, molecular, and mechanical examinations verify the preservation of red blood cells in the 5300-year-old mummy tissue. Moreover, the structure and Raman spectra of some corpuscles pointed to remnants of a haemostatic clot. This result confirmed that the Iceman sustained several injuries before his death and provided evidence for the preservation of red blood cells in particular. The Raman spectra, however, also showed that haemoglobin-specific molecular vibrations of the ancient RBCs were weaker than those of recent RBCs. This finding suggests that the haemoglobin content of the RBCs changed due to the mummification or due to blood clot degradation processes. Thus, the first insights into the degradation of blood compounds in mummy tissue were obtained. Finally, the red blood cells showed normal morphologies. Blood disorders caused by red blood cell membrane defects, such as sickle-cell disease, elliptocytosis, and spherocytosis, could therefore be excluded.

In conclusion, the preservation of collagen and red blood cells in mummy tissue was confirmed and the degree of preservation specified. The investigations on collagen revealed that both the favourable environment conditions as well as the stiffening of the ancient collagen had a major influence on the extraordinary overall preservation of the Iceman. Additionally, the morphology of the detected red blood cells testifies that the Iceman did not suffer any red blood cell membrane-specific diseases. These results indicate that several types of information can still be drawn from mummified tissue and that biological tissues with advantageous structures can become preserved in mummified tissue as old as 5300 years.

## 5. BIBLIOGRAPHY

- [1] A.C. Aufderheide, *The scientific study of mummies*, Cambridge University Press, Cambridge, 2003.
- [2] M.H. Schweitzer, J.L. Wittmeyer, and J.R. Horner, Soft tissue and cellular preservation in vertebrate skeletal elements from the Cretaceous to the present. *Proc Biol Sci* 274 (2007) 183-97.
- [3] P. Semal, and R. Orban, Collagen Extraction from Recent and Fossil Bones: Quantitative and Qualitative Aspects. *Journal of Archaeological Science* 22 (1995) 463-467.
- [4] M.H. Schweitzer, W. Zheng, C.L. Organ, R. Avci, Z. Suo, L.M. Freimark, V.S. Lebleu, M.B. Duncan, M.G. Vander Heiden, J.M. Neveu, W.S. Lane, J.S. Cottrell, J.R. Horner, L.C. Cantley, R. Kalluri, and J.M. Asara, Biomolecular characterization and protein sequences of the Campanian hadrosaur *B. canadensis*. *Science* 324 (2009) 626-31.
- [5] M.H. Schweitzer, J.L. Wittmeyer, J.R. Horner, and J.K. Toporski, Soft-tissue vessels and cellular preservation in *Tyrannosaurus rex*. *Science* 307 (2005) 1952-5.
- [6] M.H. Schweitzer, Z. Suo, R. Avci, J.M. Asara, M.A. Allen, F.T. Arce, and J.R. Horner, Analyses of soft tissue from *Tyrannosaurus rex* suggest the presence of protein. *Science* 316 (2007) 277-80.
- [7] J.M. Asara, M.H. Schweitzer, L.M. Freimark, M. Phillips, and L.C. Cantley, Protein sequences from mastodon and *Tyrannosaurus rex* revealed by mass spectrometry. *Science* 316 (2007) 280-5.
- [8] J. Schobinger, Sacrifices of the High Andes. *Natural History* 4 (1991) 62-69.
- [9] A.C. Aufderheide, M. Zlonis, L.L. Cartmell, M.R. Zimmerman, P. Sheldrick, M. Cook, and J.E. Molto, Human mummification practices at Ismant El-Kharab. *The Journal of Egyptian Archaeology* 85 (1999) 197-210.
- [10] S. Aturaliya, and A. Lukasewycz, Experimental forensic and bioanthropological aspects of soft tissue taphonomy: 1. Factors influencing postmortem tissue desiccation rate. *Journal of Forensic Science* 44 (1999) 893-96.
- [11] M. Hofreiter, D. Serre, H.N. Poinar, M. Kuch, and S. Paabo, Ancient DNA. *Nat Rev Genet* 2 (2001) 353-9.
- [12] R.E. Green, J. Krause, S.E. Ptak, A.W. Briggs, M.T. Ronan, J.F. Simons, L. Du, M. Egholm, J.M. Rothberg, M. Paunovic, and S. Paabo, Analysis of one million base pairs of Neanderthal DNA. *Nature* 444 (2006) 330-6.
- [13] W.L. Salo, A.C. Aufderheide, J. Buikstra, and T.A. Holcomb, Identification of *Mycobacterium tuberculosis* DNA in a pre-Columbian Peruvian mummy. *Proc Natl Acad Sci U S A* 91 (1994) 2091-4.
- [14] A. Zink, C.J. Haas, U. Reischl, U. Szeimies, and A.G. Nerlich, Molecular analysis of skeletal tuberculosis in an ancient Egyptian population. *J Med Microbiol* 50 (2001) 355-66.
- [15] A.R. Zink, C. Sola, U. Reischl, W. Grabner, N. Rastogi, H. Wolf, and A.G. Nerlich, Characterization of *Mycobacterium tuberculosis* complex DNAs from Egyptian mummies by spoligotyping. *J Clin Microbiol* 41 (2003) 359-67.
- [16] J. Krause, P.H. Dear, J.L. Pollack, M. Slatkin, H. Spriggs, I. Barnes, A.M. Lister, I. Ebersberger, S. Paabo, and M. Hofreiter, Multiplex amplification of the mammoth mitochondrial genome and the evolution of Elephantidae. *Nature* 439 (2006) 724-7.
- [17] W. Rom, R. Golser, W. Kutschera, A. Priller, P. Steier, and E.M. Wild, AMS 14C dating of equipment from the Iceman and of spruce logs from the prehistoric salt mines of Hallstatt. *Radiocarbon* 41 (1999) 183-197.

- [18] K. Hollemeyer, W. Altmeyer, E. Heinzle, and C. Pitra, Species identification of Oetzi's clothing with matrix-assisted laser desorption/ionization time-of-flight mass spectrometry based on peptide pattern similarities of hair digests. *Rapid Commun Mass Spectrom* 22 (2008) 2751-67.
- [19] H. Seidler, W. Bernhard, M. Teschler-Nicola, W. Platzer, D. zur Nedden, R. Henn, A. Oberhauser, and T. Sjøvold, Some anthropological aspects of the prehistoric Tyrolean ice man. *Science* 258 (1992) 455-7.
- [20] M.W. Hess, G. Klima, K. Pfaller, K.H. Kunzel, and O. Gaber, Histological investigations on the Tyrolean Ice Man. *Am J Phys Anthropol* 106 (1998) 521-32.
- [21] A. Makristathis, J. Schwarzmeier, R.M. Mader, K. Varmuza, I. Simonitsch, J.C. Chavez, W. Platzer, H. Unterdorfer, R. Scheithauer, A. Derevianko, and H. Seidler, Fatty acid composition and preservation of the Tyrolean Iceman and other mummies. *J Lipid Res* 43 (2002) 2056-61.
- [22] A.C. Williams, H.G. Edwards, and B.W. Barry, The 'Iceman': molecular structure of 5200-year-old skin characterised by Raman spectroscopy and electron microscopy. *Biochim Biophys Acta* 1246 (1995) 98-105.
- [23] W. Kowal, O.B. Beattie, H. Baadsgaard, and P.M. Krahn, Source identification of lead found in tissues of sailors from the Franklin Arctic Expedition of 1845. *Journal of Archaeological Science* 18 (1991) 193-203.
- [24] F. Van Noten, and N. Polosmak, The frozen tombs of the Scythians. *Endeavour* 19 (1995) 76-82.
- [25] W.R. Farrand, Frozen Mammoths and Modern Geology: The death of the giants can be explained as a hazard of tundra life, without evoking catastrophic events. *Science* 133 (1961) 729-35.
- [26] J.M. Lowenstein, V.M. Sarich, and B.J. Richardson, Albumin systematics of the extinct mammoth and Tasmanian wolf. *Nature* 291 (1981) 409-11.
- [27] M.R. Zimmerman, and R.H. Tedford, Histologic structures preserved for 21,300 years. *Science* 194 (1976) 183-4.
- [28] T.L. Bereuter, W. Mikenda, and C. Reiter, Iceman's Mummification - Implications from Infrared Spectroscopical and Histological Studies. *Chemistry - A European Journal* 3 (1997) 1032-38.
- [29] D. zur Nedden, R. Knapp, K. Wicke, W. Judmaier, W.A. Murphy, Jr., H. Seidler, and W. Platzer, Skull of a 5,300-year-old mummy: reproduction and investigation with CT-guided stereolithography. *Radiology* 193 (1994) 269-72.
- [30] K. Spindler, The Iceman's last weeks. *Nuclear Instruments and Methods in Physics Research Section B: Beam Interactions with Materials and Atoms* 92 (1994) 274-281.
- [31] P. Gostner, and E.E. Vigl, INSIGHT: Report of Radiological-Forensic Findings on the Iceman. *Journal of Archaeological Science* 29 (2002) 323-326.
- [32] A.G. Nerlich, B. Bachmeier, A. Zink, S. Thalhammer, and E. Egarter-Vigi, Otzi had a wound on his right hand. *Lancet* 362 (2003) 334-334.
- [33] A.G. Nerlich, O. Peschel, and E. Egarter-Vigl, New evidence for Otzi's final trauma. *Intensive Care Med* 35 (2009) 1138-9.
- [34] P. Pernter, P. Gostner, E.E. Vigl, and F.J. Rühli, Radiologic proof for the Iceman's cause of death (ca. 5'300 BP). *Journal of Archaeological Science* 34 (2007) 1784-1786.
- [35] A. Cockburn, R.A. Barraco, T.A. Reyman, and W.H. Peck, Autopsy of an Egyptian mummy. *Science* 187 (1975) 1155-60.
- [36] P.K. Lewin, Mummies That I Have Known: A Pediatrician's Venture in the Field of Paleopathology. *Archives of Pediatrics Adolescent Medicine* 131 (1977) 349-350.
- [37] P.K. Lewin, J.E. Trogadis, and J.K. Stevens, Three-dimensional reconstructions from serial X-ray tomography of an Egyptian mummified head. *Clinical Anatomy* 3 (1990) 215-218.
- [38] F.J. Rühli, G. Kuhn, R. Evison, R. Muller, and M. Schultz, Diagnostic value of micro-CT in comparison with histology in the qualitative assessment of historical human skull bone pathologies. *Am J Phys Anthropol* 133 (2007) 1099-111.



- [39] H. Piepenbrink, J. Frahm, A. Haase, and D. Matthaei, Nuclear magnetic resonance imaging of mummified corpses. *Am J Phys Anthropol* 70 (1986) 27-8.
- [40] S.J. Karlik, R. Bartha, K. Kennedy, and R. Chhem, MRI and multinuclear MR spectroscopy of 3,200-year-old Egyptian mummy brain. *AJR Am J Roentgenol* 189 (2007) W105-10.
- [41] W. Ligon, S.B. Dorn, R.J. May, and M.J. Allison, Chlorodibenzofuran and chlorodibenzo-p-dioxin levels in Chilean mummies dated to about 2800 years before the present. *Environmental Science & Technology* 23 (1989) 1286-1290.
- [42] F.J. Ruhli, H. von Waldburg, S. Nielles-Vallespin, T. Boni, and P. Speier, Clinical magnetic resonance imaging of ancient dry human mummies without rehydration. *JAMA* 298 (2007) 2618-20.
- [43] S. Paabo, Molecular cloning of Ancient Egyptian mummy DNA. *Nature* 314 (1985) 644-5.
- [44] G. Binnig, C.F. Quate, and C. Gerber, Atomic force microscope. *Phys Rev Lett* 56 (1986) 930-933.
- [45] M. Radmacher, R.W. Tillmann, M. Fritz, and H.E. Gaub, From molecules to cells: imaging soft samples with the atomic force microscope. *Science* 257 (1992) 1900-1905.
- [46] F. Ohnesorge, and G. Binnig, True atomic resolution by atomic force microscopy through repulsive and attractive forces. *Science* 260 (1993) 1451-6.
- [47] F.J. Giessibl, Atomic Resolution of the Silicon (111)-(7x7) Surface by Atomic Force Microscopy. *Science* 267 (1995) 68-71.
- [48] T. Schimmel, T. Koch, J. Küppers, and M. Lux-Steiner, True atomic resolution under ambient conditions obtained by atomic force microscopy in the contact mode. *Applied Physics A: Materials Science & Processing* 68 (1999) 399-402.
- [49] Y. Sugawara, T. Uchihashi, M. Abe, and S. Morita, True atomic resolution imaging of surface structure and surface charge on the GaAs(110). *Applied Surface Science* 140 (1999) 371-375.
- [50] N.A. Burnham, and R.J. Colton, Measuring the nanomechanical properties and surface forces of materials using an atomic force microscope. *Journal of Vacuum Science & Technology A: Vacuum, Surfaces, and Films* 7 (1989) 2906-2913.
- [51] M. Radmacher, Measuring the elastic properties of biological samples with the AFM. *Engineering in Medicine and Biology Magazine, IEEE* 16 (1997) 47-57.
- [52] M.-F. Yu, B.S. Files, S. Arepalli, and R.S. Ruoff, Tensile Loading of Ropes of Single Wall Carbon Nanotubes and their Mechanical Properties. *Physical Review Letters* 84 (2000) 5552.
- [53] J. Domke, and M. Radmacher, Measuring the Elastic Properties of Thin Polymer Films with the Atomic Force Microscope. *Langmuir* 14 (1998) 3320-3325.
- [54] M. Radmacher, M. Fritz, C.M. Kacher, J.P. Cleveland, and P.K. Hansma, Measuring the viscoelastic properties of human platelets with the atomic force microscope. *Biophysical Journal* 70 (1996) 556-567.
- [55] M. Ternes, C.P. Lutz, C.F. Hirjibehedin, F.J. Giessibl, and A.J. Heinrich, The force needed to move an atom on a surface. *Science* 319 (2008) 1066-9.
- [56] M. Erdmann, R. David, A. Fornof, and H.E. Gaub, Electrically controlled DNA adhesion. *Nat Nanotechnol* 5 (2010) 154-9.
- [57] Y. Yan, Z. Hu, X. Zhao, T. Sun, S. Dong, and X. Li, Top-down nanomechanical machining of three-dimensional nanostructures by atomic force microscopy. *Small* 6 (2010) 724-8.
- [58] M. Rief, M. Gautel, F. Oesterhelt, J.M. Fernandez, and H.E. Gaub, Reversible unfolding of individual titin immunoglobulin domains by AFM. *Science* 276 (1997) 1109-12.
- [59] M. Rief, F. Oesterhelt, B. Heymann, and H.E. Gaub, Single Molecule Force Spectroscopy on Polysaccharides by Atomic Force Microscopy. *Science* 275 (1997) 1295-7.
- [60] M. Rief, J. Pascual, M. Saraste, and H.E. Gaub, Single molecule force spectroscopy of spectrin repeats: low unfolding forces in helix bundles. *J Mol Biol* 286 (1999) 553-61.

- [61] L. Gross, F. Mohn, N. Moll, P. Liljeroth, and G. Meyer, The chemical structure of a molecule resolved by atomic force microscopy. *Science* 325 (2009) 1110-4.
- [62] T.R. Albrecht, S. Akamine, T.E. Carver, and C.F. Quate, Microfabrication of cantilever styli for the atomic force microscope. *Journal of Vacuum Science & Technology A: Vacuum, Surfaces, and Films* 8 (1990) 3386-3396.
- [63] S. Rützel, S.I. Lee, and A. Raman, Nonlinear dynamics of atomic force microscope probes driven in Lennard-Jones potentials. *Proceedings of the Royal Society of London. Series A: Mathematical, Physical and Engineering Sciences* 459 (2003) 1925-1948.
- [64] R. Garcia, and A. San Paulo, Attractive and repulsive tip-sample interaction regimes in tapping-mode atomic force microscopy. *Physical Review B* 60 (1999) 4961-4967.
- [65] G. Meyer, and N.M. Amer, Novel optical approach to atomic force microscopy. *Applied Physics Letters* 53 (1988) 1045-1047.
- [66] A. Yurtsever, Nanotribological surface characterization by frequency modulated torsional resonance mode AFM, Dissertation, Faculty of Geosciences, Ludwig-Maximilians-Universität München, München, 2008, pp. 105.
- [67] J.P. Cleveland, S. Manne, D. Bocek, and P.K. Hansma, A nondestructive method for determining the spring constant of cantilevers for scanning force microscopy. *Review of Scientific Instruments* 64 (1993) 403-405.
- [68] J.L. Hutter, and J. Bechhoefer, Calibration of atomic-force microscope tips. *Review of Scientific Instruments* 64 (1993) 1868-1873.
- [69] J.E. Sader, J.W.M. Chon, and P. Mulvaney, Calibration of rectangular atomic force microscope cantilevers. *Review of Scientific Instruments* 70 (1999) 3967-3969.
- [70] H.-J. Butt, and M. Jaschke, Calculation of thermal noise in atomic force microscopy. *Nanotechnology* 6 (1995) 1-7.
- [71] Q. Zhong, D. Inniss, K. Kjoller, and V.B. Elings, Fractured polymer/silica fiber surface studied by tapping mode atomic force microscopy. *Surface Science Letters* 290 (1993) L688-L692.
- [72] Y. Martin, C.C. Williams, and H.K. Wickramasinghe, Atomic force microscope-force mapping and profiling on a sub 100-Å scale. *Journal of Applied Physics* 61 (1987) 4723-4729.
- [73] R. Erlandsson, L. Olsson, and P. Martensson, Inequivalent atoms and imaging mechanisms in ac-mode atomic-force microscopy of Si(111)7x7. *Physical Review B* 54 (1996) R8309-R8312.
- [74] J. Tamayo, and R. Garcia, Deformation, Contact Time, and Phase Contrast in Tapping Mode Scanning Force Microscopy. *Langmuir* 12 (1996) 4430-4435.
- [75] J.P. Spatz, S. Sheiko, M. Möller, R.G. Winkler, P. Reineker, and O. Marti, Tapping Scanning Force Microscopy in Air-Theory and Experiment. *Langmuir* 13 (1997) 4699-4703.
- [76] J.P. Cleveland, B. Anczykowski, A.E. Schmid, and V.B. Elings, Energy dissipation in tapping-mode atomic force microscopy. *Applied Physics Letters* 72 (1998) 2613-2615.
- [77] A.S. Paulo, and R. Garcia, Unifying theory of tapping-mode atomic-force microscopy. *Physical Review B* 66 (2002) 041406.
- [78] T.R. Albrecht, P. Grütter, D. Horne, and D. Rugar, Frequency modulation detection using high-Q cantilevers for enhanced force microscope sensitivity. *Journal of Applied Physics* 69 (1991) 668-673.
- [79] N.A. Burnham, and et al., How does a tip tap? *Nanotechnology* 8 (1997) 67.
- [80] R.S. McLean, and B.B. Sauer, Tapping-Mode AFM Studies Using Phase Detection for Resolution of Nanophases in Segmented Polyurethanes and Other Block Copolymers. *Macromolecules* 30 (1997) 8314-8317.
- [81] I. Schmitz, M. Schreiner, G. Friedbacher, and M. Grasserbauer, Phase imaging as an extension to tapping mode AFM for the identification of material properties on humidity-sensitive surfaces. *Applied Surface Science* 115 (1997) 190-198.
- [82] F.J. Giessibl, Advances in atomic force microscopy. *Reviews of Modern Physics* 75 (2003) 949.

- [83] F.J. Giessibl, S. Hembacher, H. Bielefeldt, and J. Mannhart, Subatomic Features on the Silicon (111)-(7x7) Surface Observed by Atomic Force Microscopy. *Science* 289 (2000) 422-425.
- [84] N. Oyabu, O. Custance, I. Yi, Y. Sugawara, and S. Morita, Mechanical Vertical Manipulation of Selected Single Atoms by Soft Nanoindentation Using Near Contact Atomic Force Microscopy. *Physical Review Letters* 90 (2003) 176102.
- [85] Y. Sugimoto, P. Pou, M. Abe, P. Jelinek, R. Perez, S. Morita, and O. Custance, Chemical identification of individual surface atoms by atomic force microscopy. *Nature* 446 (2007) 64-67.
- [86] A.L. Weisenhorn, P.K. Hansma, T.R. Albrecht, and C.F. Quate, Forces in atomic force microscopy in air and water. *Applied Physics Letters* 54 (1989) 2651-2653.
- [87] U. Landman, W.D. Luedtke, N.A. Burnham, and R.J. Colton, Atomistic Mechanisms and Dynamics of Adhesion, Nanoindentation, and Fracture. *Science* 248 (1990) 454-461.
- [88] B. Cappella, and G. Dietler, Force-distance curves by atomic force microscopy. *Surface Science Reports* 34 (1999) 1-104.
- [89] H.-J. Butt, B. Cappella, and M. Kappl, Force measurements with the atomic force microscope: Technique, interpretation and applications. *Surface Science Reports* 59 (2005) 1-152.
- [90] W.C. Oliver, and G.M. Pharr, An improved technique for determining hardness and elastic modulus using load and displacement sensing indentation experiments. *Journal of Materials Research* 7 (1992) 1564-1583.
- [91] F.J. Rubio Sierra, Controlled surface manipulation at the nanometer scale based on the atomic force microscope, Dissertation, Faculty of Geosciences, Ludwig-Maximilians-Universität München, München, 2006, pp. 153.
- [92] A.L. Weisenhorn, P. Maivald, H.J. Butt, and P.K. Hansma, Measuring adhesion, attraction, and repulsion between surfaces in liquids with an atomic-force microscope. *Physical Review B* 45 (1992) 11226-11232.
- [93] N.A. Burnham, R.J. Colton, and H.M. Pollock, Interpretation issues in force microscopy. *Journal of Vacuum Science & Technology A: Vacuum, Surfaces, and Films* 9 (1991) 2548-2556.
- [94] H. Hertz, Ueber die Berührung fester elastischer Körper. *Journal für die reine und angewandte Mathematik (Crelles Journal)* 1882 (1882) 156-171.
- [95] I.N. Sneddon, The relation between load and penetration in the axisymmetric boussinesq problem for a punch of arbitrary profile. *International Journal of Engineering Science* 3 (1965) 47-57.
- [96] A.L. Weisenhorn, and et al., Deformation and height anomaly of soft surfaces studied with an AFM. *Nanotechnology* 4 (1993) 106.
- [97] M. Heuberger, G. Dietler, and L. Schlapbach, Elastic deformations of tip and sample during atomic force microscope measurements. *Journal of Vacuum Science & Technology B: Microelectronics and Nanometer Structures* 14 (1996) 1250-1254.
- [98] M. Radmacher, M. Fritz, and P.K. Hansma, Imaging soft samples with the atomic force microscope: gelatin in water and propanol. *Biophysical Journal* 69 (1995) 264-270.
- [99] B.V. Derjaguin, V.M. Muller, and Y.P. Toporov, Effect of contact deformations on the adhesion of particles. *Journal of Colloid and Interface Science* 53 (1975) 314-326.
- [100] K.L. Johnson, K. Kendall, and A.D. Roberts, Surface Energy and the Contact of Elastic Solids. *Proceedings of the Royal Society of London. A. Mathematical and Physical Sciences* 324 (1971) 301-313.
- [101] D. Maugis, Adhesion of spheres: The JKR-DMT transition using a dugdale model. *Journal of Colloid and Interface Science* 150 (1992) 243-269.
- [102] C.V. Raman, A Change of Wave-length in Light Scattering. *Nature* 121 (1928) 619-619.
- [103] C.V. Raman, and K.S. Krishnan, A New Type of Secondary Radiation. *Nature* 121 (1928) 501-502.

- [104] C.V. Raman, and K.S. Krishnan, The Optical Analogue of the Compton Effect. *Nature* 121 (1928) 711-711.
- [105] J.R. Ferraro, K. Nakamoto, and C.W. Brown, *Introductory Raman Spectroscopy*, Academic Press - Elsevier Science, San Diego, 2003.
- [106] M. Bauer, Raman spectroscopy of laser induced material alterations, Dissertation, Faculty of Geosciences, Ludwig-Maximilians-Universität München, München, 2010, pp. 128.
- [107] W. Demtröder, *Laser Spectroscopy - Basic Concepts and Instrumentation*, Springer-Verlag, Berlin, 2003.
- [108] I. Notingher, and L.L. Hench, Raman microspectroscopy: a noninvasive tool for studies of individual living cells in vitro. *Expert Rev Med Devices* 3 (2006) 215-34.
- [109] G.A. Di Lullo, S.M. Sweeney, J. Korkko, L. Ala-Kokko, and J.D. San Antonio, Mapping the ligand-binding sites and disease-associated mutations on the most abundant protein in the human, type I collagen. *J Biol Chem* 277 (2002) 4223-31.
- [110] P. Fratzl, *Collagen: structure and mechanics*, Springer Science+Business Media, New York, USA, 2008.
- [111] P.P. Provenzano, and R. Vanderby, Jr., Collagen fibril morphology and organization: implications for force transmission in ligament and tendon. *Matrix Biol* 25 (2006) 71-84.
- [112] A.P. Rumian, A.L. Wallace, and H.L. Birch, Tendons and ligaments are anatomically distinct but overlap in molecular and morphological features—a comparative study in an ovine model. *J Orthop Res* 25 (2007) 458-64.
- [113] F.H. Silver, J.W. Freeman, and G.P. Seehra, Collagen self-assembly and the development of tendon mechanical properties. *J Biomech* 36 (2003) 1529-53.
- [114] M. Franchi, A. Trire, M. Quaranta, E. Orsini, and V. Ottani, Collagen structure of tendon relates to function. *ScientificWorldJournal* 7 (2007) 404-20.
- [115] R.M. Alexander, Tendon elasticity and muscle function. *Comp Biochem Physiol A Mol Integr Physiol* 133 (2002) 1001-11.
- [116] R.E. Shadwick, Elastic energy storage in tendons: mechanical differences related to function and age. *J Appl Physiol* 68 (1990) 1033-40.
- [117] T. Fukunaga, K. Kubo, Y. Kawakami, S. Fukashiro, H. Kanehisa, and C.N. Maganaris, In vivo behaviour of human muscle tendon during walking. *Proc Biol Sci* 268 (2001) 229-33.
- [118] C. Ploetz, E.I. Zycband, and D.E. Birk, Collagen fibril assembly and deposition in the developing dermis: segmental deposition in extracellular compartments. *J Struct Biol* 106 (1991) 73-81.
- [119] K.M. Meek, and C. Boote, The organization of collagen in the corneal stroma. *Exp Eye Res* 78 (2004) 503-12.
- [120] D.M. Maurice, The structure and transparency of the cornea. *J Physiol* 136 (1957) 263-86.
- [121] A. Daxer, and P. Fratzl, Collagen fibril orientation in the human corneal stroma and its implication in keratoconus. *Invest Ophthalmol Vis Sci* 38 (1997) 121-9.
- [122] J. Myllyharju, *Intracellular Post-Translational Modifications of Collagens*, Topics in Current Chemistry: Collagen, Springer-Verlag Berlin Heidelberg, Berlin, 2005, pp. 115-147.
- [123] G.N. Ramachandran, Structure of Collagen. *Nature* 177 (1956) 710-711.
- [124] G.N. Ramachandran, and G. Kartha, Structure of Collagen. *Nature* 174 (1954) 269-270.
- [125] A. Rich, and F.H.C. Crick, Structure of Collagen. *Nature* 176 (1955) 915-916.
- [126] M. van der Rest, and R. Garrone, Collagen Family of Proteins. *FASEB Journal* 5 (1991) 2814-2823.
- [127] K.E. Kadler, D.F. Holmes, J.A. Trotter, and J.A. Chapman, Collagen fibril formation. *Biochemical Journal* 316 (1996) 1-11.

- [128] J. Gross, The behavior of collagen units as a model in morphogenesis. *J. Biophys. Biochem. Cytol* 2 (1956) 261-274.
- [129] J. Gross, J.H. Highberger, and F.O. Schmitt, Collagen Structures Considered as States of Aggregation of a Kinetic Unit - the Tropocollagen Particle. *Proceedings of the National Academy of Sciences of the United States of America* 40 (1954) 679-688.
- [130] A. Rich, and F.H. Crick, The molecular structure of collagen. *J Mol Biol* 3 (1961) 483-506.
- [131] K. Beck, and B. Brodsky, Supercoiled Protein Motifs: The Collagen Triple-Helix and the Alpha-Helical Coiled Coil. *Journal of Structural Biology* 122 (1998) 17-29.
- [132] R.D.B. Fraser, T.P. Macrae, and E. Suzuki, Chain Conformation in the Collagen Molecule. *Journal of Molecular Biology* 129 (1979) 463-481.
- [133] J. Bella, M. Eaton, B. Brodsky, and H.M. Berman, Crystal and molecular structure of a collagen-like peptide at 1.9 Å resolution. *Science* 266 (1994) 75-81.
- [134] J. Bella, B. Brodsky, and H.M. Berman, Hydration structure of a collagen peptide. *Structure* 3 (1995) 893-906.
- [135] B. Brodsky, and J.A. Ramshaw, The collagen triple-helix structure. *Matrix Biol* 15 (1997) 545-54.
- [136] D.J.S. Hulmes, Building Collagen Molecules, Fibrils, and Suprafibrillar Structures. *Journal of Structural Biology* 137 (2002) 2-10.
- [137] J.P.R.O. Orgel, T.C. Irving, A. Miller, and T.J. Wess, Microfibrillar structure of type I collagen in situ. *Proceedings of the National Academy of Sciences of the United States of America* 103 (2006) 9001-9005.
- [138] H.A. Lucero, and H.M. Kagan, Lysyl oxidase: an oxidative enzyme and effector of cell function. *Cell Mol Life Sci* 63 (2006) 2304-16.
- [139] R.C. Siegel, J.C. Fu, N. Uto, K. Horiuchi, and D. Fujimoto, Collagen cross-linking: lysyl oxidase dependent synthesis of pyridinoline in vitro: confirmation that pyridinoline is derived from collagen. *Biochem Biophys Res Commun* 108 (1982) 1546-50.
- [140] J. Molnar, K.S. Fong, Q.P. He, K. Hayashi, Y. Kim, S.F. Fong, B. Fogelgren, K.M. Szauter, M. Mink, and K. Csiszar, Structural and functional diversity of lysyl oxidase and the LOX-like proteins. *Biochim Biophys Acta* 1647 (2003) 220-4.
- [141] D.F. Holmes, C.J. Gilpin, C. Baldock, U. Ziese, A.J. Koster, and K.E. Kadler, Corneal collagen fibril structure in three dimensions: Structural insights into fibril assembly, mechanical properties, and tissue organization. *Proceedings of the National Academy of Sciences of the United States of America* 98 (2001) 7307-7312.
- [142] B.G. Frushour, and J.L. Koenig, Raman scattering of collagen, gelatin, and elastin. *Biopolymers* 14 (1975) 379-91.
- [143] M. Gniadecka, O.F. Nielsen, D.H. Christensen, and H.C. Wulf, Structure of Water, Proteins, and Lipids in Intact Human Skin, Hair, and Nail. *Journal of Investigative Dermatology* 110 (1998) 393-398.
- [144] M. Janko, P. Davydovskaya, M. Bauer, A. Zink, and R.W. Stark, Anisotropic Raman scattering in collagen bundles. *Opt Lett* 35 (2010) 2765-7.
- [145] H.G. Edwards, D.W. Farwell, J.M. Holder, and E.E. Lawson, Fourier-transform Raman spectra of ivory. III: Identification of mammalian specimens. *Spectrochim Acta A Mol Biomol Spectrosc* 53A (1997) 2403-9.
- [146] S. Leikin, V.A. Parsegian, W.-H. Yang, and G.E. Walrafen, Raman spectral evidence for hydration forces between collagen triple-helices. *Proceedings of the National Academy of Sciences of the United States of America* 94 (1997) 11312-11317.
- [147] M. Stücker, F.-G. Bechara, M. Bacharach-Buhles, P. Pieper, and P. Altmayer, What happens to skin after 2000 years in a bog? *Hautarzt* 52 (2001) 316-321.
- [148] D.H. Shin, M. Youn, and B.S. Chang, Histological analysis on the medieval mummy in Korea. *Forensic Science International* 137 (2003) 172-182.

- [149] B.S. Chang, C.S. Uhm, C.H. Park, H.K. Kim, G.Y. Lee, H.H. Cho, M.J. Kim, Y.H. Chung, K.W. Song, D.S. Lim, and D.H. Shin, Preserved skin structure of a recently found fifteenth-century mummy in Daejeon, Korea. *Journal of Anatomy* 209 (2006) 671-680.
- [150] H. Hino, T. Ammitzboll, R. Moller, and G. Asboehansen, Ultrastructure of Skin and Hair of an Egyptian Mummy - Transmission and Scanning Electron-Microscopic Observations. *Journal of Cutaneous Pathology* 9 (1982) 25-32.
- [151] G.S. Montes, R.M. Krisztan, and L.C.U. Junqueira, Preservation of Elastic System Fibers and of Collagen Molecular Arrangement and Stainability in an Egyptian Mummy. *Histochemistry* 83 (1985) 117-119.
- [152] M. Janko, A. Zink, A.M. Gigler, W.M. Heckl, and R.W. Stark, Nanostructure and mechanics of mummified type I collagen from the 5300-year-old Tyrolean Iceman. *Proceedings of the Royal Society B: Biological Sciences* 277 (2010) 2301-2309.
- [153] M.J. Buehler, Nanomechanics of collagen fibrils under varying cross-link densities: Atomistic and continuum studies. *Journal of the Mechanical Behavior of Biomedical Materials* 1 (2008) 59-67.
- [154] K. Kato, G. Bar, and H.J. Cantow, The interplay between surface micro-topography and -mechanics of type I collagen fibrils in air and aqueous media: An atomic force microscopy study. *European Physical Journal E* 6 (2001) 7-14.
- [155] F. Rollo, S. Luciani, A. Canapa, and I. Marota, Analysis of bacterial DNA in skin and muscle of the Tyrolean iceman offers new insight into the mummification process. *Am. J. Phys. Anthropol* 111 (2000) 211-9.
- [156] M.F. Paige, A.C. Lin, and M.C. Goh, Real-time enzymatic biodegradation of collagen fibrils monitored by atomic force microscopy. *International Biodeterioration & Biodegradation* 50 (2002) 1-10.
- [157] L.E. Bertassoni, and G.W. Marshall, Papain-gel degrades intact nonmineralized type I collagen fibrils. *Scanning* 31 (2009) 253-8.
- [158] P.B. Canham, The minimum energy of bending as a possible explanation of the biconcave shape of the human red blood cell. *J Theor Biol* 26 (1970) 61-81.
- [159] M.M. Guest, T.P. Bond, R.G. Cooper, and J.R. Derrick, Red Blood Cells: Change in Shape in Capillaries. *Science* 142 (1963) 1319-21.
- [160] M.I. Gregersen, C.A. Bryant, W.E. Hammerle, S. Usami, and S. Chien, Flow Characteristics of Human Erythrocytes through Polycarbonate Sieves. *Science* 157 (1967) 825-7.
- [161] R. Skalak, and P.I. Branemark, Deformation of red blood cells in capillaries. *Science* 164 (1969) 717-9.
- [162] K.A. Tanaka, N.S. Key, and J.H. Levy, Blood coagulation: hemostasis and thrombin regulation. *Anesth Analg* 108 (2009) 1433-46.
- [163] D.M. Monroe, and M. Hoffman, What does it take to make the perfect clot? *Arterioscler Thromb Vasc Biol* 26 (2006) 41-8.
- [164] M. Hoffman, Remodeling the blood coagulation cascade. *J Thromb Thrombolysis* 16 (2003) 17-20.
- [165] B. Furie, and B.C. Furie, Thrombus formation in vivo. *J Clin Invest* 115 (2005) 3355-62.
- [166] S. Butenas, K.G. Mann, and B. Butenas, Blood Coagulation. *Biochemistry (Moscow)* 67 (2002) 3-12.
- [167] M.E. Nesheim, and K.G. Mann, Thrombin-catalyzed activation of single chain bovine factor V. *J Biol Chem* 254 (1979) 1326-34.
- [168] T. Takagi, and R.F. Doolittle, Amino acid sequence studies on factor XIII and the peptide released during its activation by thrombin. *Biochemistry* 13 (1974) 750-756.
- [169] W.A. Murphy, Jr., D. Nedden Dz, P. Gostner, R. Knapp, W. Recheis, and H. Seidler, The iceman: discovery and imaging. *Radiology* 226 (2003) 614-29.

- [170] M. O'Reilly, L. McDonnell, and J. O'Mullane, Quantification of red blood cells using atomic force microscopy. *Ultramicroscopy* 86 (2001) 107-112.
- [171] B.L. Salmaso, G.J. Puppels, P.J. Caspers, R. Floris, R. Wever, and J. Greve, Resonance Raman microspectroscopic characterization of eosinophil peroxidase in human eosinophilic granulocytes. *Biophys J* 67 (1994) 436-46.
- [172] S. Hu, K.M. Smith, and T.G. Spiro, Assignment of Protoheme Resonance Raman Spectrum by Heme Labeling in Myoglobin. *Journal of the American Chemical Society* 118 (1996) 12638-12646.
- [173] M. Asghari-Khiavi, A. Mechler, K.R. Bamberg, D. McNaughton, and B.R. Wood, A resonance Raman spectroscopic investigation into the effects of fixation and dehydration on heme environment of hemoglobin. *Journal of Raman Spectroscopy* 40 (2009) 1668-1674.
- [174] K. Virkler, and I.K. Lednev, Raman spectroscopic signature of blood and its potential application to forensic body fluid identification. *Anal Bioanal Chem* 396 (2010) 525-34.
- [175] A.S. Wolberg, Thrombin generation and fibrin clot structure. *Blood Rev* 21 (2007) 131-42.
- [176] F.K. Glenister, R.L. Coppel, A.F. Cowman, N. Mohandas, and B.M. Cooke, Contribution of parasite proteins to altered mechanical properties of malaria-infected red blood cells. *Blood* 99 (2002) 1060-3.
- [177] L.H. Miller, D.I. Baruch, K. Marsh, and O.K. Doumbo, The pathogenic basis of malaria. *Nature* 415 (2002) 673-9.
- [178] S. Suresh, Mechanical response of human red blood cells in health and disease: Some structure-property-function relationships. *Journal of Materials Research* 21 (2006) 1871-1877.
- [179] R. Messmann, S. Gannon, S. Sarnaik, and R.M. Johnson, Mechanical properties of sickle cell membranes. *Blood* 75 (1990) 1711-7.
- [180] M.M. Brandao, A. Fontes, M.L. Barjas-Castro, L.C. Barbosa, F.F. Costa, C.L. Cesar, and S.T. Saad, Optical tweezers for measuring red blood cell elasticity: application to the study of drug response in sickle cell disease. *Eur J Haematol* 70 (2003) 207-11.
- [181] R.A.F. Clark, Fibrin and Wound Healing. *Annals of the New York Academy of Sciences* 936 (2001) 355-367.

## 6. LIST OF ABBREVIATIONS

|        |  |
|--------|--|
| ADP    | Adenosine Diphosphate                    |
| AFM    | Atomic Force Microscope                  |
| AGC    | automatic gain control                   |
| AM     | Amplitude Modulation                     |
| CCD    | Charge-Coupled Device                    |
| CT     | Computerized X-ray Tomography            |
| dc     | direct current                           |
| DMT    | Derjaguin-Muller-Toporov model           |
| DNA    | Deoxyribonucleic Acid                    |
| FM     | Frequency Modulation                     |
| JKR    | Johnson-Kendall-Roberts model            |
| LOX    | Lysyl Oxidase                            |
| Nd:YAG | Neodymium doped Yttrium Aluminium Garnet |
| NMR    | Nuclear Magnetic Resonance               |
| PCR    | Polymerisation Chain Reaction            |
| PLL    | Phase Locked Loop                        |
| RBC    | Red Blood Cell                           |
| rms    | root mean square                         |
| SEM    | Scanning Electron Microscope             |
| TEM    | Transmission Electron Microscope         |
| TF     | Tissue Factor                            |
| UV     | ultraviolet                              |
| vWF    | von Willebrand Factor                    |



## 7. LIST OF FIGURES

- Figure (1): Lennard-Jones potential describing the distance dependence of the interaction forces between the tip and sample. The red curve accounts for the attractive van der Waals forces; the black curve indicates the Pauli repulsion. The addition of these two terms, corresponding to the Lennard-Jones potential, is shown in blue. .... 6
- Figure (2): Centrepieces of an AFM setup. A microfabricated tip, the integral part of the cantilever, is in close proximity to the sample surface. While scanning across the surface, the cantilever deflects depending on the sample topography. The deflection is detected by a laser-photodiode system (Drawing courtesy of S. Kloft). ..... 7
- Figure (3): Effect of frequency and amplitude shift in amplitude-modulated AFM imaging. “Reprint with permission from T. R. Albrecht, Journal of Applied Physics, 69, 2, (1991). Copyright 1991, American Institute of Physics” [78]..... 9
- Figure (4): Basic F-d curves obtained on an ideally elastic (a), ideally plastic (b), and an elasto-plastic (c) material..... 10
- Figure (5): Basic Force vs. distance curve for an ideally elastic sample with marked interaction regions. The approach and withdraw curves are coloured in blue and red, respectively. The line at  $F_0$  defines the zero-force, the non-contact and the contact region. .... 11
- Figure (6): Hertz (a), DMT (b), JKR (c), and Maugis-Dugdale (d) model of an elastic sphere with radius  $R$  indenting a rigid flat sample. The contact radius,  $a$ , between the sphere and the sample surface depends on the loading force,  $F$ . The Hertz theory neglects surface forces and adhesion between the two bodies. In the DMT model, adhesion is only considered outside the contact area. The JKR theory considers adhesion inside the contact region. The Maugis-Dugdale model covers the interaction of surface forces around and within the contact region of the bodies. .... 12
- Figure (7): Deformation of a sample surface due to an indenting tip with radius  $R$ . The surface is indented by the distance  $ds$ . ..... 13
- Figure (8): Possible interaction processes between light and matter. Amongst others, the incident photons may experience reflection, diffraction, absorption or scattering. .... 17
- Figure (9): Jablonski diagrams showing possible transitions between electronic states in association with a schematic Raman spectrum. The Jablonski diagrams describe the excitation of a molecule from the vibrational ground state,  $SG$ , to a virtual state below a real excited electronic state,  $S1$ . In elastic scattering (Rayleigh scattering), the molecule is excited by an incident photon from the ground state into a virtual state and subsequently relaxes to the ground state. The released energy is emitted as a photon with the same energy, and thus frequency ( $f_0$ ), as the incident photon. Inelastically scattered photons are slightly detuned compared to the incident photons. Their frequency is either shifted to lower (Stokes shift) or to higher (anti-Stokes shift) frequencies..... 20

|              |   |    |
|--------------|---|----|
| Figure (10): | Schematic setup of the confocal Raman microscope. The excitation wavelength is coloured in green, the backscattered light is indicated in orange. ....  | 22 |
| Figure (11): | Possible interchain and intrachain hydrogen networks in the triple helix of a collagen molecule. “Reprint from <i>Matrix Biology</i> , 15, 8, B. Brodsky and J. A. M. Ramshaw, The collagen triple-helix structure, 545-554, Copyright (1997), with permission from Elsevier” [135]. ....   | 25 |
| Figure (12): | The deamination and oxidation of lysine by the enzymatic activity of lysyl oxidase. “Copyright Birkhäuser Verlag, Basel, <i>Cellular and Molecular Life Science</i> , 63, 19-20, (2006), 2304-2316, Lysyl oxidase: an oxidative enzyme and effector of cell function, H. A. Lucero and H. M. Kagan, figure 1. With kind permission from Springer Science+Business Media” [138]. ....                                      | 25 |
| Figure (13): | AFM images of (a), (b) human skin collagen (2×2 μm) and (c) bovine Achilles tendon collagen (2×2 μm). The fibrils in the skin are either arranged in parallel (a) or meshwork (b) structures. Collagen fibrils in tendons are more densely packed and aligned in highly ordered parallel structures. The characteristic D-period banding pattern is prevalent in all fibrils. ....  | 26 |
| Figure (14): | Normalised Raman spectra of collagen bundles in human skin (a) and in bovine Achilles tendon (b). Depending on the orientation of the collagen fibril to the incident laser beam, the intensity of specific bands changes. The grey squares mark the bands with the strongest anisotropic Raman scattering [144]. ....  | 27 |
| Figure (15): | Polar diagrams of the intensity of selected Raman bands as a function of the collagen fibril orientation [144]. ....  | 28 |
| Figure (16): | AFM images of collagen structures found in mummified human skin. In (a) single collagen fibrils in a meshwork are shown (1×1 μm). Images (b) and (c) show collagen fibrils arranged in parallel well-ordered sheet-like structures. All fibrils show the characteristic D-period banding pattern of 67 nm [152]. ....   | 29 |
| Figure (17): | Average Raman spectrum (600–3600 cm <sup>-1</sup> ) of recent human skin collagen (dashed black line) and of Iceman skin collagen (solid orange line). The spectrum of the mummy collagen is similar to the recent collagen spectrum. The inset shows a close-up from 840 to 1900 cm <sup>-1</sup> wavenumbers. The spectra were normalised to the 1448 cm <sup>-1</sup> peak. ....                                       | 30 |
| Figure (18): | Optical (a) and AFM amplitude images (b), (c), and (d) of collagen structures found in the mummified skin of a bog body. The optical image of the histological section was taken with 100x magnification. Figures (b) to (d) show the AFM amplitude images of the areas outlined. In (d), unsorted and overlapping fibrils in a network-like structure are shown. Each fibril features a periodic substructure. ....      | 31 |
| Figure (19): | High-resolution AFM topography (a) and amplitude image (b) of collagen structures found in the histological skin sample of the Zweeloo Woman. In figure (a), (2×2 μm) collagen fibrils with a characteristic banding pattern are revealed. The fibrils form a network-like structure and sometimes overlap. The contours of the fibrils are faint. The amplitude image (b) shows the fibril contours in more detail. .... | 32 |

- Figure (20): AFM images of RBCs. Images (a) and (b) show single RBCs from recent human tissue. Image (c) displays an assembly of RBCs. In images (d) and (e), single corpuscle, found in the Iceman right hand wound and arrowhead wound, are shown. Also an assembly of several randomly distributed corpuscles, similar to those in the recent sample (c), was found in the Iceman arrowhead wound (f). The imaged corpuscle (d-f) have the characteristic discoidic and concave surface of RBCs..... 35
- Figure (21): Raman spectra of air-dried whole blood (a), a single red blood cell (b), and a single corpuscle found in the Iceman tissue (c and d). All spectra show peaks at 1586 $\text{cm}^{-1}$ , 1395  $\text{cm}^{-1}$ , 1308  $\text{cm}^{-1}$ , and 747  $\text{cm}^{-1}$ , which are characteristic of porphyrin. With the exception of a few bands, the spectra show considerable similarities. Also shown are Raman spectra of a fibrin meshwork (e), and the agglomerated corpuscles found in the Iceman arrowhead wound (f). The spectrum obtained from the agglomerated corpuscles differs from that of the single Iceman corpuscle. It has features that are considerably similar to the spectrum of fibrin..... 36
- Figure (22): (a) Raman scan (35x35  $\mu\text{m}$ ) and AFM image (30x30  $\mu\text{m}$ ) of the RBC agglomerate. Recalculation of the Raman scan for selected Raman bands (b) gives the intensity distribution of the selected bands. (c-e) Raman map for fibrin-characteristic bands at approximately 1000  $\text{cm}^{-1}$ , 1450  $\text{cm}^{-1}$ , and 1660  $\text{cm}^{-1}$ . Red pixels define an area with high band intensity; blue and violet pixels represent a sample area with the lowest Raman band intensity. The highest band intensities are found at the sites of RBCs, indicating the presence of fibrin residues. .... 37
- Figure (23): The distribution of the Young's moduli from the corpuscle of Iceman sample B and contemporary single RBCs. The Young's modulus of the mummy particles (grey) is significantly lower than that of the recent RBCs (black). .... 38

## 8. PUBLICATIONS

### **Publication 8.1:**

#### **Anisotropic Raman scattering in collagen bundles**

Marek Janko, Polina Davydovskaya, Michael Bauer, Albert Zink and Robert W. Stark  
Optics Letters (2010), 35 (16), 2765-2767

### **Publication 8.2:**

#### **Nanostructure and mechanics of mummified type I collagen from the 5300-year-old Tyrolean Iceman**

Marek Janko, Albert Zink, Alexander M. Gigler, Wolfgang M. Heckl and Robert W. Stark  
Proceedings of the Royal Society B (2010), 277, 2301-2309

### **Publication 8.3:**

#### **Preservation of 5300 year old red blood cells in the Iceman**

Marek Janko, Robert W. Stark and Albert Zink  
Journal of the Royal Society Interfaces (2012), published online before print May 2, 2012

### **Further scientific publications resulting from the dissertation**

### **Publication 8.4:**

#### **Blood platelet adhesion to printed von Willebrand factor**

Polina Davydovskaya, Marek Janko, Florian Gaertner, Zerkah Ahmed, Özlem Simsek, Steffen Maßberg and Robert W. Stark  
Journal of Biomedical Materials Research A (2012), 100A (2), 335-341

### **Publication 8.5:**

#### **Raman spectroscopy of laser induced oxidation of titanomagnetites**

Michael Bauer, Polina Davydovskaya, Marek Janko, Melanie Kaliwoda, Nikolai Petersen, Stuart Gilder and Robert W. Stark  
Journal of Raman Spectroscopy (2011), 42, 1413-1418

# 8.1 ANISOTROPIC RAMAN SCATTERING IN COLLAGEN BUNDLES

August 15, 2010 / Vol. 35, No. 16 / OPTICS LETTERS 2765

## Anisotropic Raman scattering in collagen bundles

Marek Janko,<sup>1,2,\*</sup> Polina Davydovskaya,<sup>1</sup> Michael Bauer,<sup>1,2</sup> Albert Zink,<sup>2,3</sup> and Robert W. Stark<sup>2,4,5</sup><sup>1</sup>Department of Earth and Environmental Sciences, Ludwig-Maximilians-Universität München, Theresienstraße 41, 80333 Munich, Germany<sup>2</sup>Center for NanoSciences, Ludwig-Maximilians-Universität München, Schellingstraße 4, 80799 Munich, Germany<sup>3</sup>European Academy-Institute for Mummies and the Iceman, Viale Druso 1, 39100 Bolzano, Italy<sup>4</sup>FB Material- und Geowissenschaften, Technische Universität Darmstadt, Petersenstraße 32, 64287 Darmstadt, Germany<sup>5</sup>Center of Smart Interfaces, Technische Universität Darmstadt, Petersenstraße 32, 64287 Darmstadt, Germany

\*Corresponding author: marek.janko@lrz.uni-muenchen.de

Received May 26, 2010; revised July 7, 2010; accepted July 15, 2010; posted July 21, 2010 (Doc. ID 129058); published August 12, 2010

Collagen is the main connective tissue protein of vertebrates and shows exceptional mechanical and optical properties. The alignment of collagen fibrils correlates to the function of a specific tissue and leads to optical anisotropy. The effect of the molecular alignment on Raman scattering, however, has barely been investigated. We found that the peak intensities of the C—C, C=O, and N—H vibrational modes, which are typical for the Raman bands of the protein backbone, change with the orientation of the collagen fibrils. These observations demonstrate that Raman spectra contain specific information regarding molecular and fiber alignment. © 2010 Optical Society of America  
 OCIS codes: 300.6450, 170.1470, 170.6510, 170.6935, 190.4710.

Collagen is the most abundant structural protein of vertebrates and features unique properties. It is known for its exceptional durability [1] and tensile strength, both of which result from the hierarchical structure [2–4] and fibril alignment. According to its specific function, it is organized in bundles or in a random meshwork, determining the tensile stress, elasticity, and geometry of skin, tendons, ligaments, and artery walls, or the organic matrix of bones. In tissue that is subject to unidirectional forces, such as tendons, single collagen fibrils are equally oriented and organized in bundles. The bundles are aligned with the direction of the load, thereby, leading to anisotropic mechanical properties.

Collagen also features remarkable optical properties. Optical anisotropy, such as birefringence or differences in light scattering and propagation [5,6], reflects the structure and alignment of the fibrils. Therefore, the collagen fibril orientation is an exceptional indicator of the properties of a biological tissue. For example, in the cornea, the regularly arranged collagen bundles are transparent [7,8]. In diseased tissue, however, the molecular alignment can be disturbed, impairing the eye's optical power [9,10].

Optical methods such as second-harmonic-generation microscopy [11–13] can help to characterize the orientation of the biopolymer. To this end, confocal Raman microscopy is also a promising high-resolution technique because the conformation and molecular order of (bio) polymers can be characterized spectroscopically [1,14–16]. Here, we show that there is a strong dependency between the intensity of certain Raman bands (e.g., the amide bands around 1271 and 1668 cm<sup>-1</sup>) and the orientation of aligned collagen fibrils with respect to the polarization of the incident laser light.

We investigated 2- $\mu\text{m}$ -thick transverse sections of bovine Achilles tendon (Sigma-Aldrich) and human skin. The sections were processed following standard protocols [1]. The samples were imaged with an atomic force microscope (AFM) to identify collagen-rich areas and to verify the orientation and the banding pattern of the fibrils (Veeco Dimension 3100, Cantilever; BS Tap 300

Budget Sensors,  $D \sim 40$  N/m,  $f_{\text{res}} \sim 300$  kHz). Type I collagen has a characteristic  $D$ -periodic banding pattern of 67 nm. The measured values of  $65.2 \pm 2.0$  nm in human skin or  $65.7 \pm 2.0$  nm for the bovine tendon match the literature value. Both samples show highly ordered collagen structures with well-defined, uniaxial, parallel-aligned collagen fibrils (Fig. 1). Raman spectra were taken with a confocal Raman microscope (WITec alpha 300 R, 532 nm, 600 l/mm grating). The laser power was set to 1.0 mW to avoid denaturation. The confocal setup resulted in a focal depth of approximately 1  $\mu\text{m}$  with a diffraction-limited spot diameter of about 400 nm. Although the laser had a polarization ratio of 100:1, all measurements can be regarded as unpolarized because no analyzer was used. Three single spectra were recorded, each with 180 s of integration time. The samples

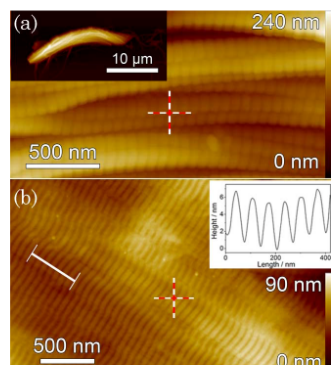


Fig. 1. (Color online) AFM images of (a) human skin collagen ( $2 \mu\text{m} \times 2 \mu\text{m}$ ) and (b) bovine Achilles tendon collagen ( $3 \mu\text{m} \times 3 \mu\text{m}$ ). Fibrils in a parallel alignment with their characteristic banding pattern prevail. The insets display (a) a bundle of skin collagen and (b) a profile of the banding pattern of Achilles tendon collagen. Raman spectra were taken at the position marked by the crosshair.

0146-9592/10/162765-03\$15.00/0

© 2010 Optical Society of America

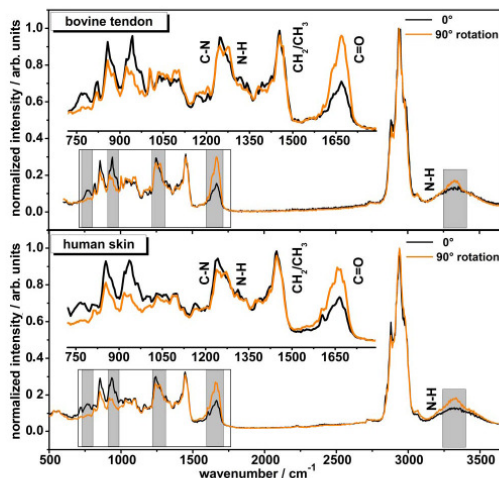


Fig. 2. (Color online) Normalized Raman spectra taken on collagen fibrils oriented parallel and perpendicular to the incident laser beam. The gray squares indicate the bands that show the strongest anisotropic Raman scattering. The inset outlines the fingerprint region of collagen.

were rotated in steps of 15°, and the measurements were repeated for each step.

The spectra shown in Fig. 2 were obtained on fibrils whose long fibril axes were aligned in parallel and perpendicular with respect to the polarization of the incident laser. The spectra were normalized to the most intense Raman band at around 2939 cm<sup>-1</sup>, which features a steady intensity and peak center position throughout the measurements and is far away from the fingerprint region of collagen (700 to 1800 cm<sup>-1</sup>; inset in Fig. 2). The spectra are consistent and feature the characteristic collagen bands [1]. The first peaks exhibiting an orientation-dependent intensity are found at about 766 and 780 cm<sup>-1</sup>  $\nu(\text{CCO})$  [15]. Their intensity nearly vanishes when rotating the sample by 90°. Such behavior could also be observed for the band at about 939 cm<sup>-1</sup> (C—C stretch) that is typical for the protein backbone [16,17]. The deformation band of the amide III  $\delta(\text{NH})$  [15–17] at 1271 cm<sup>-1</sup> also features anisotropic Raman scattering. However, the 1271 cm<sup>-1</sup> band shows behavior that is inverse to that at 766, 780, and 939 cm<sup>-1</sup>. It is less intense when the collagen fibrils are oriented in parallel and shows enhanced Raman scattering in the perpendicular configuration. The strongest polarization dependence appears in the range of 1580 to 1720 cm<sup>-1</sup>, specifically at 1668 cm<sup>-1</sup>, with the shoulder at about 1641 cm<sup>-1</sup> corresponding to the C=O stretching vibration of amide I  $\nu(\text{CO})$  [15–17]. Likewise, at about 3321 cm<sup>-1</sup>, a peak appears that is located near the broad background peak of water. Leikin *et al.* [18] reported that this band corresponds to the N—H vibration mode of amides in protein backbones.

The polar diagram in Fig. 3 outlines the peak intensities for a total rotation of 360°, illustrating the intensity as a function of the collagen orientation. The bands at about 766, 1246, 1271, 1451, 1668, and 3321 cm<sup>-1</sup> are displayed.

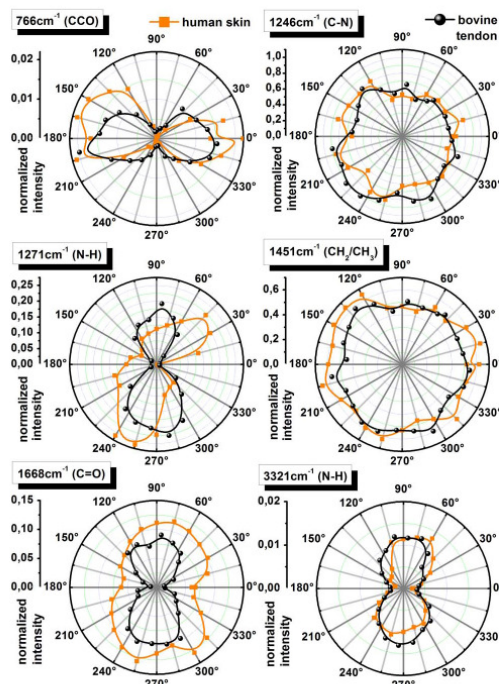


Fig. 3. (Color online) Polar diagrams of selected Raman bands displayed for a full sample rotation.

The intensities were determined by fitting a second-order polynomial to a narrow range (40 to 100 cm<sup>-1</sup>) around the peak centers. The respective fitting ranges were maintained for all sample orientations. From the asymmetric intensity distribution, the alignment of the collagen fibrils in the specimen can be derived. The shape of the intensity distribution indicates strong anisotropic Raman scattering. The amide I and amide III bands, which represent the peptide bonds within proteins and in the collagen, indicate the stabilization of the subfibrillar triple helical structure by the formation of interchain hydrogen bonds between the N—H groups of glycines and the C=O groups of prolines in neighboring chains [19,20]. The anisotropic Raman scattering at these amide groups indicates that they are oriented in the direction of the fibril backbone (long axis). The intensity distribution of the 766 cm<sup>-1</sup> band is turned by 90° compared to those of the amide bands. This observation implies that the preferential polarizability of the molecular subunit CCO that is responsible for the 766 cm<sup>-1</sup> peak could be perpendicular compared to those of the bands at 1271, 1668, and 3321 cm<sup>-1</sup>. The polarizability typically varies if the electrical field is applied parallel or perpendicular to the molecular axis or in different directions relative to the molecule. This causes a variation in the induced dipole moment ( $P = \epsilon_0 \chi E = \epsilon_0 \chi E_0 e^{i(k \cdot r - \omega t)}$ ). Hence, the Raman scattering in the collagen fibers depends on the fiber alignment and the orientation of the polarized laser. The anisotropy is expressed by the

nonzero elements  $((\partial\chi/\partial\omega_j)_0 = \chi^{(1)} \neq 0)$  of the Taylor expanded susceptibility tensor  $(\chi = \chi^{(0)} + \sum_j \chi^{(1)} Q_j + \dots)$

for Raman scattering. Therefore, a rotation of aligned collagen fibrils with respect to the incident laser causes intensity variations in several Raman bands. Thus, the orientation of the intensity distribution pattern in the polar diagrams characterizes the uniaxial orientation of the collagen bundles. The shape of these isointensities can act as an indicator for the fibril structure of bundles. For comparison, two bands (1246 and 1451  $\text{cm}^{-1}$ ) that are not affected by the rotation are also shown in Fig. 3. The 1246  $\text{cm}^{-1}$  peak is related to the amide III band and is assigned to the  $\delta(\text{NH})$  vibration of the N—H groups. Compared to the amide III band at 1271  $\text{cm}^{-1}$ , however, the Raman active N—H groups at 1246  $\text{cm}^{-1}$  are in a disordered phase [15]. The other isotropic Raman band at 1451  $\text{cm}^{-1}$  is assigned to methyl  $\delta(\text{CH}_3)$  and methylene  $\delta(\text{CH}_2)$  deformation vibrations [16,17]. Similar to the N—H groups at 1246  $\text{cm}^{-1}$ , the  $\text{CH}_3$  and  $\text{CH}_2$  groups do not show a preferential orientation. Both bands correspond to the Raman scattering of molecules that are equally distributed across the collagen amino acid sequence and, thus, homogeneous Raman scattering occurred.

In summary, the conformation and orientation of hierarchical molecules can be characterized by Raman spectroscopy. Intensity variations of several Raman bands were observed while rotating aligned collagen fibrils with respect to the polarization of the incident laser beam. This result implies that the orientation of Raman active subunits of an ordered macromolecular protein in a tissue can be determined by Raman scattering. The orientation-dependent scattering not only enables the optical characterization of the alignment of collagen fibrils, but also has to be considered in the analysis of the spectra.

We gratefully acknowledge the Deutsche Forschungsgemeinschaft (DFG) clusters of excellence Nanosystems

Initiative Munich and Center of Smart Interfaces Darmstadt for financial support.

#### References

1. M. Janko, A. Zink, A. M. Gigler, W. M. Heckl, and R. W. Stark, *Proc. R. Soc. London B* **277**, 2301 (2010).
2. J. Gosline, M. Lillie, E. Carrington, P. Guerette, C. Ortlepp, and K. Savage, *Philos. Trans. R. Soc. London B* **357**, 121 (2002).
3. M. J. Buehler, *Proc. Natl. Acad. Sci. USA* **103**, 12285 (2006).
4. J. P. R. O. Orgel, T. C. Irving, A. Miller, and T. J. Wess, *Proc. Natl. Acad. Sci. USA* **103**, 9001 (2006).
5. A. Kienle, F. K. Forster, and R. Hibst, *Opt. Lett.* **29**, 2617 (2004).
6. S. Nickell, M. Hermann, M. Essenpreis, T. J. Farrell, U. Kramer, and M. S. Patterson, *Phys. Med. Biol.* **45**, 2873 (2000).
7. D. M. Maurice, *J. Physiol.* **136**, 263 (1957).
8. G. B. Benedek, *Appl. Opt.* **10**, 459 (1971).
9. A. Daxer and P. Fratzl, *Invest. Ophthalmol. Visual Sci.* **38**, 121 (1997).
10. K. M. Meek, S. J. Tuft, Y. Huang, P. S. Gill, S. Hayes, R. H. Newton, and A. J. Bron, *Invest. Ophthalmol. Visual Sci.* **46**, 1948 (2005).
11. K. M. Hanson and C. J. Bardeen, *Photochem. Photobiol.* **85**, 33 (2009).
12. T. Yasui, Y. Tohno, and T. Araki, *Appl. Opt.* **43**, 2861 (2004).
13. J. C. Mansfield, C. P. Winlove, J. Moger, and S. J. Matcher, *J. Biomed. Opt.* **13**, 044020 (2008).
14. H. Kuzmany, J. F. Rabolt, B. L. Farmer, and R. D. Miller, *J. Chem. Phys.* **85**, 7413 (1986).
15. H. G. M. Edwards, D. W. Farwell, J. M. Holder, and E. E. Lawson, *J. Mol. Struct.* **435**, 49 (1997).
16. B. G. Frushour and J. L. Koenig, *Biopolymers* **14**, 379 (1975).
17. M. Gniadecka, O. F. Nielsen, D. H. Christensen, and H. C. Wulf, *J. Invest. Dermatol.* **110**, 393 (1998).
18. S. Leikin, V. A. Parsegian, W.-H. Yang, and G. E. Walrafen, *Proc. Natl. Acad. Sci. USA* **94**, 11312 (1997).
19. R. D. B. Fraser, T. P. Macrae, and E. Suzuki, *J. Mol. Biol.* **129**, 463 (1979).
20. A. Rich and F. H. C. Crick, *Nature* **176**, 915 (1955).

## 8.2 NANOSTRUCTURE AND MECHANICS OF MUMMIFIED TYPE I COLLAGEN FROM THE 5300-YEAR-OLD TYROLEAN ICEMAN





## Nanostructure and mechanics of mummified type I collagen from the 5300-year-old Tyrolean Iceman

Marek Janko, Albert Zink, Alexander M. Gigler, Wolfgang M. Heckl and Robert W. Stark

*Proc. R. Soc. B* 2010 **277**, 2301-2309 first published online 31 March 2010  
doi: 10.1098/rspb.2010.0377

### Supplementary data

"Data Supplement"

<http://rspb.royalsocietypublishing.org/content/suppl/2010/03/24/rspb.2010.0377.DC1.html>

### References

This article cites 55 articles, 13 of which can be accessed free

<http://rspb.royalsocietypublishing.org/content/277/1692/2301.full.html#ref-list-1>

### EXiS Open Choice

This article is free to access

### Subject collections

Articles on similar topics can be found in the following collections

[biophysics](#) (324 articles)

### Email alerting service

Receive free email alerts when new articles cite this article - sign up in the box at the top right-hand corner of the article or click [here](#)

---

To subscribe to *Proc. R. Soc. B* go to: <http://rspb.royalsocietypublishing.org/subscriptions>

---

## Nanostructure and mechanics of mummified type I collagen from the 5300-year-old Tyrolean Iceman

Marek Janko<sup>1,2</sup>, Albert Zink<sup>2,3</sup>, Alexander M. Gigler<sup>1,2</sup>,  
Wolfgang M. Heckl<sup>1,2,4</sup> and Robert W. Stark<sup>1,2,\*</sup>

<sup>1</sup>Department of Earth and Environmental Sciences, Ludwig-Maximilians-Universität München, Theresienstraße 41, 80333 Munich, Germany

<sup>2</sup>Center for NanoSciences, Ludwig-Maximilians-Universität München, Schellingstraße 4, 80799 Munich, Germany

<sup>3</sup>European Academy of Bolzano, Institute for Mummies and the Iceman, Viale Druso 1, 39100 Bolzano, Italy

<sup>4</sup>Deutsches Museum, Museumsinsel 1, 80538 Munich, Germany

Skin protects the body from pathogens and degradation. Mummified skin in particular is extremely resistant to decomposition. External influences or the action of micro-organisms, however, can degrade the connective tissue and lay the subjacent tissue open. To determine the degree of tissue preservation in mummified human skin and, in particular, the reason for its durability, we investigated the structural integrity of its main protein, type I collagen. We extracted samples from the Neolithic glacier mummy known as ‘the Iceman’. Atomic force microscopy (AFM) revealed collagen fibrils that had characteristic banding patterns of  $69 \pm 5$  nm periodicity. Both the microstructure and the ultrastructure of dermal collagen bundles and fibrils were largely unaltered and extremely well preserved by the natural conservation process. Raman spectra of the ancient collagen indicated that there were no significant modifications in the molecular structure. However, AFM nanoindentation measurements showed slight changes in the mechanical behaviour of the fibrils. Young’s modulus of single mummified fibrils was  $4.1 \pm 1.1$  GPa, whereas the elasticity of recent collagen averages  $3.2 \pm 1.0$  GPa. The excellent preservation of the collagen indicates that dehydration owing to freeze-drying of the collagen is the main process in mummification and that the influence of the degradation processes can be addressed, even after 5300 years.

**Keywords:** ancient collagen; degradation; atomic force microscopy; nanoindentation; Raman spectroscopy; Iceman

### 1. INTRODUCTION

Skin is the anatomical outer shielding of the body. Even when mummified, it guards the underlying tissue from external influences and degradation. Its function, however, persists only so long as the skin is intact. Temperature variations, ultraviolet (UV) irradiation and the actions of insects, bacteria and fungi can all cause abrasion and degradation of the skin, enabling biological agents to cross this barrier and causing further tissue decay. The main biomolecular scaffold of skin is type I collagen. It is the most abundant collagen of the human body, and it is also present in scar tissue, interstitial tissue, tendons, arterial walls, fibrocartilage and as an organic constituent of bone (Van der Rest & Garrone 1991). Apart from its high tensile strength and elasticity, type I collagen is known for its exceptional durability. Remnants have even been found in prehistoric samples, such as in the fossilized bones of *Tyrannosaurus rex* (Schweitzer *et al.* 2007a) or the fossilized skin of *Psittacosaurus* (Lingham-Soliar 2008). In these specimens, the preservation of collagen is facilitated by its

sequestration within the bone or by the mineralization of the soft organic tissue (Schweitzer *et al.* 2007b).

Excellent preservation of collagen has been reported for mummified human tissue. Optical and scanning electron microscopy (transmission electron microscopy (TEM)/scanning electron microscopy (SEM)) investigations have revealed single fibrils and bundles of type I collagen in naturally mummified bodies (Williams *et al.* 1995; Hess *et al.* 1998; Stücker *et al.* 2001; Shin *et al.* 2003; Chang *et al.* 2006) and in artificially embalmed mummies (Hino *et al.* 1982; Montes *et al.* 1985). However, the reason for the durability of mummified collagen is unclear. In this paper, we have investigated the structural integrity of mummified collagen in the oldest known glacier mummy, i.e. the ca 5300-year-old Tyrolean Iceman. This will help to determine the cause for the stability of mummified collagen and yield a clearer understanding of the mummification process.

The Iceman is a remarkably well-preserved wet mummy and was mummified naturally by a form of freeze-drying. The body was found at 3200 m above sea level, partly embedded in glacier ice. SEM studies of the mummy tissue showed that the collagen fibrils in the skin were structurally preserved (Williams *et al.* 1995; Hess *et al.* 1998). Nonetheless, neither the degree of tissue preservation nor

\* Author for correspondence ([stark@lmu.de](mailto:stark@lmu.de)).

Electronic supplementary material is available at <http://dx.doi.org/10.1098/rspb.2010.0377> or via <http://rspb.royalsocietypublishing.org>.

Received 23 February 2010  
Accepted 4 March 2010



Figure 1. (a) The Neolithic glacier mummy, the Iceman. (b) Detail of a stab trauma on the right hand of the mummy (sample A). Samples B and C were taken from a haematoma close to the vertebral column and from a wound under the left shoulder blade (*spina scapulae*), at the Iceman's back (c). Photos courtesy of M. Samadelli, South Tyrol Museum of Archaeology, Bolzano, Italy.

the reason for the preservation of the ultrastructure and molecular structure of the mummified connective tissue is known. The molecular process that led to the outstanding preservation of the Iceman remains unclear.

In this study, we performed atomic force microscope (AFM) measurements and observed typical collagen fibril assemblies in the skin of the Iceman. Complementary confocal Raman spectroscopy measurements support the observation that collagen is preserved by the freeze-drying mummification process. Because nanoindentation measurements by AFM provide access to the nanomechanical properties of collagen at the molecular level (Fratzl *et al.* 1998; Strasser *et al.* 2007; Yang *et al.* 2008), we conducted such experiments on mummified and recent collagen. The resulting data show that Young's modulus of ancient type I collagen is slightly different from that of a recent sample.

## 2. MATERIAL AND METHODS

### (a) Collagen preparation

Three  $5 \times 5$  mm skin samples were taken from the mummy by punch biopsies. For this purpose, the mummified body

(which is stored in a cooling chamber at  $-6^{\circ}\text{C}$  and a relative humidity of 98%) was thawed slightly. One specimen was derived from a stab trauma on the right hand (sample A; Nerlich *et al.* 2003). A second sample was taken from the back of the mummy close to the vertebral column (sample B) and the third sample was drawn from a wound under the left *spina scapulae*, at the back of the Iceman (sample C; figure 1). This skin wound is assumed to be the intravital point of an arrowhead entry (Gostner & Vigl 2002; Pernter *et al.* 2007). After extraction, the samples were slowly rehydrated and then fixed and embedded in paraffin wax (Nerlich *et al.* 2003). To obtain histological specimens, 2–4  $\mu\text{m}$ -thick transverse sections were cut and transferred onto glass slides. Before AFM analysis, the paraffin was dissolved in xylene. Subsequently, the sections were rehydrated with a descending alcohol series, rinsed with ultrapure water and dried under ambient conditions. As a reference, we used a comparable recent human skin sample that was taken from a volunteer. To prepare the histological section, the recent skin sample was subjected to the same processes as the mummified tissue, except that the rehydration step before fixation was omitted. After processing, all samples were stored at room temperature in coverslip boxes.

**(b) AFM measurements**

The tissue contents and arrangements were inspected using an inverted optical microscope (Axiovert 135, Zeiss, Oberkochen, Germany), and the appropriate sample areas for AFM imaging were defined. The AFM measurements were performed using a NanoWizard-II (JPK Instruments, Berlin, Germany). The AFM was operated under ambient conditions in the intermittent contact mode. Silicon cantilevers (BS Tap 300, Budget Sensors, Redding, USA) with typical spring constants of  $40 \text{ N m}^{-1}$  and nominal resonance frequencies of 300 kHz were used. The nominal tip radius was smaller than 10 nm. The images were analysed using SPIP (SPIP 4.5.2, Image Metrology, Hørsholm, Denmark). In addition, we examined the mechanical properties of single collagen fibrils using AFM nanoindentation measurements. The Young's moduli of the ancient and the recent collagen samples were determined by a fitting procedure. Both datasets were analysed with the independent two-sample Student's *t*-test. Differences were considered as statistically significant for  $p < 0.01$ . A detailed description of the measurements and the calculation of Young's modulus are given in appendix A.

**(c) Raman spectroscopy**

Confocal Raman spectroscopic measurements were performed using a WITec alpha 300 R microscope (WITec GmbH, Ulm, Germany). The excitation wavelength was 532 nm. The laser power was limited to 1.0 mW to avoid tissue damage. The spectrometer was operated with 600 and 1800  $\text{g mm}^{-1}$  gratings. We analysed the wavenumber range from 600 to 3600  $\text{cm}^{-1}$  or from 840 to 1900  $\text{cm}^{-1}$ . The spectral resolution was 3  $\text{cm}^{-1}$  per CCD-pixel for the survey spectra and 1  $\text{cm}^{-1}$  per CCD-pixel for the high-resolution spectra. For each sample, three different positions were analysed, and at least three single spectra were taken at each position to exclude external effects. The spectra were integrated for 240 s each.

**3. RESULTS****(a) AFM imaging—structural preservation of collagen**

We observed single collagen fibrils and fibrils stacked to sheet-like structures within all histological tissue samples. Networks of extremely well-preserved collagen were found, and single fibrils were unsorted and partly overlapping at some sites (figure 2). The fibrils were without any evidence of breaks or fragmentation. Higher magnification also revealed periodic banding patterns (figure 3). For sample A (figure 3*a,b*), the topographic analysis along the longitudinal axis of several fibrils indicates a mean banding pattern of 68.3 nm ( $\pm 5.9$  nm s.d.). Measuring the dimensions perpendicular to the longitudinal axis yielded a fibril width of  $89.5 \pm 5.7$  nm and a height of  $32.3 \pm 5.0$  nm. The AFM images of samples B and C showed similar collagen structures. We observed both single collagen fibrils arranged in a meshwork and stacked structures of collagen that formed sheet-like structures (figure 3*c,d*). For sample B, the average D-period derived from the banding patterns of more than 60 different fibrils was  $69.2 \pm 4.9$  nm. The fibrils from sample C showed a mean banding pattern of  $68.9 \pm 4.5$  nm. Additional AFM data has been represented as electronic supplementary material.

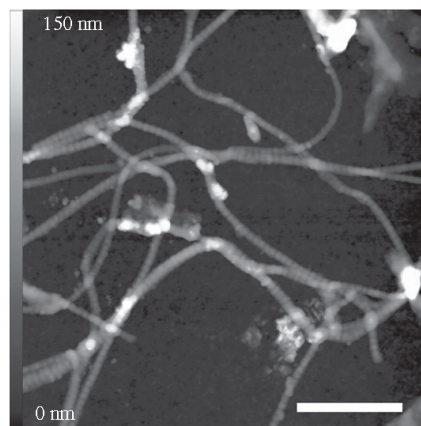


Figure 2. An AFM topography image with a scan size of  $4 \times 4 \mu\text{m}$ . A meshwork of randomly oriented single collagen fibrils within sample A can be seen in the figure. Scale bar,  $1 \mu\text{m}$ .

**(b) Raman spectroscopy—molecular preservation of collagen**

Raman spectroscopy is sensitive to both the chemical structure and the conformation of molecules. Spectra were acquired from all three Iceman samples by confocal Raman spectroscopy. The spectra are compared in the region from 1170 to 1870  $\text{cm}^{-1}$  in figure 4. The strong line at 1448  $\text{cm}^{-1}$  is the deformation vibration of methyl  $\delta(\text{CH}_3)$  and methylene  $\delta(\text{CH}_2)$  molecules that are present in proteins (Gniadecka *et al.* 1998; Jastrzebska *et al.* 2005). All of the spectra were normalized to this peak. At approximately 1240 and 1270  $\text{cm}^{-1}$ , deformation bands of amide III groups appear. They are related to the C–N stretching  $\nu(\text{CN})$  and N–H in-plane deformation  $\delta(\text{NH})$  modes (Frushour & Koenig 1975). From 1300 to 1400  $\text{cm}^{-1}$ , the prominent bands that occur arise from vibrational modes of methylene. In this region, the samples show peaks at 1315, 1339 and 1396  $\text{cm}^{-1}$ . These correspond to the twisting  $\gamma_t(\text{CH}_2)$ , wagging  $\gamma_w(\text{CH}_2)$  and deformation  $\delta(\text{CH}_2)$  modes of methylene, respectively (Frushour & Koenig 1975; Edwards *et al.* 1997). The Iceman samples feature a shoulder at 1421  $\text{cm}^{-1}$ , which is associated with a stretching mode of  $\text{COO}^-$  (Frushour & Koenig 1975). The shoulders at 1583 and 1604  $\text{cm}^{-1}$  can be assigned to the aromatic ring stretch modes  $\nu(\text{CCH})$  of the amino acids proline/hydroxyproline and tyrosine/phenylalanine, respectively (Frushour & Koenig 1975; Edwards *et al.* 1997). At approximately 1640  $\text{cm}^{-1}$  a shoulder is present, and at 1664  $\text{cm}^{-1}$  a strong band occurs. These correspond to the C=C stretching vibration  $\nu(\text{CC})$  and the C=O stretching vibration  $\nu(\text{CO})$  of amide I groups (Frushour & Koenig 1975). The spectra are consistent except in their intensities and noise levels.

Comparison of the ancient and the recent spectra of type I collagen samples reveals similar features. Representative Raman spectra ( $600\text{--}3600 \text{ cm}^{-1}$ ) for sample C and the recent collagen are shown in figure 5. The strongest band occurs in the range from 2800 to 3050  $\text{cm}^{-1}$ . This band is associated with the C–H vibrational modes  $\nu(\text{CH}_2)$  and  $\nu(\text{CH}_3)$  (Edwards *et al.* 1997). The spectra

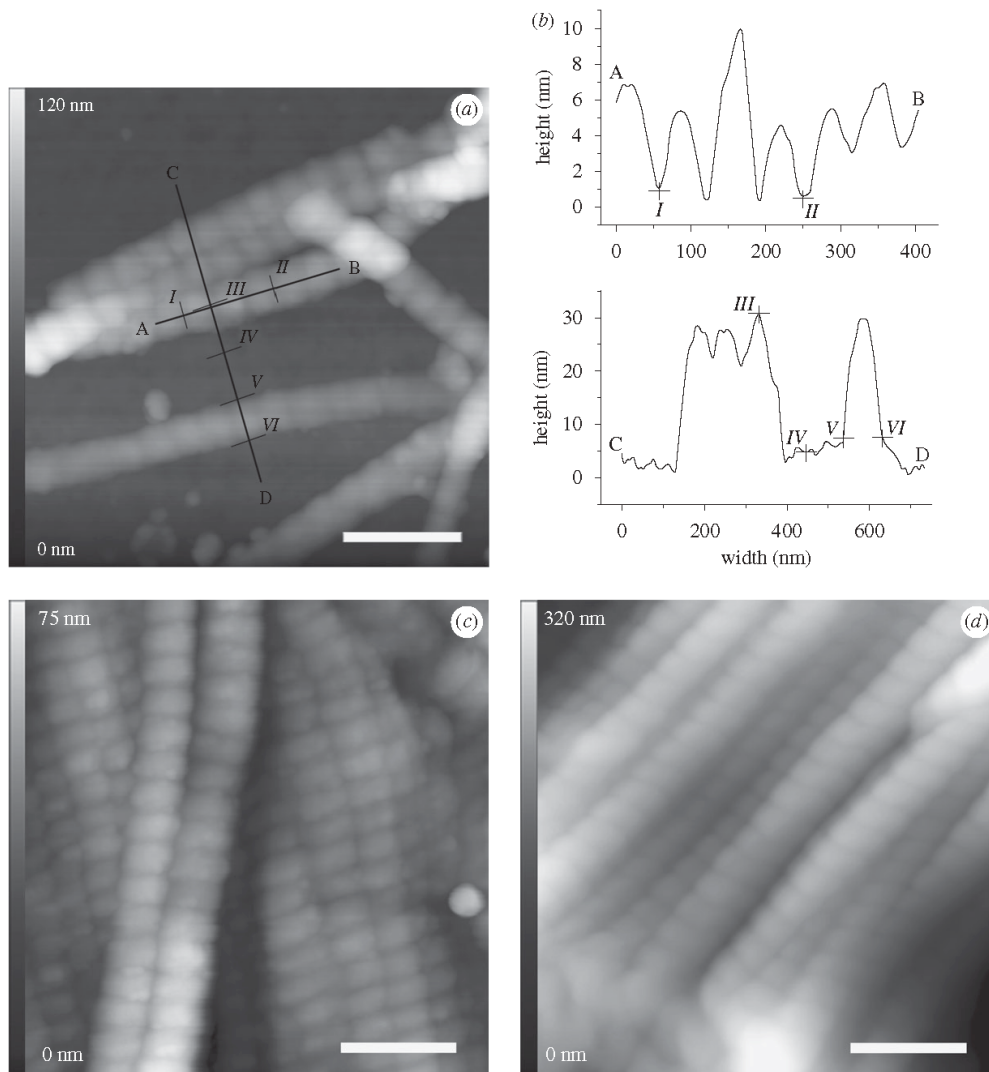


Figure 3. High-resolution images of individual collagen fibrils within Iceman sample A (*a*), showing fibrils stacked in sheet-like structures as observed for Iceman samples B and C (*c,d*). Each fibril shows the periodic banding pattern. For sample A, typical fibril profiles that were measured along line AB, perpendicular to the fibril axes (line CD), are shown in (*b*). The distance between sequential bands (e.g. from I to II) was approximately 68 nm. The height (III and IV) averaged to 32 nm and the fibril width (V and VI) was approximately 90 nm. Scale bars, (*a,c,d*) 250 nm.

were normalized to this band. From 3000 to 3800  $\text{cm}^{-1}$ , the characteristic O–H vibrations of water appear (Jastrzebska *et al.* 2005). The fingerprint region of collagen, showing the amide I and amide III peaks, is presented as the inset in figure 5. No spectral differences were observed.

#### (c) AFM nanoindentation—mechanical properties of mummified collagen

To assess the elasticity of the collagen fibrils, we conducted AFM nanoindentation experiments. The numerical value for Young's modulus was obtained as described in appendix A. Force curves that were obtained from the samples of mummified collagen featured a steeper loading-slope than that of the recent collagen.

Loading forces of 25 nN caused a 0.7 nm fibril indentation in the recent collagen. By contrast, the mummified collagen was indented by only 0.5 nm using the same forces. As shown in figure 6, Young's modulus of the mummified collagen from Iceman sample A (grey columns) exceeded Young's modulus of the reference sample (black columns). A Gaussian distribution was fitted to each histogram. The upper inset in figure 6 shows the scope of the analysed collagen fibrils, as distributed in the recent skin sample. Single fibrils are oriented randomly and sometimes overlap in multifibril structures. The lower inset displays similar entangled fibril assemblies that were analysed from the Iceman sample. For the ancient collagen that was extracted from the stab wound on the right hand of the mummy, we analysed a total number of 150 force–distance curves. The

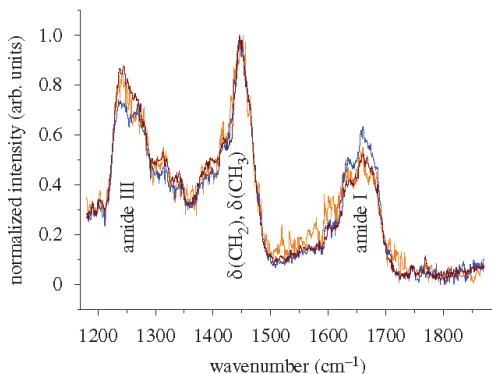


Figure 4. Raman spectra ( $1170\text{--}1870\text{ cm}^{-1}$ ) of type I collagen acquired on Iceman samples A–C. Each spectrum is averaged from at least three single spectra, taken with integration times of 240 s at three different sample positions. The spectra are normalized to the intensity of the  $1448\text{ cm}^{-1}$  band, which was assigned to methyl  $\delta(\text{CH}_3)$  and methylene  $\delta(\text{CH}_2)$  groups. Apart from minor differences in the intensities of the bands and the noise level, the spectra are similar. Orange line, Iceman sample A, blue line, Iceman sample B, brown line, Iceman sample C.

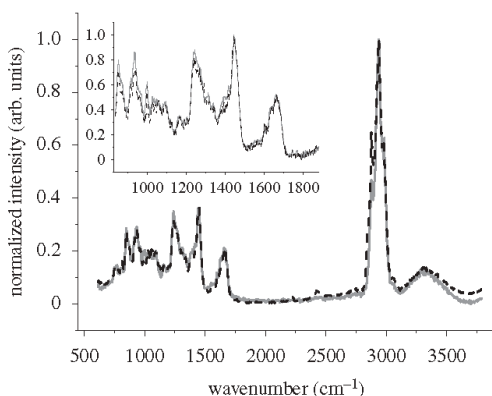


Figure 5. Average Raman spectrum ( $600\text{--}3600\text{ cm}^{-1}$ ) of recent human skin collagen (dashed line) and of Iceman sample C (solid line). The spectrum of the mummy collagen is similar to the recent collagen spectrum. The inset shows a close-up from  $840$  to  $1900\text{ cm}^{-1}$  wavenumbers, and the spectra have been normalized to the  $1448\text{ cm}^{-1}$  peak.

measurements yielded a mean value of  $4.1 \pm 1.1$  GPa, and the distribution maximum was 4 GPa. For the recent collagen sample, we evaluated 213 curves. The elasticity of the fibrils averaged  $3.2 \pm 1.0$  GPa. The distribution maximum was 3.5 GPa, and 55.4 per cent of the measured data were between 3.0 and 4.0 GPa. The difference between the mean Young's modulus of the ancient and the recent collagen was statistically significant. The scatter of the measured elasticity values can be attributed to anisotropies in the collagen fibril structure. Nanoindentation experiments by Wenger *et al.* (2007) showed that the anisotropic mechanical properties of the fibrils are owing to the tropocollagen subfibrils and their lateral displacement along the fibril axes.

*Proc. R. Soc. B* (2010)

#### 4. DISCUSSION

The structure of the tropocollagen triple helix is stabilized by the formation of one interchain hydrogen bond per sequence between the N–H groups of glycines and the C=O groups of prolines on the neighbouring chain (Rich & Crick 1955; Fraser *et al.* 1979). Staggered, parallel tropocollagen molecules covalently cross-link with each other through their aldehyde and amino groups, forming collagen fibrils (Buehler 2006). These self-assembled fibrils feature a characteristic 67 nm, D-periodic banding pattern (Williams *et al.* 1978; Orgel *et al.* 2006). Collagen self-organizes to form bundles or a meshwork that determines the tensile strength, the elasticity and the geometry of the tissue. Enzymes such as collagenase cleave the collagen and are used by micro-organisms to invade the host by degrading the native collagen in the connective tissue (Lecroisey & Keil 1979). By unfolding the triple helical conformation of collagen, the protein is denatured (Davis *et al.* 2000). Subsequently, putrefaction metabolizes the connective tissue into gases, liquids and protein debris. This degradation, caused by the attack of bacteria and fungi, is also a major factor opposing the preservation of mummified tissue.

In our study, morphologically intact type I collagen was identified by topographic analysis for all samples that were extracted from the mummy. The collagen was arranged as single fibrils in a meshwork or stacked in sheet-like structures, as is characteristic for recent skin collagen. The fibrils were undamaged and without any evidence of degradation. The D-period values agree with those found in the literature, i.e. a 67 nm axial repeat (Van der Rest & Garrone 1991; Holmes *et al.* 2001; Orgel *et al.* 2006). Measurements on recent human collagen type I revealed similar values, excluding an effect of the tissue type on variations of the D-period. The mean fibril height (32 nm) corresponds to the value reported for type I collagen (Holmes *et al.* 2001). The width of the fibrils was affected by the dilation of the cylindrical shape of the fibril and the geometry of the AFM tip. Aqueous media possibly influence the fibril diameter, as discussed, for example, by Kato *et al.* (2001) and Stücker *et al.* (2001), but this does not affect the comparison between the ancient and recent tissue, because all histological samples were processed following the same protocol and stored under the same conditions.

Our results indicate that the type I collagen fibrils were preserved through the ages in the mummified skin of the Iceman. This observation is supported by earlier SEM studies, where the preservation of collagen has been documented for other mummies. In SEM studies of 1600 to 2300-year-old bog bodies, dense collagen bundles were observed. Within the bundles, single fibrils with a banding periodicity of  $64 \pm 3$  nm were found (Stücker *et al.* 2001). Chang *et al.* (2006) found similar histological patterns in a well-preserved medieval mummy that was dated from AD 1418 to AD 1450. Good structural preservation of collagen was also indicated in SEM data obtained using a specimen taken from the Iceman. Hess *et al.* (1998) imaged collagen fibrils within the *stratum fibrosum* of the rib bone of the Iceman by TEM and found that structures which were distant from the sites of enzymatic activity were not affected by autolysis. They identified collagen that had an ultrastructural periodicity of 64–67 nm. Williams *et al.* (1995) showed that the

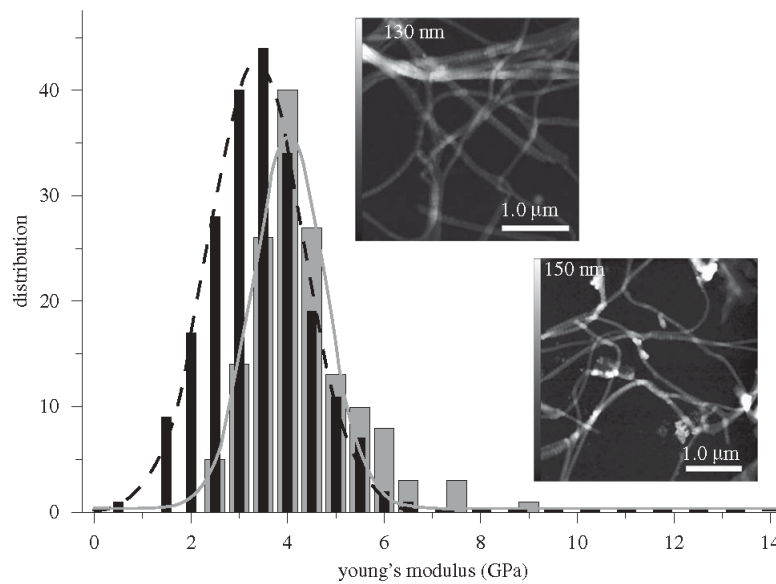


Figure 6. The distribution of Young's moduli measured from mummified and contemporary single human collagen fibrils. A total number of  $n \geq 150$  force–distance curves were evaluated for each sample. The nanoindentation measurement indicates a higher Young's modulus for the mummified human collagen (solid line) compared with the contemporary collagen (dashed line). The upper (recent) and lower (ancient) insets are AFM images showing typical fibrils. Force–distance curves were only recorded from well-separated single fibrils.

distinct skin layers of the dermis, the nucleate epidermis and the outermost skin layer—the *stratum corneum*—of the Iceman persisted over 5300 years.

By investigating collagen from wound tissue, we go a step further. Although some samples were drawn from wounds where the tissue is typically prone to degradation, the submicron structure of skin from the Iceman revealed the same features as those observed in undamaged specimens. We did not detect fibril debris or residues from degradation. From the AFM measurements, we conclude that the ultrastructure of the collagen fibrils was not altered. Based on these observations, we can exclude the decomposition and alteration of the fibril structure by insect or micro-organism infestation.

This conclusion is also confirmed by Raman measurements. Within the spectra taken from the Iceman samples, we detected bands that are characteristic of type I collagen. The presence of the amide I ( $1667\text{ cm}^{-1}$ ) and amide III ( $1245\text{--}1270\text{ cm}^{-1}$ ) bands, which represent the peptide bonds within proteins, points to a helical conformation of the collagen molecules and, hence, an intact collagen structure (Gross *et al.* 1954; Gross 1956; Frushour & Koenig 1975). In addition, we can assume that there were no molecular alterations in the collagen, because the positions of the Raman bands in the Iceman samples were similar to those found in the recent samples. Furthermore, the spectra of the Iceman samples were as distinct as the spectra of recent samples. The spectrum of sample A taken from the Iceman was slightly noisier than the spectra of samples B and C (figure 4). This is because the peak intensities in the Raman spectra of samples B and C were higher, yielding a lower signal to noise ratio for sample A. These variations in intensity may arise from different thicknesses of the samples and a different adjustment of the laser focus. A superposition

of the Raman signal of collagen with the Raman signal of the underlying glass substrate does not affect the spectral region between  $1170$  and  $870\text{ cm}^{-1}$ . Similarly, a comparison of the Raman spectra at higher wavenumbers shows that the protein molecules are preserved. The bands assigned to the C–H vibrational modes between  $2800$  and  $3050\text{ cm}^{-1}$  and the O–H vibrational modes from  $3000$  to  $3800\text{ cm}^{-1}$  are identical for ancient collagen and the spectrum from recent human skin.

Nanoindentation measurements, however, revealed small changes in the mechanical behaviour of the fibrils. Young's modulus of the mummified collagen was  $4.1 \pm 1.1\text{ GPa}$ , whereas the collagen of the contemporary skin sample was  $3.2 \pm 1.0\text{ GPa}$ . This observation indicates that some of the collagen was altered slightly. Changes in the mechanical properties of the ancient collagen may have occurred owing to freeze–thaw cycles, irradiation by UV light, or dehydration of the tissue. Freeze–thaw damage can change the molecular structure of collagen, as the crystallization of the ice can disrupt and break the fibrils. This would result in an altered Young's modulus and a distortion or fragmentation of the collagen. Nevertheless, no distortion, fragmentation or changes in the molecular structure of the collagen were observed.

The effect of UV irradiation on collagen molecules is still under debate. The impact of UV irradiation depends mainly on the time, dose and wavelength of the irradiation and on the environmental conditions. Short irradiation of collagen stored in water, or under nitrogen atmosphere increases its stability (Weadock *et al.* 1995; Sionkowska 2005). However, under ambient conditions and for longer irradiation times, the stability decreases and the mechanical stiffness is reduced. The loss of stability can be attributed to scission, fragmentation and denaturation of the collagen polypeptide chains (Miyata *et al.* 1971;

Weadock *et al.* 1995; Ohan *et al.* 2002; Sionkowska 2005). Nonetheless, the impact of UV irradiation on the mummified collagen has to be extrapolated from the level of tissue preservation, because the environmental exposure of the Iceman over the past 5300 years is unknown. Our nanoindentation measurements suggest that there have been only short periods of UV irradiation of the body because Young's modulus for the ancient collagen was increased slightly.

Dehydration and the formation of additional cross-links appear to be the major factor responsible for alterations of the mechanical properties. Removal of the interstitial water can bring the collagen subfibrils closer together, enabling the formation of additional cross-links. Kato *et al.* (2001) have shown that this leads to an increase in fibril stiffness. This effect was also observed in molecular dynamics simulations, where the absence of water in collagen-like peptides caused a distortion of the molecular conformation and, simultaneously, induced additional intra-molecular hydrogen bonds (Mogilner *et al.* 2002). Recent proliferation experiments suggest that dehydrated collagen fibrils become mechanically stiffer than fully hydrated fibrils, indicating that the level of H-bonding is increased (McDaniel *et al.* 2007). Our experimental data shows an increase of the stiffness from 3.2 GPa for the recent collagen to 4.1 GPa for the mummy collagen. We suggest that the strong dehydration of the mummy tissue led to the formation of additional interpeptide H-bonds or covalent cross-links (Buehler 2008) between the tropocollagen subfibrils.

Additional cross-linking owing to the advanced glycation endproduct (AGE) formation (Cerami *et al.* 1997; Singh *et al.* 2001; Ulrich & Cerami 2001), or genetic variations affecting the amino acid sequence and thus changing the quantity of hydrogen bonds within the collagen molecules (Uzel & Buehler 2009) can also contribute to the variation of the Young's modulus. At the present stage of investigation we cannot exclude these factors. However, we suppose that the increase in collagen stiffness caused by the formation of AGEs with biological age is small because the reference sample was drawn from a volunteer of a similar biological age as the Iceman. Furthermore genetic level differences seem to be rather unlikely, because evolutionary changes occur over considerably longer time frames.

Our nanoindentation measurements in concert with Raman spectroscopy help to relate the mechanical properties and the molecular preservation of the collagen with the mummification process. This demonstrates the potential of non-invasive methods to access the mechanical properties and the structural preservation of ancient tissue. We presume that supplementary cross-links between the tropocollagen subfibrils reinforce their structure, making lateral displacement of the subfibrils more unlikely, thus increasing Young's modulus and the stability of the mummified collagen. Our data also picture the excellent degree of preservation of the Tyrolean Iceman and may be used as a reference to monitor the conservation of the mummy on a molecular level.

## 5. CONCLUSIONS

Skin tissue samples were extracted from three sites of the Iceman to examine the structural preservation of

mummified type I collagen. The samples were processed to thin sections and analysed using AFM and Raman spectroscopy. Both methods indicate that the ultrastructure and molecular structure of the mummified collagen were preserved extremely well. Raman spectroscopy revealed spectra that were characteristic of type I collagen, and the amide I ( $1667\text{ cm}^{-1}$ ) and amide III ( $1245\text{--}1270\text{ cm}^{-1}$ ) bands indicate that the collagen molecules retained their helical conformation.

Examining single fibrils by nanoindentation demonstrated that Young's modulus of the mummified collagen was increased slightly over a recent sample. Although this stiffening might be supported by the effects of AGEs, genetic differences, or a very short period of UV irradiation of the fibrils, the most probable cause is dehydration. The loss of interstitial water resulted in a more densely packed structure of the fibrils and the generation of additional cross-links within the collagen. No evidence for collagen degradation was found that could have been caused by freeze–thaw cycles, micro-organisms or other biological influences.

Our results further show that the ultrastructure of the collagen fibrils remained unchanged for millennia owing to mummification by freeze-drying, and the enclosure of the body in glacier ice. Because of its low nutritional value, the dehydrated skin has maintained its protective function and prevented the connective tissue from decomposition. This result also shows the importance of dehydration for the mummification of connective tissue and supports the theory that the Iceman was covered by snow and ice immediately after his death (Bereuter *et al.* 1997; Rollo *et al.* 2000). Most probably, he was exposed to periodical cycles of thawing and freezing later on, which has resulted in advanced desiccation of the body.

We thank the Deutsche Forschungsgemeinschaft (DFG) cluster of excellence 'Nanosystems Initiative Munich' for financial support and are indebted to Prof. Dr Andreas Nerlich (Munich) for providing the histological specimens.

## APPENDIX A

### (a) AFM nanoindentation

The measurement of the mechanical properties of collagen provides insight into its molecular preservation. To assess the tensile mechanical properties of these protein fibrils, optical tweezers (Sun *et al.* 2002), the AFM (Graham *et al.* 2004) or dedicated microelectromechanical systems (Shen *et al.* 2008) can be used. A compressive test by nanoindentation is required to measure the mechanical properties of fibrils that completely adhere to the substrate. The mechanical properties of collagen were examined using the NanoWizard-II AFM, operated with rectangular, aluminium-coated silicon cantilevers (NSC35-B, MikroMasch, Tallinn, Estonia). The nominal spring constant,  $k_c$ , of the cantilevers was  $14\text{ N m}^{-1}$ . Before recording force–distance curves, topographic images of the samples were acquired to define adequate measurement regions. For imaging, we operated the AFM in intermittent contact mode. Subsequently, 10 force–distance curves were recorded at the centre region of the elevated banding structure of a single collagen fibril to avoid measurement errors arising from the topography (Domke & Radmacher 1998). Limiting the loading force to a maximum of 50 nN resulted in fibril indentations that



were smaller than 2 nm. This corresponds to an indentation smaller than 6 per cent of the fibril height. Blunt tips that had radii  $50 \text{ nm} < R < 100 \text{ nm}$  were favoured for the measurements. Each indentation curve was taken at a rate of 0.5 s for both the tip-approach and the tip-retraction (1024 data points). After a series of measurements, the samples were rescanned to assess plastic deformation of the fibrils. For further analysis, only force–distance curves that had been measured within the elastic regime were considered. More than six single fibrils and  $n \geq 150$  force–distance curves were analysed for the Iceman sample A and the recent sample. Young's modulus was determined from the curves using a Hertzian model (Hertz 1881). A spherical indenter geometry was assumed, because the indentation depth was restricted to less than 2 nm.

#### (b) Young's modulus calculation

When modelling the collagen fibril as a cylinder with radius  $R_f$  (Tan & Lim 2005; Heim *et al.* 2006), penetrated by a spherical indenter with radius  $R_i$ , Young's modulus ( $E$ ) can be calculated as:

$$E = \frac{3}{4} \times \frac{F(1-\nu^2)}{\sqrt{R_c} \delta^3}, \quad (\text{A } 1)$$

where  $F$  is the applied force,  $\delta$  is the indentation depth and  $\nu$  is the Poisson ratio of the material.  $R_c$  is the equivalent radius for the spherical indenter in contact with the cylinder. This equivalent radius is defined as:

$$R_c = \sqrt{\frac{R_i^2 R_f}{R_i + R_f}}. \quad (\text{A } 2)$$

The radius of the collagen fibril was measured as half the height of its highest point above the substrate. According to Hooke's law, the applied force is the product of the cantilever deflection ( $d$ ) and its spring constant,  $k_c$ .

$$E = \frac{3}{4} \times \frac{k_c d (1-\nu^2)}{\sqrt{R_c} \delta^3}. \quad (\text{A } 3)$$

The indentation depth in equation (A 3) can be substituted by the difference of the z-piezo displacement ( $z$ ) and the cantilever deflection, generating equation (A 4), where  $d_0$  and  $z_0$  are the zero deflection of the cantilever and the displacement of the z-piezo at the contact point (i.e. the point at which the tip begins to interact with the sample repulsively), respectively.

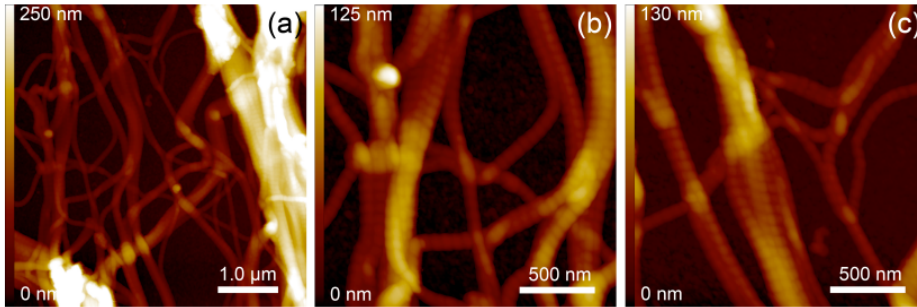
$$E = \frac{3}{4} \times \frac{k_c (d - d_0) (1-\nu^2)}{\sqrt{R_c [(z - z_0) - (d - d_0)]^3}}. \quad (\text{A } 4)$$

For the calculations, the Poisson ratio was set to 0.5, assuming an incompressible material. The actual cantilever spring constant was determined using the quality factor calibration as described by Sader *et al.* (1999), and the tip radius was measured by imaging a calibration grating (TGT01, MikroMasch, Tallinn, Estonia). All measurements were performed in air at room temperature. Young's moduli were determined by fitting equation (A 4) to each force–distance curve (Stark *et al.* 1998). The data analysis was carried out using SPM Image Processing software (JPK, JPK Instruments, Berlin, Germany).

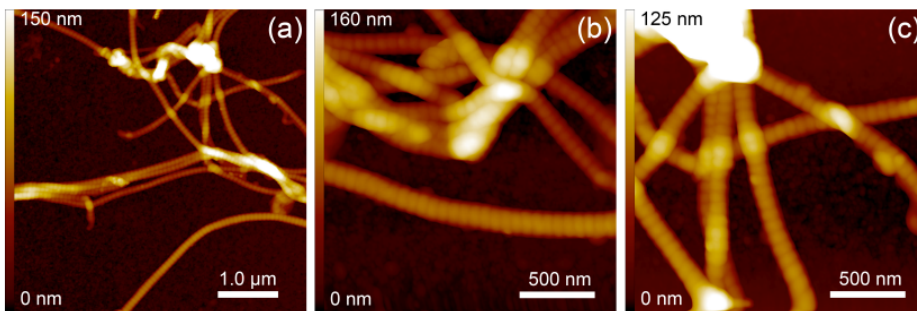
#### REFERENCES

- Bereuter, T. L., Mikenda, W. & Reiter, C. 1997 Iceman's mummification: implications from infrared spectroscopic and histological studies. *Chem.-Eur. J.* **3**, 1032–1038. (doi:10.1002/chem.19970030708)
- Buehler, M. J. 2006 Nature designs tough collagen: explaining the nanostructure of collagen fibrils. *Proc. Natl Acad. Sci. USA* **103**, 12 285–12 290. (doi:10.1073/pnas.0603216103)
- Buehler, M. J. 2008 Nanomechanics of collagen fibrils under varying cross-link densities: atomistic and continuum studies. *J. Mech. Behav. Biomed. Mat.* **1**, 59–67. (doi:10.1016/j.jmbbm.2007.04.001)
- Cerami, C. *et al.* 1997 Tobacco smoke is a source of toxic reactive glycation products. *Proc. Natl Acad. Sci. USA* **94**, 13 915–13 920. (doi:10.1073/pnas.94.25.13915)
- Chang, B. S. *et al.* 2006 Preserved skin structure of a recently found fifteenth-century mummy in Daejeon, Korea. *J. Anat.* **209**, 671–680. (doi:10.1111/j.1469-7580.2006.00607.x)
- Davis, G. E., Bayless, K. J., Davis, M. J. & Meininger, G. A. 2000 Regulation of tissue injury responses by the exposure of matricryptic sites within extracellular matrix molecules. *Am. J. Pathol.* **156**, 1489–1498.
- Domke, J. & Radmacher, M. 1998 Measuring the elastic properties of thin polymer films with the atomic force microscope. *Langmuir* **14**, 3320–3325. (doi:10.1021/la9713006)
- Edwards, H. G., Farwell, D. W., Holder, J. M. & Lawson, E. E. 1997 Fourier-transform Raman spectra of ivory. III. Identification of mammalian specimens. *Spectrochim. Acta A Mol. Biomol. Spectrosc.* **53A**, 2403–2409. (doi:10.1016/S1386-1425(97)00180-7)
- Fraser, R. D. B., Macrae, T. P. & Suzuki, E. 1979 Chain conformation in the collagen molecule. *J. Mol. Biol.* **129**, 463–481. (doi:10.1016/0022-2836(79)90507-2)
- Fratzl, P., Misof, K., Zizak, I., Rapp, G., Amenitsch, H. & Bernstorff, S. 1998 Fibrillar structure and mechanical properties of collagen. *J. Struct. Biol.* **122**, 119–122. (doi:10.1006/jsbi.1998.3966)
- Frushour, B. G. & Koenig, J. L. 1975 Raman scattering of collagen, gelatin, and elastin. *Biopolymers* **14**, 379–391. (doi:10.1002/bip.1975.360140211)
- Gniadecka, M., Nielsen, O. F., Christensen, D. H. & Wulf, H. C. 1998 Structure of water, proteins, and lipids in intact human skin, hair, and nail. *J. Invest. Dermatol.* **110**, 393–398. (doi:10.1046/j.1523-1747.1998.00146.x)
- Gostner, P. & Vigl, E. E. 2002 INSIGHT: report of radiological-forensic findings on the Iceman. *J. Archaeol. Sci.* **29**, 323–326. (doi:10.1006/jasc.2002.0824)
- Graham, J. S., Vomund, A. N., Phillips, C. L. & Grandbois, M. 2004 Structural changes in human type I collagen fibrils investigated by force spectroscopy. *Exp. Cell Res.* **299**, 335–342. (doi:10.1016/j.yexcr.2004.05.022)
- Gross, J. 1956 The behavior of collagen units as a model in morphogenesis. *J. Biophys. Biochem. Cytol.* **2**, 261–274.
- Gross, J., Highberger, J. H. & Schmitt, F. O. 1954 Collagen structures considered as states of aggregation of a kinetic unit: the tropocollagen particle. *Proc. Natl Acad. Sci. USA* **40**, 679–688. (doi:10.1073/pnas.40.8.679)
- Heim, A. J., Matthews, W. G. & Koob, T. J. 2006 Determination of the elastic modulus of native collagen fibrils via radial indentation. *Appl. Phys. Lett.* **89**, 181 902–181 903. (doi:10.1063/1.2367660)
- Hertz, H. 1881 Ueber die Berührung fester elastischer Körper. *J. Reine angewandte Mathematik* **92**, 156–171.
- Hess, M. W., Klima, G., Pfaller, K., Kunzel, K. H. & Gaber, O. 1998 Histological investigations on the Tyrolean Iceman. *Am. J. Phys. Anthropol.* **106**, 521–532. (doi:10.1002/(SICI)1096-8644(199808)106:4<521::AID-AJPA7>3.0.CO;2-L)

- Hino, H., Ammitzboll, T., Møller, R. & Asboehansen, G. 1982 Ultrastructure of skin and hair of an Egyptian mummy: transmission and scanning electron-microscopic observations. *J. Cutan. Pathol.* **9**, 25–32. (doi:10.1111/j.1600-0560.1982.tb01038.x)
- Holmes, D. F., Gilpin, C. J., Baldock, C., Ziese, U., Koster, A. J. & Kadler, K. E. 2001 Corneal collagen fibril structure in three dimensions: structural insights into fibril assembly, mechanical properties, and tissue organization. *Proc. Natl Acad. Sci. USA* **98**, 7307–7312. (doi:10.1073/pnas.111150598)
- Jastrzebska, M., Zalewska-Rejda, J., Wrzalik, R., Kocot, A., Barwinski, B., Mróz, I. & Cwalina, B. 2005 Dimethyl suberimide cross-linked pericardium tissue: Raman spectroscopic and atomic force microscopy investigations. *J. Mol. Struct.* **744–747**, 789–795. (doi:10.1016/j.molstruc.2004.11.040)
- Kato, K., Bar, G. & Cantow, H. J. 2001 The interplay between surface micro-topography and -mechanics of type I collagen fibrils in air and aqueous media: an atomic force microscopy study. *Eur. Phys. J. E* **6**, 7–14. (doi:10.1007/s101890170022)
- Lecroisey, A. & Keil, B. 1979 Differences in the degradation of native collagen by two microbial collagenases. *Biochem. J.* **179**, 53–58.
- Lingham-Soliar, T. 2008 A unique cross section through the skin of the dinosaur *Psittacosaurus* from China showing a complex fibre architecture. *Proc. R. Soc. B* **275**, 775–780. (doi:10.1098/rspb.2007.1342)
- McDaniel, D. P., Shaw, G. A., Elliott, J. T., Bhadriraju, K., Meuse, C., Chung, K. H. & Plant, A. L. 2007 The stiffness of collagen fibrils influences vascular smooth muscle cell phenotype. *Biophys. J.* **92**, 1759–1769. (doi:10.1529/biophysj.106.089003)
- Miyata, T., Sohde, T., Rubin, A. L. & Stenzel, K. H. 1971 Effects of ultraviolet irradiation on native and telopeptide-poor collagen. *Biochim. Biophys. Acta* **229**, 672–680.
- Mogilner, I. G., Ruderman, G. & Grigera, J. R. 2002 Collagen stability, hydration and native state. *J. Mol. Graph. Model* **21**, 209–213. (doi:10.1016/S1093-3263(02)00145-6)
- Montes, G. S., Krisztan, R. M. & Junqueira, L. C. U. 1985 Preservation of elastic system fibers and of collagen molecular arrangement and stainability in an Egyptian mummy. *Histochemistry* **83**, 117–119. (doi:10.1007/BF00495140)
- Nerlich, A. G., Bachmeier, B., Zink, A., Thalhammer, S. & Egarter-Vigi, E. 2003 Otzi had a wound on his right hand. *Lancet* **362**, 334. (doi:10.1016/S0140-6736(03)13992-X)
- Ohan, M. P., Weadock, K. S. & Dunn, M. G. 2002 Synergistic effects of glucose and ultraviolet irradiation on the physical properties of collagen. *J. Biomed. Mat. Res.* **60**, 384–391. (doi:10.1002/jbm.10111)
- Orgel, J. P. R. O., Irving, T. C., Miller, A. & Wess, T. J. 2006 Microfibrillar structure of type I collagen in situ. *Proc. Natl Acad. Sci. USA* **103**, 9001–9005. (doi:10.1073/pnas.0502718103)
- Pernter, P., Gostner, P., Vigl, E. E. & Ruhli, F. J. 2007 Radiologic proof for the Iceman's cause of death (ca 5300 BP). *J. Archaeol. Sci.* **34**, 1784–1786. (doi:10.1016/j.jas.2006.12.019)
- Rich, A. & Crick, F. H. C. 1955 Structure of collagen. *Nature* **176**, 915–916. (doi:10.1038/176915a0)
- Rollo, F., Luciani, S., Canapa, A. & Marota, I. 2000 Analysis of bacterial DNA in skin and muscle of the Tyrolean Iceman offers new insight into the mummification process. *Am. J. Phys. Anthropol.* **111**, 211–219. (doi:10.1002/(SICI)1096-8644(200002)111:2<211::AID-AJPA7>3.0.CO;2-M)
- Sader, J. E., Chon, J. W. M. & Mulvaney, P. 1999 Calibration of rectangular atomic force microscope cantilevers. *Rev. Sci. Instrum.* **70**, 3967–3969. (doi:10.1063/1.1150021)
- Schweitzer, M. H., Suo, Z., Avci, R., Asara, J. M., Allen, M. A., Arce, F. T. & Horner, J. R. 2007a Analyses of soft tissue from *Tyrannosaurus rex* suggest the presence of protein. *Science* **316**, 277–280. (doi:10.1126/science.1138709)
- Schweitzer, M. H., Wittmeyer, J. L. & Horner, J. R. 2007b Soft tissue and cellular preservation in vertebrate skeletal elements from the Cretaceous to the present. *Proc. R. Soc. B* **274**, 183–197. (doi:10.1098/rspb.2006.3705)
- Shen, Z. L., Dodge, M. R., Kahn, H., Ballarini, R. & Eppell, S. J. 2008 Stress-strain experiments on individual collagen fibrils. *Biophys. J.* **95**, 3956–3963. (doi:10.1529/biophysj.107.124602)
- Shin, D. H., Youn, M. & Chang, B. S. 2003 Histological analysis on the medieval mummy in Korea. *Forensic Sci. Int.* **137**, 172–182. (doi:10.1016/S0379-0738(03)00335-9)
- Singh, R., Barden, A., Mori, T. & Beilin, L. 2001 Advanced glycation end-products: a review. *Diabetologia* **44**, 129–146. (doi:10.1007/s001250051591)
- Sionkowska, A. 2005 Thermal denaturation of UV-irradiated wet rat tail tendon collagen. *Int. J. Biol. Macromol.* **35**, 145–149. (doi:10.1016/j.ijbiomac.2005.01.009)
- Stark, R. W., Drobek, T., Weth, M., Fricke, J. & Heckl, W. M. 1998 Determination of elastic properties of single aerogel powder particles with the AFM. *Ultramicroscopy* **75**, 161–169. (doi:10.1016/S0304-3991(98)00061-8)
- Strasser, S., Zink, A., Janko, M., Heckl, W. M. & Thalhammer, S. 2007 Structural investigations on native collagen type I fibrils using AFM. *Biochem. Biophys. Res. Commun.* **354**, 27–32. (doi:10.1016/j.bbrc.2006.12.114)
- Stücker, M., Bechara, F.-G., Bacharach-Buhles, M., Pieper, P. & Altmayer, P. 2001 What happens to skin after 2000 years in a bog? *Hautarzt* **52**, 316–321.
- Sun, Y. L., Luo, Z. P., Fertala, A. & An, K. N. 2002 Direct quantification of the flexibility of type I collagen monomer. *Biochem. Biophys. Res. Commun.* **295**, 382–386. (doi:10.1016/S0006-291X(02)00685-X)
- Tan, E. P. S. & Lim, C. T. 2005 Nanoindentation study of nanofibers. *Appl. Phys. Lett.* **87**, 123 103–123 106. (doi:10.1063/1.2051802)
- Ulrich, P. & Cerami, A. 2001 Protein glycation, diabetes, and aging. *Recent Prog. Horm. Res.* **56**, 1–21. (doi:10.1210/rp.56.1.1)
- Uzel, S. G. M. & Buehler, M. J. 2009 Nanomechanical sequencing of collagen: tropocollagen features heterogeneous elastic properties at the nanoscale. *Integr. Biol.* **1**, 452–459. (doi:10.1039/b906864c)
- Van der Rest, M. & Garrone, R. 1991 Collagen family of proteins. *FASEB J.* **5**, 2814–2823.
- Weadock, K. S., Miller, E. J., Bellincampi, L. D., Zawadsky, J. P. & Dunn, M. G. 1995 Physical cross-linking of collagen-fibers: comparison of ultraviolet-irradiation and dehydrothermal treatment. *J. Biomed. Mat. Res.* **29**, 1373–1379. (doi:10.1002/jbm.820291108)
- Wenger, M. P. E., Bozec, L., Horton, M. A. & Mesquida, P. 2007 Mechanical properties of collagen fibrils. *Biophys. J.* **93**, 1255–1263. (doi:10.1529/biophysj.106.103192)
- Williams, B. R., Gelman, R. A., Poppe, D. C. & Piez, K. A. 1978 Collagen fibril formation. Optimal *in vitro* conditions and preliminary kinetic results. *J. Biol. Chem.* **253**, 6578–6585.
- Williams, A. C., Edwards, H. G. M. & Barry, B. W. 1995 The Iceman: molecular structure of 5200-year-old skin characterized by Raman spectroscopy and electron microscopy. *Biochim. Biophys. Acta-Protein Struct. Mol. Enzymol.* **1246**, 98–105. (doi:10.1016/0167-4838(94)00189-N)
- Yang, L., Van der Werf, K. O., Fitie, C. F. C., Bennink, M. L., Dijkstra, P. J. & Feijen, J. 2008 Mechanical properties of native and cross-linked type I collagen fibrils. *Biophys. J.* **94**, 2204–2211. (doi:10.1529/biophysj.107.111013)

**Supplementary Data**

Supplementary Figure 1: Collagen structures found in the Iceman sample *B*. Image (a) shows individual fibrils in a randomly oriented meshwork (scan size  $5 \times 5 \mu\text{m}$ ). The high resolution images (b) and (c) clearly reveal the collagen's banding pattern. (size  $2 \times 2 \mu\text{m}$ ).



Supplementary Figure 2: Single collagen fibrils as observed for the Iceman sample *C*. The images with a scan size of (a)  $5 \times 5 \mu\text{m}$  and (b, c)  $2 \times 2 \mu\text{m}$  show individual fibrils in a randomly oriented meshwork. The uniform D-period pattern was measured along the single fibrils by analyzing the topographic profiles.

## 8.3 PRESERVATION OF 5300 YEAR OLD RED BLOOD CELLS IN THE ICEMAN

Downloaded from [rsif.royalsocietypublishing.org](http://rsif.royalsocietypublishing.org) on May 14, 2012

JOURNAL  
— OF —  
THE ROYAL  
SOCIETY

# Interface

### Preservation of 5300 year old red blood cells in the Iceman

Marek Janko, Robert W. Stark and Albert Zink

*J. R. Soc. Interface* published online 2 May 2012  
doi: 10.1098/rsif.2012.0174

|                               |   |
|-------------------------------|---|
| <b>Supplementary data</b>     | "Data Supplement"<br><a href="http://rsif.royalsocietypublishing.org/content/suppl/2012/04/30/rsif.2012.0174.DC1.htm">http://rsif.royalsocietypublishing.org/content/suppl/2012/04/30/rsif.2012.0174.DC1.htm</a>  |
| <b>References</b>             | <a href="#">This article cites 52 articles, 13 of which can be accessed free</a><br><a href="http://rsif.royalsocietypublishing.org/content/early/2012/04/26/rsif.2012.0174.full.html#ref-list-1">http://rsif.royalsocietypublishing.org/content/early/2012/04/26/rsif.2012.0174.full.html#ref-list-1</a> |
| <b>P&lt;P</b>                 | Published online 2 May 2012 in advance of the print journal.  |
| <b>EXIS Open Choice</b>       | This article is free to access  |
| <b>Email alerting service</b> | Receive free email alerts when new articles cite this article - sign up in the box at the top right-hand corner of the article or click <a href="#">here</a>  |

Advance online articles have been peer reviewed and accepted for publication but have not yet appeared in the paper journal (edited, typeset versions may be posted when available prior to final publication). Advance online articles are citable and establish publication priority; they are indexed by PubMed from initial publication. Citations to Advance online articles must include the digital object identifier (DOIs) and date of initial publication.

To subscribe to *J. R. Soc. Interface* go to: <http://rsif.royalsocietypublishing.org/subscriptions>

# Preservation of 5300 year old red blood cells in the Iceman

Marek Janko<sup>1-4</sup>, Robert W. Stark<sup>2-4</sup> and Albert Zink<sup>2,5,\*</sup>

<sup>1</sup>*Department of Earth and Environmental Sciences, Ludwig-Maximilians-Universität München, Theresienstraße 41, 80333 Munich, Germany*

<sup>2</sup>*Center for NanoSciences, Ludwig-Maximilians-Universität München, Schellingstrasse 4, 80799 Munich, Germany*

<sup>3</sup>*FB Material- und Geowissenschaften, and* <sup>4</sup>*Center of Smart Interfaces, TU Darmstadt, Petersenstrasse 32, 64287 Darmstadt, Germany*

<sup>5</sup>*European Academy of Bolzano, Institute for Mummies and the Iceman, Viale Druso 1, 39100 Bolzano, Italy*

Changes in elasticity and structures of red blood cells (RBCs) are important indicators of disease, and this makes them interesting for medical studies. In forensics, blood analyses represent a crucial part of crime scene investigations. For these reasons, the recovery and analysis of blood cells from ancient tissues is of major interest. In this study, we show that RBCs were preserved in Iceman tissue samples for more than 5000 years. The morphological and molecular composition of the blood corpuscle is verified by atomic force microscope and Raman spectroscopy measurements. The cell size and shape approximated those of healthy, dried, recent RBCs. Raman spectra of the ancient corpuscle revealed bands that are characteristic of haemoglobin. Additional vibrational modes typical for other proteinaceous fragments, possibly fibrin, suggested the formation of a blood clot. The band intensities, however, were approximately an order of magnitude weaker than those of recent RBCs. This fact points to a decrease in the RBC-specific metalloprotein haemoglobin and, thus, to a degradation of the cells. Together, the results show the preservation of RBCs in the 5000 year old mummy tissue and give the first insights into their degradation.

**Keywords:** ancient erythrocytes; haemoglobin; protein degradation; Iceman; atomic force microscope; Raman spectroscopy

## 1. INTRODUCTION

Examining mummies with sensitive analytic tools enables the reconstruction of their ancestry and genetic relationships [1,2], diet, diseases [2], living conditions, state of preservation and the mummification processes [3]. While many studies provided molecular evidence for the presence of infectious diseases in ancient populations, leading to deep insights into the evolution of such diseases [4,5], only a few reports on the recovery of blood from mummified bodies are available. Previous investigations, based on optical or electron microscopy data, postulated that blood remains or fragments could be preserved in mummies as old as 2000 years [6–10]. Although molecular verification of blood findings was not performed, detection of blood components was of major interest because it could give new perspectives on the lives and fates of our ancestors. Blood can indicate the general health status of an individual and it can be analysed to detect pathological conditions or to provide valuable information in forensic crime scene investigations.

\*Author for correspondence ([albert.zink@eurac.edu](mailto:albert.zink@eurac.edu)).

Electronic supplementary material is available at <http://dx.doi.org/10.1098/rsif.2012.0174> or via <http://rsif.royalsocietypublishing.org>.

Received 2 March 2012  
Accepted 13 April 2012

One of the oldest forensic puzzles encompasses the death of the Tyrolean Iceman. This wet-mummy, commonly known as ‘Ötzi’, was presumably killed by an arrow. The corpse was found *ca* 5300 years later [11] in 1991 [12]. The mummy was exceptionally well preserved, and it still had intact connective tissue [13,14] and nervous system components [13]. However, in contrast to the good overall preservation of its tissue, no blood has been found so far. Thus, it was initially assumed that the blood had disintegrated owing to autolysis within the corpse [13]. Later, X-ray and computed tomography images of the Iceman body gave the first hints of blood residues. A prehistoric arrowhead that was surrounded by inhomogeneous soft-tissue areas was located between the rib cage and the left scapula. The areas were interpreted as being dehydrated haematomas [15,16] and associated with a lesion in the left subclavian artery that could have led to haemorrhagic shock and the Iceman’s death [17]. Haemoglobin, a common blood protein, was detected in a skin wound on the Iceman’s right hand using a guaiac-based test. However, it did not provide evidence for intact blood cells [18]. Recently, a microscopic analysis of immunohistochemically stained histological tissue samples indicated the possible presence of blood residues [19].

2 *Iceman red blood cells* M. Janko *et al.*

Here, we report the direct detection of red blood cells (RBCs) in tissue samples from the Iceman with an atomic force microscope (AFM) and Raman spectroscopy. Single and clustered RBCs were found, and their characteristic Raman spectra were obtained. The spectra contained Raman bands of proteinaceous remnants, most likely fibrin, which indicates the formation of a blood clot. The Raman spectra, however, also document a degradation of the cells. Their spectral intensity was approximately an order of magnitude weaker than that of recent RBCs. Additional elasticity measurements on the cells imply a loss in RBC stability—which also points to degradation.

## 2. MATERIAL AND METHODS

Iceman tissue was obtained by punch biopsies from the stab trauma to the right hand (sample A) [18] and from the wound under the left spina scapulae on the Iceman's back (sample B) [15]. The extracted tissue was rehydrated for 48 h in a 9.5 parts formaldehyde (2%) and 0.5 parts Brij 35 solution, and subsequently fixed with 4 per cent formaldehyde (formalin) for 2 h, dehydrated in an ascending alcohol series and embedded into paraffin wax. Histological specimens were obtained by cutting 2–4  $\mu\text{m}$  thick transverse sections and transferring them onto glass slides. Before AFM analysis, the paraffin was dissolved in xylene. Finally, the sections were rehydrated with a descending alcohol series, rinsed with ultrapure water and dried under ambient conditions [14]. As a reference, a recent human tissue sample, taken from a volunteer and processed in the same manner as the Iceman samples, was used. Additionally, fresh capillary whole blood was drawn from the fingertip of a volunteer, applied to a glass slide and left to dry for 6 h. Furthermore, a glass slide was coated with a meshwork of fibrin, an essential protein formed during the blood clotting process. The preparation of fibrin was carried out following the protocol of Riedel *et al.* [20].

Particles with the approximate size and shape of RBCs were identified with an inverted optical microscope (Axiovert 135; Zeiss, Oberkochen, Germany). Then, high-resolution images were taken with a NanoWizard-II AFM (JPK Instruments, Berlin, Germany). The AFM was operated in the intermittent contact mode. Silicon cantilevers (BS Tap 300; Budget Sensors, Redding, CA, USA) with nominal spring constants of  $40 \text{ N m}^{-1}$ , resonance frequencies of 300 kHz and tip radii of 10 nm were used.

Additionally, within the fixed samples, individual putative RBCs were analysed by AFM nanoindentation so as to assess elasticity. Force curves of recent ( $n = 363$ ) and mummified ( $n = 213$ ) samples were obtained by indenting an AFM tip with a defined radius of 300 nm (LRCH 250; Team Nanotec, Villingen-Schwenningen, Germany) into the corpuscle surface. The nominal spring constant,  $k_c$ , of the cantilever was  $40 \text{ N m}^{-1}$ , and the loading force for each measurement was limited to 500 nN. Four recent RBCs and two corpuscles extracted from the arrowhead entry wound on the back of the mummy (sample B) were tested. Only

(putative) RBCs that were lying flat on the glass substrate were analysed to ensure good mechanical contact with the substrate. The numerical value for Young's modulus  $E$  was obtained from fitting a Hertzian model [21] on the force curves. Sneddon's extension [22,23] of the Hertzian model was used to calculate the deformation  $\delta$  of the flat elastic sample surface penetrated by a rigid spherical indenter (AFM tip) of radius  $R$ . The spherical indenter geometry was assumed because the indentation depth of the AFM tip into the sample was small compared with the tip radius. The samples' Young's modulus was calculated from

$$E = \frac{F(1 - \nu^2)}{(a + R^2/a)\delta - aR}, \quad (2.1)$$

with the sample deformation given by

$$\delta = \frac{a}{2} \ln \left( \frac{R + a}{R - a} \right), \quad (2.2)$$

with  $F$  the applied force,  $a$  the radius of the contact area between the tip and the sample, and  $\nu$  the Poisson ratio of the material analysed. The Poisson ratio was set to 0.5, assuming an incompressible material.

For the molecular analysis, a confocal Raman spectroscope (WITec alpha 300 R; WITec GmbH, Ulm, Germany; excitation wavelength 532 nm) was used. To avoid photodegradation, laser power was limited to 1.0 mW. The spectrometer was operated with an  $1800 \text{ g mm}^{-1}$  grating. The spectral resolution was  $1 \text{ cm}^{-1}$  per CCD-pixel. Three different positions were analysed for each sample, and at least three single spectra, with 180 s of integration time, were taken at each position. Owing to the confocal set-up of the microscope, Raman spectra were collected from a sample area with 300 nm diameter and a focal depth of approximately 1  $\mu\text{m}$ .

## 3. RESULTS

One corpuscle with a structure likely to be a RBC [24] was found in the hand wound tissue of the Iceman (figure 1*d*), and two single corpuscles were detected within the arrowhead wound sample. Sample B furthermore showed an agglomeration of several randomly distributed particles (figure 1*f*). The selected corpuscles exhibit a discoidal, concave surface with a diameter between 5.8 and 6.4  $\mu\text{m}$  (figure 1*d,e*). The concave shape is typical for RBCs and arises during the early stages of development in the bone marrow when the cell nuclei are discarded, leaving behind an impression on the membrane. The dip in the membrane of the corpuscle was 0.7–1.1  $\mu\text{m}$  deep. For comparison, RBCs from a recent human tissue sample, similar in structure and appearance to those found in the Iceman samples, are shown in figure 1*a–c*. The mean cell diameter of the recent RBCs was  $6.3 \pm 0.4 \mu\text{m}$ , which matches the average diameter of the ancient corpuscle. The cells are also similar when comparing the mean area and volume of the RBCs (table 1). The measured height of the recent cells and of the mummy particles differ more; however, the variation is still within the error margin.

To assess the chemical composition and structural conformation of the ancient corpuscles, Raman

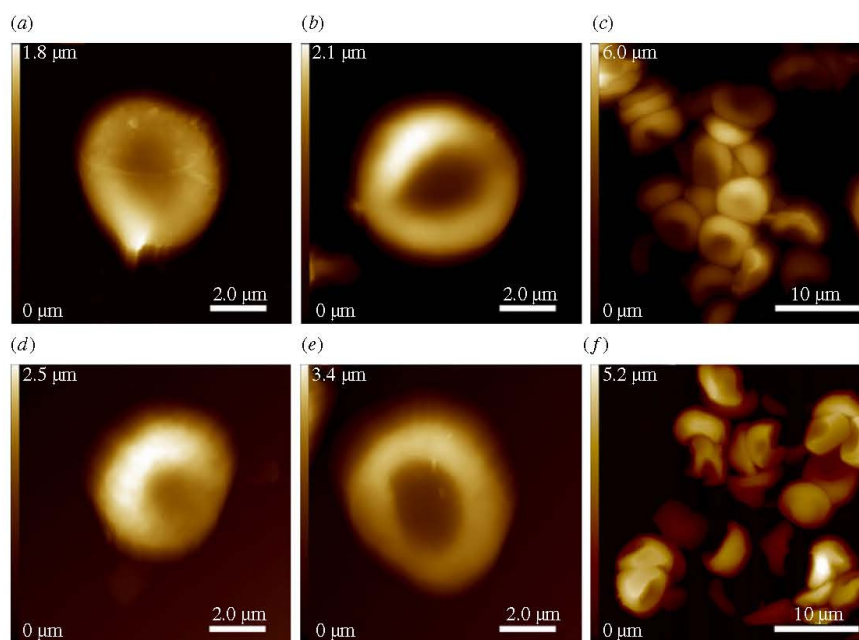


Figure 1. AFM images of RBCs. (a, b) Single RBCs from recent human tissue. (c) An assembly of RBCs. (d, e) Single corpuscles found in Iceman sample A and sample B are shown. An assembly of several randomly distributed corpuscles, similar to those found within the recent sample (c), are displayed in image (f). The imaged corpuscles (d–f) feature the characteristic discoid and concave surface of RBCs.

Table 1. Dimensions of recent RBCs and ancient corpuscles.

| sample            | quantity | height ( $\mu\text{m}$ ) | diameter ( $\mu\text{m}$ ) | area ( $\mu\text{m}^2$ ) | volume (fl)     |
|-------------------|----------|--------------------------|----------------------------|--------------------------|-----------------|
| recent RBCs       | 19       | $2.0 \pm 0.5$            | $6.3 \pm 0.4$              | $31.0 \pm 3.7$           | $40.0 \pm 12.2$ |
| ancient corpuscle | 3        | $2.5 \pm 0.2$            | $6.0 \pm 0.3$              | $28.8 \pm 3.2$           | $42.1 \pm 4.1$  |

measurements were performed. The spectral fingerprint region of the particle in Iceman sample A was compared with that of an air-dried recent whole blood sample and with that of recent single RBCs. The recent single RBCs were subjected to the same sample preparation as that of the mummy tissue before examination. All Raman spectra shown in figure 2 exhibit distinct bands at 1586, 1395, 1308 and 747  $\text{cm}^{-1}$ , which are assigned to the stretching vibration modes  $\nu_{37}$ ,  $\nu_{20}/\nu_{29}$ ,  $\nu_{21}$  and  $\nu_{15}$  of porphyrin. Porphyrin is the characteristic building unit of the major RBC protein haemoglobin [25–27]. Furthermore, bands that are typical for other protein components, such as the twisting deformation mode of methylene at approximately 1230  $\text{cm}^{-1}$ , were present. The spectrum of Iceman sample A additionally shows two small peaks at approximately 1665 and 1248  $\text{cm}^{-1}$  and two prominent bands at 1446 and 1002  $\text{cm}^{-1}$ . The latter are assigned to the proteinaceous deformation vibration of methyl  $\delta(\text{CH}_3)$  and methylene  $\delta(\text{CH}_2)$  molecules and to the vibration mode of phenylalanine [14,28]. The two small peaks at 1665 and 1248  $\text{cm}^{-1}$  are assigned to the amide I (C=O stretching) and the

amide III (C–N stretching and N–H in plane deformation modes) groups [29]. A detailed band assignment is shown in table 2. Comparing the intensities of the spectra, a strong decrease in scattering efficiency can be observed for the ancient particle. The intensity of the Raman spectrum of Iceman sample A is approximately an order of magnitude weaker than that of the recent blood samples, although the ratio between the band intensities within the spectrum remained largely unchanged.

When the fingerprint region from 700 to 1720  $\text{cm}^{-1}$  in the particles found in Iceman sample B was analysed, hardly any Raman bands indicated the presence of RBCs (figure 3). A characteristic spectrum of the corpuscles in sample B is shown in figure 3c. The first strong Raman band observed is the amide I peak at approximately 1656  $\text{cm}^{-1}$ , corresponding to the C=O stretching vibration  $\nu(\text{CO})$  typical for proteins. Further prominent bands appear between 1620 and 1600  $\text{cm}^{-1}$ , originating from the C=C vibrational stretch mode  $\nu(\text{CC})$  of the amino acids tyrosine or phenylalanine. Similar to Iceman sample A the corpuscles in sample B feature

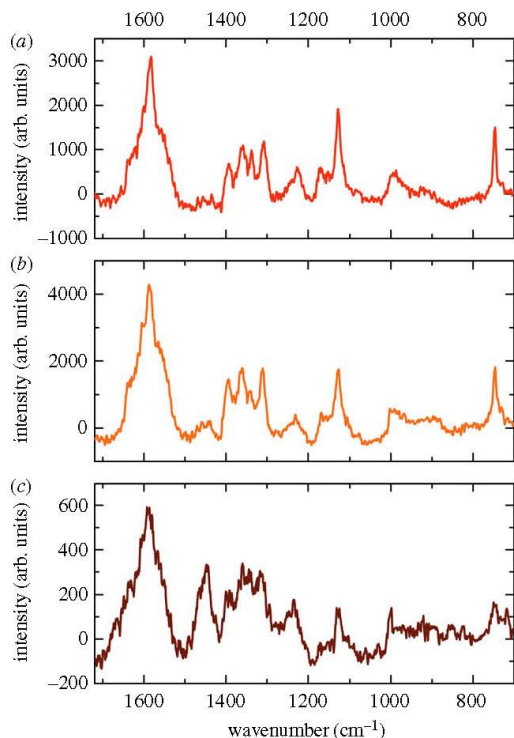
4 *Iceman red blood cells* M. Janko *et al.*

Figure 2. Raman spectra of air-dried whole blood (*a*), a single red blood cell (*b*), and the corpuscle found in the Iceman tissue sample A (*c*). All spectra show peaks at 1586, 1395, 1308 and 747  $\text{cm}^{-1}$ , which are characteristic of porphyrin. Apart from some bands, the spectra show considerable similarities.

strong methyl  $\delta(\text{CH}_3)$  and methylene  $\delta(\text{CH}_2)$  bands at approximately 1449  $\text{cm}^{-1}$  and a distinct peak at 1002  $\text{cm}^{-1}$ , which represents the vibration mode of phenylalanine. There were also bands assigned to the deformation of methylene  $\delta(\text{CH}_2)$  molecules between 1380 and 1300  $\text{cm}^{-1}$  [30,31]. Finally, the peak appearing at approximately 758  $\text{cm}^{-1}$  can be attributed to the aromatic ring breathing of tryptophan [30]. As shown in figure 3, the Raman bands observed in Iceman sample B (figure 3*c*) exhibit similarities to those observed when examining pure fibrin (figure 3*b*). The intensities of the spectra were largely similar; however, the amount of sample material analysed has to be taken into account. The reference fibrin spectrum was obtained from a thin fibrin layer a few hundred nanometres thick, and the average particle spectrum shown in figure 3*c* was recorded on a 2  $\mu\text{m}$  thick particle. Table 3 also indicates that Raman bands from sample B imply the presence of fibrin instead of RBCs. Nonetheless, some correlations between porphyrin vibration modes and the location of the ancient particles can be drawn from two-dimensional Raman scans. The data displayed in figure 4*a* associate the colour-coded Rayleigh scattering intensity of a Raman scan to an AFM topography image. Figure 4*b–g* shows the Raman data filtered for selected molecule vibrations. Red indicates sample regions with strong

Raman scattering. Areas with low intensity are in blue. Specific molecule vibrations are predominant in areas that correlate with the position of the ancient particles. Figure 4*c,e,f* illustrates the intensity distribution around the bands at 1586, 1395 and 1308  $\text{cm}^{-1}$ , which are associated with the porphyrin vibration modes  $\nu_{37}$ ,  $\nu_{20}/\nu_{29}$  and  $\nu_{21}$ . In the wavenumber range 1370–1410  $\text{cm}^{-1}$ , no Raman scattering occurred (figure 4*e*). The molecule vibrations  $\nu_{37}$  and  $\nu_{21}$ , however, show a moderate signal at the position of the ancient particles. The highest Raman signals are observed in the wavenumber range of the protein-specific bands, e.g. the amide I peak around 1656  $\text{cm}^{-1}$  (figure 4*b*), the methyl  $\delta(\text{CH}_3)$  and methylene  $\delta(\text{CH}_2)$  band at approximately 1449  $\text{cm}^{-1}$  (figure 4*d*) and the C–N stretch mode around 1125  $\text{cm}^{-1}$  (figure 4*g*).

An analysis of the mechanical properties of RBCs can give further insights into their structural integrity. In the circulatory and cardiovascular system, they are subject to deformation owing to varying flow conditions. To withstand wear, the cells feature an elastic discoidal membrane. This structure, constituting a minimum energy configuration [32], and the dynamic remodelling of their spectrin cytoskeleton [33], enables them to pass through thin capillaries and reach tissues. Because changes in the mechanical properties of RBCs are an indicator of disease and can provide an insight into their molecular preservation, nanoindentation measurements were carried out to assess the elasticity of the fixed, ancient corpuscles. A histogram with Young's modulus of the mummy corpuscles (grey) and the reference RBCs (black) is shown in figure 5. By way of illustration, a Lorentzian distribution is additionally fitted. For the fixed mummy samples, a mean Young's modulus of  $2.0 \pm 1.0$  GPa with a distribution maximum of 1.7 GPa was determined. The measurements conducted on fixed, recent RBCs yielded a mean value of  $2.5 \pm 1.2$  GPa, and the distribution maximum was 2.3 GPa. The difference between the mean Young's moduli is statistically significant and was analysed with the independent two-sample Student's *t*-test.

#### 4. DISCUSSION

To study the presence of human RBCs in the tissue of the 5300 year old Iceman, tissue samples extracted from two Iceman wounds were examined. Performing AFM measurements, isolated single corpuscles with the approximate size and shape of normal RBCs were identified in Iceman samples A and B. The corpuscles featured a discoidal and concave shape, which is typical for RBCs, and their morphology did not demonstrate any evidence of degradation, damage or disorder. Moreover, the dimensions of these ancient corpuscles matched those of the similarly prepared reference RBCs. Additionally, a cluster of several randomly agglomerated particles was revealed in sample B. In this sample, all particles greater than approximately 5  $\mu\text{m}$  showed artificial interfaces, which are presumably cutting edges that arose from the preparation of the histological specimens, i.e. slicing of the tissue with a microtome. Apart from these sectioned



Table 2. Raman peak assignment of Iceman sample A.

| whole blood wavenumber (cm <sup>-1</sup> ) | red blood cell wavenumber (cm <sup>-1</sup> ) | Iceman sample A wavenumber (cm <sup>-1</sup> ) | assignment           | mode  | literature |
|--|---|--|----------------------|---|------------|
|  |   | 1665   | amide I              | $\nu(\text{CO})$                              | [30]       |
| 1636                                       | 1639  | 1633   | $\nu_{10}$           | $\nu(\text{C}_\alpha\text{C}_m)_{\text{as}}$  | [25]       |
| 1584                                       | 1586  | 1588   | $\nu_{37}$           | $\nu(\text{C}_\alpha\text{C}_m)_{\text{as}}$  | [26,27]    |
| 1562                                       | 1563  | 1565   | $\nu_2$              | $\nu(\text{C}_\beta\text{C}_\beta)$           | [25,26]    |
| —  | —   | 1512   | $\nu_{38}$           |   | [26]       |
| —  | —   | 1491   | $\nu_3$              | $\nu(\text{C}_\alpha\text{C}_m)_{\text{sym}}$ | [25]       |
| 1468                                       | —   | —  |                      |   |            |
| 1453                                       | 1459  | —  |                      | $\text{CH}_2/\text{CH}_3$                     | [27]       |
| 1434                                       | 1441  | 1446   |                      | $\delta(=\text{C}_b\text{H}_2)_{\text{sym}}$  | [25–27]    |
| 1392                                       | 1395  | 1397   | $\nu_{20}, \nu_{29}$ | $\nu(\text{pyr quarter-ring})$                | [25]       |
| 1361                                       | 1362  | 1360   |                      |   |            |
| 1338                                       | 1340  | 1343   | $\nu_{41}$           | $\nu(\text{pyr half-ring})_{\text{sym}}$      | [25–27]    |
|  |   |  |                      | $\delta(=\text{C}_b\text{H}_2)_{\text{sym}}$  |            |
| 1308                                       | 1312  | 1314   | $\nu_{21}$           | $\delta(\text{C}_m\text{H})$                  | [25,27]    |
| 1274                                       | 1275  | 1279   |                      |   |            |
| —  | —   | 1248   | amide III            | $\nu(\text{CN})$                              | [29,31]    |
| 1225                                       | 1229  | 1233   |                      | prop $\delta(\text{CH}_2)$ twisting           | [25]       |
| 1170                                       | 1166  | —  | $\nu_{30}$           | $\nu(\text{pyr half-ring})_{\text{as}}$       | [25,26]    |
| —  | —   | 1157   |                      |   |            |
| 1150                                       | —   | —  | $\nu_{14}$           | $\nu(\text{C}_\beta\text{C}_1)_{\text{sym}}$  | [25,26]    |
| 1129                                       | 1129  | 1129   |                      |   |            |
| 1083                                       | 1079  | —  |                      | $\delta(=\text{C}_b\text{H}_2)_{\text{as}}$   | [25]       |
| —  | —   | 1063   |                      |   |            |
| 991  | 997   | 1002   | $\nu_{45}$           | $\nu(\text{C}_\beta\text{C}_1)_{\text{as}}$   | [28]       |
| —  | —   | 973  |                      | $\nu(\text{C}_c-\text{C}_d)$                  | [25]       |
| 924  | —   | 926  |                      | $\gamma(=\text{C}_b\text{H}_2)_{\text{sym}}$  | [26]       |
| —  | 896   | 901  |                      |   |            |
| —  | —   | 823  | $\gamma_{10}$        | $\gamma(\text{C}_m\text{H})$                  | [28]       |
| 747  | 746   | 747  | $\nu_{15}$           | $\nu(\text{pyr breathing})$                   | [25,26]    |

areas, the particles showed typical RBC morphology. These first results indicate that RBCs have been preserved for more than 5000 years in the wound tissue of the mummy.

To further confirm the presence of RBCs, Raman spectra were taken from the Iceman samples and compared with reference whole blood and reference RBC spectra. The stretching vibration modes  $\nu_{37}$ ,  $\nu_{20}/\nu_{29}$ ,  $\nu_{21}$  and  $\nu_{15}$ , which are characteristic of haemoglobin [25–27], dominated the spectrum of the corpuscle in Iceman sample A. This suggested that the ancient particle is a RBC. However, the scattering intensity of the ancient spectrum was approximately an order of magnitude weaker than that of the recent blood samples. The intensity  $I$  of a Raman band depends on

$$I \propto N I_0 f^4 \left( \frac{\partial \alpha}{\partial q} \right)^2, \quad (4.1)$$

where  $N$  is the number of scattering molecules within a sample,  $I_0$  is the intensity of the excitation laser,  $\partial \alpha / \partial q$  is the change in polarizability of the exited molecules and  $f$  is the frequency of the excitation laser. Because the intensity and the frequency of the laser were kept constant during the measurements, and because the bands in the ancient particle spectrum can be clearly assigned to molecule vibrations with defined polarizability, the change in the scattering intensity was most probably caused by the reduced number of

scattering molecules within the ancient particle. This fact indicates decomposition of the Iceman RBC, in association with the degradation of the majority of the RBC-specific haem compounds and hence the reduction in scattering molecules. RBC degradation is mainly caused by the action of reactive oxygen species (ROS) such as superoxide  $\text{O}_2^-$  radicals that are released during the autoxidation of oxygen-loaded haemoglobin (oxyHb) [34]. During the dismutation of superoxide, hydrogen peroxide ( $\text{H}_2\text{O}_2$ ) can also be generated [35]. Both ROS cause oxidative stress within the RBC, which eventually leads to the decomposition of proteins due to fragmentation of their peptide chains. The effectiveness of ROS is governed by the oxyHb autoxidation rate of approximately 0.5–3% per day [35,36] and the vast amount of molecular oxygen that can be bound within a single RBC. Besides the action of ROS, damage of the RBC can also be induced by freezing and thawing, as observed in cryopreservation procedures. Thereby RBC injury can be attributed to events such as intracellular and extracellular ice formation, excessive cell shrinkage, osmotic stress or dehydration [37]. Such mechanisms affect the RBC on the macroscopic scale but have less influence on the microscopic scale, i.e. the protein content and the molecular composition.

The ancient RBC spectrum also showed bands at 1665, 1446, 1248 and 1002  $\text{cm}^{-1}$ . These were assigned to the amide I band typical for proteins, the

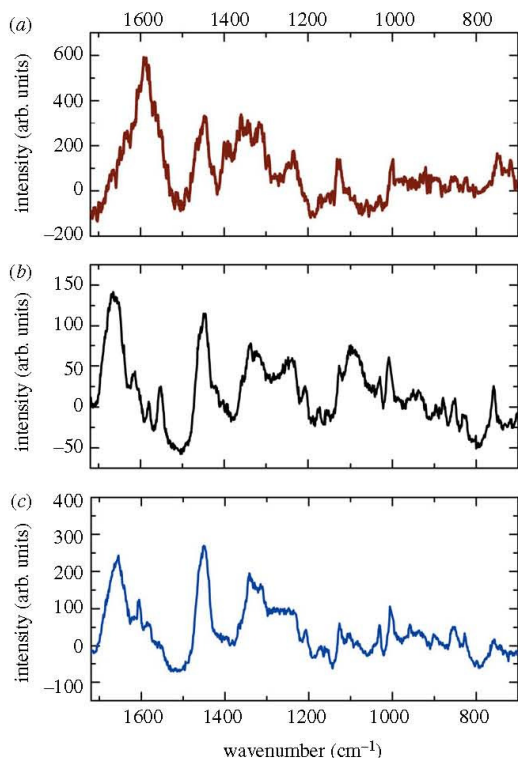


Figure 3. Raman spectra of the corpuscle in Iceman sample A (a), a fibrin meshwork (b), and the corpuscles found in the Iceman tissue sample B (c). The spectrum obtained from sample B strongly differs from that of sample A. It has features with considerable similarities to the spectrum of fibrin.

deformation vibration of methyl  $\delta(\text{CH}_3)$  and methylene  $\delta(\text{CH}_2)$ , the amide III band that represents peptide bonds and the vibration mode of phenylalanine. All these bands are common in proteins such as collagen or fibrin [30,31,38,39], and the amide III band is also occasionally observed in the spectra of air-dried RBCs and met-RBCs, as discussed by Asghari-Khiavi *et al.* [25]. Compared with reference protein spectra and those of the particle found in Iceman sample B (figure 3), the protein band at  $1665\text{ cm}^{-1}$  is very faint in the ancient RBC spectrum, whereas the other protein bands are more pronounced. Thus, the Raman spectrum of Iceman sample A is a complex composition of haemoglobin and other protein spectra.

In summary, the altered spectral signature and intensity in comparison with data of recent RBCs were most probably caused by a modification of the haemoglobin and, consequently, the porphyrin. The proteinaceous compounds may have been less strongly affected. Some molecule vibrations could have also been impaired by the effect of blood clotting and the formation of proteins such as fibrin.

Changes in molecular structure owing to protein compounds are even more evident in the corpuscle from Iceman sample B. Although the corpuscle morphology

resembles the structure of regular RBCs, the Raman spectra significantly differed from the reference RBC spectra. The corpuscles mostly lacked the previously mentioned porphyrin modes and predominantly showed bands characteristic of fibrin or other proteins such as collagen (see the electronic supplementary material). Fibrin is the end product of a complex cascade of coagulation reactions that are initiated at the moment of vascular injury. In the first step, platelets become activated and then become adherent to the damaged vessel wall. They form a primary haemostatic plug. Meanwhile, the enzyme thrombin is produced. Thrombin then cleaves fibrinogen and catalyses the polymerization of fibrin, which subsequently generates a meshwork around the platelet plug and reinforces it [20,40]. The Raman spectra and AFM images thus indicate that the single particles and the agglomerate of corpuscles in the tissue of sample B are the remnants of a haemostatic plug that formed around the Iceman's arrowhead wound. Nonetheless, it is surprising that, although the Raman spectra of the Iceman's RBCs are dominated by bands characteristic for fibrin, neither a meshwork nor single fibrin fibrils were detected in our AFM images. We therefore infer that the fibrin surrounding the haemostatic clot decomposed over time, leaving behind only RBCs and possibly some fibrin fragments.

Although our results show more complex RBC spectra, they are in agreement with measurements on recent dried human blood spots conducted by Virkler *et al.* [41], who showed that dried whole blood is chemically heterogeneous, and its Raman spectrum could be a linear combination composed mainly of the two Raman active components: haemoglobin and fibrin. The clotting process that occurs while blood dries explains the spectral combination. One hypothesis was that fibrin was formed during the clotting, and that it was therefore found in a large concentration in the dried blood spots.

Finally, when analysing the Raman spectra of the pre-processed tissue, the effect of the sample preparation must be taken into account. The ancient and the recent RBC samples were processed into histological sections, i.e. the tissue was fixed with formaldehyde, embedded into paraffin and cut with a microtome. The paraffin was then dissolved with xylene, and the sample was subsequently rehydrated in a descending alcohol series. The dehydration effects of alcohol were found to cause degradation of RBCs because it weakens the membrane–water interactions of the cell membrane [42]. This can lead to the loss of some cellular components and can therefore cause changes in the Raman spectra. Dehydration and the effect of fixatives, such as formaldehyde and glutaraldehyde, on RBC Raman spectra were also reported by Asghari-Khiavi *et al.* [25]. In their study, they showed that the Raman spectra of RBCs, which were fixed in a formaldehyde–glutaraldehyde mixture and embedded into paraffin, were very similar to the spectra of air-dried RBCs. This indicates that the processing of dried RBCs into histological tissue sections does not cause additional alterations of the RBC Raman spectra. Furthermore, because the reference RBCs and Iceman samples were processed equally, preparation-induced

Table 3. Raman peaks assigned for Iceman sample B.

| RBC wavenumber (cm <sup>-1</sup> ) | fibrin wavenumber (cm <sup>-1</sup> ) | Iceman sample B wavenumber (cm <sup>-1</sup> ) | assignment           | mode   | literature |
|------------------------------------|---------------------------------------|--|----------------------|--|------------|
| 1639                               | 1666                                  | 1656   | amide I              | $\nu(\text{CO})$   | [30]       |
| —                                  | 1617                                  | 1605   | $\nu_{10}$           | $\nu(\text{C}_\alpha\text{C}_m)_{as}$                          | [25]       |
| 1586                               | 1581                                  | 1583   | $\nu_{37}$           | $\nu(\text{C}=\text{C})$ Phe, Tyr                              | [29,30]    |
| 1563                               | 1447                                  | 1449   | $\nu_2$              | $\nu(\text{C}_\alpha\text{C}_m)_{as}$                          | [26,27]    |
| 1441                               | 1402                                  | 1399   |                      | $\nu(\text{CCH})$ Pro, Hypro                                   | [29]       |
| 1395                               | 1339                                  | 1340   |                      | $\nu(\text{C}_\beta\text{C}_\beta)$                            | [25,26]    |
| 1340                               | 1252                                  | 1248   | $\nu_{20}, \nu_{29}$ | $\delta(\text{CH}_3, \text{CH}_2)$                             | [29]       |
| 1312                               | 1208                                  | 1208   | $\nu_{41}$           | $\delta(\text{CH}_2)$  | [31]       |
| —                                  | 1174                                  | 1173   |                      | $\nu(\text{pyr quarter-ring})$                                 | [25]       |
| 1229                               | 1156                                  | 1157   |                      | $\nu(\text{pyr half-ring})_{sym}$                              | [25–27]    |
| 1166                               | 1125                                  | 1125   | $\nu_{21}$           | $\delta(=\text{C}_b\text{H}_2)_{sym}$                          | [25,27,31] |
| —                                  | 1101                                  | 1102   | amide III            | $\nu(\text{CN})$   | [29,31]    |
| 1129                               | 1075                                  | 1084   |                      | prop $\delta(\text{CH}_2)$ twisting                            | [25]       |
| —                                  | 1031                                  | 1032   |                      | $\omega(\text{CH}_2)$  | [31]       |
| 1079                               | 1004                                  | 1002   | $\nu_{30}$           | C–H bend Tyr   | [30]       |
| —                                  | 956                                   | 957  |                      | $\nu(\text{pyr half-ring})_{as}$                               | [25,26]    |
| —                                  | 937                                   | 898  |                      | C–C/C–N str  | [30]       |
| 896                                | 896                                   | 898  |                      | C–N str  | [30]       |
| —                                  | 854                                   | 855  |                      | $\delta(=\text{C}_b\text{H}_2)_{as}$                           | [25]       |
| —                                  | 829                                   | 827  |                      | C–H in-plane Phe   | [30]       |
| 997                                | 758                                   | 758  | $\nu_{45}$           | $\nu(\text{C}_\beta\text{C}_1)_{as}, \nu(\text{CC})$           | [28,30,31] |
| —                                  | —                                     | —  |                      | aromatic ring Phe  |            |
| —                                  | —                                     | —  |                      | $\nu(\text{Cc}–\text{Cd})$                                     | [25]       |
| —                                  | —                                     | —  |                      | $\gamma(=\text{C}_b\text{H}_2)_{sym}$                          | [26]       |
| —                                  | —                                     | —  | $\gamma_{10}$        | $\gamma(\text{C}_m\text{H}), \nu(\text{CC})$ aromatic ring Tyr | [28,30]    |
| —                                  | —                                     | —  |                      | $\nu(\text{CC})$ aromatic ring Tyr                             | [30]       |
| —                                  | —                                     | —  |                      | aromatic ring breath   | [30]       |
| 746                                | —                                     | —  | $\nu_{15}$           | $\nu(\text{pyr breathing})$                                    | [25,26]    |

differences are rather unlikely. Therefore, we conclude that the processing of the tissue had little influence on the comparative spectroscopic examination.

Deformation and failure phenomena of hierarchical protein materials are observed in physiologically extreme conditions and in the progression of disease [43]. The structural proteins and thus the shape, molecular structure and the elasticity of RBCs are also prone to disease-specific alterations [44]. Reduced mechanical deformability, together with increased RBC membrane stiffness, are reported in infection with the malaria parasite [45–47]. A similar phenotype appears in blood disorders such as sickle-cell disease, hereditary elliptocytosis or hereditary spherocytosis, in which the deformability of the RBC membrane is reduced and the cell shape is strongly altered [47–49]. Owing to the pre-processing of the tissue samples, however, we cannot draw conclusions on any disease-specific mechanical changes of the RBCs. Nevertheless, a relative comparison between equally processed recent and mummy RBCs helps us to assess the degree of tissue preservation. AFM nanoindentation measurements revealed changes in the mechanical behaviour of the RBCs. Young’s modulus of the ancient RBCs in sample

B was  $2.0 \pm 1.0$  GPa, whereas the modulus of the equally processed recent RBCs averaged  $2.5 \pm 1.2$  GPa.

Cross-linking owing to fixation with formaldehyde [50], age [51] or disease-specific influences would lead to an increased membrane stiffness of RBCs and, thus, to an increase in Young’s modulus. Our measurements on ancient RBCs, however, show a decrease in Young’s modulus associated with a lower stiffness of the ancient RBCs. Together with the reduced Raman scattering intensity, the softening indicates a degradation of the RBCs. Possible degradation processes include scaffold damage due to crystallization of ice during freezing, irradiation with UV light or wound healing-specific transformation processes that occur during the stages of blood clot degradation [52].

The fragmentation of the RBC cytoskeleton proteins such as the spectrin and actin filaments will cause a destabilization of the cell membrane. In addition to the aforementioned mechanisms, cleavage of membrane proteins and degradation of the cytoskeleton by the fragmentation of their protein peptide chains can also be induced by the action of ROS. The various degradation processes would ultimately lead to the softening of the RBC membrane.

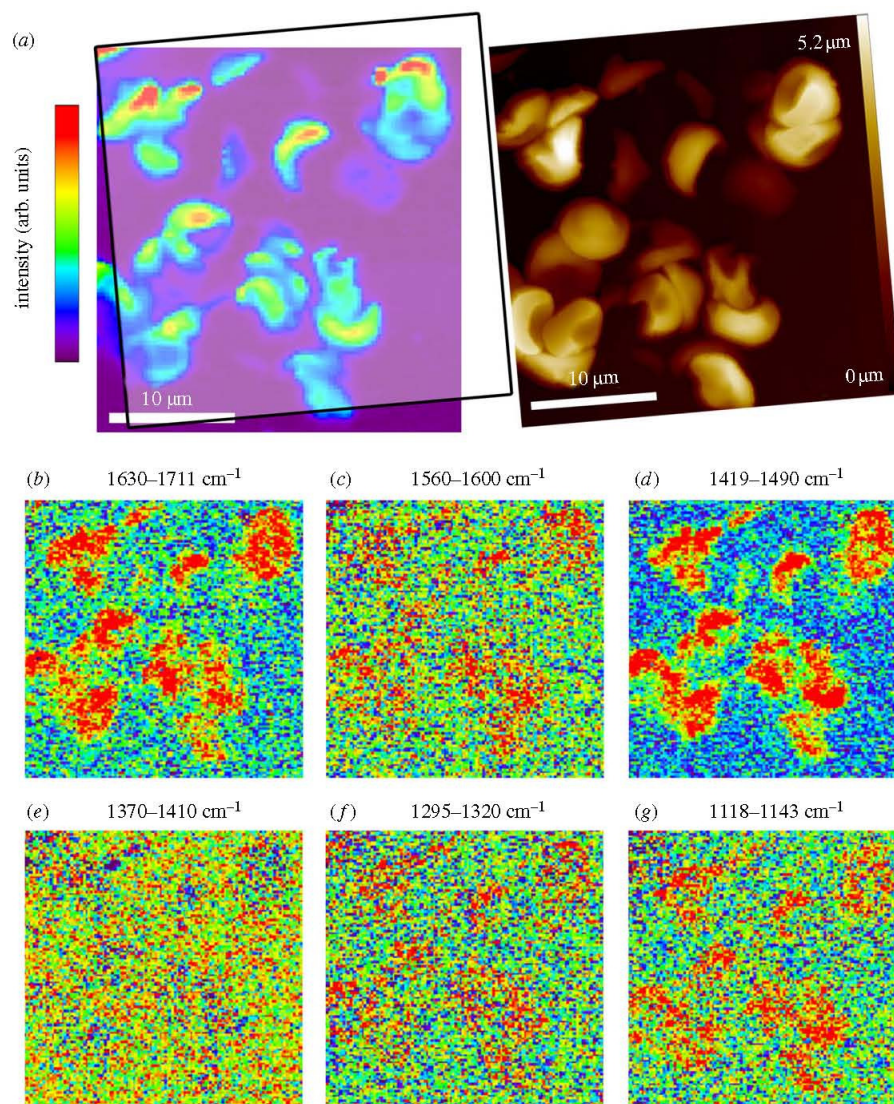


Figure 4. Raman scan and AFM image ( $30 \times 30 \mu\text{m}$ ) of the agglomerated corpuscle in Iceman sample B. The scan in (a) represents the intensity distribution of the Rayleigh scattered light. For comparison the corresponding AFM topography image is shown. (b–g) The datasets of the Raman scan filtered for porphyrin or protein-specific Raman bands around 1656, 1586, 1449, 1395, 1308 and 1125  $\text{cm}^{-1}$  wavenumbers. Red indicates regions with strong Raman intensity, and blue indicates low Raman intensities. The examined molecule vibrations largely occurred at the positions of the ancient particles.

The elasticity values determined are given for fixed recent and ancient RBCs, which were prepared following the same protocol. Obviously, the preparation comprises the mechanical properties of a tissue by the formation of methylene bridges that cross-link polypeptide chains. Thus, no conclusions on health status can be drawn from the elasticity measurements. However, comparing the elasticity values of both specimens, it is clear that the ancient samples were softer. This is in line with the observation that less Raman scattering occurred in the ancient RBCs. Both effects can be explained by a degradation of the proteinaceous content of the RBCs.

In summary, the morphology and the Raman fingerprint of some corpuscles point to remnants of a haemostatic clot. This observation confirms that the Iceman sustained several RBC injuries before his death. AFM imaging revealed RBCs with normal morphology. Blood disorders caused by RBC membrane defects, such as sickle-cell disease, elliptocytosis or spherocytosis, can thus be excluded. Nanoindentation measurements show that the elasticity of the ancient RBCs is slightly reduced, which suggests that they suffered from degradation. Complementary Raman spectroscopy also indicates a degradation of the blood cells. Nevertheless,

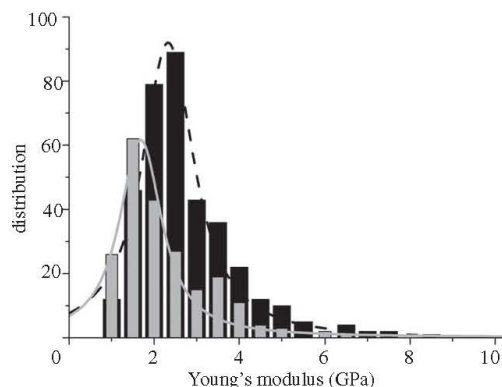


Figure 5. The distribution of Young's moduli from the corpuscle of Iceman sample B and contemporary single RBCs. Young's modulus for the mummy particles (grey) is significantly lower than Young's modulus for the recent RBCs (black).

our examinations show an unambiguous identification of RBCs in a 5300 year old mummy.

We gratefully acknowledge the Deutsche Forschungsgemeinschaft (DFG) clusters of excellence Nanosystems Initiative Munich, the Stiftung Südtiroler Sparkasse and the Center of Smart Interfaces Darmstadt for financial support.

## REFERENCES

- Hawass, Z. et al. 2010 Ancestry and pathology in King Tutankhamun's family. *JAMA* **303**, 638–647. (doi:10.1001/jama.2010.121)
- Keller, A. et al. 2012 New insights into the Tyrolean Iceman's origin and phenotype as inferred by whole-genome sequencing. *Nat. Commun.* **3**, 698. (doi:10.1038/ncomms1701)
- Lynnerup, N. 2007 Mummies. *Am. J. Phys. Anthropol.* **134**(Suppl. 45), 162–190. (doi:10.1002/ajpa.20728)
- Nerlich, A. G., Haas, C. J., Zink, A., Szeimies, U. & Hagedorn, H. G. 1997 Molecular evidence for tuberculosis in an ancient Egyptian mummy. *Lancet* **350**, 1404. (doi:10.1016/S0140-6736(05)65185-9)
- Zink, A., Haas, C. J., Reischl, U., Szeimies, U. & Nerlich, A. G. 2001 Molecular analysis of skeletal tuberculosis in an ancient Egyptian population. *J. Med. Microbiol.* **50**, 355–366.
- Zimmerman, M. R. 1973 Blood cells preserved in a mummy 2000 years old. *Science* **180**, 303–304. (doi:10.1126/science.180.4083.303)
- Riddle, J. M., Ho, K. L., Chason, J. L. & Schwyn, R. C. 1976 Peripheral blood elements found in an Egyptian mummy: a three-dimensional view. *Science* **192**, 374–375. (doi:10.1126/science.1257771)
- Lewin, P. K. 1967 Palaeo-electron microscopy of mummified tissue. *Nature* **213**, 416–417. (doi:10.1038/213416a0)
- Gerszten, P. C., Gerszten, E. & Allison, M. J. 1997 Ultrastructure of a well-preserved lymphocyte from a mummified human. *J. Electron. Microsc. (Tokyo)* **46**, 443–445.
- Shin, D. H., Youn, M. & Chang, B. S. 2003 Histological analysis on the medieval mummy in Korea. *Forensic Sci. Int.* **137**, 172–182. (doi:10.1016/S0379-0738(03)00335-9)
- Seidler, H., Bernhard, W., Teschler-Nicola, M., Platzer, W., zur Nedden, D., Henn, R., Oberhauser, A. & Sjøvold, T. 1992 Some anthropological aspects of the prehistoric Tyrolean ice man. *Science* **258**, 455–457. (doi:10.1126/science.1411539)
- Eijgenraam, F. & Anderson, A. 1991 A window on life in the Bronze Age. The remains of a 4000-year-old man may shed light on the racial structure and culture of early Europe. *Science* **254**, 187–188. (doi:10.1126/science.1925570)
- Hess, M. W., Klima, G., Pfaller, K., Kunzel, K. H. & Gaber, O. 1998 Histological investigations on the Tyrolean Ice Man. *Am. J. Phys. Anthropol.* **106**, 521–532. (doi:10.1002/(SICI)1096-8644(199808)106:4<521::AID-AJPA7>3.0.CO;2-L)
- Janko, M., Zink, A., Gigler, A. M., Heckl, W. M. & Stark, R. W. 2010 Nanostructure and mechanics of mummified type I collagen from the 5300-year-old Tyrolean Iceman. *Proc. R. Soc. B* **277**, 2301–2309. (doi:10.1098/rspb.2010.0377)
- Gostner, P. & Vigl, E. E. 2002 INSIGHT: report of radiological-forensic findings on the Iceman. *J. Archaeol. Sci.* **29**, 323–326. (doi:10.1006/jasc.2002.0824)
- Murphy Jr, W. A., Nedden Dz, D., Gostner, P., Knapp, R., Recheis, W. & Seidler, H. 2003 The iceman: discovery and imaging. *Radiology* **226**, 614–629. (doi:10.1148/radiol.2263020338)
- Pernter, P., Gostner, P., Vigl, E. E. & Rühli, F. J. 2007 Radiologic proof for the Iceman's cause of death (ca. 5'300 BP). *J. Archaeol. Sci.* **34**, 1784–1786. (doi:10.1016/j.jas.2006.12.019)
- Nerlich, A. G., Bachmeier, B., Zink, A., Thalhammer, S. & Egarter-Vigl, E. 2003 Otzi had a wound on his right hand. *Lancet* **362**, 334. (doi:10.1016/S0140-6736(03)13992-X)
- Nerlich, A. G., Peschel, O. & Egarter-Vigl, E. 2009 New evidence for Otzi's final trauma. *Intensive Care Med.* **35**, 1138–1139. (doi:10.1007/s00134-009-1409-4)
- Riedel, T., Brynda, E., Dyr, J. E. & Houska, M. 2009 Controlled preparation of thin fibrin films immobilized at solid surfaces. *J. Biomed. Mater. Res. A* **88A**, 437–447. (doi:10.1002/jbma.a.31755)
- Hertz, H. 1881 Ueber die Berührung fester elastischer Körper. *J. Reine angewandte Mathematik* **92**, 156–171.
- Sneddon, I. N. 1965 The relation between load and penetration in the axisymmetric Boussinesq problem for a punch of arbitrary profile. *Int. J. Eng. Sci.* **3**, 47–57. (doi:10.1016/0020-7225(65)90019-4)
- Heuberger, M., Dietler, G. & Schlapbach, L. 1996 Elastic deformations of tip and sample during atomic force microscope measurements. *J. Vac. Sci. Technol. B Microelectron. Nanometer Struct.* **14**, 1250–1254. (doi:10.1116/1.588525)
- O'Reilly, M., McDonnell, L. & O'Mullane, J. 2001 Quantification of red blood cells using atomic force microscopy. *Ultramicroscopy* **86**, 107–112. (doi:10.1016/S0304-3991(00)00081-4)
- Asghari-Khiavi, M., Mechler, A., Bamberg, K. R., McNaughton, D. & Wood, B. R. 2009 A resonance Raman spectroscopic investigation into the effects of fixation and dehydration on heme environment of hemoglobin. *J. Raman Spectrosc.* **40**, 1668–1674. (doi:10.1002/jrs.2317)
- Hu, S., Smith, K. M. & Spiro, T. G. 1996 Assignment of protoheme resonance Raman spectrum by heme labeling in myoglobin. *J. Am. Chem. Soc.* **118**, 12638–12646. (doi:10.1021/ja962239e)
- Salmaso, B. L., Puppels, G. J., Caspers, P. J., Floris, R., Wever, R. & Greve, J. 1994 Resonance Raman microspectroscopic characterization of eosinophil peroxidase

- in human eosinophilic granulocytes. *Biophys. J.* **67**, 436–446. (doi:10.1016/S0006-3495(94)80499-0)
- 28 Wood, B. R., Caspers, P., Puppels, G. J., Pandiancherri, S. & McNaughton, D. 2007 Resonance Raman spectroscopy of red blood cells using near-infrared laser excitation. *Anal. Bioanal. Chem.* **387**, 1691–1703. (doi:10.1007/s00216-006-0881-8)
- 29 Frushour, B. G. & Koenig, J. L. 1975 Raman scattering of collagen, gelatin, and elastin. *Biopolymers* **14**, 379–391. (doi:10.1002/bip.1975.360140211)
- 30 Nottingher, I. & Hench, L. L. 2006 Raman microspectroscopy: a noninvasive tool for studies of individual living cells *in vitro*. *Expert Rev. Med. Devices* **3**, 215–234. (doi:10.1586/17434440.3.2.215)
- 31 Edwards, H. G., Farwell, D. W., Holder, J. M. & Lawson, E. E. 1997 Fourier-transform Raman spectra of ivory. III. Identification of mammalian specimens. *Spectrochim. Acta A Mol. Biomol. Spectrosc.* **53A**, 2403–2409. (doi:10.1016/S1386-1425(97)00180-7)
- 32 Li, J., Dao, M., Lim, C. T. & Suresh, S. 2005 Spectrin-level modeling of the cytoskeleton and optical tweezers stretching of the erythrocyte. *Biophys. J.* **88**, 3707–3719. (doi:10.1529/biophysj.104.047332)
- 33 Li, J., Lykotraftis, G., Dao, M. & Suresh, S. 2007 Cytoskeletal dynamics of human erythrocyte. *Proc. Natl Acad. Sci. USA* **104**, 4937–4942. (doi:10.1073/pnas.0700257104)
- 34 Misra, H. P. & Fridovich, I. 1972 The generation of superoxide radical during the autoxidation of hemoglobin. *J. Biol. Chem.* **247**, 6960–6962.
- 35 Kaniyas, T. & Acker, J. P. 2010 Biopreservation of red blood cells—the struggle with hemoglobin oxidation. *FEBS J.* **277**, 343–356. (doi:10.1111/j.1742-4658.2009.07472.x)
- 36 Umbreit, J. 2007 Methemoglobin—It's not just blue: a concise review. *Am. J. Hematol.* **82**, 134–144. (doi:10.1002/ajh.20738)
- 37 Scott, K. L., Lecak, J. & Acker, J. P. 2005 Biopreservation of red blood cells: past, present, and future. *Transfus. Med. Rev.* **19**, 127–142. (doi:10.1016/j.tmr.2004.11.004)
- 38 Gniadecka, M., Nielsen, O. F., Christensen, D. H. & Wulf, H. C. 1998 Structure of water, proteins, and lipids in intact human skin, hair, and nail. *J. Invest. Dermatol.* **110**, 393–398. (doi:10.1046/j.1523-1747.1998.00146.x)
- 39 Marx, J., Hudry-Clergeon, G., Capet-Antonini, F. & Bernard, L. 1979 Laser Raman spectroscopy study of bovine fibrinogen and fibrin. *Biochim. Biophys. Acta* **578**, 107–115.
- 40 Wolberg, A. S. 2007 Thrombin generation and fibrin clot structure. *Blood Rev.* **21**, 131–142. (doi:10.1016/j.blr.2006.11.001)
- 41 Virkler, K. & Lednev, I. K. 2010 Raman spectroscopic signature of blood and its potential application to forensic body fluid identification. *Anal. Bioanal. Chem.* **396**, 525–534. (doi:10.1007/s00216-009-3207-9)
- 42 Deng, J. L., Wei, Q., Zhang, M. H., Wang, Y. Z. & Li, Y. Q. 2005 Study of the effect of alcohol on single human red blood cells using near-infrared laser tweezers Raman spectroscopy. *J. Raman Spectrosc.* **36**, 257–261. (doi:10.1002/jrs.1301)
- 43 Buehler, M. & Yung, Y. 2009 Deformation and failure of protein materials in physiologically extreme conditions and disease. *Nat. Mater.* **8**, 175–188. (doi:10.1038/nmat2387)
- 44 Diez-Silva, M., Dao, M., Han, J., Lim, C. T. & Suresh, S. 2010 Shape and biomechanical characteristics of human red blood cells in health and disease. *MRS Bull.* **35**, 382–388. (doi:10.1557/mrs2010.571)
- 45 Glenister, F. K., Coppel, R. L., Cowman, A. F., Mohandas, N. & Cooke, B. M. 2002 Contribution of parasite proteins to altered mechanical properties of malaria-infected red blood cells. *Blood* **99**, 1060–1063. (doi:10.1182/blood.V99.3.1060)
- 46 Miller, L. H., Baruch, D. I., Marsh, K. & Doumbo, O. K. 2002 The pathogenic basis of malaria. *Nature* **415**, 673–679. (doi:10.1038/415673a)
- 47 Suresh, S. 2006 Mechanical response of human red blood cells in health and disease: some structure–property–function relationships. *J. Mater. Res.* **21**, 1871–1877. (doi:10.1557/jmr.2006.0260)
- 48 Messmann, R., Gannon, S., Sarnaik, S. & Johnson, R. M. 1990 Mechanical properties of sickle cell membranes. *Blood* **75**, 1711–1717.
- 49 Brandao, M. M., Fontes, A., Barjas-Castro, M. L., Barbosa, L. C., Costa, F. F., Cesar, C. L. & Saad, S. T. 2003 Optical tweezers for measuring red blood cell elasticity: application to the study of drug response in sickle cell disease. *Eur. J. Haematol.* **70**, 207–211. (doi:10.1034/j.1600-0609.2003.00027.x)
- 50 Puchtler, H. & Meloan, S. N. 1985 On the chemistry of formaldehyde fixation and its effects on immunohistochemical reactions. *Histochem. Cell Biol.* **82**, 201–204. (doi:10.1007/BF00501395)
- 51 Strasser, S., Zink, A., Kada, G., Hinterdorfer, P., Peschel, O., Heckl, W. M., Nerlich, A. G. & Thalhammer, S. 2007 Age determination of blood spots in forensic medicine by force spectroscopy. *Forensic Sci. Int.* **170**, 8–14. (doi:10.1016/j.forsciint.2006.08.023)
- 52 Clark, R. A. F. 2001 Fibrin and wound healing. *Ann. N. Y. Acad. Sci.* **936**, 355–367. (doi:10.1111/j.1749-6632.2001.tb03522.x)

## 8.4 BLOOD PLATELET ADHESION TO PRINTED VON WILLEBRAND FACTOR



### Blood platelet adhesion to printed von Willebrand factor

Polina Davydovskaya,<sup>1</sup> Marek Janko,<sup>1,2,3</sup> Florian Gaertner,<sup>4</sup> Zerkah Ahmad,<sup>4</sup> Özlem Simsek,<sup>1</sup> Steffen Maßberg,<sup>4</sup> Robert W. Stark<sup>2,3,5</sup>

<sup>1</sup>Department of Earth and Environmental Sciences, Ludwig-Maximilians-Universität München, Theresienstraße 41, 80333 Munich, Germany

<sup>2</sup>Center for NanoSciences, Ludwig-Maximilians-Universität München, Schellingstraße 4, 80799 Munich, Germany

<sup>3</sup>Center of Smart Interfaces, Technische Universität Darmstadt, Petersenstraße 32, 64287 Darmstadt, Germany

<sup>4</sup>Deutsches Herzzentrum München, Technische Universität München, Lazarettstrasse 60, 80636 Munich, Germany

<sup>5</sup>Material- und Geowissenschaften, Technische Universität Darmstadt, Petersenstraße 32, 64287 Darmstadt, Germany

Received 15 June 2011; revised 12 September 2011; accepted 12 September 2011

Published online in Wiley Online Library (wileyonlinelibrary.com). DOI: 10.1002/jbm.a.33275

**Abstract:** Von Willebrand factor (vWF), a glycoprotein in blood, mediates the adhesion of blood platelets and thus plays a crucial role in hemostasis and thrombosis. Functional coating of surfaces with vWF allows the investigation of *in vitro* adhesion of blood platelet. We used soft lithography to create a functional patterned substrate. vWF was printed on plasma-treated glass and mica surfaces, producing elongated network-like fibril structures. A minimum layer thickness of 3 nm was observed, corresponding to the height of a monolayer of vWF. The stability of the patterns was verified

in a laminar fluid flow, and the bioactivity of the structures was tested with platelet adhesion experiments. Platelets adhered to and spread on printed vWF. These results indicate that printed vWF substrates are stable and functional in typical perfusion experiments, and thus provide a useful tool for studying thrombus formation *in vitro*. © 2011 Wiley Periodicals, Inc. *J Biomed Mater Res Part A*: 00A: 000–000, 2011.

**Key Words:** von Willebrand factor, atomic force microscope, micro contact printing, blood platelet adhesion, lab on a chip

**How to cite this article:** Davydovskaya P, Janko M, Gaertner F, Ahmad Z, Simsek Ö, Maßberg S, Stark RW. 2011. Blood platelet adhesion to printed von Willebrand factor. *J Biomed Mater Res Part A* 2011;00A:000–000.

#### INTRODUCTION

Surfaces that are functionalized with blood proteins allow investigation into the complex processes that lead to thrombosis *in vitro*. One of the most important blood plasma proteins in hemostasis and thrombosis is von Willebrand Factor (vWF), a large glycoprotein consisting of several subunits, which is produced in the Weibel-Palade bodies of the endothelium, in subendothelial connective tissue, and in mature megakaryocytes.<sup>1</sup> This factor occurs in two shear rate dependent conformations. Below a critical shear rate of 5000 s<sup>-1</sup>, vWF takes on a globular shape.<sup>2</sup> At higher shear rates, vWF changes in conformation to an extended fibrous structure.<sup>3</sup> In this stretched conformation, vWF promotes the adhesion and aggregation of blood platelets.<sup>4,5</sup> To study thrombus formation *in vitro*, it is thus essential to pattern surfaces with vWF in a conformation that is accessible to blood platelets. Soft lithographic methods show great promise for producing the well-defined patterns required for such applications.

Microcontact printing in particular is a cost-effective and time-saving method,<sup>6,7</sup> which is widely used because it makes patterns with feature sizes anywhere between tens

of micrometers and a few nanometers feasible.<sup>8</sup> Various proteins can be printed, creating biofunctional patterns<sup>9</sup> without loss of those proteins' biological activity.<sup>10</sup>

To study cell adhesion, small length scale biofunctionalized structures are needed. To this end, various protein surface patterning approaches have been established over the years.<sup>11,12</sup> Polylysine layers have been fabricated on both glass and polyethylene glycol surfaces.<sup>13,14</sup> Bernard et al.<sup>12</sup> fabricated polyclonal chicken IgG monolayers on silicon wafers. Schmalenberg et al. printed laminin on polymethylmethacrylate (PMMA) surfaces.<sup>15</sup> Basabe-Desmonts et al. patterned surfaces with vWF to study platelet function using a lab-on-a-chip device for platelet cytometry.<sup>16</sup> However, the functionality and quality of microcontact printed vWF structures, as well as their stability in microfluidic applications, need to be verified.

In this study, we show that microcontact printing is suitable for functionalizing surfaces with the blood protein vWF. Atomic force microscopy (AFM) reveals that it is possible to create monolayers of the protein, and perfusion tests show that their adhesion to the surface is sufficient for microfluidic applications. Platelet adhesion experiments in static assays confirm the biofunctionality of the vWF

Additional Supporting Information may be found in the online version of this article.

**Correspondence to:** R. W. Stark; e-mail: stark@csi.tu-darmstadt.de

Contract grant sponsors: Clusters of Excellence Center of Smart Interfaces Darmstadt; Nanosystems Initiative Munich, NIM

structures. Using these patterned structures, the activation state of platelets on distinct surfaces can be determined.

## MATERIALS AND METHODS

### Protein

Von Willebrand factor (lyophilized powder) from human plasma was purchased from Calbiochem (Cat no. 681300, Lot no. D0001309) and diluted in phosphate-buffered saline (PBS) to a concentration of 0.01 mg/mL, which corresponds to the concentration found in blood.<sup>2,4</sup> The protein solution was stored in a freezer at  $-18^{\circ}\text{C}$  prior to use.

### Substrates

vWF was printed on mica and standard glass slides. The mica was cleaved and used immediately without further treatment. Prior to printing, the glass slides (Menzel, Braunschweig, Germany; chemical composition see Ref. 17) were rinsed with acetone, isopropanol, and ultra pure water and dried with nitrogen. The slides were then treated with oxygen plasma for 1 min at 50 W and 0.4 mbar (Femto Standard, Diener, Ebhausen, Germany) to improve the wettability.

### Atomic force microscopy

The printed structures were characterized with an AFM. The AFM measurements were carried out on a Dimension 3100 AFM with a Nanoscope IV controller (Bruker, Santa-Barbara, CA) in ambient conditions. The measurements were performed in tapping mode, to minimize abrasion of the molecule layer by the AFM tip. Silicon cantilevers (NSC 35 AIBS C, Mikromasch, Estonia) with a nominal resonance frequency of 150 kHz, spring constant of  $4.5\text{ N m}^{-1}$ , and tip diameter of less than 10 nm were used. All images were taken at a resolution of  $512 \times 512\text{ pixel}^2$ . Image analysis was performed with SPIP 4.7.2.0 software (Image Metrology, Denmark). A plane correction procedure was used to compensate for the sample tilt. Structure heights were measured by averaging 11 adjacent height profiles.

### Microfabrication

Stamps and microfluidic channels were made of polydimethylsiloxane (PDMS) (Sylgard® 184, Dow Corning GmbH), which provides a sufficient degree of hemocompatibility for medical devices which are in contact with blood.<sup>18</sup> The structures were cast from a mold and placed in a desiccator to remove gas bubbles. The casting mold was then placed in an oven for 24 h at a temperature of  $60^{\circ}\text{C}$  to allow for curing.

The master wafers for the microcontact printing and microfluidic systems were structured and processed by contact photolithography. For the fabrication, 4-inch silicon wafers were spin-coated with negative photoresist SU-8, exposed to UV through a chromium mask in a mask aligner, and finally developed. The master wafers with inverted microstructures were used for multiple PDMS replica castings. To improve the release of the elastomer, the master was coated with plasma-deposited PTFE. The master structure consisted of circles and squares  $20\text{ }\mu\text{m}$  in diameter or width

and  $8\text{ }\mu\text{m}$  in height and checkerboard patterns  $30\text{ }\mu\text{m}$  in width and  $2\text{ }\mu\text{m}$  in height. Microfluidic masters consisted of channels  $500\text{ }\mu\text{m}$  wide and  $150\text{ }\mu\text{m}$  high. The circles and squares on the replicated PDMS stamps were smaller than those on the master structures and averaged  $17\text{ }\mu\text{m}$  in width.

### Microcontact printing

Before printing, the stamps were cut out of the structured PDMS (diameter  $\sim 5\text{ mm}$ ), cleaned for 10 min in 70% ethanol in an ultrasonic bath and then dried under a flow of dry nitrogen. A  $20\text{ }\mu\text{L}$  droplet of vWF solution was pipetted onto the stamp. During the 2 h of incubation, the vWF-covered stamp was kept in a box covered with aluminum foil to avoid light irradiation and dehydration. Subsequently, the stamp was carefully dried under a dry nitrogen stream until the remaining solution had evaporated. For microcontact printing, the stamp was placed on the substrate and loaded with a mass of 20 g. After 10 min, the sample substrate was removed and the printed area was marked and analyzed with the AFM.

### Perfusion

Microfluidic systems with channels  $500\text{ }\mu\text{m}$  wide and  $150\text{ }\mu\text{m}$  deep were used to perfuse the substrate with PBS. The microfluidic system was placed on the protein functionalized substrate and connected to a syringe pump. The flow rate and flow volume were regulated by a Labview program. The perfusion was observed using an optical microscope (Axiovert 200, Zeiss, Oberkochen, Germany) equipped with a CCD camera (Zeiss Axiocam).

### Platelet adhesion assay

Five milliliters of human whole blood was collected from healthy donors into syringes containing  $750\text{ }\mu\text{L}$  acid citrated extrose. Then, 5 mL of modified Tyrode's buffer (10 mM HEPES, 1.4M NaCl, 26 mM KCl, 121 mM  $\text{NaHCO}_3$ , 0.1% BSA, 0.1% glucose, and pH 6.5) was added, and the samples were centrifuged for 20 min at  $80g$ . The supernatant containing platelet-rich plasma was carefully removed, washed in 10 mL Tyrodes buffer, and pelleted for 10 min at  $1277g$  in the presence of PGI2 ( $2\text{ }\mu\text{g/mL}$ ). The majority of the plasma was removed by washing the platelets thus also preventing the degradation of large vWF polymers by plasma ADAMTS-13 activity.<sup>19</sup> Subsequently, the cells were resuspended in Tyrode's buffer (pH 7.4) and adjusted to a final concentration of  $10 \times 10^3$  platelets per  $\mu\text{L}$ . A total of  $2.5 \times 10^5$  platelets were layered onto vWF-printed glass slides and subsequently activated with  $10\text{ }\mu\text{M}$  U46619 (Enzo Life Sciences GmbH) and  $10\text{ }\mu\text{M}$  ADP (Sigma-Aldrich). After incubation ( $37^{\circ}\text{C}$ , 5%  $\text{CO}_2$ ) for 60 min, the supernatant was removed and adherent platelets were fixed with 4% PFA for 10 min. Then the samples were carefully rinsed with distilled water and dried under a low nitrogen stream and immediately analyzed with the AFM.

### Statistical analysis

A platelet adhesion assay was performed on a  $30 \times 30\text{ }\mu\text{m}^2$  checkerboard pattern of vWF. To quantify platelet adhesion,



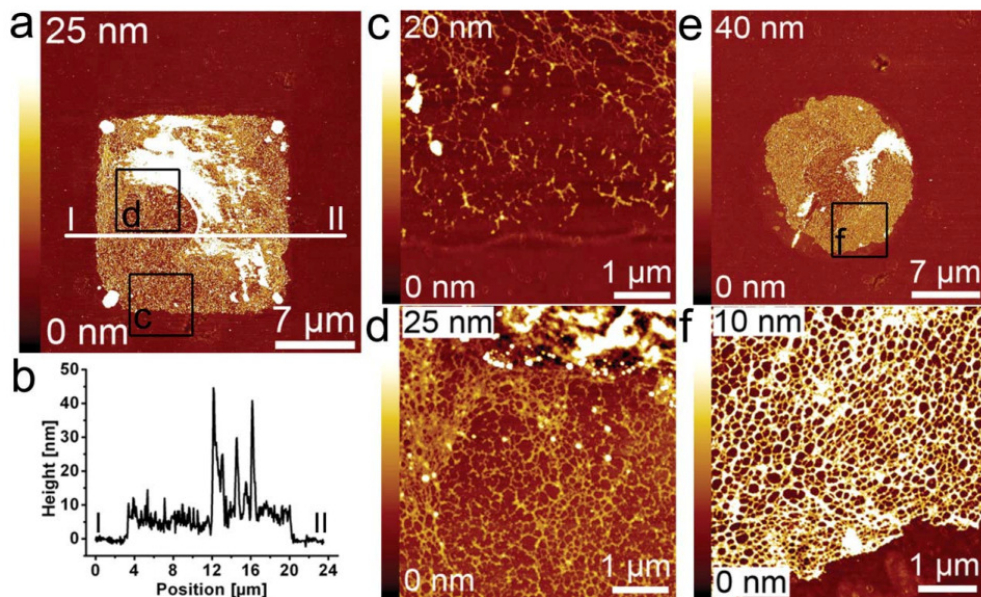


**FIGURE 1.** Topographic AFM images of a square vWF pattern printed on a plasma-treated glass slide. (a) Overview image of a pattern 17  $\mu\text{m}$  in width (image size:  $30 \times 30 \mu\text{m}^2$ ). The line between I and II indicates the location where 11 parallel height profiles were taken to obtain an averaged height profile. The black squares indicate the regions of interest detailed in (c) and (d). (b) Averaged height profile with an average height between 5 and 10 nm. (c) Detail image of the edge of the printed structure (image size:  $5 \times 5 \mu\text{m}^2$ ) (d) Detail image of the central region (image size:  $5 \times 5 \mu\text{m}^2$ ) (e) AFM image of a circular pattern on the same substrate (image size:  $30 \times 30 \mu\text{m}^2$ ). (f) Detail image ( $5 \times 5 \mu\text{m}^2$ ) of a network-like vWF structure. [Color figure can be viewed in the online issue, which is available at [wileyonlinelibrary.com](http://wileyonlinelibrary.com).]

17 AFM images were taken at different sample areas. The image size was  $90 \times 90 \mu\text{m}^2$  with a resolution of  $512 \times 512 \text{ pixel}^2$ . For image analysis, regions of interest were defined that contained four squares of the printed structure, two coated and two uncoated. Platelets in all four squares were counted manually. Platelets that had spread onto both a coated and uncoated square were counted as half a platelet for each. The number of platelets was normalized by the coated and uncoated surface areas, respectively. The surface area of the platelets was evaluated using SPIP 5.1.32.0 software (Image Metrology, Denmark). Each area of interest was marked using the "Add polygon AOI" function. The platelets were detected using the "Grain and Pore analysis" function. The "Particles threshold level" and "minimum detection area" controls were adjusted separately for each image section to reduce errors because of sample waviness. The surface area of the coating and the surface area of platelets were detected using the "detect particles" function.

## RESULTS

Von Willebrand factor with a concentration of 0.01 mg/mL was printed on plasma activated glass slides. The AFM revealed printed 17- $\mu\text{m}$ -structures [Fig. 1(a)]. This size corresponds to the dimension of the structures on the PDMS stamps after the fabrication process. As shown in Figure 1(a,e), the areas within the printed patterns were densely covered with vWF. The overall topography of the structures

was between 4 and 13 nm high. Occasionally, deposits of 50 nm height were found. Magnifying AFM images to a dimension of  $5 \times 5 \mu\text{m}^2$  showed spherical particles and predominantly network-like fibril structures [Fig. 1(c,d,f)].

The stability of the printed layers was tested by perfusion experiments. PBS was pumped through a microfluidic system that was placed onto the functionalized substrate. The perfusion was performed for 10 s at a flow rate of 10  $\mu\text{L/s}$  and followed by a second perfusion for 60 s at the same flow rate. Figure 2(a,b) represent a printed structure before and after the perfusion experiments. The liquid flow did not affect the structure, and the height remained the same (average 3.5 nm).

Structures were also printed on freshly cleaved mica surfaces at a concentration of 0.01 mg/mL. The structures had a width of 18  $\mu\text{m}$  and an average height of 4.5 nm with the exception of some round particles in the middle of the area [Fig. 3(a)]. Network-like fibrils were formed [Fig. 3(b)]. Valid perfusion experiments could not be conducted because liquid seeped in between mica layers through surface defects during perfusion, which repeatedly lead to delamination of the topmost layer. Because the experiments on mica were not reliable, no statistical analysis was carried out for those specimens.

The biofunctionality of the printed 30  $\mu\text{m}$  wide checkerboard patterns [Fig. 4(a)] was tested by platelet adhesion experiments using static assays with preactivated platelets.

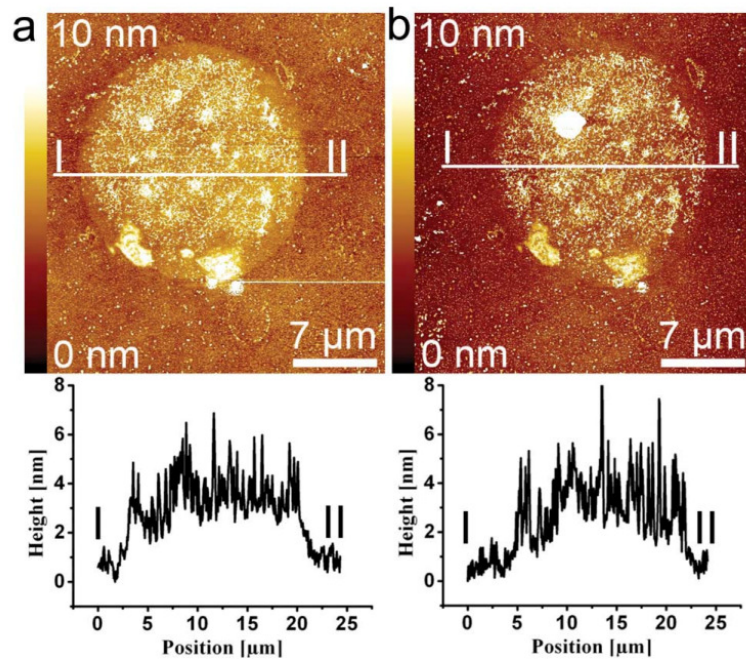


**FIGURE 2.** AFM images of a circular pattern on plasma activated glass (a) before and (b) after two perfusion experiments. The lines indicate the positions of the corresponding averaged profiles. The averaged profiles were calculated from 11 adjacent profiles. Both height profiles show a similar average height of 3 nm. [Color figure can be viewed in the online issue, which is available at [wileyonlinelibrary.com](http://wileyonlinelibrary.com).]

The platelets preferentially spread on the coated areas. Although, platelet adhesion was also observed on the uncoated areas, those platelets showed a different morphology. On the uncoated substrate, platelets featured only an early state of shape change; that is, they took on a slightly flattened shape showing a spread dendritic state with some short filopodia and limited lamellipodium forma-

tion. The bodies of the platelets were still hemispherically shaped, rising above the substrate (c.f. Ref. 20). In contrast, platelets on coated surfaces were round, fully spread, and had developed flat lamellipodia, mostly without filopodia (i.e., pancake shaped).<sup>20</sup> The morphology of the platelets in the border region between the coated and uncoated surfaces is highlighted in Figure 4(b). The figure, a  $12 \times 12 \mu\text{m}^2$

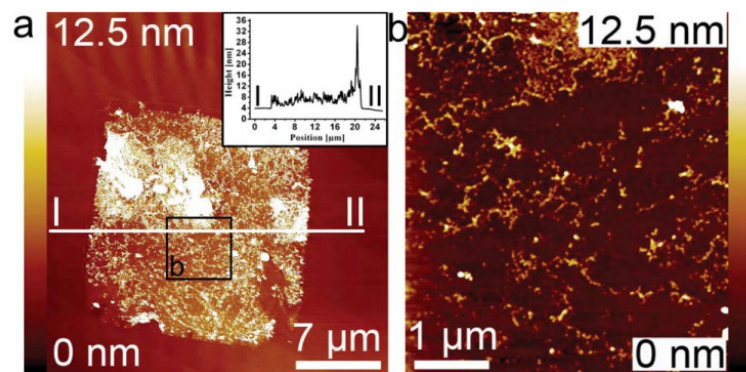


**FIGURE 3.** AFM image of a printed pattern on a mica surface. (a) Overview image of the vWF coated surface. The line indicates the position of the height profile. Inset shows the averaged height profile. (b) Detail image showing the connected structures developed by the vWF. [Color figure can be viewed in the online issue, which is available at [wileyonlinelibrary.com](http://wileyonlinelibrary.com).]

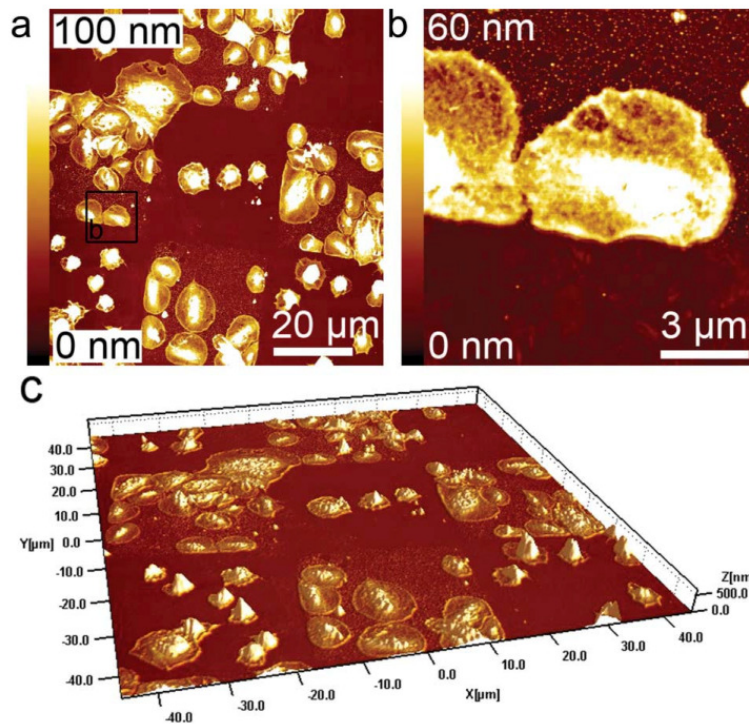


**FIGURE 4.** AFM topography taken after a static platelet adhesion assay. (a) The overview image shows repeating quadratic checkerboard areas 30  $\mu\text{m}$  in width (image size:  $95 \times 95 \mu\text{m}^2$ ). The platelets preferentially adhere to vWF coated areas. On vWF the platelets are well spread, exhibiting the typical shape of activated platelets. On bare glass the platelets are less spread. (b) The detail image shows a corner of the printed structure (image size:  $12 \times 12 \mu\text{m}^2$ ). Platelet spreading is limited by the functionalized surface. (c) Three-dimensional view of the topography in (a). [Color figure can be viewed in the online issue, which is available at [wileyonlinelibrary.com](http://wileyonlinelibrary.com).]

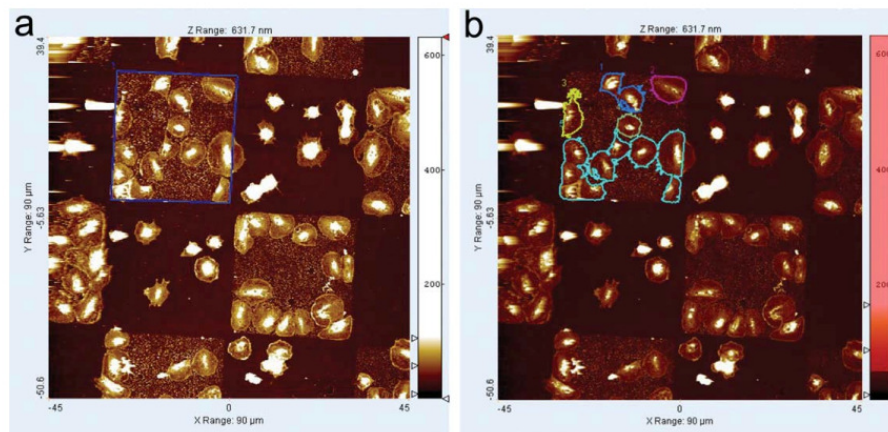


**FIGURE 5.** Image processing procedure for the statistical evaluation. (a) The coated area is marked with the “Add polygon AOI” function, and its area is detected and calculated using the “Grain and Pore analysis” dialog. (b) The platelets inside the marked area in (a) are detected using the “Grain and Pore analysis” dialog and their area is calculated. [Color figure can be viewed in the online issue, which is available at [wileyonlinelibrary.com](http://wileyonlinelibrary.com).]

image, shows the edge of a printed square with activated spread platelets and their typical network-like structure. It is observed that the spread platelets in the border region exhibit flat fronts towards the bare uncoated substrate and thus that the spreading of the platelets is limited to the coated surface area [Fig. 4(b)]. The small spherical particles on the uncoated areas are most likely PFA clots remaining from the fixation process.

The image processing procedures are summarized in Figure 5, where the amount and state of spreading of the platelets are related to the functionalization of the substrate. As shown in Figure 6(a), the average platelet density was  $0.005/\mu\text{m}^2$  on the uncoated glass and  $0.012/\mu\text{m}^2$  on the coated. Thus, more than two-thirds of the adherent platelets were found on the coated surface. The surface coverage of platelets on glass was about 14%, whereas the surface coverage of the platelets on the coated surface was 46% [Fig. 6(c)].

#### DISCUSSION

Atomic force measurements of vWF printed on plasma treated glass and mica surfaces revealed printed structures with thicknesses of 3–13 nm. Similar structures were observed by Raghavachari et al., who studied surface dependent adsorption of vWF under aqueous conditions at physiological pH and ionic strength using an AFM.<sup>21</sup> AFM measurements on mica revealed vWF multimer chains with globular domains and rod-like interconnecting sections of  $(3.2 \pm 0.9)$  nm and  $(2.0 \pm 0.5)$  nm in height.<sup>21</sup> Marchant et al. imaged dried vWF on mica using an AFM in constant force mode and detected structures 3–5 nm in height.<sup>22</sup> The heights of our printed vWF monolayers are consistent with these values, which correspond to one monolayer (or very few layers) of vWF molecules. This result shows that controlled microcontact printing is feasible for patterning vWF onto a substrate. Reference printing experiments performed solely with PBS on plasma treated glass surfaces did not yield structures, thus confirming surface purity after the printing process (data not shown).

Our AFM images [Figs. 1(c,d,f) and 3(b)] revealed network-like structures on the printed areas as described by Raghavachari et al.<sup>21</sup> We infer that the network-like fibrils are vWF molecules in their extended conformation. Shear-induced stretching of vWF fibers and their adsorption onto collagen surfaces was studied by Schneider et al.<sup>2</sup> and Barg et al.<sup>19</sup> Below critical shear, globular vWF molecules on collagen surfaces were observed. Above critical shear, vWF molecules formed network-like structures.<sup>2,19</sup> We observed similar networks confined to the regions defined by the stamp. Occasional spherical particles were also observed, which can be assumed to originate from globular vWF molecules. For instance, Slayter et al. demonstrated that the diameters of globular vWF molecules can reach 60–200 nm.<sup>3</sup>

We verified the stability of printed vWF structures on glass substrates with microfluidic perfusion experiments. The adhesion of the protein to glass at a flow rate of  $10 \mu\text{L/s}$ , corresponding to a shear rate of  $6900 \text{ s}^{-1}$  in the  $500 \mu\text{m}$  channel, was sufficient for a perfusion time of at least 70 s. The incubation experiments support the

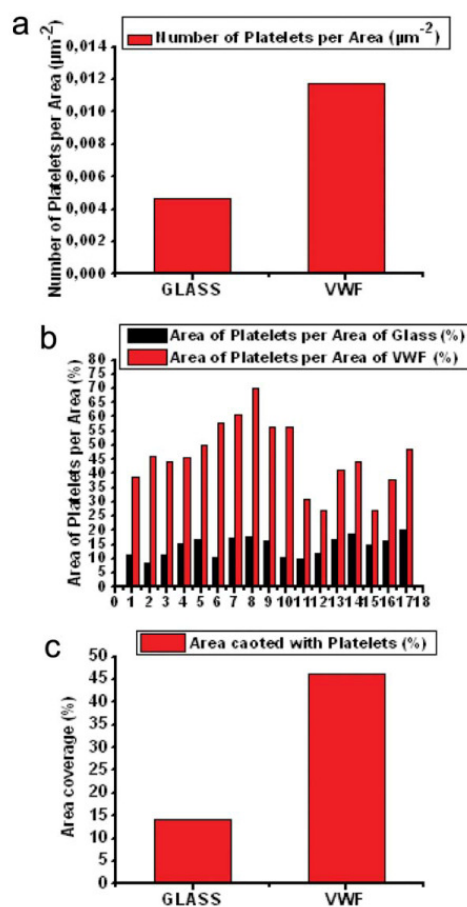


**FIGURE 6.** Statistical analysis of platelet adhesion. Seventeen randomly chosen AFM images were evaluated. (a) Number of platelets that adhered to  $1 \mu\text{m}^2$  of the coated and uncoated surfaces. On average 0.005 platelets settled on  $1 \mu\text{m}^2$  of uncoated surface, whereas 0.012 platelets on average settled on  $1 \mu\text{m}^2$  of coated surface. (b) Platelet density. (c) Relative surface area coated with platelets. Platelets covered 14% of the glass and 46% of the vWF coated surface. [Color figure can be viewed in the online issue, which is available at [wileyonlinelibrary.com](http://wileyonlinelibrary.com).]

assumption that the printed patterns consist of stretched vWF because platelet adhesion was confined to the coated surfaces.

As shown in Figure 6, approximately two-thirds of the total number of adherent platelets attached to the surface coated with vWF. One-third of the platelets settled on the uncoated surface. Platelet morphology on the coated areas differed from that on the unstamped areas. Platelets on the vWF coating showed advanced spreading and an increased area<sup>23</sup> as compared to platelets on the uncoated glass surface (Fig. 6). The height of the platelets on the coated substrate areas was lower than on the uncoated, indicating advanced spreading of those platelets. The contact activation

of platelets by the functionalized surface leads to an initial shape change, the formation of filopodia, and ultimately to lamellipodia protrusion and full spreading.<sup>24</sup> The spontaneous abruption of platelet spreading at the boundary between coated and uncoated areas clearly demonstrates the biological importance of immobilized vWF as a matrix for platelet spreading.

#### CONCLUSION

Microcontact printing is suitable for creating patterned structures of the blood protein vWF. Monolayers of vWF were produced on glass and mica substrates. Printed vWF featured network-like structures. The firm adhesion of these protein layers to a glass surface was verified by perfusion experiments, which confirmed the stability of the printed pattern even at high shear rates. The bioactivity of printed vWF layers was experimentally verified in platelet adhesion assays. The concentration of platelets on the vWF-coated surface was approximately two and a half times higher than on uncoated glass, and the platelets that adhered to vWF were in an advanced spreading state. Those platelets covered an area three times that of the platelets adhering to glass. According to these results, microcontact printing of vWF can be used to design and pattern surfaces that mimic those in patients with cardiovascular diseases for testing platelet function with lab-on-a-chip devices.

#### ACKNOWLEDGMENTS

The authors wish to thank Ferdinand Walter and Alexander Gigler (both LMU Munich) for fruitful discussions.

#### REFERENCES

- Sadler JE. Biochemistry and genetics of von Willebrand factor. *Annu Rev Biochem* 1998;67:395–424.
- Schneider SW, Nuschele S, Wixforth A, Gorzelanny C, Alexander-Katz A, Netz RR, Schneider MF. Shear-induced unfolding triggers adhesion of von Willebrand factor fibers. *Proc Natl Acad Sci U S A* 2007;104:7899–7903.
- Slayter H, Loscalzo J, Bockenstedt P, Handin RI. Native conformation of human vonwillebrand protein-analysis by electron-microscopy and quasi-elastic light-scattering. *J Biol Chem* 1985; 260:8559–8563.
- Siedlecki CA, Lestini BJ, KottkeMarchant K, Eppell SJ, Wilson DL, Marchant RE. Shear-dependent changes in the three-dimensional structure of human von Willebrand factor. *Blood* 1996;88: 2939–2950.
- Lincoln B, Ricco AJ, Kent NJ, Basabe-Desmonts L, Lee LP, MacCraith BD, Kenny D, Meade G. Integrated system investigating shear-mediated platelet interactions with von Willebrand factor using microliters of whole blood. *Anal Biochem* 2010;405: 174–183.
- Kumar A, Whitesides GM. Features of gold having micrometer to centimeter dimensions can be formed through a combination of stamping with an elastomeric stamp and an alkanethiol ink followed by chemical etching. *Appl Phys Lett* 1993;63:2002–2004.
- Xia Y, Whitesides GM. Soft lithography. *Annu Rev Mater Sci* 1998;28:153–184.
- Quist AP, Pavlovic E, Oscarsson S. Recent advances in microcontact printing. *Anal Bioanal Chem* 2005;381:591–600.
- Kane RS, Takayama S, Ostuni E, Ingber DE, Whitesides GM. Patterning proteins and cells using soft lithography. *Biomaterials* 1999;20:2363–2376.
- Bernard A, Renault JP, Michel B, Bosshard HR, Delamarche E. Microcontact printing of proteins. *Adv Mater* 2000;12:1067–1070.
- Chalmeau J, Thibault C, Carcenac F, Vieu C. Micro-contact printing of two different biomolecules in one step using deformable poly(dimethylsiloxane)-based stamp. *Jpn J Appl Phys* 2008; 47:5221–5225.
- Bernard A, Delamarche E, Schmid H, Michel B, Bosshard HR, Biebuyck H. Printing patterns of proteins. *Langmuir* 1998;14: 2225–2229.
- James CD, Davis RC, Kam L, Craighead HG, Isaacson M, Turner JN, Shain W. Patterned protein layers on solid substrates by thin stamp microcontact printing. *Langmuir* 1998;14:741–744.
- Ruiz A, Valsesia A, Bretagnol F, Colpo P, Rossi F. Large-area protein nano-arrays patterned by soft lithography. *Nanotechnology* 2007;18:505306.
- Schmalenberg KE, Buettner HM, Uhrich KE. Microcontact printing of proteins on oxygen plasma-activated poly(methyl methacrylate). *Biomaterials* 2004;25:1851–1857.
- Basabe-Desmonts L, Ramstrom S, Meade G, O'Neill S, Riaz A, Lee LP, Ricco AJ, Kenny D. Single-step separation of platelets from whole blood coupled with digital quantification by interfacial platelet cytometry (iPC). *Langmuir* 2010;26:14700–14706.
- Menzel. <http://www.menzel.de/Produkte.655.0.html>. 28. Feb. 2011.
- Haines SR, Beamson G, Williams RL, Weightman P. Changes in the electronic structure of silicone rubber surfaces induced by oxygen plasma treatment. *Surf Interface Anal* 2007;39:942–947.
- Barg A, Ossig R, Goerge T, Schneider MF, Schillers H, Oberleithner H, Schneider SW. Soluble plasma-derived von Willebrand factor assembles to a hemostatically active filamentous network. *Thromb Haemost* 2007;97:514–526.
- Sheppard JI, McClung WG, Feuerstein IA. Adherent platelet morphology on adsorbed fibrinogen-effects of protein incubation-time and albumin addition. *J Biomed Mater Res* 1994;28: 1175–1186.
- Raghavachari M, Tsai HM, Kottke-Marchant K, Marchant RE. Surface dependent structures of von Willebrand factor observed by AFM under aqueous conditions. *Colloids Surf B Biointerfaces* 2000;19:315–324.
- Marchant RE, Lea AS, Andrade JD, Bockenstedt P. Interactions of von Willebrand-factor on mica studies by atomic force microscopy. *J Colloid Interface Sci* 1992;148:261–272.
- Park K, Mao FW, Park H. Morphological characterization of surface-induced platelet activation. *Biomaterials* 1990;11:24–31.
- Gawaz MP. *Blood Platelets*. Stuttgart: Georg Thieme Verlag; 2001.

## 8.5 RAMAN SPECTROSCOPY OF LASER-INDUCED OXIDATION OF TITANOMAGNETITES

### Research Article

Journal of  
**RAMAN  
SPECTROSCOPY**

Received: 1 July 2010

Accepted: 21 October 2010

Published online in Wiley Online Library: 19 January 2011

(wileyonlinelibrary.com) DOI 10.1002/jrs.2849

# Raman spectroscopy of laser-induced oxidation of titanomagnetites

Michael Bauer,<sup>a,b</sup> Polina Davydovskaya,<sup>a,b</sup> Marek Janko,<sup>a,b</sup>  
Melanie Kaliwoda,<sup>c</sup> Nikolai Petersen,<sup>a</sup> Stuart Gilder<sup>a</sup>  
and Robert W. Stark<sup>b,d,e\*</sup>



Titanomagnetites are important carriers of magnetic remanence in nature and can track redox conditions in magma. The titanium concentration in magnetite bears heavily on its magnetic properties, such as saturation moment and Curie temperature. On land and in the deep ocean, however, these minerals are prone to alteration which can mask the primary magnetic signals they once recorded. Thus, it is essential to characterize the cation composition and oxidation state of titanomagnetites that record the paleomagnetic field. Raman spectroscopy provides a unique tool for both purposes. Nonetheless, the heat generated by the excitation laser can itself induce oxidation. We show that the laser power threshold to produce oxidation decreases with increasing titanium content. With confocal Raman spectroscopy and magnetic force microscopy (MFM) on natural and synthetic titanomagnetites, a non-destructive Raman imaging protocol was established. We applied this protocol to map out the composition and magnetization state within a single ex-solved titanomagnetite grain in a deep-sea basalt. Copyright © 2011 John Wiley & Sons, Ltd.

Supporting information may be found in the online version of this article.

**Keywords:** titanomagnetite; alterations; local heating; MFM; confocal Raman

### Introduction

The composition of magnetic minerals provides information on the conditions of rock genesis and alteration.<sup>[1]</sup> Minerals from the titanomagnetite solid solution series ( $\text{Fe}_{3-x}\text{Ti}_x\text{O}_4$ ,  $0 < x < 1$ ) are of particular relevance because they carry the remanent magnetization of oceanic basalts.<sup>[2,3]</sup> The composition of titanomagnetite is close to  $x = 0.6$  with a Curie temperature of  $140^\circ\text{C}$  when formed at a spreading ridge.<sup>[1]</sup> Their equilibrium oxygen fugacity is on the order of  $10^{-7}$  atm, implying a strong tendency to oxidize under sea-floor conditions.<sup>[4]</sup> Raman imaging techniques are valuable tools in characterizing the composition and oxidation state of titanomagnetite.<sup>[5]</sup> Raman spectroscopic characterization and compositional analysis of rock-forming minerals will also be important tools in future planetary missions.<sup>[6,7]</sup> Iron oxides, however, are poor Raman scatterers and strongly absorb in the range of the wavelengths of typical excitation lasers, and high laser intensities are required to obtain an adequate signal.<sup>[1,8]</sup> Thus, the heat generated by the strongly focused excitation laser may lead to alteration of the sample. To obtain reliable Raman data on titanomagnetite, the measurement conditions need to be optimized to reduce the measurement time without altering the specimen.

Stoichiometric titanomagnetites ( $\text{Fe}_{3-x}\text{Ti}_x\text{O}_4$ ) can be synthesized in a wide range of compositions.<sup>[9]</sup> Magnetite, i.e.  $x = 0$ , also referred to as TM00, is a special case of a ferrite with the general formula  $\text{Fe}^{2+}\text{Fe}_2^{3+}\text{O}_4$  corresponding to  $\text{FeO}\cdot\text{Fe}_2\text{O}_3$  (simplified  $\text{Fe}_3\text{O}_4$ ) with an inverse spinel structure.<sup>[10]</sup> TM60 ( $x = 0.6$ ) represents an idealized natural titanomagnetite with the composition  $\text{Fe}_{2.4}\text{Ti}_{0.6}\text{O}_4$ . The long-range order in synthetic TM60 single crystals is a function of nonstoichiometry, with higher cation vacancy concentrations producing a more random cation distribution.<sup>[11]</sup> The magnetic stability of synthetic titanomagnetite can be in-

creased by oxidation and subsequent annealing in vacuum.<sup>[12]</sup> Natural titanomagnetite often intergrows with ilmenite ( $\text{FeTiO}_3$ ). Atoms in the titanomagnetite lattice can also be replaced by other atoms, such as magnesium, aluminium, nickel, zinc, chromium, and vanadium.<sup>[1]</sup> Confocal Raman microscopy has the potential to provide compositional information with high spatial resolution and to reveal the key properties of titanomagnetite grains in rocks. To avoid laser-induced alteration processes, we determined the laser power threshold for the oxidation of minerals from the titanomagnetite solid solution series. With the optimized settings, we have characterized single titanomagnetite grains in deep-sea basalts.

### Materials and Methods

To determine the laser power threshold, we investigated synthetic magnetite (TM00) and titanomagnetites produced using the floating zone technique.<sup>[11]</sup> The titanium concentration of the

\* Correspondence to: Robert W. Stark, Center of Smart Interfaces, Petersenstrasse 32, 64287 Darmstadt, Germany. E-mail: stark@csi.tu-darmstadt.de

a Department of Earth and Environmental Sciences, Ludwig-Maximilians-Universität München, 80333 Munich, Germany

b Center for NanoScience (CeNS), 80799 Munich, Germany

c Mineralogical State Collection, LMU, 80333 Munich, Germany

d FB Material-und Geowissenschaften, TU Darmstadt, 64287 Darmstadt, Germany

e Center of Smart Interfaces, TU Darmstadt, 64287 Darmstadt, Germany

synthetic samples ranged from 0 to 86%. Their titanium concentration was verified by thermomagnetic analysis.<sup>[2]</sup> To demonstrate compositional mapping, we studied titanomagnetites in late Cretaceous sea-floor basalt, drilled in the middle South Atlantic Ocean during the deep-sea drilling project 73 (DSDP/ODP Leg 73, hole 524, core 33) at a water depth of 4796 m, 330 m below the sea floor.

Raman spectra were measured with a confocal Raman microscope (alpha 300 R; WITec GmbH, Ulm, Germany). For excitation, we used the second harmonic generation (532 nm,  $P_{\text{max}} = 22.5$  mW) of a Nd:YAG laser, focused with a 100 $\times$  objective (Nikon NA = 0.90, 0.26 mm working distance). The objective was also used for collection of the backscattered light. The light was guided through a multimode optical fibre to the spectrometer, using the 50- $\mu\text{m}$  diameter fibre core as a pinhole for the confocal setup. The diffraction-limited focus resulted in a lateral resolution of about 400 nm, and a focal depth of about 1  $\mu\text{m}$ . The power distribution within the laser beam profile was Gaussian due to the TEM<sub>00</sub> laser mode. Therefore, the energy input in the central region was higher than at the rim of the laser spot.

A sharp edge filter rejected the elastically scattered photons (Rayleigh scattering). Raman spectra were acquired with a lens-based spectrometer with a CCD camera (1024  $\times$  128 pixel, cooled to  $-65^\circ\text{C}$ ) on each point with a spectral resolution of 3.51  $\text{cm}^{-1}$  per CCD pixel for the 600 lines/mm grating. The compositional maps were generated either by integrating the counts in the range of wavenumbers (sum filter) of characteristic Raman peaks or by using peak centre and peak width obtained by a Lorentzian fit.

The magnetic force microscope (MFM) was equipped with NanoScope IV controller (Veeco Metrology Inc., Santa Barbara, CA) using force sensors with a thin magnetic coating at the tip of the cantilever (Multi75M-G, BudgetSensors, Sofia, Bulgaria). The sensors were magnetized shortly before use by placing them on one pole of a strong permanent magnet. For magnetic imaging, an atomic force microscope (AFM) was operated in the tapping mode. The phase shift was recorded in the lift mode after each topographic line scan (interleave mode).

An electron microprobe (Cameca SX100) was used to measure the elemental composition of a similar titanomagnetite grain in the same thin section located a few millimetres away from the grain analysed by Raman spectroscopy. The operating parameters were 15 kV accelerating voltage and 20 nA beam current with a beam diameter of 1  $\mu\text{m}$ . Counting rates of 30 s were used for Al, Ni, and Ca; 100 s for Ti; and 20 s for all other elements. Synthetic minerals and oxides were taken into account for calibration and a Pouchou and Pichoir (PAP) correction was applied to the raw data.<sup>[13]</sup>

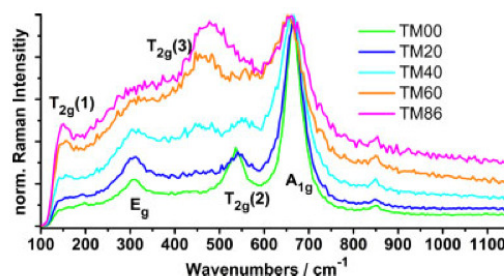


Figure 1. Raman spectra of synthetic titanomagnetite normalized to the  $A_{1g}$  peak.

## Results

### Laser-induced oxidation

Reference spectra of the different titanomagnetites were obtained at a laser power of 1.5 mW. The Raman spectra were normalized to the  $A_{1g}$  peak and are shown in Fig. 1. The Raman spectra did not depend on the orientation of the samples TM00 to TM86 (data not shown). Table 1 summarizes the Raman peak centres of the synthetic specimen as obtained by a Lorentzian fit.

Confocal Raman microscopy on titanomagnetite is affected by laser absorption, which leads to local heating. One can quantify the onset of oxidation with a series of Raman spectra measured with different laser intensities (Fig. 2). Shown are the spectra for the natural titanomagnetite and the synthetic magnetite ( $x = 0$ , TM00,  $\text{Fe}_3\text{O}_4$ ). Each spectrum was integrated for 30 s. A progressive oxidation of titanomagnetite occurred as a function of the laser power. In an intermediate laser power range, the measured Raman spectra show features of both titanomagnetite and haematite. Both signatures were observed in the Raman spectra of the geological titanomagnetite sample measured at a laser power of 14.9 mW ( $\sim 1.1$  MW/cm<sup>2</sup>). Figure S1 (see Supporting Information) gives the spectra for the synthetic samples with a titanium content of  $x = 20$  (TM20,  $\text{Fe}_{2.8}\text{Ti}_{0.2}\text{O}_4$ ) to 86% titanium (TM86,  $\text{Fe}_{2.14}\text{Ti}_{0.86}\text{O}_4$ ).

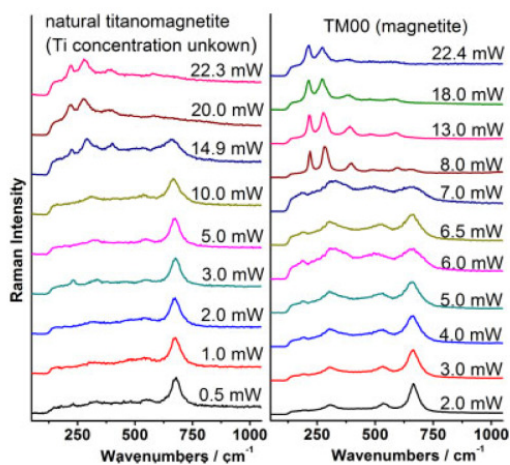
The threshold for initiating oxidation as a function of the titanium concentration was explored as illustrated in Fig. 3. A series of Raman spectra were taken by increasing step-wise the laser power (Figs. 2 and S1). All spectra were recorded with 30 s integration time. To detect the spectral changes, the spectra were normalized to the  $A_{1g}$  peak, and then the spectrum taken at the previous power step was subtracted. Variations were considered

Table 1. Raman peak centres of the synthetic specimen as obtained by a Lorentzian fit, together with literature values for magnetite

| Ti/(Fe + Ti)<br>Mode | Raman peak centre ( $\text{cm}^{-1}$ ) |       |             |             |          |
|----------------------|--|-------|-------------|-------------|----------|
|                      | $T_{2g}(1)$                            | $E_g$ | $T_{2g}(3)$ | $T_{2g}(2)$ | $A_{1g}$ |
| TM00 <sup>a</sup>    | 192                                    | 306   | –           | 538         | 668      |
| TM00                 | 197.8                                  | 304.4 | –           | 536.8       | 664.9    |
| TM20                 | 193.2                                  | 309.0 | –           | 540.7       | 664.1    |
| TM40                 | 155.8                                  | 309.2 | 455.1       | 549.7       | 647.5    |
| TM60                 | 155.7                                  | 318.2 | 464.2       | –           | 647.5    |
| TM86                 | 154.4                                  | –     | 477.7       | –           | 654.3    |

<sup>a</sup> A. Wang et al., *Am. Miner.* **2004**, *89*, 665.

Laser-induced oxidation of titanomagnetites



**Figure 2.** Laser-induced oxidation of natural titanomagnetite and synthetic magnetite. Above a certain laser power threshold, the Raman spectra of haematite signature occurred. Each spectrum was integrated for 30 s. Additional spectra for synthetic samples with a titanium content of  $x = 20$  (TM20) to 86% titanium (TM86) are shown in Fig. S1.

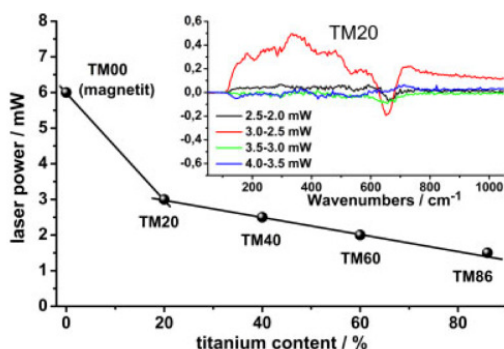


**Figure 3.** Laser power threshold for the oxidation of titanomagnetite. The inset shows the spectral differences.

significant if the differences exceeded 10% of the intensity in the range from 100 to 3600  $\text{cm}^{-1}$  (Fig. 3 inset).

Another important parameter is the irradiation time. To investigate the time dependence of the oxidation, a series of Raman spectra were recorded at the same position for the synthetic TM60 sample. The laser power was set at 2.2 mW ( $0.183 \text{ MW/cm}^2$ ), which is slightly below the threshold for oxidation at 30 s irradiation time. Spectra were recorded continuously with an integration time of 30 s and normalized to the Rayleigh peak. After 2 min of irradiation, the spectrum began to show signs of alteration (Fig. 4). Peaks at about 220 and 290  $\text{cm}^{-1}$  developed, which correspond to the spectral signature of haematite ( $A_{1g}$  and  $E_g$ , respectively).

AFM and MFM measurements were made after the laser irradiation to inspect whether the titanomagnetite surface was altered. Figure 5 shows the topography and the magnetic image of a locally oxidized surface of the natural titanomagnetite. The surface was irradiated for 5 s with laser powers of 5, 10, 15, and

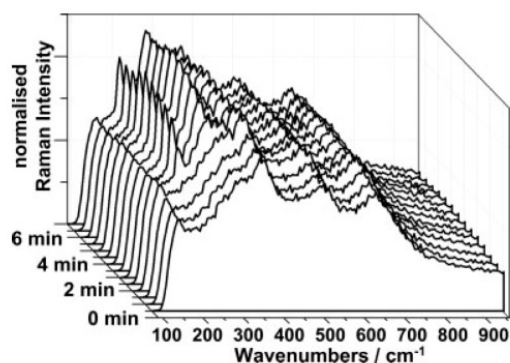


**Figure 4.** Time dependence of the laser-induced oxidation of TM60. The spectra were taken with a laser power of 2.2 mW. After 2 min of irradiation, haematite peaks occurred at 220  $\text{cm}^{-1}$  ( $A_{1g}$ ) and 290  $\text{cm}^{-1}$  ( $E_g$ ).

20 mW, respectively. Circular oxidation craters with diameters of a few micrometres were generated (Fig. 5(c)). Oxidation leads to a progressively deformed surface (Fig. 5(a)). The same circular structure prevails in the MFM phase image (Fig. 5(b)). Figure 5(d) and (e) show an oxidation crater directly after a laser irradiation with 20 mW. After 26 days, further changes of the deformed surface could be observed (Fig. 5(f) and (g)). The small depression that was formed directly after laser irradiation in the centre (Fig. 5(d)) likely underwent a process akin to an isostatic rebound 26 days later (Fig. 5(f)).

### Compositional mapping

Composition and structural characteristics of a titanomagnetite grain from ocean-floor basalt were determined using the Raman imaging procedure explained above. The optical micrograph revealed a striped pattern with varying reflectivity (Fig. 6(a)). The blue rectangle marks an area of  $7 \times 5 \mu\text{m}^2$  ( $60 \times 80$  points), which was analysed with Raman spectroscopy using 10 s integration time at a laser power of 2 mW. The compositional map Fig. 6(b) was calculated with a sum filter that integrates the counts from 210 to 260  $\text{cm}^{-1}$ . Sum filtering from 500 to 580  $\text{cm}^{-1}$  (Fig. 6(d)) results in an inverted contrast. Two distinct materials were found, as seen in the average spectra for the individual stripes (Fig. 6(c)). The filter ranges for sum filtering are indicated by the light and dark grey regions within the spectrum. The  $A_{1g}$  peak was also taken into account for a more detailed analysis regarding peak position and peak width.

Lamellae with a width of a few micrometres in parallel with two large cracks were observed in the optical micrograph (Fig. 6(a)). In the following, we will refer to the material as 'bright lamella' (red curve) and 'dark lamella' (black curve) as they appear in Fig. 6(b). Average spectra of both regions were compared with the reference spectra obtained on the synthetic samples (Fig. 6(c)). All spectra show the characteristic  $A_{1g}$  peak; other peaks change in position [ $T_{2g}(1)$ , from  $\sim 190$  to  $\sim 150 \text{ cm}^{-1}$ ], appear [ $T_{2g}(3)$ , 480  $\text{cm}^{-1}$ ], or vanish [ $E_g$ , 310  $\text{cm}^{-1}$ ;  $T_{2g}(2)$ , 540  $\text{cm}^{-1}$  and the peak at 850  $\text{cm}^{-1}$ ] with increasing titanium content.

Figure 7 correlates the chemical information of the Raman spectra with information obtained by AFM and MFM measurements on the geological sample. The topographical image in Fig. 7(a) also reveals a striped pattern, which implies differences



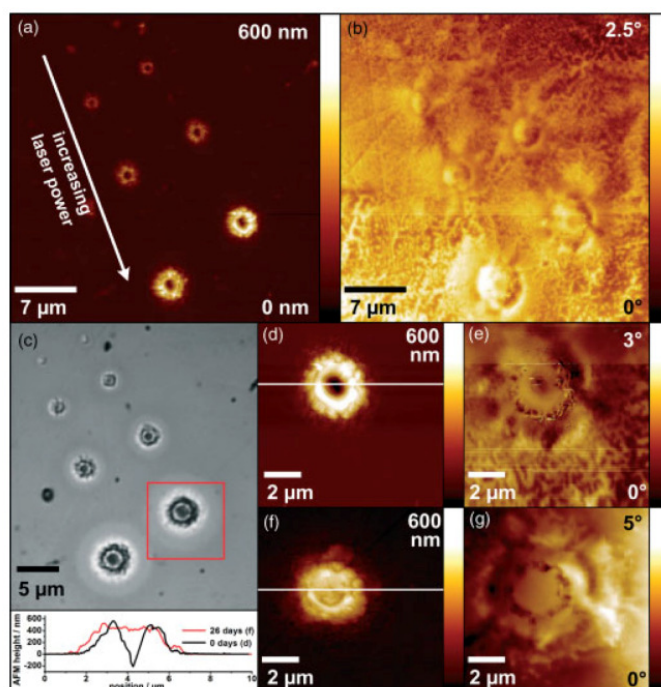


**Figure 5.** MFM and AFM images of a laser-irradiated natural titanomagnetite surface. Oxidation was achieved by means of 5-s laser irradiation with 5, 10, 15, and 20 mW (top to bottom). (a) Topography, (b) the corresponding MFM phase image (lift height 100 nm), and (c) the optical micrograph. (d,e) Topography and MFM images of the oxidation spot generated with 20 mW were measured directly after the laser irradiation (lift height 40 nm). (f,g) The same spot after 26 days of storage at ambient laboratory conditions. The inset at the lower left shows the topographic cross section of (d) and (f). The central depression disappeared after 26 days.

in material hardness. The magnetic image in Fig. 7(b) shows a clear stripe pattern alternating between magnetic and non-magnetic phases. The Raman map in Fig. 7(c) was obtained from the peak centre position of a Lorentz fit on the  $A_{1g}$  peak and also shows these stripes. The inset outlines the variation of the  $A_{1g}$  Raman peak at about  $660\text{ cm}^{-1}$ , which is characteristic of titanomagnetite. The Lorentz fit results in better contrast with decreased noise level as compared to the images calculated with the simple sum filter (Fig. 6). All images clearly show the identical lamellar pattern. The structures in the MFM image correlate with the same structures as visible in the titanomagnetite distribution determined with Raman spectroscopy. An elemental microprobe analysis of a similar natural titanomagnetite revealed a slight exchange of magnesium against iron and titanium, and an aluminium content that fluctuated (data not shown).

## Discussion

### Laser power

The alteration threshold decreases rapidly between titanium concentrations of TM00 to TM20; thereafter, the threshold decreases more slowly, yet linearly, above TM20. This variation in laser power threshold of TM20 corresponds to changes in the  $\text{Fe}^{2+}$  and  $\text{Fe}^{3+}$  cation distribution in tetrahedral and octahedral

sites.<sup>[14]</sup> Depending on the laser power, a partial oxidation could be observed within a certain range. Local temperatures towards the centre of the laser spot induced alteration, whereas oxidation did not occur near the rim. In the spectrometer, however, scattered light from the centre and the surrounding region is averaged. When analysing titanomagnetites of unknown composition, the laser power should be limited to  $1.5\text{ mW}$  ( $0.08\text{ MW/cm}^2$ ) with integration times of several minutes. At laser powers  $<1.5\text{ mW}$ , a safe mode of operation could be verified for the geological and synthetic samples. Only spectra taken at laser powers below this threshold should be used for an uncompromised compositional analysis.

The results clearly show that laser-induced oxidation should be taken into account for any spectroscopic characterization of (titano-)magnetites. In addition, one also might adjust the oxygen fugacity during the measurement. Magnetite and titanomagnetite oxidize above  $\sim 240^\circ\text{C}$  in a normal atmosphere.<sup>[8,15,16]</sup> Raman measurements in an oxygen-free atmosphere might help to reduce the tendency to oxidize. It should be mentioned, however, that noble gases can diffuse into synthetic magnetite above  $500^\circ\text{C}$  during growth.<sup>[17]</sup> At about  $600^\circ\text{C}$ , a phase transition from magnetite to other iron oxides can occur.<sup>[17–19]</sup> Such high temperatures may be achieved at high laser powers or strong focusing. For practical measurements under ambient conditions, one has to balance the measurement time and laser power to avoid alteration.

Laser-induced oxidation of titanomagnetites

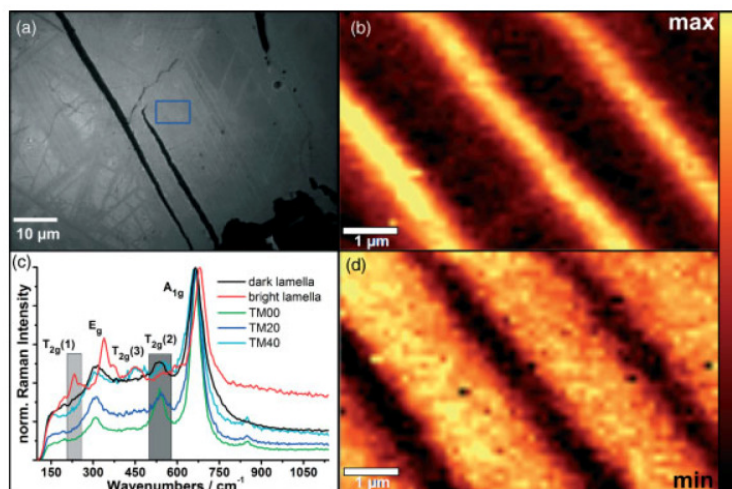


**Figure 6.** Compositional mapping of a natural titanomagnetite grain from a mid-oceanic ridge basalt. (a) Optical micrograph. The region of the Raman maps was located close to a shrinkage crack and is marked with a blue rectangle. (b) Compositional map calculated with a sum filter from 210 to 260  $\text{cm}^{-1}$ . (c) Average spectra obtained from both types of stripes. The red curve is an average over the bright lamella in (b), the black curve over the dark ones. For comparison, reference spectra of synthetic titanomagnetites are also shown (normalized to the intensity of  $A_{1g}$ ). (d) Compositional map calculated with sum filter from 500 to 580  $\text{cm}^{-1}$ . Both sum filter regions are marked in light and dark grey.

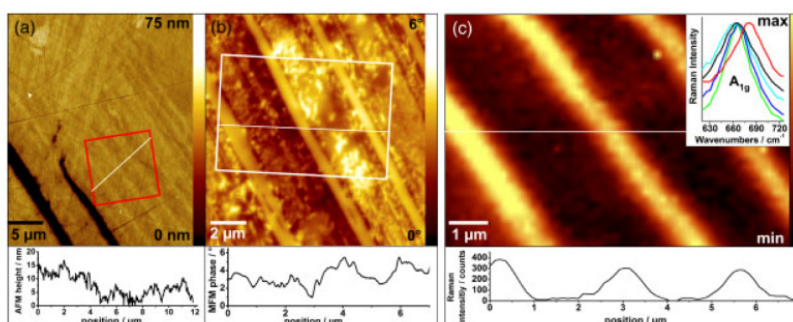


**Figure 7.** AFM, MFM, and Raman maps of a titanomagnetite from a sea-floor basalt. (a) Topographic overview. (b) The MFM phase shift with 50 nm lift height taken in the region of interest indicated in (a). (c) Raman map acquired in the region indicated in (b). The Raman image was derived from the peak centre position of the  $A_{1g}$  peak determined with a Lorentz fit. The inset shows the variation of the  $A_{1g}$  peak as given in Fig. 6(c).

**Deep-sea basalt**

With these optimized settings, the composition of a natural titanomagnetite was mapped spectroscopically, and two distinct phases was observed. A comparison with the reference spectra obtained on the synthetic specimen revealed only subtle differences, which made the identification of the mineral phases difficult. The peaks in the Raman spectra of the dark lamella (black curve) match best to the TM20 reference spectrum (Fig. 6(c)). The peak centre ( $665 \text{ cm}^{-1}$ ) of the  $A_{1g}$  also better agrees with that of TM20 ( $664 \text{ cm}^{-1}$ ). The peak width ( $74 \text{ cm}^{-1}$ ), however, better matches that of TM40 ( $76 \text{ cm}^{-1}$ ). The MFM measurements show that the dark lamella is a magnetic phase. Thus, it is reasonable to assume that the dark lamellae correspond to a titanomagnetite with a titanium content around 20–40%.

The identification of the bright phase in Fig. 6(b) is ambiguous. The relative intensities of the  $T_{2g}(2)$  and  $T_{2g}(3)$  peaks match those

of the TM40 spectrum. The peak width ( $66 \text{ cm}^{-1}$ ) is between the values for TM20 ( $54 \text{ cm}^{-1}$ ) and TM40. However, the peak at  $235 \text{ cm}^{-1}$  is missing in the reference spectra of the synthetic minerals. Also, the  $A_{1g}$  peak position ( $673 \text{ cm}^{-1}$ ) does not fit well to the respective peak position of the synthetic titanomagnetites. These results indicate that the phase is most likely not a pure titanomagnetite phase but another iron oxide mineral. Various Raman spectra are available in the literature for chemically related iron oxides. For example, Faria *et al.* reported similar Raman spectra for a laser-heated wüstite, where decomposition leads to  $\alpha\text{-Fe}$  and  $\text{Fe}_3\text{O}_4$ , and assumed that  $\text{Fe}_3\text{O}_4$  has been transformed into haematite ( $\alpha\text{-Fe}_2\text{O}_3$ ).<sup>[15]</sup> Raman spectra of maghemite ( $\gamma\text{-Fe}_2\text{O}_3$ ), which can be seen as the iron-deficient form of magnetite, also coincide with those of the bright lamella.<sup>[20–22]</sup> Ilmenite is another candidate because the peaks at  $235 \text{ cm}^{-1}$  in bright lamella and  $229 \text{ cm}^{-1}$  in ilmenite match. However, there are discrepancies for the  $A_{1g}$  peak position ( $680 \text{ cm}^{-1}$  for ilmenite) and in particular

the peak at  $\sim 480\text{ cm}^{-1}$ , which is not present in ilmenite. The bright lamella is not ferromagnetic because in MFM the bright lamella does not show a signal (Fig. 7(b)). Titanomagnetites with  $x = \sim 0.75$  are paramagnetic at room temperature and therefore such a titanomagnetite phase cannot be excluded with the MFM measurements. However, maghemite and ilmenite were disproved with MFM, given that both phases are magnetic.

Microprobe data provides additional insights into the composition of the mineral phases. Also, the elemental composition showed an alternating exchange of ions. The variations may be caused by growth-zoning in natural magnetite. It is reasonable to assume that the variation observed by the microprobe measurement also affects the Raman spectra. The exchange of iron and magnesium ions could explain the deviation of the spectrum of the bright lamella from a pure mineral phase. The composition of that phase, however, remains an open question to further study.

## Conclusion

Titanomagnetite Raman spectra vary in peak position, intensity, and width as a function of titanium concentration and degree of oxidation. Hence, Raman spectroscopy can identify the composition and oxidation state of the minerals of the magnetite-ülvöspinel solid solution series. Depending on the titanium content, the mineral starts to oxidize above a certain laser power threshold. Adjusting the laser power just below the threshold for immediate oxidation is insufficient because time-dependent oxidation processes can still occur. The laser heating causes an altered spot on the surface whose diameter and height depend on the laser power and irradiation time. Oxidation continues weeks after laser application. The laser power should be maintained well under the threshold to avoid oxidation.

On the basis of these findings, we investigated a natural basalt sample collected from the deep ocean floor. Compositional Raman mapping revealed a lamellar structure. One mineral phase could be attributed to a titanomagnetite with a titanium content of about 20–40%. The other phase could not be unambiguously identified.

## Acknowledgements

We thank Gloria Almonacid Caballer for fruitful discussions and the Deutsche Forschungsgemeinschaft (DFG) for funding this project under grant STA 1026/2-1.

## Supporting information

Supporting information may be found in the online version of this article.

## References

- [1] A. Wang, K. E. Kuebler, B. L. Jolliff, L. A. Haskin, *Am. Mineral.* **2004**, *89*, 665.
- [2] S. A. Gilder, M. Le Goff, *Geophys. Res. Lett.* **2008**, *35*, L10302.
- [3] M. Marshall, A. Cox, *Nature* **1971**, *230*, 28.
- [4] J. Verhoogen, *J. Geol.* **1962**, *70*, 168.
- [5] L. Tatsumi-Petrochilos, S. A. Gilder, P. Zinin, J. E. Hammer, M. D. Fuller, *AGU Fall Meeting Abstracts*, **2008**, A791+.
- [6] A. Ellery, D. Wynn-Williams, *Astrobiology* **2003**, *3*, 565.
- [7] J. Popp, M. Schmitt, *J. Raman Spectrosc.* **2004**, *35*, 429.
- [8] O. N. Shebanova, P. Lazor, *J. Raman Spectrosc.* **2003**, *34*, 845.
- [9] H. C. Soffel, E. Appel, *Phys. Earth Planet. Inter.* **1982**, *30*, 348.
- [10] L. V. Gasparov, D. B. Tanner, D. B. Romero, H. Berger, G. Margaritondo, L. Forro, *Phys. Rev. B* **2000**, *62*, 7939.
- [11] B. J. Wanamaker, B. M. Moskowitz, *Geophys. Res. Lett.* **1994**, *21*, 983.
- [12] M. Lewis, *Geophys. J. R. Astron. Soc.* **1968**, *16*, 295.
- [13] J. L. Pouchou, F. Pichoir, *La Recherche Aérospatiale* **1984**, *3*, 13.
- [14] Z. Kakol, J. Sabol, J. M. Honig, *Phys. Rev. B* **1991**, *44*, 2198.
- [15] D. L. A. de Faria, S. V. Silva, M. T. de Oliveira, *J. Raman Spectrosc.* **1997**, *28*, 873.
- [16] B.-K. Kim, J. A. Szpunar, *Scr. Mater.* **2001**, *44*, 2605.
- [17] T. Matsumoto, K. Maruo, A. Tsuchiyama, J.-I. Matsuda, *Earth Planet. Sci. Lett.* **1996**, *141*, 315.
- [18] D. P. Burke, R. L. Higginson, *Scr. Mater.* **2000**, *42*, 277.
- [19] J. Tominaga, K. Wakimoto, T. Mori, M. Murakami, T. Yoshimura, *Trans. Iron Steel Inst. Japan* **1982**, *22*, 646.
- [20] I. Chamritski, G. Burns, *J. Phys. Chem. B* **2005**, *109*, 4965.
- [21] J. C. Rubim, M. H. Sousa, J. C. O. Silva, F. A. Tourinho, *Braz. J. Phys.* **2001**, *31*, 402.
- [22] M. H. Sousa, F. A. Tourinho, J. C. Rubim, *J. Raman Spectrosc.* **2000**, *31*, 185.

## **9. APPENDIX**

### **Submitted Draft**

### **Publication 9.1:**

**Evidence of Dyschondrosteosis and Dicrocoeliasis in a bog body from the Netherlands**  
Raffaella Bianucci, Don Brothwell, Wijnand van der Sanden, Christina Papageorgopoulou, Paul Gostner, Patrizia Pernter, Eduard Egarter-Vigl, Frank Maixner, Marek Janko, Dario Piombino-Masali, Grazia Mattutino, Frank Rühli and Albert Zink  
submitted to Journal of Archaeology in the Low Country

## **9.1 EVIDENCE OF DYSCHONDROSTEOSIS AND DICROCOELIASIS IN A BOG BODY FROM THE NETHERLANDS**

### **Draft**

### **Evidence of Dyschondrosteosis and Dicrocoeliasis in a Bog Body from the Netherlands**

Raffaella Bianucci<sup>1,2</sup>, Don Brothwell<sup>3</sup>, Wijnand van der Sanden<sup>4</sup>, Christina Papageorgopoulou<sup>5</sup>, Paul Gostner<sup>6</sup>, Patrizia Pernter<sup>6</sup>, Eduard Egarter-Vigl<sup>7</sup>, Frank Maixner<sup>8</sup>, Marek Janko<sup>9,10</sup>, Dario Piombino-Mascali<sup>8</sup>, Grazia Mattutino<sup>1</sup>, Frank Rühli<sup>11</sup>, Albert Zink<sup>8</sup>

*1Laboratory of Criminalistic Sciences, Department of Anatomy, Pharmacology and Legal Medicine, University of Turin, Corso Galileo Galilei 22, 10126 Turin, Italy.*

*2Biocultural Anthropology Unit, UMR 6578 CNRS-EFS, Faculty of Medicine, Secteur Nord, Batiment A-CS80011, University of Marseilles, Boulevard Pierre Dramard, 13344 Marseilles, France.*

*3Drents Plateau, Stationsstraat 11, 9401 KV Assen, The Netherlands.*

*4Institut für Anthropologie, Johannes Gutenberg- Universität, SB-II Colonel Kleinmann-Weg 2, D-55128 Mainz, Germany.*

*5Department of Nuclear Medicine, General Regional Hospital, Via L. Böhler 5, 39100 Bozen, Italy.*

*6 Department of Pathology, General Regional Hospital, Via L. Böhler 5, 39100 Bozen, Italy.*

*7 EURAC- Institute for Mummies and the Iceman, Viale Druso 1, 39100 Bozen, Italy.*

*8 Department of Earth and Environmental Sciences, Ludwig- Maximilians- Universität München, Schellingstraße 4, 80799 Munich, Germany.*

*9 Center for NanoSciences, Ludwig- Maximilians- Universität München, Schellingstraße 4, 80799 Munich, Germany.*

*10Zentrum für Evolutionäre Medizin, Zürich Irchel- Universität, Winterthurerstraße 190, 8057 Zürich, Switzerland.*

Key- words: bog bodies, dyschondrosteosis, dicrocoeliasis, The Netherlands

### **Abstract**

The bog corpse of an adult female individual dating to the Roman period (78- 233 AD) was unearthed, in 1951, by peat cutters in the “Damsel’s Bog” northwest of the village of Zweeloo (Drenthe province, The Netherlands).

Even if shrunken and deformed by the prolonged stay in the bog, Zweeloo Woman’s skeleton shows clear signs of a pathologic disorder affecting both the forearms and lower legs.

Long bone measurements, stature assessment and PET-CT scan were carried out to assess the degree of micromelia and possibly dwarfism. The radiological findings were consistent with L ry-Weill dyschondrosteosis (DSC), a dominantly inherited dysplasia marked by short stature with mesomelic shortening of middle segments of the forearms and lower legs. Only three cases of probably or indicative DSC have been described so far in pre-modern societies. This is the first case of DSC syndrome recognized in a 2nd century bog body from The Netherlands.

Atomic force microscopy imaging (AFM) and histology were used to assess the degree of preservation. AFM of the skin showed evidence of a moderate decomposition of type I collagen fibrils. A good state of preservation of bones and abdominal organs was shown histologically. The eggs of the lancet liver fluke *Dicrocoelium dendriticum* were found embedded in the liver parenchima. Dicrocoeliasis is contracted by the oral uptake of infected ants attached to vegetables. This infection is quite rare in humans and has never been described in a bog body.

 Literature reports that a substantial number of the individuals that were found in bogs died a violent death. At least 21 cuts made by a short blade to the Zweeloo Woman bones were found. Nonetheless, there's no evidence of trauma except possibly to the posterior aspect of the left shoulder, on the outer skin surface. Whether Zweeloo Woman was intentionally killed or died a natural death still remains unclear.

## 1- The discovery

On December 5 1951, peat cutters working in 'Juffersveen' ('Damsel's Bog') northwest of the village of Zweeloo in the Dutch province of Drenthe discovered a bog corpse (Van der Sanden 1990a, 70). The Mayor of Zweeloo was informed of this remarkable discovery and he contacted the Biologisch-Archaeologisch Instituut (Institute for Biology and Archaeology)[1] of Groningen University. The next day, Prof. Dr. A.E. van Giffen and his assistant W. van Zeist visited the site. They soon discovered that they were too late. The peat cutters had already dug up the human remains and had severely damaged them in the process, especially the front side of the body. All the archaeologists could do was study the peat section at the findspot. The peat layer was only 60 cm thick. The upper half consisted of poorly humified light brown peat, the lower half of highly humified blackish brown peat. The peat cutters said they had found the body at a depth of 45 cm, i.e. in the blackish brown peat. The section next to the spot where the body had been found was systematically sampled for pollen analysis. The human remains were placed in a large zinc box and taken to Groningen. Van Giffen explained to journalists that he certainly did not expect the body to be two thousand years old.

## 2- The post-excavation research (1955-1995)

In 1952 Van Zeist published a short article in German on the bog find. He stated that analyses of the human remains at the Laboratorium voor Anatomie en Embryologie (Laboratory for Anatomy and Embryology) had shown that they represented a female who was approximately 170 cm tall).[2] He also discussed the pollen diagram, noting a remarkable hiatus: subatlantic peat lying directly on top of boreal peat. He wrote that he took a pollen sample from 'between the toes of the undamaged foot'. The results of the analysis confirmed the peat cutters'

statement that they had found the body in the lower layer of blackish brown peat. According to Van Zeist this implied that the woman lived in the first centuries AD.

Van Zeist finally mentioned that the intestines contained many husks of millet (*Panicum miliaceum*) - an observation that did not contradict the find's palynological date.

Four years later Van Zeist (1956) published some new information. The woman's hair had been cut around the time of her death and her body had been deposited in an old turf cutting (which would explain the conspicuous hiatus in the pollen diagram). The time of deposition, he estimated, was 'after AD 200'. After that, Zweeloo Woman sank into oblivion for at least 30 years.

In 1985, the skin and intestines were presented to the Drents Museum in Assen. The skin is far from complete: the lower arms and hands, the lower legs and feet and the neck and head are missing (the head is represented by only a few small pieces of skin with attached hair with a length of 2.5- 3.5 cm). All that remains of the front side of the body are some loose pieces of skin. The manubrium and corpus of the sternum are still attached to one of the pieces. The skin and intestines were stored separately from the bones, which may have come into the museum's possession at an earlier stage (but when that may have been cannot be inferred from the museum's inventories).

In 1987, one of the authors (WVDS) launched a major bog body research project (Van der Sanden, 1990). The first and main aim was a totally fresh analysis of the preserved corpses and the finds associated with them. Lack of information and the fact that the bones had been stored separately from the other remains of Zweeloo Woman had led to the conclusion that the two were separate finds. The bones were thought to represent a skeleton that had been found in part of Bourtanger Moor called Aschbroeken (near Weerdinge) in 1931, and they were published as such (Van der Sanden 1990b, 89- 90).

The physical anthropologist dr. H.T. Uytterschaut of the Laboratory of Anatomy and Embryology of Groningen University analysed and described the remains (Uytterschaut 1990b, 115- 117, 122- 123). She singled out five bones of the 'Aschbroeken skeleton' as differing from the others in colour and consistency. They are a first rib (from the left side), the first and second cervical vertebrae and a thoracic and a lumbar vertebra. It was assumed that those bones derived from the same body as the surviving remains of skin and intestines, i.e. the Zweeloo bog body. Uytterschaut concluded that it was not possible to infer the individual's sex from the skin remains. If the five bones indeed came from the same body as the skin, they indicated a person of at least 35 years old, as the lumbar vertebra shows lipping.

The 'Aschbroeken skeleton' could be sexed more easily. The shape of the pelvis and the size of the processus mastoideus indicate that the individual was female. Her age at the time of death was estimated on the basis of various observations. Epiphyseal union in the long bones, pelvis and scapula indicates a minimum age of 25, the morphology of the pubic symphysis points to an age of between 30 and 60, and the sutures of the skull imply an age of between 20 and 30.

Histological analysis (Uytterschaut 1985) of a thin section of the shaft of the left femur indicated that 'Aschbroeken Woman' died at an age of  $34 \pm 7$  years. All this evidence led to

the conclusion that the age at the time of death was probably around 35 years (Uytterschaut 1990b, 117). The marked differences between some of the bones of the left part of the skeleton and their counterparts on the right side (e.g. the pelvis) caused a lot of discussion, as the observations were not in accordance with any known physical disorder. Postmortem deformation was suggested as the most likely explanation (Uytterschaut 1990c, 132- 135). On the basis of the bones of the right side of the body the individual was estimated to have been around 1.38 m tall, but at the same time it was assumed that this would not be entirely correct due to postmortem shrinkage (Uytterschaut 1990a, 102).

Both the 'Zweeloo skin' and the 'Aschbroeken skeleton' were radiocarbon dated. The date of the skin is  $1835 \pm 40$  BP (GrN-15458), that of the skeleton  $1940 \pm 70$  BP (OxA-1727) (Van der Sanden 1990c, 98).

In August 1992 the real Aschbroeken skeleton was discovered in the stores of the Biologisch-Archaeologisch Instituut.[3] It is the skeleton of an adult man dating from around 1000 BC (Van der Sanden, Haverkort and Pasveer 1991-1992). This could only mean that the previously described skeleton belonged to the Zweeloo bog corpse.

The skin was re-examined, and this time a small piece of bone was discovered, deriving from the shoulder region of the left side of the body. The edge of this piece of bone was found to mirror the edge of the skeleton's incomplete left scapula (the two parts could not be fitted together due to distortion). Furthermore, dr. M. Voortman and his associates of the Laboratorium voor Gerechtelijke Pathologie (now Nederlands Forensisch Instituut/Dutch Forensic Institute) in Rijswijk identified the vulva, navel and a breast (right side). These results support the assumption that the bones and skin derive from the same individual. A final argument is that the otherwise largely complete skeleton lacks a breastbone.

Until 1994 our understanding of the Zweeloo bog body was as follows. The body is that of an adult female person. She was probably of blood group O (Connolly 1990, 148) and suffered parasitic infections caused by whipworm (*Trichuris*) and mawworm (*Ascaris*) (Paap 1990, 164-166). Her last meal consisted of a gruel whose main ingredient was coarsely ground common millet (*Panicum miliaceum*). The presence of a large quantity of blackberry pips (*Rubus fruticosus*) indicates that she died in late summer/early autumn. In addition, the intestines contained remains of *Polygonum lapathifolium* (curlytop knotweed/pale smartweed), *Polygonum aviculare* (knotgrass), *Brassica* sp. (black mustard or rapeseed), *Linum usitatissimum* (common flax), *Bromus* sp. (grass), *Triticum* sp./*Secale* sp. (wheat or rye), *Hordeum* sp. (barley), *Avena* sp. (oat), a few animal hairs and the wing case of a beetle (*Tenebrio obscurus*) (Van der Sanden 1990d, 136; Hakbijl 1990, 170-171; Holden 1990, 265-269). Analysis of pollen samples from the intestines confirmed the macroscopic results (Troostheide 1990). No DNA was found in the skin or kidney (Osinga and Buys 1990; Osinga, Buys & Van der Sanden 1992). The woman's hair was cut around the time of her death (Uytterschaut 1990d, 136). Zweeloo Woman lived in the Roman period. The average of the two aforementioned radiocarbon dates is  $1861 \pm 35$  BP (calibrated  $2\sigma$ : 78-233 cal AD).[4] How she died we do not know; no signs of any external violence are visible on her skin. She was buried in a pit in a bog, probably naked.

In 1994 dr. R.W. Stoddart of the Department of Pathological Sciences of Manchester University expressed his doubts about the deformed bones being simply a case of



pseudopathology. He closely examined the skeleton, measuring and weighing the bones and subjecting some of them to soft X-rays and tomographic scanning, and came to the conclusion that the asymmetry is indeed a postmortem development, but the short forearms and lower legs are on the contrary to be classified as a pathological phenomenon (Figure 1).

Figure 1- Zweeloo Woman's preserved skeleton (a) and skin (b). In (c) and (d) the shortened and bowed forearms and lower legs are shown.

The conclusion of his report (Stoddart 1995), in which he describes the skeleton as that of a woman aged 16-24, is as follows. [5]

‘The cadaver shows shortening of the forearms and lower legs by about 50% relative to normal, and corresponding low weights of demineralised bones of these parts. Apart from a mild degree of malformation of the radii, the affected bones are short rather than distorted. There is no remaining evidence of nutritional deficit or infectious illness and no other part of the skeleton appears to be affected. The girdles, proximal portions of the limbs, hands and feet show no abnormality of size, though there is evidence of reactive change in the bones of the feet consequent upon the inevitably abnormal gait.’

Several conditions can be excluded. This is not a case of hypopituitary dwarfism, since it is not a generalised failure of growth. Similarly, it is not a phocomelic type of dwarfism, since only a specific segment of each limb is involved and the skull is unaffected. The normal hands and feet argue against an effect of the ‘thalidomide-injury’ type, for example following a viral infection. An ‘anti-Marfan’ type of syndrome can also be excluded, since the equivalent segment is involved in each limb and the skull, hands and feet are spared. There is no evidence of nutritional or infectious cause and the localised nature of the abnormality argues against these. The most probable class of disorder in this case is dyschondrosteosis. This develops during later childhood and adolescence, for unknown reasons, producing the type of malformation seen here. The name is purely descriptive and may cover several syndromes. The condition is rare and the origin (or origins) appear to be genetic.’ (Stoddart 1995, 9). This diagnosis was quoted in the book accompanying the bog body exhibition that was held in Silkeborg, Denmark, in 1996 (Van der Sanden 1996, 140-141).

Stoddart also provides detailed information on the position of the body in the peat: ‘It is likely that the body lay on its right side in the marsh, in a somewhat ‘fetal’ position, but with the arms and legs more extended. The right arm was fairly straight, the left more bent and the right forearm lay on top of the left wrist, so that the thumbs of both hands pointed outward. The right leg was more bent than the left and lay beneath and in front of it, so that the right heel was close to the left ankle. The pelvis was probably tilted slightly back, or at least was not inclined downwards. In general the left side – which I hypothesise to be uppermost – has suffered greater damage by cutting, while the right side of the pelvis, the right scapula and the right side of the skull show more evidence of pressure distortion than does the left side.’ (Stoddart 1995, 7).

### 3- The findspot

At the time of discovery, little information was recorded on the findspot of the Zweeloo bog body. In his daily reports, Van Zeist refers to 'Juffersveen' and 'a small peat bog', but without specifying its size and location. Contemporary newspaper reports also refer to the findspot as 'Juffersveen'. Thanks to information provided by the then Mayor Greebe the site of the former bog was located on a map in 1988 (Van der Sanden 1990a, 70). It lies in an area known as Aalder Veld northwest of the village of Aalden (in those days part of the municipality of Zweeloo, now of the municipality of Coevorden).

According to members of the local historical society, Juffersveen lay a little further south than the area indicated by Greebe. On a land-consolidation map they sketched a bog measuring around 400 x 200 m extending on either side of Gebbeveenweg.[6] Their bog coincides reasonably well with an elongated NW-SE-oriented bog measuring approximately 350 x 125 m that is indicated on a topographic map from around c. 1900 (Wieberdink 1990, sheet 224).[7] If this is indeed Juffersveen, and considering that Mayor Greebe indicated the findspot as lying immediately to the west of Gebbeveenweg, it is likely that the body was buried in the central part of the bog. Aalder Veld incidentally contained quite a few more small bogs, one of which was called Diepveen.[8] It lay close to Juffersveen, whose name – 'Damsel's Bog' – is thought to refer to a legend featuring a girl on the run who allegedly perished miserably in the bog many centuries ago.

#### **4- Other bog bodies from Zweeloo**

Zweeloo Woman is not the only bog body from Zweeloo – that is, if the sources are reliable. An early source (Drie Podagrissen 1843, 197-198) reports the discovery of a body in a small bog near Zweeloo. It is described as the body of a woman 'whose clothing and adornments suggest she was a lady of high rank'. The body is said to have come to light around 1820. 'A simple peasant had come across it while cutting turfs or sods at the site. First an arm had emerged from the peat, but closer inspection showed that the shocked man had actually already dug up the entire body; he then threw down his spade and fled from the scene as fast as his legs would carry him. The body should still be in the aforementioned bog pool, though its exact location is unknown.'

Although it is not entirely clear by whom the aforementioned source was written, and moreover doubtful whether the described hike actually took place, there are no compelling reasons to doubt the reported discovery of a bog body near Zweeloo. To the best of our knowledge this is the earliest report of a body found in a bog in the northern part of the Netherlands. So it is not very likely that the author or authors were 'inspired' by an earlier find. But whether details such as the quoted 'adornments' are correct is by no means certain. Ornaments are hardly ever found in association with bog bodies. It is quite possible that the true elements of the find gradually acquired a fictional veneer over the years in which the tale of its discovery was passed on orally.

Another source reports a bog body that was allegedly found near Zweeloo in 1956. The informant concerned thought he could recall having seen the body shortly after its discovery. The findspot is believed to have lain around 500 m southeast of that of the bog body that had come to light in 1951. The body was found in the context of the land consolidation of Aalderveld and Mepperveld (1940- 1961). The peat cutters laid the body beneath a dump cart,

presumably in the hope of hushing up their discovery. The body was most likely thrown back into the bog (Van der Sanden 2002, 178).

## 5. New set of investigations on Zweeloo woman's remains

Since 2009 a multidisciplinary team of researchers re-examined the human remains of Zweeloo Woman. A variety of analyses were carried out (PET-CT scan, AFM, histology) with the aim of confirming or infirming the previous diagnosis of dyschondrosteosis and to verify the overall state of preservation of both hard and soft tissues. Herewith we provide an overview of the latest findings.

### 5.1 On bone shrinkage, measurement, stature and tissues preservation

A major problem in interpreting the abnormalities of the Zweeloo Woman has been the difficulty of determining how far shrinkage has occurred following bone decalcification. Clearly this is important to try and resolve in order to assess the degree of micromelia and possible dwarfism which might have occurred.

It seems likely that the skull illustrates well the reduction of size which has occurred in some parts of the body (Figure 2). The frontal arc (85 mm) is likely to be 25 mm smaller than even small measurements for female skulls in northern Europe (BOT, 1957). Similarly, the sagittal arc (93 mm) is 20 mm lower than usual for small skulls (BOT, 1957).

Figure 2- Zweeloo Woman's "exploded" skull (a) and a particular of the frontal bone (b) which shows signs of a cut made by a short blade above the left orbit.

It is very unlikely to be indicating microcephaly, a condition which does not normally reduce facial dimensions, but in this case palate length (30 mm) is 15 mm less than usual. If we consider ratios of humerus to radius length and femur to tibia, then normally the arm in Europeans would show a ratio around 1.4: 1.0, but in this case it is 2.2: 1.0. For the leg, the normal ratio is about 1.2: 1.0, but the Zweeloo ratio is 1.6: 1.0. So reduction in both forearms is considerable, but the length ratio difference in the lower leg is far less and also shows a side to side asymmetry (the right leg ratio is 1.28: 1.0). In the case of congenital reductions in longitudinal segments of the limbs in some forms of micromelia, forearm reductions can produce ratios of 1.8: 1.0 (personal radiographic observation), which is similar to the Zweeloo ratio.

Estimating dimensions from the outer body surface of the Zweeloo Woman, taking measurements close to those defined by the Board of Trade, London (1957), a stature estimate of 155 cm was obtained (allowing for head and foot damage). It should be noted that in a sample of 4,995 British women (BOT, 1957), 2,438 (49%) were between 141-159 cm, so these are not to be viewed as dwarfed statures. Thus, it is not possible to describe the Zweeloo Woman as an example of mesomelic dwarfism. Approximate dimensions of other body measurements were also obtained on the Zweeloo Woman, and are tentatively presented in Figure 3.

Figure 3. Estimated dimensions of the Zweeloo Woman compared to a northern European sample.

Overall length of the trunk appears to be similar in the Zweeloo Woman and the British average for 30- 44 year olds (BOT, 1957). But leg length seems to be shorter (allowance having been made for the damaged feet). Interacromion width could be slightly larger than average in the Zweeloo Woman, but her waist circumference appears to be slightly smaller than the modern European mean. But neither difference is significant.

Post-cranial measurements, as seen in Table 1, were taken separately by three authors (RB, DMP and DB). The stature estimation was calculated following the regressions of Pearson (1899), Trotter/Gleser, white (1952), Trotter/Gleser, negro (1952) and a mean of Trotter/Gleser, white (1952), Trotter/Gleser, negro 1952 and Pearson (1899) as suggested by Siegmund (2010) for central European populations.

The stature was estimated based on the maximum and the minimum measurements taken by the observers as well as on a mean of the two observers. The radius was not considered to the measurements since it is abnormally short and its value would artificially affect the stature estimation.

Table 1 – Measured length of bones (in cm) of Zweeloo Woman

Additional to the stature the body proportions were also calculated after Martin 1928 (Table 2). This enables us to configure the unusual proportions of the Zweeloo Woman. Both the FHI and FTI are significantly lower compared to central European populations which vary (Siegmund 2010, p. 62, 64). The HRI shows extreme low due to the abnormal shortening of the radius.

Table 2 – Body proportion estimation of the Zweeloo Woman

The stature estimation from bones of the Zweeloo Woman ranges from 130 to 135 cm when both humerus, femur and tibia are being considered, and 137 cm to 141 cm when the tibia is not considered (Table 3).

Table 3 – Stature estimation from bones of the Zweeloo Woman

The Pearson method would be the most appropriate among the estimation methods since the reference series used corresponds in terms of body proportions better the European populations (Siegmund 2010) and Pearson considers in the regression all long bones. On the contrary, Trotter and Gleser consider only the tibia and only in case that the tibia is not available, they use the femur. This calculation would produce artefacts in the case of the Zweeloo Woman due to the short length of the tibia and the curvature of the femur.

Comparison to a long dataset of archaeological population from central Europe contemporaneous to the Zweeloo Woman show that she is significantly shorter than the mean (153,3 cm) of the female population for this period (Siegmund 2010). Considering however the standard deviation and the interquartile range, 96% of the female population for this period ranges from 144.3 to 162.3 cm. Taking into account the bone shrinkage that is a common effect on bog bodies the stature of the Zweeloo Woman could be considered short but within normal limits.

Based on the stature estimation and the femur head diameter the Body Mass Index of the Zweeloo Woman was calculated. For the Body Mass was used the formula of Auerbach and Ruff (2004) which is actually a mean of Ruff et al., (1991), Mc Henry (1992) and Grine et al., (1995) together with the stature estimation after Pearson. The Zweeloo Woman exhibits normal BMI values compared to modern data from the World Health Organisation (WHO), according to which values from 18.50 to 24.99 fall within the normal weight range (Table 4).

Table 4 – Body Mass Index estimation of the Zweeloo Woman

## 5.2- Radiographic aspects

A single radiographic evaluation of the entire skeleton was performed in 16 layers, using a CT scanner (PET/CT Gemini TF, Philips, NL). Scanning parameters were: slice thickness 0,8 and 1 mm; reconstruction interval 0,75 mm, rotation time 0.5 sec. The whole number of axial slices was 1378. Post-processing including axial scans evaluation and multiplanar reconstructions was performed with a Workstation EBW Brilliance (Philips, NL).

Determination of sex was based on parts of the skull and on the pelvis (Leopold, 1998; White and Folkens, 2005). The following bones are entirely preserved: frontal bone, right and left parietals, a fragment of the left temporal bone and a fragment of the jaws. The reduced dimensions of the skull bones are due to post-mortem shrinkage and not microcephaly. True microcephaly does not result in such pronounced reductions of the face.

The very small mastoid process of the skull and the shape of the pelvis (greater sciatic notches, longer pubic portion of the os coxae, larger subpubic angle, auricular surface more elevated) indicate that the individual was a female. The age at death has been tentatively established on the basis of various observations. Epiphyseal union in the long bones, pelvis and scapula indicated a minimum age of 25, while the morphology of the pubic symphysis points to an age between 35 and 50 (Leopold, 1998).

Regarding the post-cranial skeleton, it has almost entirely preserved even if a marked difference in size is observable between some bones of the left side of the body and their counterparts on the right side (i.e. the pelvis, the heel bones and the femora). Since these observations did not fit any pathological disorder, post-mortem deformation is suggested as the major cause of these differences. As a matter of fact, bones of bog bodies are often distorted and squashed during interment like in Lindow II and Lindow III (Pyatt et al., 1991; Schilling et al. 2008).

Both proximal and distal epiphyses of the right humerus and the preserved distal epiphysis of the left humerus are normal in shape and structure. Right and left forearms show partially deformed and under-developed epiphyses. Left and right radii are shorter than normal and moderately bowed.

The left femur is fractured and level with the fracture edge of its distal epiphysis, a small radiopaque body (1.5-2 cm, HF density between 1.000 and 2.000) is observable. This structure seems to be an intrusive stone (Figure 4).

Figure 4- Results of PET-CT scan performed on Zweeloo Woman's skeletal remains. The viscera have been positioned between the lower limbs.

Concerning the lower limbs, both lower legs appear to be hypo-developed when compared just to the femora. This difference, however, is less evident than the one observed in the forearms. Both right femora and right fibulae show a marked bowing. Coxa valga is present. The left leg appears to be shorter than the counterpart. If asymmetry is indeed a post-mortem development, the special shortening of forearms and lower legs are on the contrary to be classified as a pathological phenomenon known as dyschondrosteosis.

Proximal portions of the limbs, hands and feet show no abnormality of size, though there is possible evidence of reactive change in the bones of the feet consequent upon some degree of abnormal gait. There is no remaining evidence of nutritional deficit or infectious illness and no other part of the skeleton appears to be affected.

The diagnosis of L ry- Weill dyschondrosteosis rests on the radiological findings (Langer, 1965). In living patients, the X-ray features of dyschondrosteosis show a wide spectrum of manifestations which include: 1- shortening of the forearm in respect to the upper arm and hand; 2- dislocation of the distal ulna which cannot be maintained in position; 3- limitation of motion at the elbow and wrist; 4- shortening of the shank in relation to the upper leg which results in a mild dwarfism. This pattern of shortening in the middle segment of extremities is referred to as mesomelia.

The most prominent abnormality of dyschondrosteosis is in the wrist causing the so-called Madelung's deformity. Twelve roentgenographic criteria are used for the diagnosis of Madelung's deformity, three of which are of utmost importance: 1- a double (lateral and dorsal) bowing of the radius which involves the entire diaphysis but is more marked at the distal end; 2- a variable widening of the inter-osseous space due to lateral curvature described

above; 3- shortening of the radius as compared with the normal standard for age and in relationship to size of the other bones of the upper extremity.

In Zweeloo Woman not all carpal bones have preserved. However, the three main criteria aforementioned could be identified in her skeletal remains and might lead us to suppose, by inference, the presence of such a deformity.

Other roentgenographic features which are not part of Madelung's deformity but which have been present in some severely affected patients with dyschondrosteosis are: thickening of long bones, shortening and thickening of the metacarpal and phalanges, coxa valga, exostosis of the proximal medial tibia, and cubitus valgus. The skull, the spine and the pelvis are radiologically normal in all cases described in the literature in which these bones have been studied Zweeloo Woman included.

Differential diagnosis should include other deformities of the distal forearm. Closely simulating the deformity of dyschondrosteosis is post-traumatic fusion of the ulnar aspect of the distal radial epiphysis, but Zweeloo Woman does not show any sign of such traumatic lesions.

Less commonly, infection may result in a similar deformity. The deformity is almost always unilateral in these cases. As shown in all published cases, dyschondrosteosis may be asymmetric as regards involvement, but, invariable, the criteria of dyschondrosteosis are present radiologically, in both forearms and wrist regions.

This is not a case of hypopituitary dwarfism, since it is not a generalised failure of growth. In achondroplasia, the most common form of skeletal dysplasia, the limbs are all shortened, femur the most, then the humerus, then the bones of the lower legs and forearms. Adult stature rarely exceeds 140 cm.

### **5.3- Evidence of perimortal or post-mortem injuries**

There are at least 21 cuts to bones of the skeleton. Most cuts were short and clearly made with a sharp blade. There is no evidence of bone reaction to these injuries, and no equivalent injuries on the body surface. The distribution of these injuries is shown in Figure 5.

Figure 5- Distribution of cuts on the Zweeloo bones

Briefly, the positions were as follows: (1) frontal, above the left orbit (Figure 2b), (2) two on the inner aspect of the scapula blade, (3) a left hand phalanx and proximal phalanx of the left thumb, (4) the left femur below the trochanters (2) and at the knee, (5) at the proximal articular end of the left tibia, (6) two at the distal end of the right humerus, (7) three on the right radius and one on the right ulna, (8) two on the right femur, in the upper and lower thirds of the shaft, (9) two at the proximal end of the right tibia and two more along the shaft. What is extremely puzzling about these injuries is that there is no evidence of trauma, except possibly to the posterior aspect of the left shoulder, on the outer skin surface. So how were

they caused? It seems unlikely that the bones were cut out from within the body, as they were probably loose within the skin anyway. Are they accidents of conservation? This seems highly unlikely.

#### **5.4- Pathology**

Excluding the various cuts, and the congenital anomaly under discussion, a number of other cases of pathology were noted. The pelvis displays some long deep grooves on the left iliac blade which seems likely to be post-mortem shrinkage and distortion. Two upper thoracic and four lumbar vertebrae display varying degrees of Schmorl's nodes impressions. These were originally thought to have no clinical significance, but could well have associations with osteo-arthritic development, back stress and pain (Aufderheide and Rodriguez- Martin, 2006).

#### **5.5- Genetic and clinical aspects**

The radiological findings could indicate Léry-Weill dyschondrosteosis. Léry-Weill dyschondrosteosis (LWD) is a dominantly inherited skeletal dysplasia marked by disproportionate short stature and the characteristic Madelung's wrist deformity. LWD is inherited in a pseudo-autosomal dominant manner with each child of an affected individual having 50% chance of inheriting the mutation. Prevalence is unknown.

Short stature is present from birth with mesomelic shortening of the limbs (shortening of middle segments of the forearms and lower legs). Madelung's deformity may only be detected in puberty. The wrist deformity is bilateral and is characterised by shortened and bowed radii and ulnae leading to dorsal dislocation of the distal ulna and limited mobility of the wrist and elbow.

LWD was first described by Léry and Weill in 1929 in French literature and, since that time, occasional reports have appeared in French, German and Spanish literature (Léry-Weill, 1929; Langer, 1965). Although the disorder occurs in both sexes, it is usually more severe in females, perhaps due to sex differences in oestrogen levels (Lichtenstein et al., 1980).

However, pubertal development and fertility are generally normal in both sexes with the disorder (Ross et al., 2005). Intelligence is normal. In around 70% of cases, LWD is caused by haploinsufficiency of the short stature homeobox (SHOX) gene, which maps to the pseudoautosomal region 1 (PAR1) of the sex chromosome (Xp22.23 and Yp11.32) (Belin et al., 1998; Shears et al., 1998; Ross et al., 2001, 2003; Huber et al., 2001; Grigelioniene et al., 2000; Benito-Sanz et al., 2005).

Haploinsufficiency results from heterozygous mutations and deletion of SHOX, or of the downstream PAR1 (where SHOX enhancer elements are located). The molecular defect remains unknown in the remaining 30% of LDW cases. SHOX-associated LWD is part of a spectrum of disorders (ranging from the most severe Langer mesomelic dysplasia (LMD) to LWD, isolated Madelung deformity and so-called idiopathic short stature) all associated with SHOX/PAR1 abnormalities. The prevalence of SHOX/PAR1 mutation is estimated at 1/1000. Diagnosis of LWD is suspected on the basis of the clinical and the radiologic findings and will be investigated in a follow-up study by molecular analysis.



Achondrogenesis and thanatomorphic dysplasia, as well as captomelia dysplasia, are excluded from a differential diagnosis, since affected people die stillborn or at birth, or within the 1st year, respectively. Pseudoachondroplasia is excluded as well since it is prominent at the hips (femora) and shoulder (humeri), with irregular epiphyses and widened metaphyses resulting in premature degenerative joint disease (Aufderheide and Rodriguez Martin, 2003). Similarly, it is not a phocomelic type of dwarfism, since only a specific segment of each limb is involved and the skull is unaffected. The normal hands and feet argue against an effect of the 'thalidomide-injury' type, for example following a viral infection. An 'anti-Marfan' type of syndrome can also be excluded, since the equivalent segment is involved in each limb and the skull, hands and feet are spared.

## 5.6 Other case studies

Different cases of probable skeletal dysplasia in pre-modern societies have been previously described. The principal cases shown in literature are chronologically ranging from the Upper Paleolithic to the Middle Ages but none is referring to a bog body. The principal cases are listed below:

An upper Paleolithic individual from Italy represents the earliest case of dwarfism associated to Madelung's deformity. Other indications in this skeleton indicate that he did not possess DSC but a different form of dwarfism, an acromesomelic dysplasia, which is much more severe than DSC. The stature of this individual was estimated 1.0 to 1.30 m only (Frayer et al., 1987).

A 2nd- 3rd century AD young woman from the Talayotic site of 'S. Illot de Porros' from Mallorca (Campillo and Malgosa, 1991) who shows a bilateral brachymelia with bowing of the radius and posterior dislocation of the ulna consistent with a probably Madelung's deformity.

A mature adult male (45-50 years), the Donori man, dating to 2800 BC from Nuragic Sardinia. The main pathological features affected both forearms. Both were characterised by marked shortness and by morphological alteration of the distal epiphyses. Some major changes involved the radii whose diaphysis were shortened and strongly bowed. However, lower legs were not preserved and, therefore, the presence of mesomelia could not be evaluated and an aetiology of DCS cannot be stated with certainty (Canci et al., 2002).

A 2nd- 3rd century AD 20-25 years old male skeleton from Gloucester. The most significant abnormalities were Madelung's deformity affecting the right radius (the only one which survived the recovery sufficiently well for examination), an abnormal right humerus, curved and shorter ulnae and mesomelia suggesting a probably diagnosis of dyschondrosteosis (Waldron, 2000).

A 6th century AD 60 years old female skeleton from Geneva, Switzerland, demonstrated the forearms changes and may be an example of DCS (Kauffman et al., 1979).

A 7th century male aged between 18-20 years from the Pieve di Pava, Siena, Italy, whose skeleton shows a stature of about 150 cm with short and bowed radii, bilateral deformation of the proximal and distal epiphyses of radii and ulnae, bilateral bowing and shortening of the

tibiae and bilateral agenesis of the fibulae. These deformations are suggestive of Langer syndrome (Mongelli et al., 2010).

A 9th- 11th century Anglo-Saxon female from Black Gate cemetery, Newcastle-upon-Tyne. The age at death was estimated between 35-44 years. This skeleton revealed deformity of both forearms and shortened stature due to reduced tibial length. These were considered indicative of dyschondrosteosis (Cummings and Rega, 2008).

An 11th -13th century adult male skeleton from the Hispano-Muslim necropolis of San Nicolás de Murcia. The deformities of the forearms are quite similar to those of the Donori man, especially those concerning the cavity on the medial distal epiphysis of the radius (Campo et al., 1996).

A medieval elderly male from the Saint Gregory's Priory, Canterbury, Kent. In this case, there's no evidence of dysplasia. The right radius and ulna were shortened due to premature fusion of the distal growth plate. The radius displayed lateral and dorsal bowing and the ulna was dislocated posteriorly. The unilateral presentation, shortening of the ulna and atrophy of the hand bones suggest a post-traumatic rather than an idiopathic form of the Madelung's deformity. The normal length of the lower legs is against a diagnosis of dyschondrosteosis and Madelung's deformity associated with mesomelic dysplasia (Anderson and Carter, 1995)

Only three cases of probably or indicative DSC have been described so far. Zweeloo Woman's skeletal remains (upper and lower limbs) show a marked dysplasia consistent with a mesomelic abnormality and provide the first robust evidence for Léry-Weill syndrome in a 2nd century bog body from The Netherlands.

### **5.7- Analysis of the preservation status of the connective tissue protein collagen**

Atomic force microscope (AFM) imaging, a well established technique to provide information on the surface properties of a sample, was used to determine the collagen preservation in histological skin samples of the Zweeloo Woman.

Two- four  $\mu\text{m}$  thick transverse sections of the Zweeloo mummy skin were analysed using an atomic force microscope (NanoWizard®II, JPK Instruments, Berlin, Germany) operating in intermittent contact mode and measurements were performed in ambient conditions. Silicon cantilever (BS Tap 300, Budget Sensors, Redding, USA) with typical spring constants of 40 N/m and nominal resonance frequencies of 300 kHz were used. The tip radius was specified smaller than 10 nm. Image analysis was carried out using SPIP (SPIP 5.0.1.0, Image Metrology, Denmark).

AFM images revealed fibrils with periodic banding patterns (Figure 6, 7, 8, 9, 10) embedded into the tissue matrix. The average D-period, derived from topographic analysis along the longitudinal axis of several fibrils, was 62.8 nm ( $\pm$  4.2 nm s.d.). The fibrils were unsorted, overlapping at some sites and formed network like structures.

Figure 6- Type I collagen fibrils within the histological skin sample. (a) Zweeloo Woman tissue imaged with an optical microscope (magnification 10x). Figures (b) to (d) show

magnifying AFM amplitude images of the areas outlined. In (d) single fibrils with a periodic structure are shown.

Figure 7- Type I collagen fibrils within the histological skin sample. (a) Zweeloo Woman tissue imaged with an optical microscope (magnification 10x). Figures (b) to (d) show magnifying AFM amplitude images of the areas outlined. In (d) unsorted and overlapping fibrils in a network like structure are shown. Each fibril features a periodic substructure.

Figure 8- Representative images of type I collagen found within the histological skin sample of the Zweeloo Woman. (a) Histological tissue sample imaged with an optical microscope (magnification 10x). Figures (b) to (d) show AFM amplitude images of selected sample areas as labelled. In the image with highest resolution (d) single fibrils with a periodic substructure are revealed.

Figure 9- AFM topography and amplitude images of type I collagen found within the histological skin sample of the Zweeloo Woman. In figure (a) ( $2 \times 2 \mu\text{m}$  in size) collagen fibrils with their characteristic banding pattern are revealed. The fibrils form a network like structure and sometimes overlap. Contours of the fibrils are faint. The amplitude image (b) shows the fibril contours in more detail.

Figure 10- AFM topography and amplitude images of type I collagen found within the histological skin sample of the Zweeloo Woman. In figure (a) ( $3 \times 3 \mu\text{m}$  in size) fibrils in a network like structure are revealed. The contours of the fibrils are faint. The amplitude image (b) shows the fibril structure in more detail. The characteristic banding pattern of collagen is resolved.

The higher magnification images (Figure 6, 7, 8, 9, 10) show collagen fibrils without breaks although spherical particles may indicate collagen fragments. Moreover the fibril contour structure is very faint. Topographic analysis perpendicular to the longitudinal axis of several fibrils suggests a mean fibril height of  $12.2 \text{ nm} (\pm 3.6 \text{ nm s.d.})$ .

Type I collagen is extremely durable and can be preserved in mummified tissue over millennia (Chang et al., 2006; Janko et al., 2010). This observation also proves to be true for the structural preservation of the skin collagen from the Zweeloo mummy. Alike in recent and other mummy skin samples, the collagen fibrils in the skin of the Zweeloo Woman are typically arranged in networks or in sheet like structures and they feature a periodic banding pattern.

Compared to results by Stücker et al (2001) who observed well preserved collagen bundles in the dermis of six bog bodies, our results however, indicate a moderate decomposition of the Zweeloo Woman type I collagen. The Zweeloo Woman collagen showed considerable differences in fibril contour and size to the type I collagen found in recent human skin or of other mummies.

High resolution images, taken with the AFM revealed soft outlines of the collagen fibrils indicating an inferior degree of collagen preservation. The characteristic banding pattern averaged to  $62.8 \pm 4.2$  nm and was thus smaller compared to the literature value of 67 nm. The average fibril height of 12.2 nm ( $\pm 3.6$  nm s.d.) was also reduced compared to the collagen fibril diameter of 32 nm as for e.g. Iceman skin collagen (Janko et al., 2010).

The reduction in fibril height may be caused by a decomposition of the collagen fibrils as observed in previous AFM studies (Paige et al., 2002; Bertassoni and Marshall, 2009) showing the degradation of type I collagen by enzymatic action e.g. by collagenase or papain-gel. It was suggested that the enzymes degrade the entire fibrillar structure in a non-specific manner causing the fibrils to become both shorter and thinner.

An analogous effect may have occurred in the bog causing the type I collagen to be slightly degraded and thus reduced in size. The different degree in degradation is most probable due to the composition e.g. acidic environment of the bog which conditions the preservation and the mummification process.

### **5.8 Histological analysis of bony material and viscera.**

Bone and viscera samples from Zweeloo Woman were processed for histological analyses in order to assess their state of preservation.

A bone sample was analyzed according to the protocol outlined by Maat and colleagues (Maat and Aarents, 2000); the intestine samples, liver and kidney, were typed according to their shape and internal localization in the mummy's bundle of viscera (Van der Sanden 1996). Small tissue biopsies (0.5 cm x 0.5 cm), that we macroscopically typed as liver and kidney tissues, were analyzed according to the methods described in Mekota and Vermehren (Mekota and Vermehren 2005).

After rehydration in Solution III for 48 h, samples were fixed for 24 h in 4% formaldehyde, dehydrated and finally embedded in paraffin blocks. The embedded samples were cut on a microtome in 3 $\mu$ m thick sections (Leica, RM2245). The paraffin sections were histochemically counterstained with either hematoxylin and eosin stain (H&E) or Gram stain (Mulisch and Welsch 2010).

Skeletal decalcification is the feature which is commonly shared by bog bodies. Decalcification can be so marked that bones or even the entire limbs can be grossly deformed on such hypocalcified extremities. Histology revealed a surprisingly good state of preservation of the bony material which showed important osseous organizations such as Haversian canals and lamellae (Figure 11) (Pyatt et al., 1991).

Figure 11- Ground section of the bone tissue. Bar = 20 $\mu$ m

The high degree of conservation of bone microstructure might indicate that the Zweeloo Woman body was recovered from a slightly acidic peat bog with higher bone tissue-preserving qualities compared to highly acidic highland peat bogs (Petska et al., 2010)

In bog bodies, in general, viscera do not preserve as well as skin does. Liver and kidney, the two organs in which the majority of the volume is composed of epithelial cells, show to be commonly reduced in size, deformed by the pressure of the peat bog layers or unrecognisable while lungs and intestinal wall (but not its lining epithelium) are probably the most common preserved, recognizable viscera (Aufderheide, 2003).

In our specific case, we were able to confirm the results of the initial macroscopic identification. The paraffin sections of the kidney displayed a perfect overview of the kidney tissue including major characteristic regions such as the cortex and the renal pelvis (Figure 12A). Additionally, tubules-like structures were identified in the renal corpuscle (Figure 12B).

Figure 12- Paraffin section of the kidney. (A) Kidney overview picture composed of three grouped pictures. The kidney capsule (□) and the renal pelvis (▲) are highlighted. Gram stain, bar = 100µm. (B) Detailed view of the kidney cortex with tubular profiles. Gram stain, bar = 10µm.

Compared to the kidney sample, the liver material appeared less well preserved. Nevertheless, liver parenchyma with polygonal shaped hepatocytes and connective tissue could be still clearly distinguished in the paraffin sections (Figure 13A).

Figure 13- Paraffin section of the liver. (A) Liver parenchyma with polygonal shaped hepatocytes (colored brownish) and connective tissue (colored purple). H&E stain, bar = 20µm. (B) Egg of *Dicrocoelium dendriticum* embedded in the liver parenchyma. Gram stain, bar = 20µm.

By far the most important finding of the histological analysis, however, is the relatively high load of eggs of the lancet liver fluke *Dicrocoelium dendriticum* observed in the liver paraffin sections (Figure 13 B).

The trematode *Dicrocoelium dendriticum* with its complex life cycle is known to infect only in rare cases the bile duct and the liver of humans (Otranto and Traversa 2002; Karadag et al., 2005). This “real” infection, the so called dicrocoeliasis, occurs by ingestions of the second intermediate host (ant). There exist numerous reports of the detection of *Dicrocoelium* sp. parasite eggs in ancient coprolite samples suggesting a long-term host-parasite evolution (Le Bailly and Bouchet, 2010). Nevertheless, detection of parasite eggs in human stool samples is in most cases not indicative for a “real” infection but rather may indicate a pseudoparasitism

due to the ingestion of undercooked infected liver (Magi et al., 2009). Here we provide suggestive evidence of a “real” *dicrocoeliasis* case in a bog body.

## 6- Possible archaeological significance

The new series of investigations carried out on this bog body confirm the previous diagnosis of dyschondrosteosis as the cause of the disabling defect which affected Zweeloo Woman during her life. While it is a matter for further debate as to why prehistoric bodies/skeletons are found in bogs, it is quite probable that some have sacrificial and ritual significance. In which case, was there a selection process by which victims were earmarked for death? And, if so, would visible body defects have been a criteria used in the selection process? Was the Lindow III individual selected because one hand probably displayed an extra digit (Brothwell and Bourke, 1995)? Was Yde Girl selected because of her scoliosis, Bolkilde Man because of his crippled condition and the Døjringe Men because of their defects in their upper arms (Van der Sanden 1996, 138-143)?

The Zweeloo Woman and her defects again raises this question. Indeed, in random samples the size of the well preserved European bog bodies, would one expect to find even one case of a visible abnormality? The conditions seen in e.g. Zweeloo and Lindow III (Brothwell and Bourke, 1995) are uncommon at least, yet they appear in the bog samples. The survival of these individuals to adulthood shows that visible congenital abnormalities were tolerated in their communities but, that at some point in time, their abnormal physical condition led the same community to set them apart and see them as cursed or blessed persons, perfect victims/candidates for a sacrificial death.

If the life of Zweeloo Woman was indeed taken by members of her own local community, she might have lived in a settlement that was situated close to the present village of Aalden, which is situated to the west of Zweeloo. The findspot of Zweeloo Woman is situated within the boundaries of the village territory (Marke) of Aalden, which go back to the Middle Ages and probably to even earlier times. The eastern boundary is formed by the brook valley of the Aelder Stroom. The Roman period settlement in which she may have lived has not yet been found, but most likely it is still hidden under the plaggen soil ‘Aelder Esch’, situated to the south of Aalden (an indication of this might here an Early Medieval cemetery was excavated). The distance between the bog in which Zweeloo Woman was discovered and her (assumed) settlement is ca. 2.5-3 km. Hence, Aalden Woman would be a more appropriate name for this unfortunate individual.

## Acknowledgments

We thank Vincent van Vilsteren, curator of the Drents Museums of Assen, The Netherlands, for allowing us to study this specimen. We thank Karl Reinhardt, Scott Gardner and John Janovy for the fast and straightforward help with the identification of the liver fluke eggs. Astrid Grumer and Kati Dagefoerde are highly acknowledged for their help with the histological analysis.

## Notes

1. Now known as Groninger Instituut voor Archeologie/Groningen Institute of Archaeology.

2. Unfortunately the name of the anatomist involved is not reported.
3. See note 1.
4. Calibrated using Wincal25.
5. In a letter to one of the authors (WVDS) he writes that the woman will have been about 1.52 m tall.
6. Information provided to the senior author (WVDS) by F. Kuipers and J. Warmolts, Zweeloo, on 5 February 2010.
7. By the time of the discovery the peat bog no longer had his shape. Topographic maps from the 1920s show that Juffersveen had by then “broken up” into smaller parts.
8. See note 6.

## Bibliography

- Anderson T., Carter A.R. 1995, The First Archaeological Case of Madelung’s Deformity?, *International Journal of Osteoarchaeology* 5, 168- 173.
- Auerbach, B.M., Ruff, C.B. 2004, Human Body Mass Estimation: A Comparison of “Morphometric” and “Mechanical” Methods. *American Journal of Physical Anthropology* 125: 331-342.
- Aufderheide, A.C. 2003. *The Scientific Study of Mummies*, Cambridge (Cambridge University Press).
- Aufderheide, A.C., Rodriguez-Martin, C. 2006, *The Cambridge Encyclopedia of Human Paleopathology*, Cambridge (Cambridge University Press).
- Belin, V., Cusin, V., Viot, G., Girlich, D., Toutain, A., Moncla, A., Vekemans, M., Le Merrer, M., Munnich, A., Cormier-Daire, V. 1998, SHOX mutations in dyschondrosteosis (Léry-Weill syndrome), *Nature Genetics* 19, 67- 69.
- Benito-Sanz, S., Thomas, N.S., Huber, C., Gorbenko del Blanco, D., Aza- Carmona, M., Crolla, J.A., Maloney, V., Argente, J., Campos- Barros, A., Cormier- Daire, V., Heath, K.E. 2005, A novel class of pseudoautosomal region 1 deletions downstream of SHOX is associated with Léry-Weill dyschondrosteosis, *American Journal of Human Genetics* 77, 533- 544.
- Bertassoni, L.E., Marshall, G. W. 2009, Papain-gel degrades intact nonmineralized type I collagen fibrils, *Scanning* 31, 253- 258.
- Board of Trade 1957, *Women’s Measurement and Sizes*, London HMSO.
- Brothwell, D.R. 1981, *Digging up Bones*, London (British Museum- Natural History).
- Brothwell, D., Bourke, J.B. 1995, The Human Remains from Lindow Moss 1987- 8. In: R.C. Turner & R.G. Scaife (eds), *Bog Bodies, New Discoveries and New Perspectives*, London (British Museum Press), 52-58.

- Campillo, D., Malgosa, A. 1991, Braquimelia en un esqueleto procedente de la necropolis Tayaotica de "S'Illot de Porros" (Mallorca), *Acts of the IX Congreso Nacional de la Historia de la Medicina*, Zaragoza, 1179-1188.
- Campo, M., Robles, F.J., González, A. 1996, Un caso de deformidad de Madelung en la España Musulmana, in: A. Pérez-Pérez A (Ed.), *Salud, Enfermedad y Muerte en el Pasado*, Barcelona (Fund. Uriach), 179- 182.
- Canci, A., Marini, E., Mulliri, G., Usai, E., Vacca, L., Floris, G. and S. Borgognini Tarli, 2002, A Case of Madelung's Deformity in a Skeleton from Nuragic Sardinia, *International Journal of Osteoarcheology* 12, 173- 177.
- Chang, B.S., Uhm, C.S., Park, C.H., Kim, H.K., Lee, G.Y., Cho, H.H., Kim, M.J., Chung, Y.H., Song, K.W., Lim, D.S., Shin, D.H. 2006, Preserved skin structure of a recently found fifteenth-century mummy in Daejeon, Korea, *Journal of Anatomy* 209, 671- 680.
- Cummings, C., Rega, E. 2008, A Case of Dyschondrosteosis in an Anglo-Saxon Skeleton, *International Journal of Osteoarchaeology* 18, 431- 437.
- Connolly, R.C. 1990, Bloedgroepen. In: W.A.B. van der Sanden (ed.), *Mens en moeras – veenlijken in Nederland van de bronstijd tot en met de Romeinse tijd*, Assen (Drents Museum), 144- 150.
- Drie podagrissen 1843, Drenthe in vlugtige en losse omtrekken geschetst door drie podagrissen, Coevorden.
- Frayser, D.W., Horton, W.A., Macchiarelli, R., Mussi, M. 1987, Dwarfism in an adolescent from the Italian late Upper Paleolithic, *Nature* 330, 60- 62.
- Grigelioniene, G., Eklof, O., Ivarsson, S.A., Westphal, O., Neumeyer, L., Kedra, D., Dumanski, J., Hagenas, L. 2000, Mutations in short stature homeobox containing gene (SHOX) in dyschondrosteosis but not in hypochondroplasia, *Human Genetics* 107, 145- 149.
- Grine, F.E., Jungers, W.K., Tobias, P.V., Pearson, O.M. 1995, Fossil Homo femur from Berg Aukas, northern Namibia, *American Journal of Physical Anthropology* 26, 67– 78.
- Hakbijl, T. 1990, Insekten. In: W.A.B van der Sanden (ed.), *Mens en moeras – veenlijken in Nederland van de bronstijd tot en met de Romeinse tijd*, Assen (Drents Museum), 168-173.
- Holden, T.G. 1990, Taphonomic and methodological problems in reconstructing diet from ancient human gut and faecal remains, unpublished thesis, London.
- Huber, C., Cousin, V., Le Merrer, M., Mathieu, M., Sulmont, V., Dagoneau, N., Munnich, A., Cormier- Daire, V. 2001, SHOX point mutations in dyschondrosteosis, *Journal of Medical Genetics* 38, 323.
- Janko, M., Zink, A., Gigler, A.M., Heckl, W.M., Stark, R.W. 2010, Nanostructure and mechanics of mummified type I collagen from the 5300-year-old Tyrolean Iceman, *Proceedings of the Royal Society B: Biological Sciences* 277, 2301- 2309.
- Karadag, B., Bilici, A., Doventas, A., Kantarci F., Selcuk D., Dincer N., Oner Y.A., Erdinçler D.S. 2005, An unusual case of biliary obstruction caused by *Dicrocoelium dentriticum*, *Scandinavian Journal of Infectious Diseases* 37(5), 385- 388.



- Kauffman, H., Lagier, R., Baud, C. 1979, Un Cas de Nanisme par Dyschondrostéose au VI<sup>e</sup> Siècle à Genève (A case of dyschondrosteotic dwarfism from 6th century in Geneva), Association Internationale des Anthropologues de Langue Française, Actes du XIII Colloque Anthropologie et Médecine (Caen), 204- 211.
- Langer, L.O. Jr. 1965, Dyschondrosteosis, a heritable bone dysplasia with characteristic roentgenographic features, *American Journal of Roentgenology* 95, 178- 188.
- Le Bailly, M., Bouchet, F. 2010, Ancient dicrocoeliosis: Occurrence, distribution and migraine, *Acta Tropica* 115(3): 175- 180.
- Leopold, D. 1998, Identifikation unbekannter Toter, *Interdisziplinäre Methodik, Forensische Osteologie*. In: S. Berg, B. Brinkmann (ed. Schmid- Römschil), Vol 22, 304- 308.
- Léri, A., Weill, J. 1929, Une affection congénitale et symétrique du développement osseux: la dyschondrostéose, *Bulletin et Mémoire de la Société Médicale des Hôpitaux de Paris* 35: 1491- 1494.
- Lichtenstein, J.R., Sundaram, M., Burdge, R. 1980, Sex-influenced expression of Madelung's deformity in a family with dyschondrosteosis, *Journal of Medical Genetics* 17, 41- 43.
- Trotter, M., Gleser, G.C., 1952, Estimation of stature from long bones of American Whites and negroes, *American Journal of Physical Anthropology* 10(4), 355- 356, 463- 514.
- Maat, J.R., Van Den Bos, R.P.M., Aarents M.J. 2000, Manual for the preparation of ground sections for the microscopy of bone tissue, *Barge's Anthropologica* 7: 1- 17.
- Magi, B., Frati, E., Bernini, L., Sansoni A., Zanelli, G. 2009, *Dicrocoelium dendriticum*: a true infection? *Infezioni in Medicina* 17(2): 115-116.
- Martin, R. 1928, *Lehrbuch der Anthropologie in systematischer Darstellung: mit besonderer Berücksichtigung der anthropologischen Methoden*, 2. vermehrte Aufl., 3 Bde. (Jena).
- Mekota, A.M., Vermehren, M. 2005. Determination of optimal rehydration, fixation and staining methods for histological and immunohistochemical analysis of mummified soft tissues, *Biotechnique and Histochemistry* 80(1), 7- 13.
- McHenry, H.M. 1992. Body size and proportions in early Hominids, *American Journal of Physical Anthropology* 87, 407– 431.
- Mongelli, V., Campana, S., Felici, Cr., Lubritto C., Fornaciari, G. 2010, A case of acromesomelic dysplasia of the 7th century AD (Pieve di Pava, Siena, Italy). Abstract book of the 18th European Meeting of the Paleopathology Association (Vienna), 174.
- Mulisch, M., Welsch, U. 2010, *Romeis - Mikroskopische Techniken*, Spektrum Akademischer Verlag (18. Auflage).
- Osinga, J., C.H.C.M. Buys 1990, DNA-onderzoek. In: W.A.B van der Sanden (ed.), *Mens en moeras – veenlijken in Nederland van de bronstijd tot en met de Romeinse tijd*, Assen (Drents Museum), 125- 127.
- Osinga, J., C.H.C.M. Buys & W.A.B. van der Sanden 1992, DNA and the Dutch bog bodies, *Ancient DNA Newsletter* 1, 21- 22.

- Otranto, D., Traversa D. 2002, A review of dicrocoeliosis of ruminants including recent advances in the diagnosis and treatment, *Veterinary Parasitology* 107(4): 317-335.
- Paap, N.A. 1990, Parasieten. In: W.A.B. van der Sanden (ed.), *Mens en moeras – veenlijken in Nederland van de bronstijd tot en met de Romeinse tijd*, Assen (Drents Museum), 162- 167.
- Paige, M.F., Lin, A.C., Goh, M.C. 2002, Real-time enzymatic biodegradation of collagen fibrils monitored by atomic force microscopy, *International Biodeterioration & Biodegradation* 50, 1- 10.
- Pearson, K. 1899, *Mathematical contributions to the theory of evolution. V. On the reconstruction of the stature of prehistoric races* *Philosophical Transactions of the Royal Society of London Series A* 192, 169- 244.
- Petska, J.M., Barvencick, Fl., Beil F.T., Marshall R.P., Jopp E., Schilling A.F., Bauerochse A., Fansa, M., Püschel K., Amling, M. 2010, Skeletal analysis and comparison of bog bodies from Northern European peat bogs, *Naturwissenschaften* 97: 393- 402.
- Pyatt, F.B., Beaumont, E.H., Buckland, P.C., Lacy, D., Storm, E.E. 1991, An examination of the mobilisation of elements from the skin and bone of the bog body Lindow II and a comparison with Lindow III, *Environmental Geochemistry and Health* 13: 153-159.
- Ross, J.L., Bellus, G., Scott, C.I. Jr., Abboudi, J., Grigelioniene, G., Zinn, A.R. 2001, Phenotypes associate with SHOX deficiency, *Journal of Clinical Endocrinology & Metabolism* 86, 5674- 5680.
- Ross, J.L., Scott, C.I. Jr., Marttila, P., Kowal, K., Nass, A., Papenhausen, P., Abboudi, J., Osterman, L., Kushner, H., Carter, P., Ezaki, M., Elder, F., Wei, F., Chen, H., Zinn, A.R. 2003, Mesomelic and rhyzomelic short stature: the phenotype of combined Léry-Weill dyschondrosteosis and achondroplasia or hypocondroplasia, *American Journal of Medical Genetics* 116A, 61- 65.
- Ruff, C.B., Scott, W.W., Liu, A.Y-C. 1991, Articular and diaphyseal remodelling of the proximal femur with changes in body mass in adults, *American Journal of Physical Anthropology* 86, 397–413.
- Sanden, W.A.B. van der (ed.) 1990, *Mens en moeras – veenlijken in Nederland van de bronstijd tot en met de Romeinse tijd*, Assen (Drents Museum).
- Sanden, W.A.B. van der 1990a, *Veenlijken in Nederland, een overzicht*. In: W.A.B. van der Sanden (ed.), *Mens en moeras – veenlijken in Nederland van de bronstijd tot en met de Romeinse tijd*, Assen (Drents Museum), 46- 77.
- Sanden, W.A.B. van der 1990b, *De vondstgeschiedenis*. In: W.A.B. van der Sanden (ed.), *Mens en moeras – veenlijken in Nederland van de bronstijd tot en met de Romeinse tijd*, Assen (Drents Museum), 80- 93.
- Sanden, W.A.B. van der 1990c, *De ouderdomsbepaling*. In: W.A.B. van der Sanden (ed.), *Mens en moeras – veenlijken in Nederland van de bronstijd tot en met de Romeinse tijd*, Assen (Drents Museum), 94- 100.
- Sanden, W.A.B. van der 1990d, *De laatste maaltijd (1), de macroresten*. In: W.A.B. van der Sanden (ed.), *Mens en moeras – veenlijken in Nederland van de bronstijd tot en met de Romeinse tijd*, Assen (Drents Museum), 151- 157.
- Sanden, W.A.B. van der 1996, *Through nature to eternity – the bog bodies of northwest Europe*, Amsterdam (Batavian Lion International).

- Sanden, W.A.B. van der 2002, Mens en moeras 3: nieuwe veenlijk-vondsten in Noord-Nederland, Nieuwe Drentse Volksalmanak 119, 168-185.
- Sanden, W.A.B. van der, C. Haverkort & J. Pasveer 1991-1992, Een menselijk skelet uit de Aschbroeken bij Weerdinge (Drenthe) – reconstructie van een misverstand, *Palaeohistoria* 33- 34, 155- 163.
- Schilling, A.F., Kummer T., Marshall R.P., Bauerochse, A., Jopp, E., Püschel K., Amling, M. 2008, Brief communication: Two and Three-Dimensional Analysis of Bone Mass and Microstructure in a Bog Body From the Iron Age, *American Journal of Physical Anthropology* 135: 479- 483.
- Shears, D.J., Vassal, H.J., Goodman, F.R., Palmer, R.W., Reardon, W., Superti-Furga, A., Scambler, P.J., Winter, R.M. 1998, Mutation and deletion of the pseudoautosomal gene SHOX cause Léri-Weill dyschondrosteosis, *Nature Genetics* 19, 70- 73.
- Siegmund, F. 2010. Die Körpergröße der Menschen in der Ur- und Frühgeschichte Mitteleuropas und ein Vergleich ihrer anthropologischen Schätzmethode, Norderstedt.
- Stoddart, R.W. 1995, The bones of the Zweeloo Woman, unpublished report, Manchester University.
- Stücker, M., Bechara, F.G., Bacharach-Buhles, m., Pieper, P., Altmeyer P. 2001, What happens to skin after 2000 years in a bog?, *Der Hautarzt* 52, 316- 321.
- Troostheide, C.D. 1990, De laatste maaltijd (2): de stuifmeelkorrels. In: W.A.B. van der Sanden (ed.), *Mens en moeras – veenlijken in Nederland van de bronstijd tot en met de Romeinse tijd*, Assen (Drents Museum), 158- 161.
- Trotter, M. 1970, Estimation of stature from intact long bones. In: T.D. Stewart (ed.), *Personal Identification in Mass Disasters*, Washington DC (Smithsonian Institution Press), 71- 83.
- Uytterschaut, H.T. 1985, Determination of skeletal age by histological methods, *Zeitschrift für Morphologie und Anthropologie* 75, 331- 340.
- Uytterschaut, H.T. 1990a, De invloed van het veen op de lijken. In: W.A.B. van der Sanden (ed.), *Mens en moeras – veenlijken in Nederland van de bronstijd tot en met de Romeinse tijd*, Assen (Drents Museum), 101-103.
- Uytterschaut, H.T. 1990b, De anatomische beschrijving. In: W.A.B. van der Sanden (ed.), *Mens en moeras – veenlijken in Nederland van de bronstijd tot en met de Romeinse tijd*, Assen (Drents Museum), 104-124.
- Uytterschaut, H.T. 1990c, Trauma en pathologie. In: W.A.B. van der Sanden (ed.), *Mens en moeras – veenlijken in Nederland van de bronstijd tot en met de Romeinse tijd*, Assen (Drents Museum), 129-135.
- Uytterschaut, H.T. 1990d, Het haar, in: W.A.B. van der Sanden (ed.), *Mens en moeras – veenlijken in Nederland van de bronstijd tot en met de Romeinse tijd*, Assen (Drents Museum), 136-140.
- Waldron, A. 2000, A case of dyschondrosteosis from Roman Britain, *Journal of Medical Genetics* 37, e27 <http://jmedgenet.com/cgi/content/full/37/10/e27>
- White, T.D., Folkens P.A. 2005, *The Human Bone Manual*, London (Elsevier Academic Press).

Wieberdink, G.L. 1990, Historische Atlas Drenthe. Chromotopografische Kaart des Rijks 1: 25.000, Den Ilp (Uitgeverij Robas Producties).

Zeist, W. van 1952, Zur Datierung einer Moorleiche, Acta Botanica Neerlandica 1, 546- 550.

Zeist, W. van 1956, Palynologisch onderzoek van enkele Drentse veenlijken, Nieuwe Drentse Volksalmanak 74, 199- 209.

# ACKNOWLEDGEMENTS

I would like to seize the occasion to thank those organisations, the Deutsche Forschungsgemeinschaft (DFG) cluster of excellence ‘Nanosystems Initiative Munich’ (NIM) and the European Academy of Bolzano (EURAC), whose financial support, and the people whose mental and physical support, made this thesis possible.

For their supervision, the fruitful meetings and for giving me the opportunity to work on this thesis, I particularly like to thank Dr. Robert W. Stark and Dr. Albert Zink. Many thanks also for enabling the stays and studies in Bolzano, for the pick-up and delivery services and the pleasant working atmosphere. I am also grateful to Dr. Wolfgang W. Schmahl and Dr. Wolfgang M. Heckl, for giving me the opportunity to conduct part of my investigations in their laboratories, and using their instruments. Moreover, I would like to thank Dr. Stefan Sotier for introducing me to the Nanoscience group at the ‘Sektion Kristallographie’ of the LMU.

Further special thanks to Dr. Michael Bauer for sharing his expertise on laser technology and Raman spectroscopy, as well as him, Polina Davydovskaya and Özlem Simsek for the enjoyable and pleasant collaborations and teamwork. Special thanks also to Florian Gärtner and Zerkah Ahmed from the ‘Deutsches Herzzentrum’ and Katharina Klein from the clinical centre ‘Rechts der Isar’ for supporting me with whatever was needed and for their medical and biological expertise.

Thanks also to Dr. Alexander Gigler for assistance with the Witec system and organising the annual interdisciplinary ‘group meeting’ and to Dr. Marc Hennemeyer for his guidance with microfluidics and blood processing.

Finally for the extraordinary pleasant working conditions, the marvellous working atmosphere, the numerous fruitful scientific and non-scientific discussions as well as for all the social activities, I would like to thank Dr. Rico Gutzler and Dr. Hermann Walch as well as the past and present members of the AFM and the STM groups, namely Dr. Markus Lackinger, Stephan Kloft, Thommi Sirtl, Jürgen Dienstmaier, Georg Eder, Christoph Heining, Stefan Schlögl, Johanna Eichhorn, Wentao Song, Kim Lieu Phuong, Dr. Ferdinand Walther, Dr. Ayhan Yurtsever, Maria Wieland, Anne-Kathrin Maier, and Sophie Lappe. Only because of you will I miss the meals in the canteen.

Last but not least, honour to whom honour is due; my family and Astrid, for supporting me before and throughout my work. You are the ones this work is dedicated to.

Thank you!

# CURRICULUM VITAE

## Personal

Name                      Marek Janko  
Born in                     München

## Education

|               |   |                       |
|---------------|---|-----------------------|
| 1996 – 1998   | Technical secondary school, Staatliche Fachoberschule                                 | München               |
| 1999 – 2004   | Undergraduate Study, University of Applied Science<br>and Nottingham Trent University | München<br>Nottingham |
| 2005 – 2007   | Graduate Study, University of Applied Science   | München               |
| 2008 – 2011   | PhD candidate, Ludwig-Maximilians-Universität   | München               |
| since 05/2011 | Research fellow, Technische Universität Darmstadt                                     | Darmstadt             |